Atmospheric drivers of surface melting on the Larsen C ice shelf, Antarctic Peninsula

Ella Gilbert

degree of Doctor of Philosophy (PhD)

University of East Anglia, School of Environmental Sciences and
British Antarctic Survey

A thesis submitted to the School of Environmental Sciences of the University of East Anglia in partial fulfilment of the requirements for the degree of Doctor of Philosophy

March 2020

This copy of the thesis has been supplied on condition that anyone who consults it is understood to recognise that its copyright rests with the author and that use of any information derived therefrom must be in accordance with current UK Copyright Law. In addition, any quotation or extract must include full attribution.

Abstract

Observational data and high resolution (<4 km grid spacing) Met Office Unified Model (MetUM) output is used to investigate the dominant causes of surface melting on the Larsen C ice shelf. In the first two parts of the thesis, a case study approach is used to examine the role of wintertime foehn winds and summertime cloud phase on the surface energy balance (SEB) of Larsen C, and therefore surface melting. Firstly, wintertime foehn events are shown for the first time to drive significant and unseasonal surface melting by greatly enhancing surface sensible heat fluxes. Secondly, it is demonstrated that cloud phase, and particularly liquid water content, strongly influences the SEB and surface melting. More accurate model representations of cloud phase are shown to reduce biases in SEB terms and melt. As part of this work, an optimised MetUM configuration is developed for the Antarctic Peninsula.

Thirdly, the final part of the thesis presents and analyses a novel, multi-decadal (1998-2017) model hindcast for Larsen C. The hindcast reproduces observed patterns of foehn-driven melt, making it one of the first long model simulations to do so. Solar radiation is the dominant driver of melting, but cloud phase is shown to determine its extent and duration via feedbacks on temperature and energy fluxes, and foehn winds are especially important for producing melt in non-summer seasons. Large-scale patterns of climate variability like the Southern Annular Mode (SAM) establish conditions for foehn- and cloud-mediated melting to occur.

This advanced understanding of processes contributing to surface melting on Larsen C establishes a baseline for future projections. If recent trends towards a more positive SAM and higher temperatures continue in future, surface melting could increase enough to destabilise the ice shelf, potentially contributing to sea level rise.

Access Condition and Agreement

Each deposit in UEA Digital Repository is protected by copyright and other intellectual property rights, and duplication or sale of all or part of any of the Data Collections is not permitted, except that material may be duplicated by you for your research use or for educational purposes in electronic or print form. You must obtain permission from the copyright holder, usually the author, for any other use. Exceptions only apply where a deposit may be explicitly provided under a stated licence, such as a Creative Commons licence or Open Government licence.

Electronic or print copies may not be offered, whether for sale or otherwise to anyone, unless explicitly stated under a Creative Commons or Open Government license. Unauthorised reproduction, editing or reformatting for resale purposes is explicitly prohibited (except where approved by the copyright holder themselves) and UEA reserves the right to take immediate ‘take down’ action on behalf of the copyright and/or rights holder if this Access condition of the UEA Digital Repository is breached. Any material in this database has been supplied on the understanding that it is copyright material and that no quotation from the material may be published without proper acknowledgement.

Contents

1 Introduction 1

2 Literature Review 3

2.1 Climatological setting . . . 3
2.2 The Larsen C ice shelf . . . 5
2.3 Antarctic Peninsula ice shelf glaciology . . . 6
2.3.1 Recent ice shelf changes on the Antarctic Peninsula . . . 6
2.3.2 The role of surface melting in ice shelf disintegration and glacier dynamics 7
2.3.3 Observed surface melting on Larsen C . . . 8
2.3.4 High-resolution regional atmospheric modelling on Larsen C . . . 9
2.3.5 Recent surface melt trends on Larsen C . . . 11
2.4 Foehn winds on Larsen C . . . 12
2.4.1 Definitions . . . 12
2.4.2 The effect of foehn on the surface energy balance . . . 15
2.4.3 Trends in foehn frequency . . . 16
2.5 The importance of cloud for the surface energy balance on Larsen C . . . 17
2.5.1 Cloud properties . . . 17
2.5.2 Observations of Antarctic cloud . . . 20
2.5.3 Model representation of cloud . . . 21
2.6 Current knowledge gaps . . . 22

3 Data and methods 25

3.1 Data description . . . 25
3.1.1 AWS measurements, instrumentation and data treatment . . . 25
3.1.2 Aircraft measurements, instrumentation and data treatment . . . 30
3.2 Model description . . . 32
3.2.1 Core physics and model description . . . 35
3.2.2 Model domains and methodology . . . 35

3.2.3 Updated orography dataset 36
3.2.4 Important parameterisation schemes 38

4 The influence of foehn winds on surface melting over Larsen C in non-summer seasons 43
4.1 Introduction 43
4.1.1 Aims and objectives 43
4.1.2 Research questions 44
4.1.3 Novelty of research 44
4.2 Research question 1: Do foehn events occur on Larsen C during winter? . . . 44
4.2.1 Synoptic conditions 45
4.2.2 Surface conditions 45
4.2.3 Model representation of atmospheric vertical structure during foehn . 50
4.2.4 The effect of higher resolution on the representation of foehn 53
4.2.5 The effect of improved orography on the representation of foehn . . . 55
4.2.6 Can biases be improved by choosing a more representative grid point? 57
4.3 Research question 2: What is the effect of wintertime foehn on the SEB of Larsen C? 58
4.4 Research question 3: Do wintertime foehn events cause melting on Larsen C? 63
4.5 Conclusion 67

5 The effect of summertime cloud phase on surface melting over Larsen C 69
5.1 Introduction 69
5.1.1 Aims and objectives 69
5.1.2 Research questions 69
5.1.3 Novelty of research 70
5.2 Data, modelling and methods 70
5.2.1 Methods 70
5.2.2 Data 72
5.2.3 Model experiments 72
Regional atmosphere physics configurations 72
Double moment cloud microphysics 74
5.3 Results and discussion 75
5.3.1 Observed cloud phase during f150 and f152 76

5.3.2 Research question 1: Is the MetUM able to represent observed cloud phase and microphysics? 76
5.3.3 Research question 2: How does cloud phase influence the surface energy balance in observations and the MetUM? 80
5.3.4 Research question 3: Can a double moment microphysics scheme improve simulations of cloud phase? 82
Double-moment model representation of case f152 82
Double-moment model representation of case f150 84
5.3.5 Research question 4: How does summertime cloud phase influence the surface energy balance during the entire OFCAP period? 88
5.3.6 Summary of optimisations to the MetUM to better represent summertime mixed phase cloud and surface energy balance over Larsen C 92
5.4 Summary and conclusions 92

6 Simulated surface melting on Larsen C in a 20-year hindcast of the Antarctic Peninsula 95
6.1 Introduction 95
6.1.1 Aims and objectives 95
6.1.2 Research Questions 95
6.1.3 Novelty of research 96
6.2 Hindcast model configuration 98
6.3 Validation 99
6.4 Research question 1: How does the surface energy balance vary throughout the year? 100
6.5 Research question 2: How does cloud influence surface melting on Larsen C? 104
6.5.1 The influence of cloud on the surface energy balance and surface melting105
6.6 Research question 3: Where and when do foehn events occur? 106
6.6.1 Diagnosis methods 106
6.6.2 Modelled foehn frequency 109
6.6.3 MAM 2016: a high-foehn season 110
6.6.4 Spatial patterns of foehn occurrence 111
6.6.5 Correlations between modelled foehn and SAM index 115
6.7 Research questions 4 and 5: How does surface melting vary in time and space? 116
6.7.1 Comparing hindcast- and satellite-derived estimates of melt 116

6.7.2 Modelled meltwater production 116
6.8 Research question 6: What are the most important drivers of surface melting on Larsen C 1998-2017? 121
6.8.1 Time series correlations 121
6.8.2 Spatial correlations 126
6.8.3 Regimes influencing melt on Larsen C 127
6.9 Summary and conclusions 137

7 Summary and conclusions **141**

Appendices **147**

A Appendix: Kuipers Munneke et al. (2018) **149**

B Appendix: Gilbert et al. (2020) **159**

C Appendix: Additional sensitivity testing of the RA1M_mod model configuration for use in the model hindcast **175**
C.1 RA1M_mod model sensitivity testing 175
C.1.1 Sensitivity tests with amended boundary layer mixing length 175
C.1.2 The importance of ground heat flux, G_S 176
C.2 Summary of sensitivity tests 180

D Appendix: Detailed hindcast validation **181**

E Appendix: Diagnosing foehn events from hindcast model output, data processing and sensitivity testing **193**
E.1 Methods for detecting foehn in model output and observations 193
E.1.1 Optimum thresholds for foehn detection on Larsen C using the surface method for observations 194

F Appendix: Modelled seasonal mean foehn occurrence during the hindcast period **199**

G Appendix: Seasonal mean derived "foehn index" during the hindcast period **201**

H Appendix: Hindcast regime criteria and regions used for compositing **203**
H.1 Data sources and treatment 204

Bibliography **207**

List of Figures

2.1 Map of the Antarctic Peninsula region showing the Larsen C ice shelf and its tributary inlets, plus the remnant Larsen B ice shelf (labelled "Scar Inlet") and the Larsen A and B embayments. The main inlets referred to in the thesis are indicated as green triangles, and the location of ice shelf grounding lines is shown as a teal line. The mean height of orography is indicated with coloured contours, and is derived from the RAMP2 200 m elevation model (Liu et al., 2015). . . . 5

3.1 Locations of the AWSs used in the thesis. Topography is shaded, where darker colours indicate higher terrain. 26

3.2 Images of the standard "Type II" AWS set-up used by IMAU before 2014 and the latest "iWS" setup used at Cabinet Inlet. Panels a) and b) show the set-up of AWS 17 (Scar Inlet) and detail of the instrumentation, respectively, while panels c) and d) show the same for AWS 18 (Cabinet Inlet). All images are from IMAU. . 29

3.3 Schematic illustration of instrumentation on the British Antarctic Survey DHC Twin Otter aircraft. 31

3.4 Model domains used in the thesis. The 4.4 km and 1.5 km domains are used in Chapter 4, while only the 1.5 km domain is used in Chapter 5. The 4.0 km domain is used in Chapter 6 only. 34

3.5 Difference between default and updated surface elevation (orography) and land-sea mask (LSM) files used in MetUM runs. The default orography and land-sea mask are based on the 1 km resolution GLOBE dataset (Hastings and Dunbar, 1999). The updated land-sea mask is derived from the SCAR Antarctic Digital Database, and updated orography is based on the Ohio State University RAMP 200 m digital elevation model (Liu, 1999), produced by Tony Phillips at BAS. Blue colours indicate where land is removed from the updated land-sea-mask compared to the default, and where surface elevation is lower than in the default, while red colours indicate the opposite. 37

4.1 Synoptic conditions over the Antarctic Peninsula at the onset of foehn conditions: a) 12:00 UTC on 9 May and b) 12:00 UTC on 25 May, derived from ERA-5 reanalysis at 31 km grid spacing. Colour contours show 1.5 m temperature in degrees celsius, unfilled contours show mean sea level pressure and overlaid vectors show 750 hPa winds in m s^{-1}. A 10 m s^{-1} scale vector is included at top left for reference. 45

4.2 Time series of near-surface meteorological variables during CS1: a) relative humidity, b) wind speed, c) 1.5 m air temperature, d) surface temperature. In all panels, the black line shows observations from the Cabinet Inlet AWS, while the blue and pink lines show the model output at 4.4 and 1.5 km resolution, respectively. 47

4.3 Time series of near-surface meteorological variables during CS2: a) relative humidity, b) wind speed, c) 1.5 m air temperature, d) surface temperature, as in Figure 4.2. 47

4.4 Modelled near-surface conditions shortly after the onset of foehn conditions in a) CS1 at 12:00 UTC on 10 May and b) CS2 at 00:00 UTC on 26 May from the 1.5 km resolution model domain. Filled contours show 1.5 m air temperatures, while vectors indicate 10 m wind speeds. A scale vector of 20 m s^{-1} is shown top centre for reference. 48

4.5 Scatterplots of observed vs. modelled (1.5 km resolution) surface variables at the Cabinet Inlet AWS during CS1. Correlations (r values) are given in the top right hand corner of each panel: bold values indicate statistical significance at the 99% level. The dashed line in each plot indicates perfect agreement between model and observations. Panels a – d show surface meteorological variables: surface temperature, T_S; near-surface air temperature, T_{air}; relative humidity; and wind speed; and panels e – h show SEB terms: downwelling longwave, $LW_{\downarrow}$; downwelling shortwave, $SW_{\downarrow}$; net radiative, R_{net} and melt, E_{melt}, fluxes. 51

4.6 Scatterplots of observed vs. modelled surface variables at the Cabinet Inlet AWS during CS2, with details as in Figure 4.5. 52

4.7 Vertical cross-sections through the Antarctic Peninsula mountains into Cabinet Inlet at the onset of foehn during CS1 (top row, panels a and b) on 10 May at 12:00 UTC, and during CS2 (bottom row, panels c and d) on 26 May 2016 at 00:00 UTC. Filled colour contours show potential temperature (in degrees celsius) and contours show zonal wind velocity, in m s^{-1}. The first column (panels a and c) show 4.4 km MetUM output, and the second column (panels b and d) show 1.5 km MetUM output. A similar plot has been published in Kuipers Munneke et al. (2018). 54

4.8 Near-surface (1.5 m) air temperatures and 10 m wind speeds during non-foehn (left column; panels a and c) and foehn conditions (right column; panels b and d) during CS2 using the default MetUM orography and land-sea mask (top row; panels a and b) and updated orography and land-sea mask (bottom row; panels c and d). Non-foehn panels show hourly mean conditions for the period 23:00 UTC 22 May - 00:00 UTC 23 May and foehn panels show hourly mean conditions for the period 11:00 - 12:00 UTC 26 May. Filled contours show 1.5 m air temperatures, while vectors show 10 m wind speeds. A scale vector of 10 m s^{-1} is given at top centre for reference. 56

4.9 Time series of surface meteorological variables during CS2 in AWS observations at Cabinet Inlet (black) and 1.5 km MetUM output using the default MetUM orography and land-sea mask (purple) and updated set-up (turquoise). Panel a) shows relative humidity; b) 10 m wind speed; c) near-surface air temperature; and d) surface temperature. 57

4.10 Time series of total SEB during CS1, May 9-–15, in a) observations, and b) and c) 1.5 km model output. Panel b) includes directly modelled melt flux, while panel c) shows the melt flux calculated using observed surface temperatures (as discussed in main text). Net SW and LW fluxes are shown in purple and red, respectively, sensible and latent heat fluxes are shown in orange and blue, respectively, and melt flux is shown in dark grey. All fluxes are given in W m^{-2}. 60

4.11 Time series of total SEB during CS2, May 23–30, with details as in Figure 4.10. 61

4.12 Time series of surface energy fluxes at Cabinet Inlet during CS1, May 9 – 15, in observations (black line) and model output at 1.5 km (pink) and 4.4 km (blue) resolution. Panels show individual surface energy balance (SEB) components: a) downwelling shortwave, $SW_{\downarrow}$; b) downwelling LW, $LW_{\downarrow}$; c) sensible heat, H_S; and d) latent heat, H_L fluxes. 63

4.13 Time series of surface energy fluxes at Cabinet Inlet during CS2, May 23 – 30, with details as in Figure 4.12. 64

4.14 Energy available for melting at the Cabinet Inlet AWS from November 2014 until September 2016. The blue lines show instantaneous melt fluxes (in W m^{-2}), while the pink line shows cumulative meltwater production over the entire time series in units of mm w.e.. 66

5.1 The inner 1.5 km resolution MetUM model domain used in this chapter, centred on the Larsen C Ice Shelf. The model's surface elevation is indicated by shaded contours. The flight track of the f150 (a) and f152 (b) case studies is also shown, where the aircraft's altitude is indicated by the scale shown on the right, and the location of AWS 14 is marked with a cross. 71

5.2 Mean vertical profiles of cloud a) ice and b) liquid mass mixing ratios, in g kg^{-1}, and mean modelled cloud gridbox volume fractions of c) ice cloud and d) liquid cloud during f152 when the aircraft was sampling over Larsen C. Observations are shown in a) and b) with the solid black line and model output above AWS 14 is shown in all panels with coloured lines with markers. Solid lines with heavy markers indicate the two "base" configurations, while dashed lines with lighter markers show their modified counterparts. The experimental configurations are detailed in Table 5.1. 77

5.3 As in Figure 5.2, observed and modelled vertical profiles of a) water vapour mass mixing ratio, in g kg^{-1}, and b) air temperature (in degrees celsius) during flight f152. Colours and markers are as indicated in Figure 5.2. 80

5.4 As in Figure 5.2, but showing mean vertical profiles of cloud ice and liquid mass mixing ratios from double-moment experiments using CASIM (Cooper, DeMott2010 and no ice) during f152. 83

5.5 Time series of modelled ice and liquid water paths, plus downwelling LW and SW radiation over AWS 14 during f152 on 18 January 2011 in RA1M_mod. Panel a) shows mean modelled ice (IWP) and liquid (LWP) water paths, both in g m^{-2}, and indicated with the blue line with starred markers, and brown line with triangle markers, respectively. Panel b) shows downwelling LW and SW radiation ($LW_{\downarrow}$ and $SW_{\downarrow}$, respectively, both in W m^{-2}) and indicated with the green line with crossed markers and blue line with circle markers, respectively. The approximate time during which the aircraft was sampling over Larsen C is indicated with the grey shading. 85

5.6 Mean longitudinal transects (at ~67.0°S) of in-cloud liquid mass mixing ratios, in g kg^{-1}, during f150 when the aircraft was sampling over Larsen C. Observations are shown in turquoise, with individual data points indicated with square markers and the transect mean given with the solid line. The total in-cloud observed mean liquid mass mixing ratio for the entire flight is shown as a dashed black line. Other coloured lines indicate the various experiments examined during f150: RA1M_mod, Cooper, DeMott2010, no ice and RH_{crit} = 0.85 (details in Table 5.1). 86

5.7 Scatterplots of observed energy available for melting (E_{melt}) against a) downwelling shortwave ($SW_{\downarrow}$) and b) downwelling longwave ($LW_{\downarrow}$) at AWS 14. Data plotted are instantaneous values outputted at 30-minute intervals. Pearson correlation coefficients, significant at the 99% level, are given at top centre of each panel. . 87

5.8 Mean surface temperature, T_S during the OFCAP period in observations (black) and as modelled by the RA1M_mod simulation (blue, with circle markers). . . . 91

5.9 As in Figure 5.8, but for mean modelled melt flux, E_{melt}, during the OFCAP period. 91

6.1 Scatterplots of observed vs. modelled daily means of surface variables at AWS 14. Correlation coefficients (r values) are given in the bottom right hand corner of each panel: all values are statistically significant at the 99% level. The dashed line in each plot indicates perfect agreement between model and observations. Panels a – d show surface meteorological variables: surface temperature, T_S; near-surface air temperature, T_{air}; relative humidity; and wind speed; and panels e – h show surface energy budget terms: downwelling longwave, $LW_{\downarrow}$; downwelling shortwave, $SW_{\downarrow}$; net radiative, R_{net} and melt, E_{melt}, fluxes. 101

6.2 Mean modelled diurnal cycle, averaged over each season, of SEB components during DJF (top row, panels a and b) and JJA (bottom row, panels c and d) at ice shelf (first column, panels a and c) and inlet stations (second column, panels b and d) during 1998-2017. The sum of all fluxes, E_{tot}, is shown in black. For ease of understanding, the diurnal cycle is presented in local time such that local noon is at 12:00 h (UTC -4 h), equivalent to 16:00 UTC. 103

6.3 Composited mean modelled meteorological conditions and melt flux anomalies during "cloudy" (top row, panels a-d) and "clear" (bottom row, panels e-h) periods in summer (DJF) and winter (JJA) over Larsen C during the hindcast period, using the thresholds of Kay et al. (2008) given in Table 6.2. Panels a, c, e and g show synoptic conditions, where coloured shading shows the mean daily maximum 1.5 m air temperature anomaly (in °C) during periods when each condition is diagnosed, while contours and vectors show the mean mean sea level pressure (in hPa) and 10 m winds (in m s^{-1}) during each regime, respectively. A wind speed scale vector of 10 m s^{-1} is given at top left for reference. Panels b, d, f and h show mean daily mean melt flux anomalies (in W m^{-2}) across Larsen C associated with each regime. 107

6.4 Mean modelled synoptic meteorological conditions and surface flux anomalies during 15 April – 31 May 2016. Panel a) shows mean modelled meteorological conditions, where colours indicate the mean daily maximum 1.5 m air temperature anomaly (in °C), contours show mean mean sea level pressure (hPa) and vectors show mean 10 m wind speed and direction. Panels b) to f) show flux anomalies, in W m^{-2}, relative to the 1998-2017 model climatology for 15 April – 31 May, of LW_{net}, H_L, H_S, E_{tot} and E_{melt}, respectively. In all panels, blue colours indicate negative anomalies while red colours show positive anomalies. 112

6.5 Mean meltwater production over Larsen C during 15 April – 31 May 2016. Panel a) shows the maximum cumulative melt produced along an east-west transect, indicated by the grey box in panel b). Panel b) shows the mean cumulative meltwater production anomaly with respect to the 1998-2017 model climatology for 15 April – 31 May. 113

6.6 Mean percentage of time over the period 1998-2017 where foehn conditions are diagnosed over the model domain, using the surface-based foehn diagnosis method of Turton et al. (2018) with an additional requirement, as in King et al. (2017), that there be a westerly wind component ($u_{Z1} \geq 2.0$ m s^{-1}). See text for more details. The 50 m elevation contour (approximately the height of the ice shelf at the grounding line), is shown. 114

6.7 Time series of total seasonal foehn frequency diagnosed from model output at inlet and ice shelf stations (coloured lines) against seasonally-averaged SAM index, after Marshall (2003). Foehn frequency and SAM index are both shown as seasonal means. 115

6.8 Mean melt duration (in number of melt days per melt season) over the Larsen C ice shelf in satellite observations and the hindcast. Panel a) shows the mean number of melt days per melt season calculated from QSCAT morning and ASCAT satellite retrievals during the period 1999/2000 to 2016/2017, and is reproduced from Bevan et al. (2018) "Decline in Surface Melt Duration on Larsen C Ice Shelf Revealed by The Advanced Scatterometer (ASCAT)" *Earth & Space Science* 5, doi: 10.1029/2018EA000421. Copyright (c) 2018, the authors, under Creative Commons CC BY-NC 3.0 license. Panel b) shows the annual mean number of days per melt year where melting is modelled during at least one 3-hour period over the Antarctic Peninsula model domain for the same period. The plot is designed for comparison with both Luckman et al. (2014) and Bevan et al. (2018) and uses the same colour scale. The grey contour shows where annual mean modelled melt duration is equal to 50 days per year. 117

6.9 Seasonal SAM index and annual mean and maximum cumulative meltwater production rates across the Larsen C ice shelf in each melt year during the hindcast simulation, in mm w.e. yr^{-1}. The seasonal mean SAM index is shown with the blue line in panel a and is calculated after Marshall (2003), while cumulative melt production is shown in panel b. The region over which the totals are calculated is shown in Figure H.1. 120

6.10 Total annual cumulative snow melt amount (in mm meltwater equivalent per year, mm w.e. yr^{-1}) across the Larsen C ice shelf for each melt year (August - July, defined as in Luckman et al., 2014 and Bevan et al., 2018) in the period 1998-2017, plus the mean of all full melt years (bottom right panel). The 50 m elevation contour is given, approximately the height of the modelled ice shelf at the grounding line. 122

6.11 Pearson correlation coefficient across the Larsen C ice shelf between derived foehn index, FI (see main text), and simulated melt amount during a) MAM and b) SON. Areas where the correlation is significant at the 90% level are indicated with shading and stippling. 126

6.12 Composited mean conditions during the "high melt" regime (melt amount > 75^{th} percentile) for all seasons in the hindcast. Panels a) to d) show mean synoptic meteorological conditions, where coloured shading shows the mean daily maximum 1.5 m air temperature throughout this period, and contours and vectors give mean mean sea level pressure and 10 m winds, respectively. Panels e) to h) show seasonal mean melt flux anomalies relative to the 1998-2017 model climatology. 131

6.13 Composited mean conditions during the "low melt" regime (melt amount < 25^{th} percentile) during DJF in the hindcast. Panel a) shows synoptic meteorological conditions, with colours, vectors and contours as in panels a - d of Figure 6.12. Panel b) shows seasonal mean melt flux anomalies, as in panels e - h of Figure 6.12. 132

6.14 Composited mean synoptic meteorological conditions and mean E_{melt} anomalies in DJF associated with three regimes that reduce E_{melt} relative to climatology: the barrier wind ("barrier", panels a and b), negative SAM ("SAM-", panels c and d) and deep ASL ("ASL", panels e and f) regimes. Colours, contours and vectors are as in previous plots. 134

6.15 Composited mean conditions modelled during positive and negative phases of SAM and ENSO (SAM+ and ENSO-, respectively) during DJF and MAM. As in Figure 6.12, panels a to d show synoptic near-surface meteorological conditions associated with each regime, while panels e to h show mean E_{melt} anomalies associated with each regime. The upper and lower rows show composites for SAM+ and ENSO- regimes, respectively. 135

6.16 Composited mean synoptic meteorological conditions and mean E_{melt} anomalies in MAM associated with three regimes that increase E_{melt} relative to climatology: the flow-over ("flow-over", panels a and b), positive SAM ("SAM+", panels c and d) and negative ENSO ("ENSO-", panels e and f) regimes. Colours, contours and vectors are as in previous plots. 136

C.1 Mean surface temperature, T_S, as in Figure 5.8, during the OFCAP period in observations (black) and as modelled by the control RA1M_mod (blue, with circle markers) and lambda (pink, dashed, with triangle markers) simulations. 177

C.2 As in Figure C.1, but for melt energy, E_{melt}. 177

C.3 As in Figure C.1, but for E_{tot}. 178

C.4 As in Figure C.1, but for $LW_{\downarrow}$. 178

D.1 Monthly mean MetUM modelled and observed surface meteorological variables (relative humidity, RH, wind speed, FF, 1.5 m air temperature, T_{air}, and surface temperature, T_S) during the hindcast period 1998-2017 at inlet and ice shelf stations. Modelled time series are shown with lighter hues, while observed time series are indicated with darker hues and crosses, and the modelled monthly minima and maxima are shown with the shaded region. 181

D.2 As in Figure D.1, but for monthly mean surface energy fluxes (downwelling shortwave, $SW_{\downarrow}$, downwelling longwave, $LW_{\downarrow}$, sensible heat, H_S, and latent heat, H_L) during the MetUM hindcast period. 182

D.3 Wind roses of MetUM modelled wind speed and direction at each of the four AWSs shown in Figure 3.1 during the hindcast period, 1998-2017. 183

D.4 Scatterplots of observed vs. modelled surface variables at AWS 17. Correlation coefficients (r values) are given in the bottom right hand corner of each panel: all are statistically significant at the 99% level. The dashed line in each plot indicates perfect agreement between model and observations. Panels a - d show surface meteorological variables: surface temperature, T_S; near-surface air temperature, T_{air}; relative humidity; and wind speed; and panels e - h show surface energy budget terms: downwelling longwave, $LW_{\downarrow}$; downwelling shortwave, $SW_{\downarrow}$; net radiative, R_{net} and melt, E_{melt}, fluxes. 184

D.5 As in D.4, but showing observed vs. modelled correlations at AWS 18. 185

D.6 Daily mean melt flux, E_{melt}, at AWS 14 for all times where observations are available. Observed fluxes are shown in black, while modelled values at the corresponding location are shown in blue. 190

D.7 As in Figure D.6, but at AWS 17. 191

D.8 As in Figure D.6, but at AWS 18. 192

E.1 Schematic diagram of the isentrope-based method of foehn detection (method 3), after Bannister (2015). u_{Z1} refers to the mean zonal wind at height Z_1, the peak height of orography, at an upstream location one Rossby radius of deformation from the peak of the mountains (λ_R). The isentrope θ_{Z1} is calculated at this point and its minimum height (Z_2) on the lee side over a given transect distance is calculated. If the change in height of the isentrope, i.e. $Z_3 = Z_1 – Z_2$ is > 500 m over 6 hours, foehn is detected. 195

G.1 Mean modelled foehn index during 1998-2017 for each season: a) DJF, b) MAM, c) JJA, d) SON and e) annually (ANN). 202

H.1 Map showing the four regions used in the diagnosis of large-scale regimes. Abbreviations used in the plot are as follows. "X": location at which u_{Z1} is calculated, used in "blocked" and "flow-over" regimes, as well as for foehn diagnosis, "A": Deep Amundsen Sea Low regime, "B": barrier wind regime, "LCIS": Larsen C box used to calculate means for "melt25", "melt75", "cloudy", "clear", "LWP25" and "LWP75" regimes (high/low). 203

List of Tables

3.1 Summary of metadata, measured parameters, data availability and use of AWS data throughout the thesis. 28

3.2 Summary of differences between MetUM model configurations used in each chapter. 36

4.1 Observed and modelled means, plus biases, percent root mean square error ("% RMSE") and correlation coefficients ("Correlation (r)") during both cases at 1.5 km resolution for surface variables: surface temperature, T_S (°C); near-surface air temperature, T_{air} (°C); relative humidity, RH (%); wind speed, FF (m s^{-1}); and fluxes of downwelling and upwelling shortwave and longwave $SW_{\downarrow}$, $SW_{\uparrow}$, $LW_{\downarrow}$ and $LW_{\uparrow}$, respectively; net shortwave, SW_{net}; net longwave, LW_{net}; sensible heat, H_S; latent heat, H_L; total energy, E_{tot}; melt energy, E_{melt} and melt energy with observed T_S prescribed, $E_{melt,forced}$, all measured in W m^{-2}. 53

4.2 Mean observed and modelled melt fluxes (top row, in W m^{-2}) during periods when the surface temperature is at melting point, and cumulative meltwater production (bottom row, in mm w.e.) for both case studies. Model results at 1.5 km resolution are shown. 65

5.1 Configurations for model experiments used in this study. Varying model schemes and parameterisations used in each model experiment are summarised in the second column ("options"), and the cases that each experiment is used to simulate are indicated in the last column ("case"). 73

5.2 Mean observed surface energy fluxes, defined as in Equation 3.3, Chapter 3, and associated model biases of each experiment at AWS 14 during f152. All fluxes are given in W m^{-2}, and are abbreviated as in Chapter 3. Fluxes and biases are positive when directed towards the surface. The smallest biases are highlighted in bold text and standard deviations are given in brackets. 78

5.3 Pearson correlation coefficients between cloud cover (CC), downwelling longwave ($LW_{\downarrow}$) and shortwave fluxes ($SW_{\downarrow}$), and melt flux (E_{melt}), at AWS 14 during 1 January – 7 February 2011. Correlation coefficients between observed components are shown in columns one to four, while modelled coefficients are given in columns five to eight. Correlation coefficients in bold text are significant at the 99% level. 87

5.4 Mean observed surface energy fluxes at AWS 14 ("AWS 14 (observed)") and mean model biases of the RA1M_mod simulation of the OFCAP period ("Mean bias"), as in Table 5.2. Mean biases reported by King et al. (2015) are given in the third column ("King et al. (2015) bias", and mean biases, RMSEs and Pearson correlation coefficients of the RA1M_mod OFCAP simulation are given in columns four to six, respectively. As in Table 5.2, the smallest biases are highlighted in bold, and fluxes and biases are positive when directed towards the surface. . . . 88

6.1 Summary statistics for inlet and ice shelf stations in observations and model output. Annual means (shown in bold), plus the fifth and ninety-fifth percentiles of surface variables are given, where abbreviations and units are as follows: T_S: surface temperature (°C); T_{air}: 1.5 m air temperature (°C); RH: relative humidity (%), FF: 10 m wind speed (m s^{-1}); P: surface pressure (hPa); u: 10 m zonal wind speed (m s^{-1}); v: 10 m meridional wind speed (m s^{-1}); $SW_{\downarrow}$: downwelling shortwave radiation (W m^{-2}), $SW_{\uparrow}$: upwelling shortwave radiation (W m^{-2}); SW_{net}: net shortwave radiation (W m^{-2}); $LW_{\downarrow}$: downwelling shortwave radiation (W m^{-2}); $LW_{\uparrow}$: upwelling shortwave radiation (W m^{-2}); LW_{net}: net shortwave radiation (W m^{-2}); H_S: sensible heat flux (W m^{-2}); H_L: latent heat flux (W m^{-2}); E_{tot}: sum of all fluxes (W m^{-2}); E_{melt}: melt flux (W m^{-2}). All fluxes are positive when directed towards the surface. 102

6.2 Percentage of time during the hindcast period where simulated daily mean cloud fraction averaged over the Larsen C region (see Figure H.1) meets the criteria of Kay et al. (2008). The cloud regimes of Kay et al. are determined using cloud fraction thresholds, derived from Arctic cloud satellite observations. Standard deviations of the percentage of time each category is simulated are given in brackets. 104

6.3 Summary seasonal modelled foehn frequency statistics for ice shelf and inlet stations over the period 1998-2017. Means, medians and standard deviations ("SD") are given for each season and annual totals. 109

6.4 Mean modelled MAM foehn occurrence during the model hindcast period ("1998-2017 mean"), mean modelled MAM foehn occurrence during the hindcast period plus one standard deviation ("Mean + SD") and modelled foehn occurrence during MAM 2016 ("MAM 2016") at each station. 110

6.5 Pearson correlation coefficients between modelled foehn frequency at inlet and ice shelf stations with the observed SAM index of Marshall (2003). Correlations that are statistically significant at the 95% level are given in bold, while statistical significance of 99% is indicated with an asterisk. 116

6.6 Total and maximum modelled meltwater production over the Larsen C ice shelf and tributary glaciers (region marked "LCIS" in Figure H.1, Appendix H) plus the standard deviation of annual mean cumulative melt during each melt year (August-July) in the hindcast period. Annual ice-shelf integrated and maximum modelled meltwater production greater than one standard deviation above the mean are indicated with red-orange shading and bold text, while modelled meltwater production less than one standard deviation below the mean is indicated with green shading and italics. The standard deviation of annual cumulative mean melt across Larsen C, that is, a measure of the spatial variability of cumulative melt totals, is given in the final column. 119

6.7 Pearson correlation coefficients between daily mean modelled variables over the Larsen C ice shelf during the entire hindcast period, for all months. Only values that are significant at the 99% level are given. Correlations between E_{melt} and other variables are indicated in bold. 123

6.8 As in Table 6.7, but for individual seasons. 124

6.9 Percentage of modelled cumulative meltwater produced during each season. . . 129

6.10 Percentage of modelled meltwater production associated with each regime during each season, and the frequency at which they occur. Standard deviations are given in brackets next to each value. Regimes are abbreviated as defined in the main text, and as follows. "SAM+": positive SAM; "SAM-": negative SAM; "ENSO+" positive ENSO (La Niña conditions); "ENSO-": negative ENSO (El Niño conditions); "ASL": deep Amundsen Sea Low; "barrier": low-level southerly barrier jet over Larsen C; "blocked": blocked flow conditions; "flow-over": flow-over conditions; "LWP25": mean LWP $< 25^{th}$ percentile; "LWP75": mean LWP $> 75^{th}$ percentile; "melt25": mean meltwater production $< 25^{th}$ percentile; "melt75": mean meltwater production $> 75^{th}$ percentile; "cloudy": mean cloud fraction > 0.75; and "clear": mean cloud fraction < 0.31. 133

C.1 Mean observed surface energy fluxes at AWS 14 and mean model biases of the RA1M_mod control and "lambda" experiments during the OFCAP period, as in Table 5.3. Validation statistics for near-surface meteorological parameters (1.5 m air temperature, T_{air}, surface temperature, T_S, relative humidity, RH, and 10 m wind speed, FF) are also given in addition to the SEB terms shown in Table 5.3. Mean biases, RMSEs and Pearson correlation coefficients (r) in the RA1M_mod and lambda OFCAP simulations are given in columns three to five and six to eight, respectively. E_{tot} and E_{melt} fluxes, both with and without observed G_S prescribed ($+G_S$), are shown in the bottom four rows for each. As in Table 5.3, the smallest biases are highlighted in bold, and fluxes and biases are positive when directed towards the surface. Values for temperatures are given in °C, RH is given in %, FF is given in m s^{-1} and all fluxes are given in W m^{-2}. 179

D.1 Daily mean model validation statistics (bias, correlation coefficient, standard error and root mean square error) for the period 1998-2017 at all stations during summer (DJF) and winter (JJA). Correlation coefficients between observed and modelled time series are emboldened when significant at the 99% level, and given in italics when significant at the 95% level. Insignificant correlations are given in plain text.. 188

E.1 Percentage of time foehn were diagnosed from observations at AWS 14 using the surface method and thresholds specified in Turton et al. (2018), Wiesenekker et al. (2018) and Datta et al. (2019). 196

E.2 Summary statistics for the foehn diagnosis methods tested, at inlet (AWS 17 and 18) and ice shelf (AWS 14 and 15) stations. Means, medians and standard deviations ("SD") are presented as percentages of time that foehn conditions are diagnosed per year. The results of a dependent variable student's t-test to test the difference between inlet and ice shelf stations using each method are shown in the final column ("Sig dif?"). 197

F.1 Percentage of time foehn conditions are diagnosed from model output at each AWS during each season and each year using the combined method detailed in Chapter 6. Foehn conditions are given as percentages of time. The mean, median and standard deviation of each time series is also given (also in percent) at far right. 200

H.1 Indicator variables, thresholds and regions used in diagnosing each of the regimes used for compositing in Chapter 6. Regimes are defined as in Chapter 6, where the acronyms "SAM", "ENSO", "ASL" and "LWP" refer to the Southern Annular Mode, El Niño Southern Oscillation, Amundsen Sea Low and liquid water path, respectively. The regions used are indicated in Figure H.1. 205

Acknowledgements

Thanks are due first and foremost to my supervisors, Andrew Orr, John King, Tom Lachlan-Cope and Ian Renfrew, who provided me with invaluable encouragement, advice and support throughout my PhD. To TLC, thanks for letting me hitch a ride to Antarctica with you - it was a life-changing experience that I will never forget. To that end, I would also like to thank EnvEast and NERC for providing the funds to get me to Rothera, and for funding this horrible, wonderful PhD journey. To the excellent humans I have shared an office with over the years: notably Zoe, Emily, Christine, Amy and Mike - thanks for the perspective and for sharing in the trials, tribulations and successes of academic life. I would also like to thank all those in the AIC team at BAS (and now beyond!) who helped me along the way, particularly Tony Phillips, James Pope and Gillian Young for their help and advice with data processing, modelling, data analysis and all the infuriating experiences that come with those. On the subject of computing, I also acknowledge the use of the MONSooN system, a collaborative facility supplied under the Joint Weather and Climate Research Programme, a strategic partnership between the Met Office and the Natural Environment Research Council. It has been a pleasure to work with collaborators in the UK and further afield: honourable mention goes to Paul Field, Stu Webster, Jonathan Wilkinson, Ian Boutle and Adrian Hill at the Met Office, Andy Elvidge at UEA and to Peter Kuipers Munneke and Paul Smeets at IMAU, all of whom have provided advice, data, co-authorship or a combination thereof during the last 3.5 years.

Finally, the personal thanks. I couldn't have done this PhD without the support and encouragement of my incredible and inspiring parents, who fostered in me a fierce curiosity and passion for the natural world from before I can remember. To two unforgettably unorthodox teachers: Jonathan Earle, thank you for fuelling my indignation, for teaching me the importance of failure, and for always, always getting the best out of me - I wouldn't be where I am today if it hadn't been for you. Phil Davison, thanks for the politics, for *that* character reference, and for always having my back. To the good ship 438 and all who've sailed in her: thank you for tolerating me, through the boxing weight-cuts, the deadline

stresses, and more. HUGE love to all at Islington Boxing Club, who have kept me sane through the stress and headaches of the last 3.5 years. Special thanks to the Haglands (all of you), my punchy bff 10-round-super-Dan, and all the girls who punch me in the face three times a week, but especially the almost-60 kg crew: Sunni "the Terror" Torgman, Dr. Weis, Fitzy G, Original Amy and Zoe. Big shout outs to Tess, Carrie, Jem, Char, young Alex and Demi too. Sharing a locker room with you all is an honour and a privilege.

Lastly - before you think I'd forgotten you - to Pete: thank you for putting up with me on this journey, for always knowing how to make me laugh, for bringing light into the darkest moments, and for making life three thousand times better. The last 3.5 years has been a rollercoaster, but you've made it almost as good as The Big One.

Thank you.

Dedication

This thesis is for everyone. Because science should be.

1

Introduction

This thesis will investigate the atmospheric causes of surface melting on the Larsen C ice shelf on the Antarctic Peninsula. It aims to identify key processes contributing to surface melting, and to quantify their effects in the present and in recent decades. This understanding will be instrumental for deriving estimates of how surface melting on Larsen C might change in the future, with implications for the surface mass balance of the Antarctic Peninsula and its contribution to global sea level rise.

The over-arching research question that underpins this entire thesis is:

"What are the most important atmospheric processes that drive surface melting on the Larsen C ice shelf?"

To answer this question, this thesis will first examine current knowledge of the most important processes on Larsen C, and then present work that addresses areas of uncertainty. Chapter 2 synthesises the published literature, summarises current scientific understanding, and identifies important knowledge gaps that this thesis will address.

The primary analytical tool used throughout the thesis is the UK Met Office Unified Model (MetUM), a numerical weather and climate prediction model used for operational and research purposes. Model case studies, longer simulations and a multi-decadal hindcast are all produced using the MetUM, and these are compared with available in situ data for validation and comparison. Further detail of the model physics, parameterisations and setup is given in Chapter 3 and the specific experiments, methods and adaptations used for each section of work is outlined at the start of the relevant results chapter. Similarly, information about the primary data sources is provided in Chapter 3 and summarised in each results chapter (Chapters 4 - 6).

The three sections of work presented in Chapters 4 - 6 investigate specific atmospheric features or processes in detail using model simulations of case studies, longer simulations and a multi-decadal hindcast. Specifically, Chapter 4 evaluates the role of orographically-driven foehn winds in driving wintertime surface melting on Larsen C during two specific case studies in May 2016. It aims to address three key research questions: 1) Do foehn events occur on Larsen C during winter? 2) What is the effect of wintertime foehn on the surface energy balance (SEB) of Larsen C? 3) Do wintertime foehn events cause melting on Larsen C?

Chapter 5 investigates the importance of cloud phase in determining the amount and evolution of surface melting during summer. It aims to determine the influence of cloud phase on the summertime SEB of Larsen C and how this is represented in the MetUM by drawing together two observational datasets and evaluating model performance during two case studies and one longer model simulation. It investigates several key questions: 1) Is the MetUM able to represent observed cloud phase and microphysics? 2) How does cloud phase influence the SEB in observations and the MetUM? 3) Can a double-moment microphysics scheme improve simulations of cloud phase? 4) How does summertime cloud phase influence the SEB during the entire OFCAP period? Chapter 5 identifies an optimum MetUM configuration that best represents summertime mixed-phase cloud properties and their effect on the SEB of Larsen C, which is then used to produce the model hindcast presented in Chapter 6.

Chapter 6 synthesises understanding from the preceding two results chapters, as well as published studies summarised in Chapter 2, to evaluate the role of various atmospheric processes in a high-resolution MetUM model hindcast of the period 1998-2017. Chapter 6 explores the mean near-surface meteorology of Larsen C, and presents a climatology of several pertinent variables such as temperatures, winds and surface energy fluxes. The importance of foehn winds are again evaluated, and the frequency and variability of these events is calculated annually, seasonally and inter-annually, as is the importance of foehn for the evolution of surface melting. The importance of cloud phase is again explored, and the role of large-scale circulation patterns and regional atmospheric features such as the Southern Annular Mode, El Niño Southern Oscillation and Amundsen-Sea Low in establishing conditions for melting is comprehensively evaluated. Chapter 6 examines six main research questions: 1) How does the SEB of Larsen C vary throughout the year? 2) How does cloud influence surface melting on Larsen C? 3) Where and when do foehn events occur? 4) Where and when does the most melting occur? 5) What is the current modelled ice shelf-integrated surface melt rate? 6) What are the most important drivers of surface melting on Larsen C?

The thesis concludes with a summary of the most important findings from each chapter and the thesis as a whole, and suggests areas for future research to explore the topic further.

Literature Review

2

Declaration: parts of this literature review have been adapted from **Gilbert, E.**, Orr, A., King, J. C., Renfrew, I. A., Lachlan-Cope, T., Field, P. F., Boutle, I. A. (2020). "Summertime cloud phase strongly influences surface melting on the Larsen C ice shelf, Antarctica." *Quarterly Journal of the Royal Meteorological Society*, 2020, 1–16, doi: https://doi.org/10.1002/qj.3753. The paper is reproduced in Appendix B.

2.1 Climatological setting

The Antarctic Peninsula, the northernmost part of the Antarctic continent (Figure 2.1), is the warmest part of Antarctica, and the only place where widespread melting can take place at the surface (van Wessem et al., 2016). The peninsula is fringed by ice shelves, which are the floating extensions of glaciers that flow off the steep terrain of the Antarctic Peninsula mountains and are at the ocean/atmosphere interface, making them useful indicators of change in both domains (Luckman et al., 2014; Oza, 2015). The mountains, which are on average ∼2000 m high, present a significant barrier to the prevailing westerly winds that intersect the peninsula, and make the western side relatively warmer than the east (Orr et al., 2008). Air masses are typically of maritime origin on the west, while cold continental air dominates on the east (Elvidge et al., 2015).

Quantifying atmospheric trends on the Antarctic Peninsula is challenging because of the limited temporal and/or spatial resolution of many datasets. Station and upper air observations can be of limited quality and intermittent (Turner et al., 2005). The installation of many automatic weather stations (AWSs) has increased data coverage on the peninsula, but these datasets do not yet have sufficient temporal coverage to examine decadal-scale changes and trends, and can have data quality issues (Picard et al., 2007; Lazzara et al., 2012).

Station observations show an annual mean surface air temperature increase of 3°C on the northern peninsula in the second half of the twentieth century, with the most pronounced effect in autumn and winter (Turner et al., 2005; Cape et al., 2015). Warming has also been detected in reanalysis products, which are frequently used to quantify long-term change in the Antarctic because of the long time series available compared to limited in situ observations (Bracegirdle and Marshall, 2012; Nygard et al., 2016). This warming trend has been attributed to ozone depletion (Thompson and Solomon, 2002), sea ice changes (Turner et al., 2013), stronger circumpolar westerly winds associated with the Southern Annular Mode (SAM, Marshall et al., 2006), and tropical teleconnections to the El Niño Southern Oscillation (ENSO, Ding et al., 2011; Clem and Fogt, 2013). Warming has contributed to mass loss from more than half of the region's ice shelves, including the collapse of the Prince Gustav, Larsen A and B ice shelves (Cook and Vaughan, 2010). Since the late 1990s/early 2000s, however, cooling has been observed, especially in summer, dampening the overall warming trend (Turner et al., 2016).

Large-scale circulation patterns such as the SAM, ENSO and Amundsen-Sea Low (ASL) strongly influence weather and climate on the Antarctic Peninsula. ENSO and SAM are negatively correlated throughout the instrumental and reconstructed proxy record (Dätwyler et al., 2019). The SAM is the dominant mode of variability in the Southern Hemisphere and exerts a major influence on warming, especially in autumn (Marshall, 2003; Clem and Fogt, 2013), whereas ENSO exerts its largest effect in spring/winter and on the western side of the peninsula (Clem et al., 2016). Both patterns affect the depth and location of the ASL, which influences the frequency and intensity of cyclones in the Bellingshausen Sea that advect warm air across the peninsula (Clem et al., 2016).

The collapse of the Larsen A and B ice shelves in 1995 and 2002, respectively, on the cooler eastern side of the peninsula, has been linked to a more positive SAM (Marshall, 2003; Marshall et al., 2006; Orr et al., 2008; van Lipzig et al., 2008). The positive phase of the SAM is associated with stronger circumpolar westerly winds, which increases the flow of warmer air along the western side of the peninsula and, importantly for Larsen C, warms the eastern side by increasing the frequency of foehn winds (Orr et al., 2004). Foehn wind frequency increases because stronger circumpolar westerly winds advect more warm maritime air over the peninsula, which is then adiabatically warmed and dried as it descends, causing surface temperatures to rise (Cape et al., 2015). This contributes to surface melting, especially during summer when temperatures are warmer, but also during other seasons (Kuipers Munneke et al., 2018; Datta et al., 2019). Surface melting has been linked to the destabilisation of both Larsen A and B (Scambos et al., 2000; Scambos et al., 2003; Bell et al., 2018), and foehn winds are thought to have played a role in their demise (Grosvenor et al., 2014; Luckman et al., 2014). Following ice shelf collapse, tributary glaciers can accelerate significantly because the buttressing capacity of the shelf is removed (Scambos et al., 2004), thereby contributing to sea level rise (Cook and Vaughan, 2010). The southward progression of ice shelf disintegration on the Antarctic Peninsula has motivated the study of Larsen C (Bevan et al., 2017; Schannwell et al., 2018, Figure 2.1), which neighbours the now-absent Larsen A and B ice shelves and so is regarded as vulnerable.

2.2 The Larsen C ice shelf

Larsen C is the largest remaining ice shelf on the Antarctic Peninsula. It has an area of 47,000 km^2 (Bevan et al., 2017), and is located east of the Antarctic Peninsula mountains at a latitude of approximately 66°S - 69°S (Figure 2.1). The mountains, which stretch north-south along the length of the peninsula, separate the relatively warm climate of the western side from the east, which can be between 5-10°C colder (Cape et al., 2015). The mountains present a significant barrier to approaching (often westerly) flow, so atmospheric conditions over Larsen C are usually influenced by cold air masses that flow down from the cold, high Antarctic plateau as a southerly barrier jet (Schwerdtfeger, 1974; King et al., 2008). This means that Larsen C can be considerably colder than locations at a comparable latitude on the western side, such as Rothera research station.

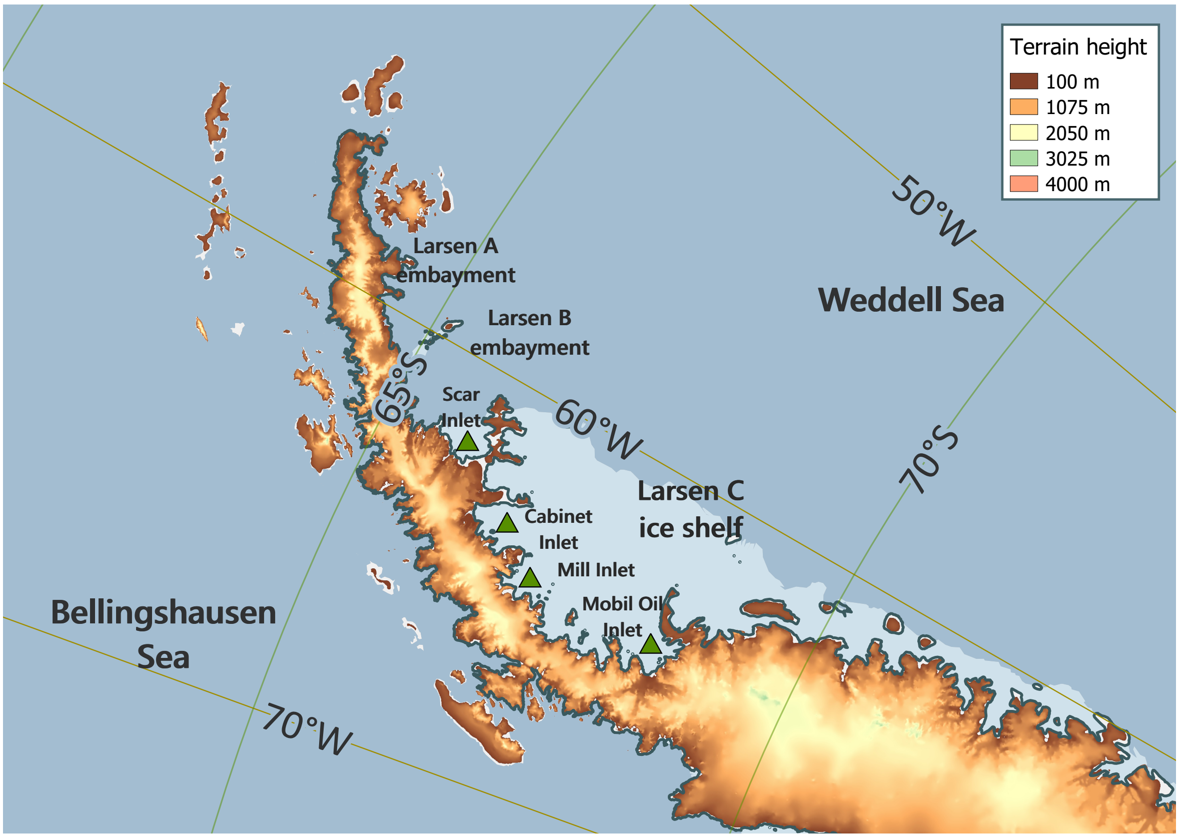
Terrain height
100 m
1075 m
2050 m
3025 m
4000 m
50°W
Weddell Sea
Larsen A embayment
Larsen B embayment
65°S
Scar Inlet
60°W
Larsen C ice shelf
70°S
Cabinet Inlet
Mill Inlet
Mobil Oil Inlet
Bellingshausen Sea
70°W

Figure 2.1.: Map of the Antarctic Peninsula region showing the Larsen C ice shelf and its tributary inlets, plus the remnant Larsen B ice shelf (labelled "Scar Inlet") and the Larsen A and B embayments. The main inlets referred to in the thesis are indicated as green triangles, and the location of ice shelf grounding lines is shown as a teal line. The mean height of orography is indicated with coloured contours, and is derived from the RAMP2 200 m elevation model (Liu et al., 2015).

Although a comprehensive climatology of the Larsen C ice shelf has yet to be published, Kuipers Munneke et al. (2012) present two years of automatic weather station (AWS) data at two sites (AWS 14 and AWS 15, see Figure 3.1) revealing typical meteorological conditions, and van Wessem et al. (2015) have produced a regional model climatology of wind and near-surface temperature over the shelf. These both show mean annual 2 m air temperatures of around -15°C, and 10 m wind speeds of approximately 4 m s^{-1}. The atmosphere is typically stably stratified with a temperature inversion near the surface. In winter, this inversion is driven by a radiation deficit at the surface, while in summer it is usually only observed during night-time when warm air is advected over a melting surface (Kuipers Munneke et al., 2012).

Kuipers Munneke et al. (2012) also examine the surface energy balance (SEB) of the ice shelf, which is the "net amount of energy received at the surface" (Lenaerts et al., 2017, pp. 3355). The SEB comprises net radiation (the sum of upwelling and downwelling longwave and shortwave fluxes), turbulent (latent and sensible heat) and ground heat fluxes. The total amount of energy received at the surface, E_{tot}, can therefore be calculated as the sum of these components, as in King et al. (2015) and as given in Chapter 3 (Equation 3.3). Fluxes are defined as positive when directed towards the surface. Melting occurs when E_{tot} is positive and the surface temperature is at the melting point, 0°C. The SEB therefore influences the surface mass balance because surface melting has been one of the dominant drivers of ice mass loss over Antarctic Peninsula ice shelves (Bell et al., 2018).

During austral summer (DJF), when the SEB is dominated by incoming solar shortwave (SW) radiation, net radiation is compensated by the turbulent upward flux of moisture and heat, i.e. negative sensible and latent heat fluxes, as a result of weak convection and sublimation (Kuipers Munneke et al., 2012). In winter, when solar forcing is absent, longwave (LW) cooling is balanced by turbulent mixing of heat towards the surface (positive sensible heat flux) (Kuipers Munneke et al., 2012). Consequently, melting is dominated by SW fluxes in summer, while turbulent fluxes become increasingly important outside of DJF (Grosvenor et al., 2014; Elvidge et al., 2020).

2.3 Antarctic Peninsula ice shelf glaciology

2.3.1 Recent ice shelf changes on the Antarctic Peninsula

Since the mid-twentieth century, seven out of the Antarctic Peninsula's 12 ice shelves have retreated or collapsed (Cook and Vaughan, 2010). The loss of ice shelves contributes to sea level rise because although ice shelves displace their own weight in water, they exert backstress on tributary glaciers that feed into them: this is their "buttressing capacity" (Borstad et al., 2013). Ice shelf thinning or loss reduces buttressing and increases the flow velocity of tributary glaciers and hence the input of ice into the ocean (Rignot et al., 2004; Trusel et al., 2015; Fürst et al., 2016). For example, tributary glaciers accelerated following the collapses of Larsen A and B in 1995 and 2002, respectively, because of the reduction in backstress (Borstad et al., 2013; De Rydt et al., 2015; Royston and Gudmundsson, 2016). Greater mass loss from Larsen C's accelerating tributary glaciers has been caused by observed ice shelf thinning in recent decades, which has reduced its buttressing capacity (Khazendar et al., 2011; Chen et al., 2016). Thinner ice shelves may also be less resistant to collapse because the reduction in backstress allows fractures to form and penetrate through the shelf, further destabilising already weakened ice shelves (Borstad et al., 2017).

2.3.2 The role of surface melting in ice shelf disintegration and glacier dynamics

Surface melting can trigger a series of glaciological processes that destabilise an ice shelf and can lead to its collapse (van den Broeke, 2005). Because surface melting is largely influenced by the SEB, this makes it an excellent indicator of atmospheric processes that alter the SEB (Kuipers Munneke et al., 2014). For example, the exceptional surface melt event that preceded the collapse of Larsen B was driven by an atmospheric circulation anomaly that persisted for three months, reducing sea ice concentrations in the Weddell Sea and allowing warm, maritime air to penetrate onto the ice shelf (van den Broeke, 2005).

Surface melt is also the most important driver of firn densification (Scambos et al., 2000; Holland et al., 2011). Firn is a porous, low-density medium formed as snow develops into ice where meltwater percolates and refreezes, thereby acting as a "buffer" for surface melt processes (Kuipers Munneke et al., 2014). However, if the rate of melt and refreezing within the firn layer exceeds the rate at which new firn is produced, then the layer can become saturated with refrozen meltwater. Both firn densification and firn air contents are an indicator of saturation, and consequently ice shelf stability, because meltwater becomes denser when it refreezes, filling pore spaces and thereby expelling air (Holland et al., 2011; Luckman et al., 2014). Once the firn layer is saturated with refrozen meltwater, meltwater begins to collect in ponds on the surface because it cannot drain away (Scambos et al., 2000; Kuipers Munneke et al., 2014). This allows hydrofracturing to occur, which causes ice shelves to disintegrate extremely rapidly: over about a month in the case of Larsen B (Scambos et al., 2003).

Hydrofracturing is the process whereby water-filled crevasses widen as a result of the hydrostatic pressure acting at the crevasse tip (Kuipers Munneke et al., 2014). Meltwater collecting on the surface percolates into existing rifts and crevasses, causing them to propagate once they fill above a critical threshold of ~90% (Scambos et al., 2003). Firn densification and hydrofracturing are believed to have been the most significant factors contributing to the collapse of Larsen A and B (Kuipers Munneke et al., 2014; Trusel et al., 2015). Melt ponds were observed over the Wilkins and Larsen A and B ice shelves before their respective collapses, and more extensive ponding was associated with areas that calved more icebergs (Scambos et al., 2003). Ponding is also observed in satellite imagery of Larsen C (Luckman et al., 2014), but less extensively than was seen over its now-absent neighbours.

2.3.3 Observed surface melting on Larsen C

Estimating mean ice-shelf integrated meltwater production over Larsen C is important to investigate its stability. Meltwater production rates over Larsen B surpassed 600 mm w.e. yr^{-1} (mm meltwater equivalent per year) prior to its collapse, so this threshold may be an important benchmark for ice shelves on the Antarctic Peninsula (Trusel et al., 2015). Trusel et al. (2013) find mean annual meltwater production of 220 mm w.e. yr^{-1} over the whole Larsen C ice shelf during the period 1999-2009, with meltwater production peaking at $>$ 400 mm w.e. yr^{-1} in the northwestern inlets, and Trusel et al. (2015) find "contemporary" mean melt of ~300 mm w.e. yr^{-1}. Several studies show that melting occurs predominantly in the north of Larsen C, and in inlets close to the mountains (Holland et al., 2011; Luckman et al., 2014; Hubbard et al., 2016; Ashmore et al., 2017; Bevan et al., 2017; Bevan et al., 2018). The north-south gradient in melt duration observed by Luckman et al. (2014) and Bevan et al. (2018) is explained by greater SW radiation and warmer temperatures at more northerly latitudes, which means the melting point is more frequently reached. The east-west gradient superimposed upon this pattern is related to the occurrence of foehn winds, which cause the cumulative annual number of melt days to be higher nearest the mountains (Elvidge et al., 2020). In western inlets, the onset of melt and refreezing happens earlier and later, respectively, by several days relative to locations further out on the ice shelf (Holland et al., 2011; Luckman et al., 2014; Grosvenor et al., 2014).

Melting has been measured on Larsen C using various methods, including satellite observations of melt inferred from backscatter (Luckman et al., 2014; Bevan et al., 2018) or brightness temperature (e.g. Datta et al., 2019), radar or laser satellite altimetry estimates of surface elevation changes (Griggs and Bamber, 2009; Chuter and Bamber, 2015), airborne and ground-based radar surveys of firn air content and ice shelf structure (Holland et al., 2011; McGrath et al., 2014; Holland et al., 2015), borehole observations of firn density (Hubbard et al., 2016; Ashmore et al., 2017; Bevan et al., 2017), and ground penetrating radar, snowpit and sonic height ranger observations of surface elevation, firn density and air content (Kuipers Munneke et al., 2017). Many types of model are also used to investigate patterns and trends in Antarctic surface melt, including firn models (Kuipers Munneke et al., 2014; van Wessem et al., 2016; Bevan et al., 2017), flowline models (Bevan et al., 2017), SEB models (Kuipers Munneke et al., 2012; Bevan et al., 2018), mass balance models (van Wessem et al., 2016), regional climate models (Kuipers Munneke et al., 2014; Kuipers Munneke et al., 2017; Datta et al., 2019; Elvidge et al., 2020) or coupled models like atmosphere-snowpack models (Trusel et al., 2013).

2.3.4 High-resolution regional atmospheric modelling on Larsen C

High-resolution atmospheric modelling can be particularly useful to overcome the sparsity of in situ observations and limitations of satellite and reanalysis products in the Antarctic. Many regional climate models are run over the Antarctic Peninsula, including WRF (Deb et al., 2016; Deb et al., 2018; Listowski and Lachlan-Cope, 2017; Turton et al., 2018; Hines et al., 2019), RACMO (Lenaerts et al., 2016a; Lenaerts et al., 2018; van Wessem et al., 2014; van Wessem et al., 2015; van Wessem et al., 2016; van Wessem et al., 2018), the MetUM (Orr et al., 2014; Elvidge, 2013; Elvidge et al., 2015; Elvidge et al., 2016; Elvidge and Renfrew, 2016; Elvidge et al., 2020; Gilbert et al., 2020), HIRHAM (Walther, 2016), MAR (Agosta et al., 2018; Datta et al., 2019), CAM (Nicolas et al., 2017), CESM (Lenaerts et al., 2016b) and COSMO-CLM (Souverijns et al., 2019). These produce four-dimensional output (three spatial dimensions over time), providing a complete picture, where observations are typically one- or two-dimensional. Horizontal grid-spacing is of first-order importance for accurately resolving topography and thus flow conditions creating features like foehn winds (van Lipzig et al., 2008; Elvidge et al., 2016; Turton et al., 2018) or cloud microphysics and precipitation (Rotstayn et al., 2000; Lebo et al., 2017; Favier et al., 2017). This makes high-resolution regional atmospheric models (horizontal grid spacing $\sim$5 km or finer, $\sim$40 vertical levels, timesteps $< \sim$10 min) particularly useful (Hong and Dudhia, 2012). For example, on Larsen C, Elvidge et al. (2016) find that foehn winds are much better resolved using the MetUM at 1.5 km than at 4 km, and Turton et al. (2017) report similar results using WRF at 5 km and 1.5 km resolution.

However, even at relatively high resolution, models are often unable to reproduce the observed foehn-driven east-west gradient in surface melt shown by remote sensing and in situ observations. For example, King et al. (2017) and van Wessem et al. (2016) find that AMPS and RACMO, respectively, do not simulate sufficient melting in the inlets close to the foot of the mountains on Larsen C. Both are high-resolution regional models optimised for polar regions, but RACMO has a much more sophisticated snow scheme than the one used in AMPS, so may be expected to reproduce observed spatial patterns more closely. However, atmospheric properties must still be realistically simulated, and both of these studies use models at approximately 5 km horizontal grid spacing, which is likely not sufficient to resolve the atmospheric processes that drive melting, such as foehn. Additionally, RACMO is a hydrostatic model, which means that important dynamical processes relating to vertical motion at the mesoscale are not adequately resolved. Using the MetUM at 1.5 km resolution, Elvidge et al. (2020) are able to resolve increased melt rates in inlets. Increased model resolution may be necessary to accurately resolve observed foehn-related patterns of melt, but spatial resolution may not be the only factor determining how realistically melt patterns are simulated. The varying performance of regional models in simulating spatial patterns of melt on Larsen C indicates that resolution, model dynamics, resolved processes and the representation of important atmospheric properties (such as cloud phase, discussed in section 2.5) are all important in determining simulation quality.

High resolution is frequently achieved in models using dynamical downscaling methods, where a smaller, higher resolution domain (or series of domains) is embedded within a larger global domain, taking its forcing data from this outer region (Pielke Sr and Wilby, 2012; Ekström et al., 2015). Statistical downscaling can also achieve the same goal via statistical functions that describe observed relationships between large-scale and local-scale variables such as temperature or pressure (Pielke Sr and Wilby, 2012). Both methods have been shown to improve model skill at reproducing observed conditions, although statistical methods rely on observed relationships, which are not robustly constrained in the Antarctic because of the dearth of observations. There is also no guarantee that relationships between variables will not change over time, so dynamical downscaling methods are more commonly used (Hong and Kanamitsu, 2014).

Reanalysis data is typically used as forcing, the quality of which strongly influences simulation quality (Bromwich et al., 2013). For example, reanalyses have well-documented biases in the Antarctic due to the low availability of observations for assimilation (Yu et al., 2010; Bracegirdle and Marshall, 2012; Fréville et al., 2014; Nygard et al., 2016; Jones et al., 2016; Jonassen et al., 2019) and their coarse resolution means complex features such as foehn winds or precipitation and accumulation gradients near steep topography are not adequately resolved (Bracegirdle and Marshall, 2012; Bromwich et al., 2013; van Wessem et al., 2015). On the Antarctic Peninsula, Nygard et al. (2016) find that eight different reanalyses are too moist, with under-estimated wind speeds and over-estimated near-surface air temperatures on the eastern side and a cold bias to the west. No single reanalysis stands out as the best for all purposes, but newer reanalyses with improved spatial resolution tend to out-perform coarser ones (Nygard et al., 2016; Gossart et al., 2019). Bromwich et al. (2013) find that ERA-Interim is best for providing initial and lateral boundary conditions in Antarctica.

2.3.5 Recent surface melt trends on Larsen C

Melt trends have been extensively assessed on the Antarctic Peninsula using some of the techniques outlined above. For example, Barrand et al. (2013) showed positive, statistically significant trends in melt duration at four out of six stations on the Antarctic Peninsula since 1948 using station records, satellite data and a positive degree day model, concurrent with observed warming (Turner et al., 2005). In contrast, Liu et al. (2006) use satellite observations from 1978-2004 to show that melt duration trends on the Antarctic Peninsula were negative, but exhibited high inter-annual variability, with some very high melt years. This is consistent with Fahnestock et al. (2002) and van den Broeke (2005), who show that the collapse of Larsen A and B were driven largely by “exceptional” melt events forced by meteorological factors, rather than a gradual, climatically driven increase in mean melt duration over time.

Melting on Larsen C was shown to be increasing in the late twentieth and early twenty-first centuries, as inferred by Shepherd et al. (2003) from an observed ice shelf thinning of 0.27 ± 0.11 m yr^{-1}, and by Holland et al. (2011) from a surface lowering of 0.2 m yr^{-1}. This surface lowering corresponds to an increasing trend of 0.5 melt days yr^{-1} per year over the period 1978/79 – 2008/09, and a total increase of $\sim$15 melt d yr^{-1} by 2008/09. This is consistent with Tedesco (2009), who finds a larger rising trend in melt days of 1.2 d yr^{-1} per year over Larsen C. However, both surface and basal melting has reduced since 2009 (Datta et al., 2019) and surface elevation has consequently increased: Adusumilli et al. (2018) found a surface lowering over Larsen C of 1.0 ± 0.3 m from 1994-2009, but an increase in surface elevation of 0.5 ± 0.3 m from 2009-2017. Similarly, Bevan et al. (2018) find that the number of melt days per year declined by 1-2 d yr^{-1} during 1999-2017 over much of the ice shelf, with the exception of inlets, where the number of melt days increased.

These melt trends are consistent with the aforementioned temperature trends on the Antarctic Peninsula, which were considerable and positive until the turn of the century (e.g. 2.8°C warming observed between 1951-2000 at Faraday/Vernadsky: Turner et al., 2005), but then reversed, indicating a cooling trend from the late 1990s (Turner et al., 2016). Cooling temperatures likely limit melting under non-foehn conditions, when melt is largely driven by incoming SW radiation (Grosvenor et al., 2014; Gilbert et al., 2020; Elvidge et al., 2020), whereas an ongoing trend towards an increasingly positive SAM (Marshall, 2003; Gillett et al., 2006; Swart et al., 2015) more frequently establishes conditions conducive to foehn (Marshall et al., 2006; van Lipzig et al., 2008; Orr et al., 2008, see also section 2.4). Thus, the enhanced melting in inlets reported by Bevan et al. (2018) is likely caused by a strengthening of the circumpolar westerly winds, whereas the decline in melting across much of the ice shelf can be explained by cooling temperatures, which cause the surface to reach melting point less often, therefore reducing melt duration. Foehn winds are demonstrably important for driving surface melting on Larsen C: the following section describes their characteristics and effects.

2.4 Foehn winds on Larsen C

2.4.1 Definitions

Foehn winds are warm, dry winds generated by air descending in the lee of steep topography (Elvidge and Renfrew, 2016). At the surface, these winds cause relative humidity to fall, while wind speeds and near-surface air temperatures rise (Elvidge et al., 2016). This leeside "foehn effect" can be quite pronounced, producing temperature increases of up to 25°C over an hour (Elvidge and Renfrew, 2016). Foehn is commonly observed in inlets on the eastern side of the peninsula mountains because the mountains are oriented approximately north-south, and are consistently ~2000 m high, while the prevailing wind direction is westerly (Orr et al., 2008; Elvidge and Renfrew, 2016; King et al., 2017), which produces conditions favourable to foehn occurrence.

Several mechanisms known to produce foehn winds are quantified in Elvidge and Renfrew (2016):

1. The thermodynamic mechanism: orographic uplift and condensation and precipitation on the windward side leading to latent heat release and warming on the lee side;
2. Isentropic drawdown: upwind flow blocking at lower elevations, causing air to be drawn down from a higher altitude where it has higher potential temperature; and
3. Mechanical mixing: mixing of potentially warmer air from above into lower-level flow.

In the classical "thermodynamic" mechanism, air is cooled as it ascends over steep terrain, and any moisture is forced to condense into clouds, which can eventually precipitate, making the process irreversible. This process warms and dries the air mass because latent heat is released and moisture is removed during condensation. This more frequently occurs when the air impinging on the peninsula is moving fast enough to overcome internal buoyancy forces and ascend over the obstacle ("linear" conditions identified in Elvidge et al., 2016, and described below, page 13). Conversely, when air flow is slower and therefore non-linear, flow "blocking" commonly occurs because air cannot ascend over the mountains (Smith, 1990b), which generates foehn via mechanism 2. This "isentropic drawdown" mechanism means air reaching the surface as a foehn wind originates at higher altitude (Elvidge and Renfrew, 2016). Air masses impinging on the Antarctic Peninsula are frequently stably stratified (King et al., 2008), so air sourced from higher up has higher potential temperature and often lower relative humidity (Elvidge and Renfrew, 2016). Mechanism 3 causes warming of leeside low-level flow by mixing in potentially warmer (and drier) air from higher levels, generating a positive sensible heat flux (Elvidge and Renfrew, 2016). As a result of mechanisms 1 to 3, air downwind of the mountains is often drier and hence cloud-free (Hoinka, 1985): this "foehn clearance" allows more SW radiation to reach the surface, which heats radiatively (Elvidge and Renfrew, 2016; Grosvenor et al., 2014).

The characteristics of the lee-side response to air flowing perpendicular to a barrier - such as whether a foehn wind occurs, by which mechanism it is produced, and its extent and intensity - depend on the properties of the barrier, and of the cross-barrier flow (Elvidge et al., 2016). The linearity of the flow can be measured using the non-dimensional mountain height, $\hat{h}$, defined as:

$$\hat{h} = \frac{Nh}{u} \tag{2.1}$$

where N is the Brunt Väisälä frequency, a measure of atmospheric stability (typically 0.01 s^{-1}), h is the height of the mountain barrier (1500-2000 m for the Antarctic Peninsula) and u is the velocity of the oncoming flow (Orr et al., 2004). N and u must be determined at least one Rossby radius of deformation ($\lambda_R = Nh/f$ where f is the Coriolis parameter) upwind of the barrier, such that they are not influenced by the barrier (Orr et al., 2008; Elvidge et al., 2016). Flow regimes, and/or foehn occurrence may also be diagnosed using a related parameter, the Froude number, defined as the inverse of $\hat{h}$, i.e. u/Nh, as in Bannister (2015).

When $\hat{h}$ « 1, the whole air mass is able to pass over the mountain easily and "flow-over" conditions prevail (Orr et al., 2008; van Lipzig et al., 2008), but as $\hat{h}$ increases to $\sim$1 or above, non-linear effects like upwind flow blocking, wave breaking and leeside hydraulic jumps are observed (Orr et al., 2008; Elvidge et al., 2016). Strongly stably stratified, slow-moving flow approaching the peninsula is more non-linear, and so is more likely to promote upwind blocking, where flow stagnates upstream of the barrier (Orr et al., 2008) and causes air to flow along the length of the peninsula mountains. Slower moving, non-linear flow often causes foehn to be generated via mechanism 2, while faster moving flow may result in flow-over conditions, producing leeside foehn via mechanism 1 (Elvidge et al., 2016). Linear flow typically produces more extensive foehn events with higher associated melt rates because the warm, dry air is able to flow over the ice shelf at low levels. This delivers large fluxes of sensible heat and mechanically mixes warmer air towards the surface, preventing an inversion from being established (Elvidge et al., 2016). By contrast, non-linear events are usually associated with a more intense but confined foehn signal on the lee side because non-linear effects like hydraulic jumps cause the foehn flow to rebound from the surface, so it does not cause melting further out on the ice shelf (Elvidge et al., 2016).

The leeside response to foehn is also related to the geography of the region. Elvidge et al. (2015) describe three different foehn events over the Larsen C ice shelf that have varying characteristics. They describe "foehn jets", which are a type of mountain gap flow that occur during foehn conditions, and typically emanate from the mouths of inlets. These so-called foehn jets are associated with accelerated wind speeds but cooler and moister air relative to foehn conditions downstream of higher elevation orography. Elvidge et al. (2015) argue that this dampened foehn effect in jet regions results from air flowing through lower elevation mountain passes, which produces less orographic uplift in the case of linear events produced by mechanism 1 and causes air to be sourced from lower altitudes in the case of more non-linear events produced by mechanism 2. Adjacent "wake" regions that they also identify are usually warmer and drier (Elvidge et al., 2015).

Because foehn winds are produced by specific synoptic meteorological conditions, foehn occurrence on Larsen C varies throughout the year. For example, strong westerly winds impinging on the Antarctic Peninsula, which typically occur when the SAM is most positive, often generate foehn. Estimates of foehn frequency have been conducted using AWS data and high-resolution regional modelling. For example, across the northern Antarctic Peninsula, Cape et al. (2015) find monthly mean foehn occurrence ranging between 5-25%, while Wiesenekker et al. (2018), Turton et al. (2018) and King et al. (2017) find that foehn occur on average

14%, 15% and 21% of the year, respectively, across the whole Larsen C ice shelf. All of these studies, as well as Datta et al. (2019), find maximum foehn occurrence in spring (SON), with Turton et al. (2018) estimating that foehn occur 50% of the time in SON.

2.4.2 The effect of foehn on the surface energy balance

Kuipers Munneke et al. (2012) show that foehn conditions have a notable effect on the near-surface meteorology and SEB of Larsen C. They identify foehn events in observations from two AWSs on Larsen C that are associated with reduced downwelling longwave ($LW_{\downarrow}$), and higher downwelling shortwave ($SW_{\downarrow}$) radiation, and elevated melt rates. During summer, higher SW fluxes can drive considerable melting. Indeed, Grosvenor et al. (2014) suggest that the increase in SW radiation associated with foehn-induced cloud clearance is the most important driver of melting during the summertime foehn cases they examine. As is also noted in Elvidge et al. (2015) and Elvidge et al. (2016), the foehn events shown in Kuipers Munneke et al. (2012) are accompanied by much higher sensible heat fluxes, driven by the delivery of air that has been adiabatically warmed and dried on its descent over the peninsula mountains. The presence of warm, dry air above the ice surface also drives sublimation, resulting in a negative latent heat flux (Kuipers Munneke et al., 2012). This inverse relationship between the sensible and latent heat fluxes over Larsen C is also shown by King et al. (2008) in stable conditions.

Foehn events contribute to greater surface melting because the reduction in the latent and LW fluxes is smaller than the increase in the SW and sensible heat fluxes (Kuipers Munneke et al., 2012). The importance of sensible heat fluxes is even more apparent during wintertime foehn events when $SW_{\downarrow}$ is either zero or very small. For example, Kuipers Munneke et al. (2018) attribute foehn-driven melting in May 2016 to sensible heat fluxes of up to 200-300 W m^{-2}. Fluxes of this magnitude represent a considerable departure from their usual (non-foehn) values, which are typically negative, and of the order of tens of W m^{-2} (Kuipers Munneke et al., 2012; Kuipers Munneke et al., 2018). Elvidge et al. (2020) show that melting on Larsen C during foehn, especially outside of the summer months (DJF), is primarily forced by elevated turbulent heat fluxes, particularly of sensible heat: events where sensible heat is the dominant contributor to the SEB and melting occur 76% of the time in their observations from Cabinet Inlet (whose location is shown in Figure 2.1).

The spatial characteristics of foehn also affect melting. For instance, Elvidge (2013) found less melting in inlets, which are often jet regions discussed above, in contrast to the results of e.g. Luckman et al. (2014), who find enhanced melting in these locations. However, the cases examined in Elvidge (2013) were accompanied by cool air temperatures and therefore limited melting (Elvidge et al., 2020). Although foehn occurrence can be higher in jet regions due to the channelling effect of orography, they can be less intense – in some cases when latent heat fluxes dominate over sensible heat fluxes, the surface can cool because higher wind speeds enhance shear-dominated turbulence (Elvidge et al., 2020). The competing effects of higher occurrence/reduced drying and warming in jet regions, in addition to the effect of foehn on local boundary layer stability, could explain why Grosvenor et al. (2014) found no coherent effect of foehn jets on melting.

While several studies have focused on the causes, mechanisms, and effects of foehn on melting over the Antarctic Peninsula (Orr et al., 2004; van Lipzig et al., 2008; Elvidge, 2013; Elvidge et al., 2015; Elvidge et al., 2016; Cape et al., 2015; Elvidge and Renfrew, 2016; King et al., 2017), almost all have examined the role of the phenomenon during summertime. However, foehn winds occur throughout the year, and foehn-driven melting can occur even in winter (Cape et al., 2015; Kuipers Munneke et al., 2018). Kuipers Munneke et al. (2018) used a comprehensive set of satellite records, AWS observations and regional climate model output to demonstrate this concretely for the first time, using a case study from May 2016. Analysis included in this study is developed in Chapter 4. Datta et al. (2019) reported similar results, showing that melting occurred outside the summer season in their regional model climatology and satellite observations of the period 1982-2017. Elvidge et al. (2020) use high-resolution MetUM simulations to build on Kuipers Munneke et al. (2018), and show that foehn-driven melting is extremely important on Larsen C: despite occurring just 15% of the time, foehn conditions are associated with 45% of the melt in their study. They also find that foehn-driven melting is especially important outside the summer months, accounting for 90% of the melting occurring in winter, spring and autumn (JJA, SON and MAM, respectively). Almost all studies of foehn winds on Larsen C have used high-resolution regional modelling to examine the phenomenon (Elvidge, 2013; Grosvenor et al., 2014; Elvidge et al., 2015; Elvidge et al., 2016; King et al., 2017; Kuipers Munneke et al., 2018; Wiesenekker et al., 2018; Turton et al., 2018; Kirchgaessner et al., 2019), because surface observations are sparse and those available are confined to the near-surface.

2.4.3 Trends in foehn frequency

There is uncertainty regarding trends in foehn frequency on the Antarctic Peninsula and Larsen C, their relationship with large-scale circulation like the SAM, and the effect that trends have on the SEB and melting. For example, Cape et al. (2015) find a strong positive correlation on the Antarctic Peninsula between SAM index, surface temperature, foehn frequency and melting, especially during DJF, over the period 1962-2010. This supports previous work (Scambos et al., 2003; van den Broeke, 2005) that increased foehn frequency was important in driving the collapse of Larsen B. However, although a consistent warming trend was observed alongside a trend towards more positive SAM index values until the early 2000s, since 2004-05 a mean cooling trend has been present (Turner et al., 2016), particularly in summer and autumn, accompanied by a decline in foehn frequency (Cape et al., 2015). Similarly, the decline in melt duration over Larsen C since the early 2000s reported by Bevan et al. (2018) is mostly related to falling mean annual surface temperatures (Turner et al., 2016), despite a recent trend towards more positive SAM values. As outlined above, a more positive SAM index is related to stronger westerly winds, which increases the frequency of foehn events and thus melting. However, the correlation between SAM and melting over Larsen C is weakest and insignificant during summer, when the majority of melting occurs (Cape et al., 2015; Bevan et al., 2018). Additionally, more cold air was advected onto the Larsen C ice shelf during the early 2000s because of changes to large-scale circulation patterns, which produced more cyclonic easterly/south-easterly flow and pushed sea ice from the Bellingshausen Sea closer to the peninsula (Turner et al., 2016). Air flowed over the relatively colder sea ice rather than over the ocean, restricting the source of heat from the ocean and causing temperatures to be cooler (Bevan et al., 2018). Against this backdrop of decreasing annual mean temperatures and an overall decline in melting across the entire Larsen C ice shelf , Bevan et al. find an increase in melt duration of 2 d yr^{-1} in inlets. This indicates that positive SAM trends still increase foehn frequency closest to steep topography, but that the competing effects of large-scale circulation patterns drive down average temperatures over the wider Larsen C region.

Foehn winds have been shown in this section to influence the SEB and surface melting. However, clouds also strongly influence the SEB: their effects are summarised next.

2.5 The importance of cloud for the surface energy balance on Larsen C

2.5.1 Cloud properties

Despite their importance in the polar climate system, Antarctic clouds are among the most under-sampled in the world because of the difficulties of in situ data collection in this harsh, remote environment (Lachlan-Cope, 2010; Bromwich et al., 2012). The effect of Antarctic clouds on the SEB can determine whether the ice surface remains frozen or melts (Kalesse et al., 2016; Nicolas et al., 2017), with consequent implications for ice sheet mass balance and, potentially, for global sea level rise. Clouds can alter the onset, extent, intensity and duration of surface melting via their effect on the SEB (Scott et al., 2017). Cloud impacts on the SEB are most important in warmer regions like the Antarctic Peninsula, where surface temperatures can rise above freezing in summer and cause melting, and where fractional cloud cover is typically 80-90% (Lachlan-Cope, 2010).

Cloud phase strongly influences cloud radiative properties. Mixed-phase clouds dominate in summer over coasts and ice shelves like Larsen C (Lachlan-Cope, 2010; Listowski et al., 2019) and have a complex vertical profile, with multiple thin layers in a "water-over-ice" structure of supercooled liquid droplets above heavier ice crystals (Barrett et al., 2017a). Listowski et al. (2019) use the DARDAR product to show that mixed-phase clouds across Antarctica occur ~10-30% of the time, and that unglaciated supercooled liquid clouds occur up to ~20% of the time continent-wide (in summer), and exist down to temperatures as low as -38°C. This is because there are very few ice nucleating particles (INPs, particles that initiate ice formation) in pristine Antarctic air to trigger glaciation (Lawson and Gettelman, 2014). Clouds with higher liquid water paths, comprised of many small droplets, are less transmissive to incoming SW radiation, and more emissive in the infrared, so radiate more LW radiation back to the surface (Zhang et al., 1996). However, the vertical position of liquid within the cloud is important: for instance, the supercooled liquid upper layer of mixed-phase clouds can reflect lots of SW, but has little effect on LW emission (Barrett et al., 2017a).

Atmospheric models typically struggle to represent cloud phase or vertical structure correctly, especially at high latitudes. For example, Klein et al. (2009) find that models cannot usually simulate enough liquid water in Arctic stratocumulus because too much ice is formed at the expense of supercooled liquid. Many atmospheric models, including the MetUM, exhibit this bias in cloud phase and structure because their microphysical parameterisations are developed for the mid-latitudes and are relatively simple. For example, poor representations of processes like riming (Furtado et al., 2016) and vapour deposition (Furtado and Field, 2017), as well as large-scale cloud phase partitioning (Abel et al., 2017) have been shown to cause the MetUM to over-estimate cloud ice and under-estimate cloud liquid contents. Model ice nucleation parameterisations can also strongly influence cloud phase; for instance Listowski and Lachlan-Cope (2017) show that in WRF, the most accurate simulations of Antarctic Peninsula summertime cloud liquid water contents is only achieved using more sophisticated

INP parameterisations, such as that of DeMott et al. (2010), which are not included in the model. In many models, including in the MetUM, errors in cloud phase produce significant SEB biases, most notably over the Southern Ocean (Bodas-Salcedo et al., 2012; Hyder et al., 2018), where cloud radiative effect is most sensitive to the presence of liquid water (Lawson and Gettelman, 2014). This is because sub-grid scale spatial variability in temperature and humidity are necessarily parameterised in models by large-scale cloud schemes, which compute liquid and ice cloud fractions that are then fed into the microphysics scheme. In reality, ice and liquid can co-exist in spatially segregated pockets (Tan and Storelvmo, 2016), but in many models it is difficult to sustain a separation between the phases. For instance, when total cloud fraction in the MetUM exceeds 100%, ice and liquid phases are assumed to overlap within a homogeneously mixed mixed-phase region (Abel et al., 2017). In this mixed-phase region, ice forms preferentially because of the lower saturation vapour pressure over ice than liquid.

Modelled cloud has been implicated as a primary driver of surface radiation biases over Antarctica (Bromwich et al., 2013) and specifically over Larsen C (King et al., 2015). King et al. (2015) find that three different regional atmospheric models simulate either too little cloud, or cloud that is optically too thin over the ice shelf. Summertime clouds over Larsen C in the MetUM are optically too thick in the SW part of the spectrum, while being too thin in the infrared, which results in negative $SW_{\downarrow}$ and $LW_{\downarrow}$ biases. Overall, they find a negative net downward LW bias and positive net downward SW bias because too little SW radiation is reflected by the surface. These net SW and LW fluxes do not entirely cancel, which produces a positive net downward energy flux at the surface and can cause the MetUM to over-estimate melt on Larsen C. High resolution regional climate models are typically able to represent the radiative effects of mixed-phase cloud more accurately than global models because more processes can be explicitly resolved (Vergara-Temprado et al., 2018). However, computational constraints still necessitate parameterisations that approximate sub-grid scale cloud properties, which produce errors in the SEB. These are examined in further detail in the next section.

Inaccurately representing cloud phase over the Southern Ocean produces large radiative biases and therefore sea surface temperature biases, which degrades the quality of future projections made with regional and global models (Bodas-Salcedo et al., 2016; Vergara-Temprado et al., 2018; Hyder et al., 2018). Cloud radiative effect is strongly influenced by cloud microphysics, with ice phase microphysics demonstrated to be one of the most important determinants of cloud phase in the Southern Ocean and Antarctic (Vergara-Temprado et al., 2018). This is supported by the results of Field et al. (2014), who found that altering modelled INP particle size distributions in their experiments allowed more supercooled water to persist.

Microphysical properties, such as particle size, shape and number concentration, are related to cloud phase and have varying effects on cloud radiative effect and the SEB. For example, cloud condensation nuclei, which initiate the formation of liquid droplets, are around 10^5 - 10^6 times more numerous than ice nucleating particles that trigger ice formation (Rotstayn et al., 2000; Morrison et al., 2012). Ice crystals therefore tend to be larger, because the same amount of condensate is divided between fewer particles, making them more likely to gain enough mass to precipitate out of the cloud (Pruppacher and Klett, 1978; Wilson and Ballard, 1999; McCoy et al., 2016). The lifetime of ice clouds is therefore lower than for liquid clouds because particles precipitate, causing the cloud to dissipate, which has especially large effects on the SEB in polar regions (Kalesse et al., 2016). Ice nucleation in mixed-phase clouds is the main control on cloud lifetime (Seinfeld et al., 2016; Barrett et al., 2017a).

Cloud phase and microphysical properties can produce competing SW and LW effects, for example high ice clouds have a surface net LW warming effect because they reduce LW losses to space by being colder and less emissive than the surface, but their SW effect is strongly determined by microphysical properties like ice crystal size, habit and optical depth (Wendisch et al., 2005; Wallace and Hobbs, 2006; Cotton et al., 2011). Clouds at high latitudes tend to warm the surface and cool the atmosphere because they are rarely more reflective to SW than the ice surface and are more emissive in the LW than the atmosphere (Cotton et al., 2011). In particular, optically thin, low-level clouds with high water contents can play an important role in the polar SEB because they are transmissive to SW but emissive in the infrared (Miller et al., 2015; Scott et al., 2017). For instance, Bennartz et al. (2013) found that clouds with low liquid water paths were responsible for sustaining the prolonged melt event observed over the Greenland ice sheet in 2012 by maintaining temperatures above melting point.

2.5.2 Observations of Antarctic cloud

Although airborne campaigns are one of the best ways of sampling cloud, very few have been conducted on the Antarctic Peninsula. Data from the 2010 and 2011 JASPER and OFCAP campaigns, respectively, described in Grosvenor et al. (2014), Lachlan-Cope et al. (2016) and Listowski and Lachlan-Cope (2017), are some of the only available aircraft observations of clouds on the Antarctic Peninsula. Surface-based visual observations of cloud type, coverage and height are made at many staffed stations on the peninsula, particularly during summer, when they are often coupled with ceilometer observations (Bromwich et al., 2012). For example, Kirchgaessner (2010) used surface observations at Vernadsky station to assess trends in cloudiness over the western Antarctic Peninsula. In situ observations are also possible when cloud reaches the ground: although this is less frequently observed on the peninsula, Lachlan-Cope et al. (2001) describe observations of cloud and precipitation particles from Avery Plateau. Ground-based remote sensing, for instance with LIDAR (Nott and Duck, 2011; Rowe et al., 2016; Silber et al., 2018) and radar (Gorodetskaya et al., 2015; Silber et al., 2018) has been used to profile clouds bottom-up, while airborne (Morley et al., 1989) and spaceborne remote sensing are frequently used to retrieve cloud properties top-down. Satellites can measure clouds either passively (e.g. MODIS, AVHRR) or actively (e.g. CALIOP) and the emergence of more sophisticated products like DARDAR-CLOUD that combine techniques has increased understanding of the microphysics of Antarctic clouds (Delanoë and Hogan, 2010; Ceccaldi et al., 2013; Listowski et al., 2019). The importance of cloud for global climate, as well as the lack of observations and the limitations of satellite products has motivated the development of more sophisticated atmospheric models that can resolve or parameterise cloud.

2.5.3 Model representation of cloud

Clouds remain the largest source of uncertainty in global climate models used for climate projections and so are an important area of research (Komurcu et al., 2014; Baran et al., 2014; Seinfeld et al., 2016). This is largely because cloud processes, which must be parameterised, are too complex to resolve explicitly, and often occur at smaller scale than a model gridbox (Mechoso and Arakawa, 2015; Pu and Kalnay, 2012). Parameterisations can introduce biases and uncertainties into model output, and the choice of these can therefore critically impact simulation quality (Gettelman et al., 2010; Mechoso and Arakawa, 2015). For instance, Barrett et al. (2017b) show that the parameterisation of ice phase cloud microphysics is the dominant source of error in their simulations of mixed-phase altocumulus and King et al. (2015) speculate that limitations in the representation of cloud microphysics accounts for the majority of SEB errors in their simulations over Larsen C. Further, Grosvenor et al. (2017) show that the treatment of sub-grid cloud has as large an effect on simulated SW fluxes as increasing aerosol loading by an order of magnitude.

In particular, phase partitioning parameterisations can influence microphysical process rates. For example, as outlined in section 2.5.1 above, the assumption in many parameterisations that ice and liquid are homogeneously mixed results in over-active vapour deposition that produces too much ice at the expense of liquid (Klein et al., 2009; Field et al., 2014; Tan and

Storelvmo, 2016). In the MetUM, Abel et al. (2017) show that limiting mixing between phases can double simulated liquid water path. Listowski and Lachlan-Cope (2017) show using WRF that more sophisticated microphysics parameterisations produce much more supercooled liquid in summertime Antarctic Peninsula clouds, and hence downwelling LW radiation is represented better. In particular, they show that double-moment or bin microphysics schemes perform better and that the parameterisation of INP within each scheme is important, with the DeMott (2010) scheme most closely matching observations (Listowski and Lachlan-Cope, 2017). Furtado and Field (2017) show that reducing the parameterised efficiency of cold-cloud ice processes like riming in the MetUM increases the amount of cloud liquid and reduces SEB biases relative to observations.

Non-microphysical processes also impact cloud though, for instance parameterisations of sub-grid turbulence can strongly impact cloud phase (Klein et al., 2009). Furtado et al. (2016) demonstrate that improving the MetUM's parameterisation of sub-grid scale turbulence can increase modelled cloud liquid and reduce radiative biases in the Arctic and Southern Ocean. Because parameterisation schemes interact, the order in which they are called in the model can also impact the final solution: Donahue and Caldwell (2018) find that model output is sensitive to ordering because each process "feels" the effects of those preceding.

2.6 Current knowledge gaps

This chapter has presented current understanding of atmospheric processes contributing to surface melting on Larsen C, and areas of uncertainty. As detailed in section 2.4, it is unclear how foehn frequency on the Antarctic Peninsula is changing in response to evolving large-scale atmospheric circulation. On Larsen C, the spatial distribution of foehn occurrence has not been quantified. In addition, while the impact of foehn on the SEB and melting has been examined on Larsen C during case studies (Grosvenor et al., 2014; Elvidge et al., 2015; Elvidge et al., 2016; Elvidge et al., 2020; Kuipers Munneke et al., 2018), this kind of analysis has not been performed over longer (multi-year) timescales. Climatologies have focused solely on near-surface meteorology (van Wessem et al., 2018) or the importance of foehn for the evolution of the snowpack (Datta et al., 2019) but no studies have been published that explicitly link meteorology, foehn occurrence, the SEB and surface melting. There is also a gap in scientific understanding regarding the influence of cloud phase on the SEB and surface melting over Antarctic Peninsula ice shelves, and models typically cannot represent cloud well (section 2.5). King et al. (2015) conclude that cloud properties are a likely cause of modelled SEB biases. However, although observed cloud phase has been assessed by Grosvenor et al.

(2012) and Lachlan-Cope et al. (2016) and modelled by Listowski and Lachlan-Cope (2017), no work has been done to explicitly connect these properties to the SEB. The representation of polar clouds should be a research priority because it is of critical importance for climate model development (Lenaerts et al., 2017) and can therefore strongly affect model projections of future climate change (Barrett et al., 2017a; Barrett et al., 2017b). Lastly, although some broad estimates of surface meltwater production on Larsen C have been made (Trusel et al., 2013; Trusel et al., 2015), there has been little work done to quantify the effect of the most important processes contributing to surface melting there. Few models have been able to reproduce the observed east-west gradient in melting associated with foehn occurrence on Larsen C because they do not capture the main processes that create this pattern.

This thesis will address these gaps by examining the influence of foehn, cloud and meteorology on the SEB and surface melting in observations and model output. The following chapter will outline the primary data sources and methods used to do this.

Data and methods

3

This chapter describes the datasets and methods used throughout the thesis. It will provide an overview of relevant technical information and data treatment, although chapter-specific uses or configurations will be described in the relevant results chapter.

3.1 Data description

3.1.1 AWS measurements, instrumentation and data treatment

The difficulty of making meteorological measurements in Antarctica noted in Chapter 2 means that most in situ near-surface observations on Larsen C come from AWSs. Although some intensive sampling campaigns have taken place, these are limited in their temporal coverage. Time series of surface meteorology and energy fluxes from four AWSs are employed throughout the thesis to answer the research questions outlined in Chapter 1. All are operated by the Institute for Marine and Atmospheric research at Utrecht University (IMAU) and maintained by the British Antarctic Survey (BAS). Metadata and specific uses for AWS data in this thesis are summarised in Table 3.1. The selection of AWSs for each chapter depends on data availability during the time period considered, as well as the research question. For instance, to evaluate the effect of foehn winds on the SEB it is necessary to use data from a station which measures the full SEB close to the foot of the mountains where the foehn effect is most pronounced. The Cabinet Inlet AWS (AWS 18) is therefore used to evaluate the influence of foehn in Chapters 4 and 6. Similarly, AWS 14 is used to evaluate the impact of cloud phase on the SEB over a larger area of the ice shelf in Chapter 5 because it is representative of a wider area and uninfluenced by topography.

All stations measure surface meteorology, as well as the full SEB (AWS 14, 17 and 18) or radiative fluxes (AWS 15). AWS 14 is located around 125 km east of Larsen C's grounding line, at approximately 40 m above sea level (a.s.l.). It is currently operational. AWS 15 was emplaced in January 2009, and was operational until June 2014. It is located approximately 75 km southwest of AWS 14, slightly further inland from the ice shelf edge. The area surrounding both AWS 14 and 15 is relatively flat and homogeneous, meaning that measurements taken at both stations are representative of a wider area (King et al., 2015). AWS 17 is located on the remnant Larsen B ice shelf, in Scar Inlet (shown in Figure 2.1), where near-surface

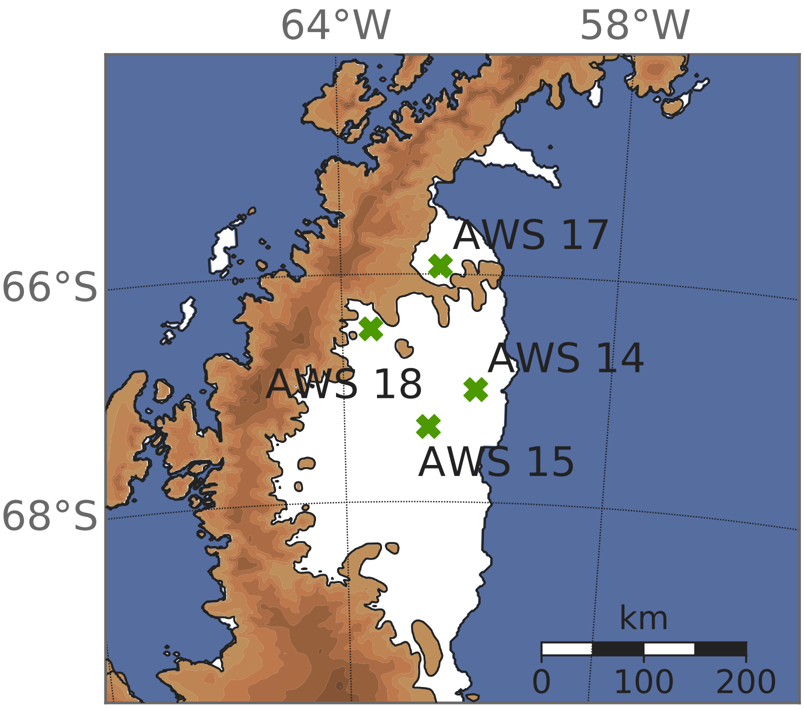

Figure 3.1.: Locations of the AWSs used in the thesis. Topography is shaded, where darker colours indicate higher terrain.

meteorology is influenced by localised topographic features. It was operational from February 2011 until March 2016. AWS 18 is located in Cabinet Inlet on the northwest of Larsen C, close to the foot of the Antarctic Peninsula mountains and is still operational. It is also surrounded by steep topography, which makes the meteorology very localised. The locations of all AWSs used are given in Table 3.1 and shown in Figure 3.1.

AWSs 14, 15 and 17 use the same basic meteorological sensors and are a "Type II" station used by IMAU for all stations 1997-2014 (Figure 3.2a and b), while AWS 18 is a next-generation "intelligent weather station for polar use" (iWS, Figure 3.2c and d), which has been developed at IMAU and used at stations erected since 2014 (van den Broeke et al., 2013). At the "Type II" stations, a Vaisala HMP35AC is used to measure relative humidity and air temperature at 2 m above the surface, while a Vaisala PTB101B sensor measures air pressure. The air temperature and humidity instrument is unventilated, which can lead to positive temperature biases in calm, sunny conditions, so a correction is applied to the final dataset using concurrent thermocouple observations after Smeets (2006) and Smeets et al. (2018). Additionally, relative humidity measurements are corrected to account for solar heating of the housing of the unventilated instrument, as well as its slow response time (Kuipers Munneke et al., 2018). Wind speed and direction are measured with a Young wind monitor (model

05105 at "Type II" stations, model 05103 at AWS 18). Upwelling and downwelling radiative fluxes (SW$_\downarrow$, SW$_\uparrow$, LW$_\downarrow$ and LW$_\uparrow$) are observed by a Kipp and Konen radiometer (CNR1 at "Type II" stations, CNR4 at AWS 18), and SW fluxes are adjusted for the tilt of the sensor using in-built tilt sensors for AWS 14, 15 and 17, and after the MODIS-satellite guided procedure of Wang et al. (2016) for AWS 18. All variables from AWS 14, 15 and 17 are sampled at 6 minute resolution (except air pressure, which is sampled hourly) and recorded as hourly averages, while data from AWS 18 is recorded at half-hourly resolution.

The iWS setup (van den Broeke et al., 2013) uses ultra-low power consumption instruments and data logger, contained within a single housing to make it more robust for use in polar environments. Air temperature, pressure, relative humidity and snow height sensors, as well as a GPS unit, batteries and communication antenna are all included inside. A propeller-vane Young anemometer and Kipp & Konen CNR4 radiometer are installed outside the housing to measure wind speed, direction and radiation.

A SEB model (Kuipers Munneke et al., 2009; Kuipers Munneke et al., 2012) is used to compute the SEB at AWS 14, 17 and 18. This model uses various quantities (pressure, relative humidity, air temperature, wind speed, SW$_\downarrow$, LW$_\downarrow$ and SW$_\uparrow$ radiation) to close the energy budget and compute the turbulent fluxes of sensible and latent heat using the bulk method. The sensible (H$_S$) and latent (H$_L$) heat fluxes are calculated using the bulk aerodynamic equations given in Equations 3.1 and 3.2, respectively,

$$H_S = \rho_a C_p u^* T^* \tag{3.1}$$

$$H_L = \rho_a L_{(v,s)} u^* q^* \tag{3.2}$$

where ρ_a is the density of air, C_p is the specific heat capacity of dry air, $L_{(v,s)}$ is the latent heat of vaporisation or sublimation (which of these is used is determined from the surface temperature, T_S), u^* is the friction velocity and T^* and q^* are the turbulent scaling parameters for temperature and humidity, respectively, calculated using the iterative bulk aerodynamic method based on Monin-Obhukov similarity theory and described in Kuipers Munneke et al. (2009).

The ground heat flux, G_S, is calculated using a multi-layer snowpack model. Because the model accounts for subsurface radiation absorption, the amount of melt energy, E_{melt}, is the sum of surface and subsurface melt (Kuipers Munneke et al., 2012). The subsurface model is set up using various constants, such as the scalar roughness length (0.11 mm, derived from directly measured turbulent fluxes), roughness lengths for temperature and humidity (derived from Andreas, 1987), snowpack LW emissivity (0.98), snow grain size (100 μm) and snow density profiles (derived from snow pits dug in January 2011, and being relatively constant at around 400-500 kg m^{-3} between 0-0.6 m below the surface).

Table 3.1.: Summary of metadata, measured parameters, data availability and use of AWS data throughout the thesis.

Station name	Location	Elevation	Data coverage	Available measurements	Use in this thesis
AWS 14 (Larsen North)	67°00’44”S 61°30’00”W	40 m a.s.l.	January 2009 - present	Surface meteorology, radiative fluxes, subsurface snowpack information, full SEB, radiosondes during OFCAP (Jan/Feb 2011)	SEB information in Chapter 5, hindcast validation in Chapter 6
AWS 15 (Larsen South)	67°34’14”S 62°09’06”W	50 m a.s.l.	January 2009 – June 2014	Surface meteorology, radiative fluxes	Radiative fluxes in Chapter 5, hindcast validation in Chapter 6
AWS 17 (Scar Inlet)	65°56’ “S 61°51’ “W	50 m a.s.l.	February 2011 – March 2016	As AWS 14	Hindcast validation in Chapter 6
AWS 18 (Cabinet Inlet)	66°28’58”S 63°22’16”W	70 m a.s.l.	November 2014 - present	As AWS 14	Foehn wind detection and impact on SEB in Chapters 4 and 6, hindcast validation in Chapter 6

Radiative components (SW$_{\downarrow}$, SW$_{\uparrow}$, LW$_{\downarrow}$ and LW$_{\uparrow}$) and meteorological variables from AWS 15 (67.57°S, 62.15°W) are also used. All stations measure temperature, pressure, humidity, winds and radiation terms, and snowpack sensors down to 15 m are installed at AWS 14. A full description of the instrumentation is given in Kuipers Munneke et al. (2012), and an explanation of the model used to calculate additional flux terms can be found in Kuipers Munneke et al. (2009).

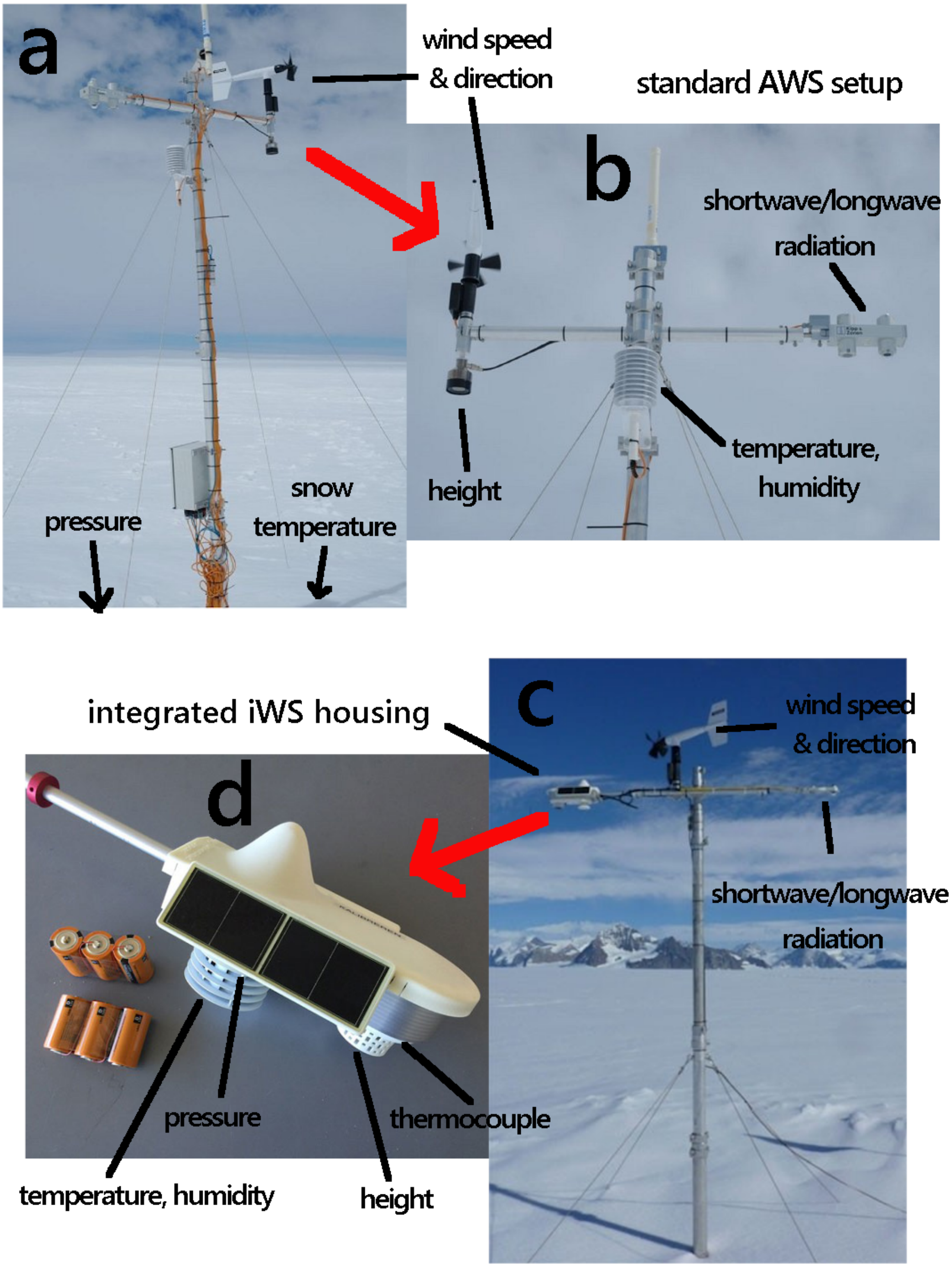
a
wind speed
& direction
standard AWS setup
b
shortwave/longwave
radiation
snow
temperature
pressure
height
temperature,
humidity
integrated iWS housing
c
d
wind speed
& direction
shortwave/longwave
radiation
pressure
thermocouple
temperature, humidity
height

Figure 3.2.: Images of the standard "Type II" AWS set-up used by IMAU before 2014 and the latest "iWS" setup used at Cabinet Inlet. Panels a) and b) show the set-up of AWS 17 (Scar Inlet) and detail of the instrumentation, respectively, while panels c) and d) show the same for AWS 18 (Cabinet Inlet). All images are from IMAU.

The SEB is defined as the "net amount of energy received at the surface" (Lenaerts et al., 2017, pp. 3355), and is formulated as follows:

$$E_{tot} = LW_{\uparrow} + LW_{\downarrow} + SW_{\uparrow} + SW_{\downarrow} + H_S + H_L + G_S \tag{3.3}$$

where $LW_{\uparrow}$ and $LW_{\downarrow}$ are the upwelling and downwelling components of LW radiation, respectively, $SW_{\uparrow}$ and $SW_{\downarrow}$ are the upwelling and downwelling components of SW radiation, respectively, and H_S, H_L and G_S are the surface sensible, latent and ground heat fluxes, respectively. All fluxes are defined as positive when directed towards the surface.

Surface melt energy is defined as in King et al. (2015), as

$$E_{melt} = \begin{cases} E_{tot} & T_S \geq 0°C \\ 0 & T_S < 0°C \end{cases} \tag{3.4}$$

such that melt only occurs when there is a surplus of energy at the surface (E_{tot} in Equation 3.3 is positive) and surface temperature is at the melting point.

3.1.2 Aircraft measurements, instrumentation and data treatment

In situ data collected using the British Antarctic Survey's instrumented De Havilland Twin Otter aircraft are used in Chapter 5 to examine the effect of cloud microphysics on the SEB. The dataset includes positional information from standard aircraft sensors, meteorological information such as three-dimensional winds, temperature, humidity and pressure, and cloud microphysical information from a cloud probe fitted on a wing pylon (Figure 3.3). A full description of the aircraft instrumentation is given in King et al. (2008).

Basic meteorological information is measured by the standard instrument suite. Two humidity instruments are fitted: a Rosemount mounted Vaisala Humicap and a Buck 1011C cooled-mirror hygrometer. Temperature is measured via Goodrich Rosemount probes on the nose of the aircraft, and de-iced (model 102AU1AG) and non de-iced (model 102E4AL) measurements are available. Pressure is measured using standard Honeywell HPA aircraft sensors, which also record GPS position, aircraft roll, pitch and yaw, speed and altitude. Laser (Riegl LD90-3800VHS-FLP) and radar (in-built aircraft sensors) altimeters both measure height above the surface. A NOAA/ARA "Best Aircraft Turbulence" (BAT) probe is fitted on a boom extending from the nose of the aircraft, and measures acceleration, as well as pressures and exposed thermocouple temperatures from nine holes in the probe. Temperature and pressure data are combined with attitude information from the aircraft sensors to calculate

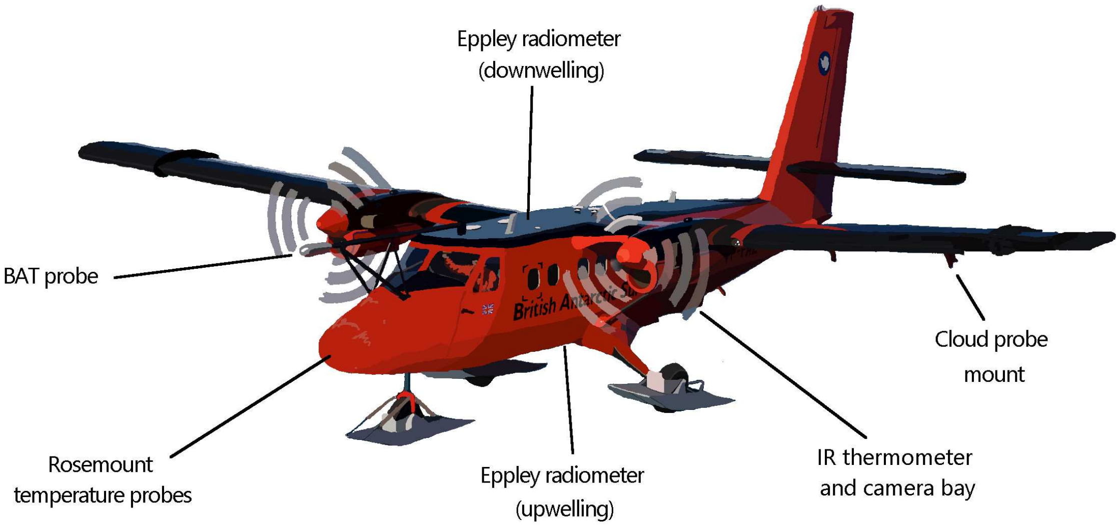
Eppley radiometer (downwelling)
BAT probe
Cloud probe mount
Rosemount temperature probes
Eppley radiometer (upwelling)
IR thermometer and camera bay
British Antarctic Survey

Figure 3.3.: Schematic illustration of instrumentation on the British Antarctic Survey DHC Twin Otter aircraft.

turbulence using the eddy covariance method. $SW_{\uparrow}$, $SW_{\downarrow}$, $LW_{\uparrow}$ and $LW_{\downarrow}$ are measured with Eppley pyranometers and pyrgeometers mounted on the underside and roof of the aircraft, and a downward-facing camera records surface conditions. An infrared thermometer (Heimann model KT19.82) can also be mounted in the floor hatch panel to measure surface temperature.

Data from the Orographic Flows and Climate of the Antarctic Peninsula (OFCAP) campaign in January/February 2011 is examined in Chapter 5. During OFCAP, a Droplet Measurement Technologies Cloud, Aerosol and Precipitation Spectrometer (CAPS) probe (Baumgardner et al., 2001) was fitted on a wing pylon to measure cloud microphysics. The CAPS probe contains three distinct instruments:

1. The Cloud and Aerosol Spectrometer (CAS) measures particles in the size range 0.5 – 50 μm at 1 Hz frequency. In practice, these particles tend to be either cloud droplets or aerosol particles during summer on the Antarctic Peninsula. A correction is applied to the data to account for the lack of anti-shatter inlet on the sensor, which was shown by Grosvenor et al. (2012) to increase the particle count from the CAS by 1.47 times due to air acceleration within the tube (Lachlan-Cope et al., 2016).
2. The hotwire liquid water content (LWC) sensor measures the amount of liquid in air using a heated wire. The instrument features a heated copper wire mounted between two arms, which is maintained at a constant temperature. The instrument measures the power needed

to maintain the temperature of the wire as it is cooled by the evaporation of liquid particles colliding with it (King et al., 1978). A simple relationship is used to relate the power output to LWC. The data are used only to validate CAS data because the instrument is known to underestimate peaks in LWC (Lachlan-Cope et al., 2016).

3. The Cloud Imaging Probe (CIP) measures particles with diameters between 25 μm and 1.5 mm at a pixel resolution of 25 μm. It works by imaging particles as they pass through a charge coupled device array. Particles project a silhouette and this signal is processed to produce number concentrations of ice particles and large liquid droplets.

CIP data are quality controlled and processed according to the method of Crosier et al. (2011), and ice water contents are computed from CIP imagery using the mass-dimensional relationship of Brown and Francis (1995). Data were pre-processed before use by Russell Ladkin, Tom Lachlan-Cope and Constantino Listowski. Ice and liquid particles are distinguished based on their circularity, C, defined as:

$$C = \frac{P^2}{4\pi A} \tag{3.5}$$

where P is the particle perimeter and A is the particle area, both as measured by the CIP. To discriminate between ice and liquid, A must be a minimum of 50 pixels, which translates to a particle of approximately 200 μm in diameter. Below this threshold, the phase of particles cannot be determined. As noted by Lachlan-Cope et al. (2016), these particles comprised less than 2-3% of all particles observed by the CAS, and were consequently disregarded. Circular particles with values of C between 0.9 and 1.2 are classified as liquid drops, while irregular particles of $C > 1.4$ are considered to be ice. Particles with circularity of 1.2 - 1.4 were categorised on a case-by-case basis by visually analysing example images outputted by the CIP. During summer on the Antarctic Peninsula, these particles were classified as ice, as in Lachlan-Cope et al. (2016).

3.2 Model description

The MetUM is used throughout the thesis, and is the primary analysis tool. It is used by the UK Met Office operationally for forecasting as well as for research purposes. It is run as an atmosphere-only model, but can also be used as a coupled model. The MetUM uses input data, in this thesis either operational analysis or reanalysis, to force a global model, which is dynamically downscaled using a series of increasingly high-resolution domains.

The outermost global domain is initialised using atmospheric fields (such as pressure, temperature, moisture and three-dimensional winds) from operational analysis in Chapters 4 and 5, and reanalysis in Chapter 6. Both inputs are relatively coarse resolution (for example, MetUM global "N512" operational output has a horizontal grid spacing of ~27 km at mid-latitudes and ERA-Interim reanalysis ~79 km), which is unsuitable for local, regional or process-scale studies such as are conducted in this thesis (Lo et al., 2008). However, their large-scale (global) features are robust, and can therefore be dynamically downscaled to add regional detail where observations are sparse (Yoshimura and Kanamitsu, 2008; Storch et al., 2017). Models forced with reanalysis often out-perform reanalysis alone, for example in North America (Castro et al., 2012; Bastola and Misra, 2014), Portugal (Soares et al., 2012) and Southern Africa (Haensler et al., 2011).

Information about global-scale atmospheric circulation is fed into the nested inner domain via lateral boundary conditions (LBCs) within a defined relaxation region around the boundaries. The inner domain then simulates conditions across the rest of the domain given this information. This nesting approach, whereby regional domains take LBCs from the outer domain they are nested within, can be repeated as many times as required to achieve the desired spatial resolution. Further details of the configurations used are given in Table 3.2 and section 3.2.2.

The accuracy of simulations increases with more frequent re-initialisations, which constrain the simulation more closely to observed values. Regional models that are initialised just once at the beginning of an integration ("free-running" models) can drift more considerably from observations than re-initialised models. Lo et al. (2008) outline three methodologies typically used with dynamical downscaling and show that the choice of method can influence simulation quality:

1. Continuous integration ("free-run"), where the limited-area model running over the regional nested domain is initialised once at the beginning, and then permitted to run freely as a continuous integration, using forcing from the parent global model. While this method is computationally least demanding, there is a danger that the inner domain can drift from the outer domain and develop physically inconsistent features during long integrations (Lo et al., 2008);
2. Frequent re-initialisations ("forecast mode") where the model is frequently re-initialised and allowed to run only short forecasts, which are then stitched together into a continuous time series, typically discarding the first section of each forecast;

3. Nudged runs ("nudging") where the model is allowed to run as in method 1 but the inner regional domain is "nudged" towards climatologies or observations to prevent model drift.

Method 1 is typically unsuitable for long simulations because the model drifts from observations without data input and can develop internal features different to the LBCs and large-scale fields (Lo et al., 2008). Methods 2 and 3 increase the utilisation of observations by periodically integrating them via frequent re-initialisations, or by nudging to bring simulated values in the regional model closer to the driving fields (Lo et al., 2008). Both prevent model drift and improve the skill of the simulation: for example, Rockel et al. (2008) find that applying nudging improves the representation of large-scale features like total kinetic energy in downscaled regional domains compared with un-nudged simulations. Good quality regional model output is required to reliably simulate atmospheric features such as foehn winds. Sensitivity tests showed that MetUM simulations using "forecast mode" were of better quality than "free running" mode, and this methodology was therefore applied in this thesis. Nudging is impossible in the MetUM.

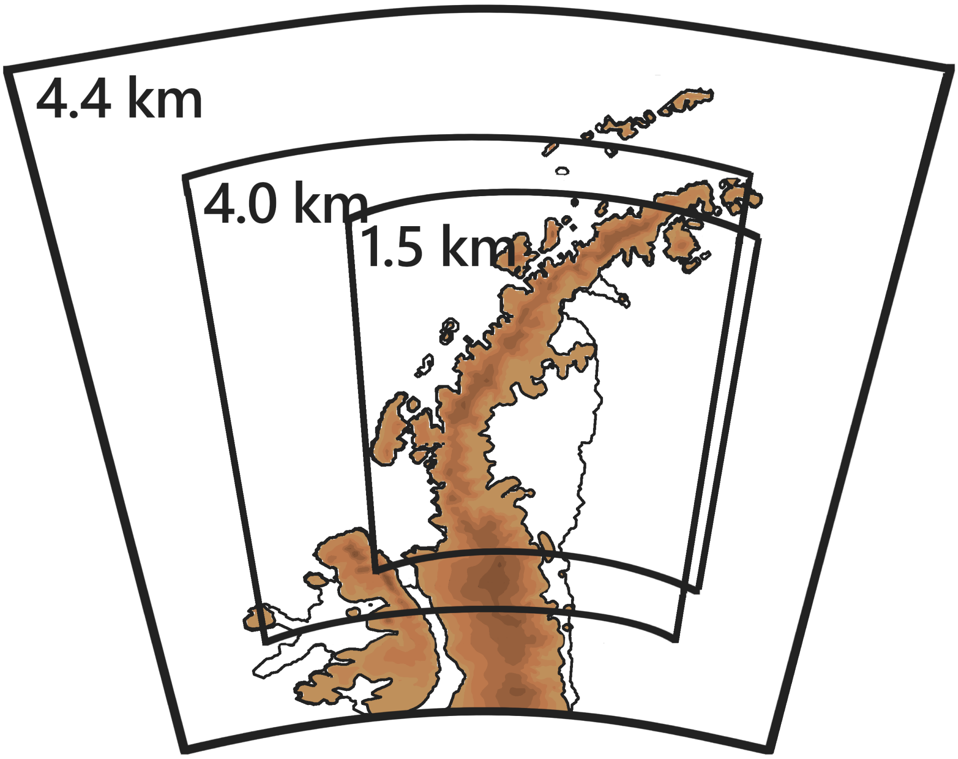

Figure 3.4.: Model domains used in the thesis. The 4.4 km and 1.5 km domains are used in Chapter 4, while only the 1.5 km domain is used in Chapter 5. The 4.0 km domain is used in Chapter 6 only.

3.2.1 Core physics and model description

The MetUM contains a non-hydrostatic, fully compressible dynamical core (ENDGame) with semi-implicit time stepping and semi-Lagrangian advection. Atmospheric prognostic variables are the dry virtual potential temperature, Exner pressure, dry density and three-dimensional winds, and moist prognostics such as cloud fields and specific humidity are advected as atmospheric tracers (Walters et al., 2017). Prognostic variables are discretised horizontally on an Arakawa-C grid and a terrain-following hybrid vertical coordinate with Charney-Phillips staggering is used in the vertical. When run as a regional, limited area model (LAM), the MetUM uses a rotated latitude-longitude grid to maintain uniform resolution across the domain. The LAM takes its boundary conditions from the coarser outer domain it is nested within, and the predicted solutions of the inner and outer nests are blended within a "halo region" around the edge of the inner domain.

3.2.2 Model domains and methodology

An atmosphere-only configuration of the model is used with a nested LAM centred on the Antarctic Peninsula. The specific domains used vary between chapters: in Chapter 4, two nests are used to downscale archived global operational MetUM analysis from N512 (~27 km horizontal grid spacing at mid-latitudes) to 4.4 km and then 1.5 km resolution, in a manner similar to Orr et al. (2014). The domains used in each chapter are shown in Figure 3.4. In Chapter 5, the inner nest, at 1.5 km grid spacing, is forced directly at the boundaries by a global model run at N768 (~17 km resolution at mid-latitudes), initialised from archived operational MetUM global analysis, while in Chapter 6, the inner nest is smaller and coarser resolution (4 km horizontal resolution), and the global model (N512) is initialised from ERA-Interim re-analysis data. The model domain sizes, boundaries and resolutions were selected firstly to maximise the number of pertinent processes that could be explicitly resolved, secondly to ensure that driving synoptic-scale circulation features could be included, and thirdly to limit the number of grid points within the domain to maximise computational efficiency. The global model is always run using GA6.1 physics (Walters et al., 2017) and in all chapters, the LAM configuration has 70 vertical levels up to 40 km.

Simulations are run in "forecast mode" described above, whereby the global domain is reinitialised periodically and runs a global forecast (typically 24 hours). The global model output provides the LBCs for the inner nested domain (which provides LBCs for the next nested domain, if applicable). Time series are created by discarding the first 12 hours of each 24-hour model forecast and concatenating the t+12 h to t+24 h series.

Table 3.2.: Summary of differences between MetUM model configurations used in each chapter.

Parameter	**Wintertime melt cases (Chapter 4)**	**Cloud microphysics (Chapter 5)**	**Hindcast (Chapter 6)**
Resolution of driving global model	N512 (~27 km at mid-latitudes)	N768 (~17 km at mid-latitudes)	N768 (~17 km at mid-latitudes)
Forcing data	Archived Met Office operational analysis	Archived Met Office operational analysis	ERA-Interim reanalysis
Number and resolution of limited area nests	1. 4.4 km and 2. 1.5 km	1. 1.5 km	1. 4.0 km
Finest horizontal resolution	1.5 km	1.5 km	4.0 km
Number of grid points in finest nest	400 x 400	400 x 400	220 x 220
Time step of nest	60 s	60 s	100 s
Model parameterisations used	Default settings	Variable: see Table 5.1, Chapter 5.	Optimised settings developed in Chapter 5 (see Table 5.1, Chapter 5).
Model version	10.4	10.8 (single-moment), 11.1 (CASIM)	11.1

A summary and comparison of the model set-ups used in each chapter is given in Table 3.2.

3.2.3 Updated orography dataset

By default, the MetUM takes information about coastlines (land-sea mask) and orography from the GLOBE dataset, which contains data about the Antarctic Peninsula collected in 1993 (Hastings and Dunbar, 1999). These data are averaged from their native 30 arc-second (~1 km) resolution to 1 arc-minute resolution for use in the global model, which are then downscaled to the regional nest. This makes the dataset relatively low resolution, particularly for simulating topographically-driven features such as foehn winds. Additionally, the default land-sea mask is outdated and includes the now-collapsed Larsen A and B ice shelves.

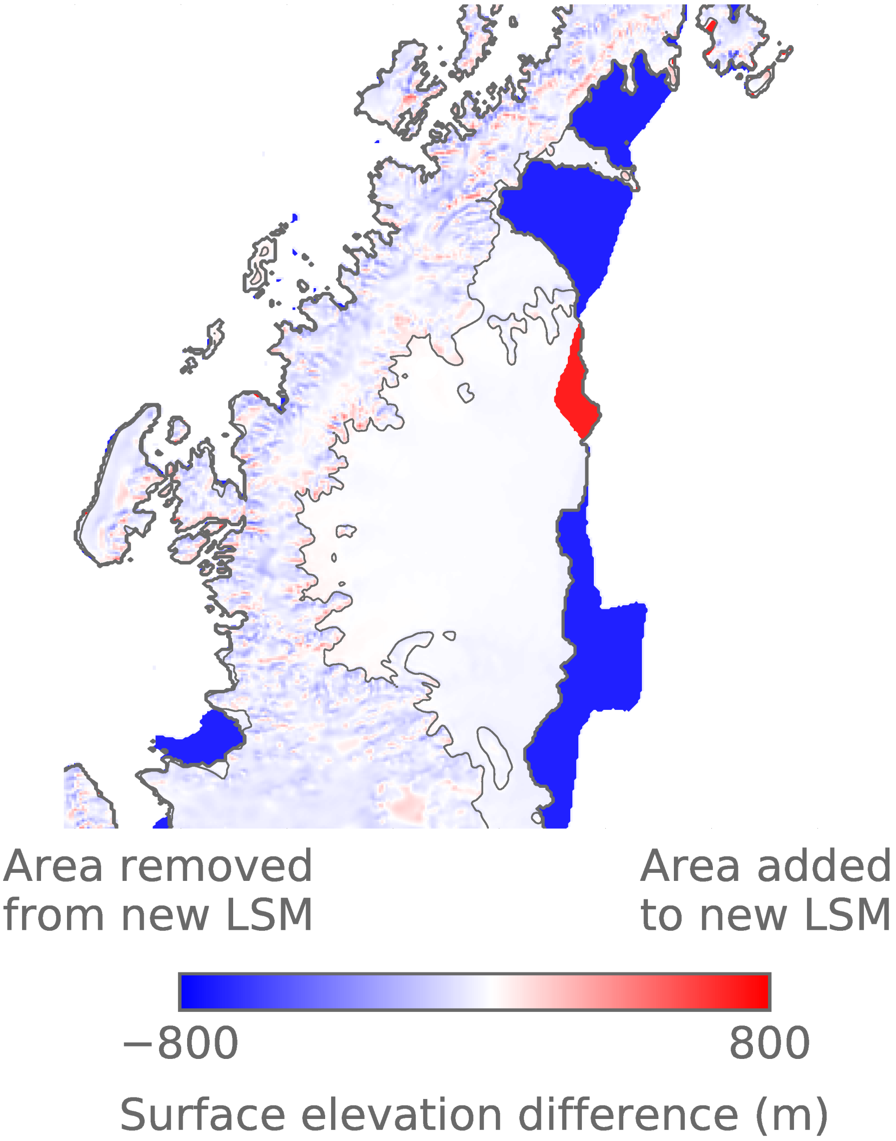

Figure 3.5.: Difference between default and updated surface elevation (orography) and land-sea mask (LSM) files used in MetUM runs. The default orography and land-sea mask are based on the 1 km resolution GLOBE dataset (Hastings and Dunbar, 1999). The updated land-sea mask is derived from the SCAR Antarctic Digital Database, and updated orography is based on the Ohio State University RAMP 200 m digital elevation model (Liu, 1999), produced by Tony Phillips at BAS. Blue colours indicate where land is removed from the updated land-sea-mask compared to the default, and where surface elevation is lower than in the default, while red colours indicate the opposite.

Updated orography and land-sea mask files were consequently generated for use in the thesis by Tony Phillips at BAS. The land-sea mask is based on the SCAR Antarctic Digital Database coastline, version 7.0 (released January 2016 and available at https://www.add.scar.org/). The orography file is based on the Ohio State University RAMP 200 m resolution Antarctic digital elevation model (Liu, 1999), and is converted for use in the MetUM by interpolating the dataset onto each model domain used in the thesis (the 4.4 km domain used in Chapter 4, the 1.5 km domain used in Chapters 4 and 5, and the 4.0 km domain used in Chapter 6) and applying smoothing as follows. Firstly, unsmoothed orography was created by calculating for each model grid box a mean of all heights in the corresponding region in the digital elevation model. The smoothed orography was created by applying a 2D 1-2-1 filter with convolution and setting all points not classified as land in the new mask to a height of 0 m. The differences in orography and land-sea mask between the standard MetUM files and the updated data used are shown in Figure 3.5.

3.2.4 Important parameterisation schemes

The following sections summarise important parameterisation schemes used in the MetUM.

The radiation scheme is built on code from SOCRATES (Suite of Community RAdiative Transfer codes) and is based on Edwards and Slingo (1996). It computes gaseous absorption of SW and LW radiation in six and nine bands, respectively, and includes absorption by water vapour, ozone, oxygen and carbon dioxide. Absorption and scattering by aerosols such as sea salt, mineral dust and black carbon is calculated using climatological or prognostic aerosol concentrations. Aerosol concentrations are also used to calculate cloud droplet number concentration after Jones et al. (1994; 2001) and cloud droplets are parameterised using "thick averaging" described in (Edwards and Slingo, 1996), with Padé fits used to parameterise variations in droplet effective radius with droplet number concentration. Ice is parameterised according to Edwards et al. (2007) and Baran et al. (2014).

The boundary layer scheme parameterises turbulent motions that occur at a finer scale than can be explicitly resolved using a 3D smagorinsky-type scheme, and uses the formulation of Lock et al. (2000), with modifications documented in Lock (2001) and Brown et al. (2008). Adiabatically conserved heat and moisture variables as well as momentum and tracers are mixed in a first-order turbulence closure scheme (Walters et al., 2017). Unstable boundary layers are parameterised using two types of diffusion coefficients: one for turbulence originating from the surface (surface heating, wind shear) and another for cloud-top driven turbulence (evaporative or radiative cooling) (Walters et al., 2017). Stable boundary layers are parameterised using the scheme of Brown et al. (2008). Turbulent fluxes (above the surface) are computed from local conditions with an eddy diffusivity method, which are proportional to mixing length, vertical wind shear, and local stability. Stability is diagnosed using a Richardson number-dependent stability function, and several options are available which produce varying amounts of mixing (Lock, 2011). Mixing length is proportional to the surface roughness length, which for snow-covered land and sea ice is prescribed as 5×10^4 m (Orr et al., 2014).

The purpose of the large scale cloud scheme is to calculate the amount of condensation that occurs at each model timestep, and to diagnose the ice, liquid and mixed-phase cloud fractions (that is, the fraction of the gridbox occupied by ice, liquid or mixed-phase cloud) for use by the radiation and precipitation (microphysics) schemes. This is done by assuming instantaneous condensation and by parameterising sub-grid scale variations in moisture and temperature using a probability distribution function. Two variants are available in the MetUM: the diagnostic scheme based on Smith (1990a) and PC2 (Wilson et al., 2008). These are described in turn.

The diagnostic scheme is based on Smith (1990a). It calculates sub-grid scale variations in liquid condensate, s, by assuming a symmetric triangular probability distribution function representing the within-gridbox deviation of liquid condensate fractions from the gridbox mean. The parameterisation also relies on diagnosing a critical relative humidity, RH$_{crit}$, at which condensation occurs. RH$_{crit}$ profiles are prescribed such that condensation is permitted when gridbox mean relative humidity is less than 100% to capture the effect of local, sub-grid scale variations in humidity that can produce condensation in smaller pockets. This enables the scheme to compute vapour mass mixing ratios and liquid cloud fractions assuming knowledge only of total condensate, relative humidity and temperature, and means that it takes into account spatial heterogeneity within a gridbox. Ice cloud fraction is parameterised in the scheme in an analagous way to the liquid fraction. The total and mixed-phase cloud fractions are calculated assuming minimal overlap between ice and liquid.

The prognostic cloud, prognostic condensate (PC2) scheme (Wilson et al., 2008) prognostically computes ice, liquid and mixed-phase cloud fractions and advects these in space and time by calculating sources and sinks of condensate. Like the Smith (1990a) scheme it calculates sub-grid scale variations in liquid condensate by assuming a probability density function of s. However, in PC2, cloud fractions are updated incrementally to include the effect of individual processes that can act as sources or sinks of condensate, such that each scheme (convection, radiation, boundary layer, precipitation etc.) produces an effect on cloud fractions. In further contrast to the Smith (1990a) scheme, the autoconversion process in the microphysics scheme does not influence liquid cloud fractions, which in practice means that extensive, optically thin liquid clouds with high liquid cloud fraction but low liquid water contents can persist. An advantage of this method is that individual process contributions can be extracted, and cloud may be advected, permitting more realistic simulation of cloud evolution.

The large-scale precipitation (microphysics) scheme, calculates process rates that increase or decrease cloud ice, liquid and water vapour. Two schemes are used in this thesis: the default single-moment scheme based on Wilson and Ballard (1999), which simulates particle mass only, and the newly developed multi-moment scheme, which simulates mass and number concentrations. Both are described in turn.

The default large-scale precipitation formulation is a physically-based, single moment microphysics scheme based on Wilson and Ballard (1999), with modifications. It represents four phases of water: water vapour, cloud water, rain droplets and snow (encompassing all ice in the gridbox). Cloud liquid is produced by condensation and its sinks are autoconversion to precipitation, loss via settling, and conversion to ice via deposition and riming. Rain is produced by autoconversion, melting of ice, and accretion, and lost by evaporation or ice growth. Rain droplet sedimentation can increase or decrease rain mass mixing ratios as rain descends through model levels. Sedimentation acts similarly on ice, which is produced via depositional growth, riming or capture of rain, and lost by sublimation and melting (Field et al., 2014).

The scheme represents only the first moment of the hydrometeor size distribution, mass, so cloud droplet number concentrations (the number of activated cloud nuclei) are prescribed. This value is set to 100 cm $^{-3}$ over open water and 300 cm $^{-3}$ over land (including ice shelves). Whilst these assumed values of cloud droplet number concentrations are unrealistic over Antarctic ice shelves, initial sensitivity tests (not shown) revealed that the choice of values had a negligible effect on the quality of simulations. The particle size distribution of rain drops is parameterised as in Abel and Boutle (2012), with fall velocities parameterised using Abel and Shipway (2007). For ice aggregates, a generic size distribution is used where ice number concentration is calculated using the relation between ice water content and temperature given in Field et al. (2005) and Field et al. (2005). The Hallett-Mossop secondary ice formation process is switched off because the model frequently over-estimates ice water contents as described in Chapter 2.

The newly developed Cloud AeroSol Interaction Microphysics scheme (CASIM) (Shipway and Hill, 2012; Hill et al., 2015; Grosvenor et al., 2017) is a multi-moment microphysical parameterisation scheme with five hydrometeor classes that permits one- or two-way cloud-aerosol interactions. The size distribution of each class is described with a gamma distribution, and CASIM calculates prognostic mass mixing ratios and number concentrations (Miltenberger et al., 2018). Fixed density, mass-diameter and fall speed relationships are assumed. Details of the parameterisation of the various microphysical processes described by CASIM can be found in Miltenberger et al. (2018) and Grosvenor et al. (2017). In the configuration used in Chapter 5, two soluble modes of aerosol - accumulation mode aerosol and coarse dust - are represented, with one-way coupling between cloud and aerosol, meaning that the cloud field is forced by aerosol, but that cloud development does not deplete aerosols during the simulation. Mass mixing ratios and number concentrations of accumulation mode aerosol are prescribed as 4.56 $\times$ 10^{-9} kg kg^{-1} and 3.8 $\times$ 10^{8} kg^{-1}, respectively, whereas the coarse aerosol mode is prescribed as a profile that varies with height. The Abdul-Razzak and Ghan (2000) droplet activation scheme is used, and several ice nucleation schemes are available: some of these are tested and documented in Chapter 5. The convection parameterisation is switched off in Chapter 5 because the LAM is sufficiently high resolution to resolve convective systems.

The MetUM configurations in this thesis use the Met Office Surface Exchange Scheme (MOSES-II) (Cox et al., 1999; Essery et al., 2001; Essery et al., 2003) because the newer, more sophisticated JULES land surface scheme (Best et al., 2011) has not been widely tested or tuned for Antarctica. When configured to run with a single-layer snowpack, JULES defaults to MOSES-II settings. The scheme calculates the surface radiative, turbulent and ground heat fluxes (i.e. the SEB) and surface temperature interactively by specifying land types and parameters (Cox et al., 1999). In Antarctica, a single-layer snowpack is represented. Water is not allowed to penetrate into the subsurface, and all runs off the surface, with no refreezing. Over snow-covered surfaces, the only surface processes considered are sublimation, snowfall, snowmelt and surface runoff. This means the moisture flux from snow-covered surfaces comes exclusively from the sublimation of lying snow.

Surface net radiation (R$_{net}$) is parameterised using direct and diffuse albedos for each gridbox in the SW and LW bands (Essery et al., 2003). SW$_{\downarrow}$ and LW$_{\downarrow}$ is calculated by the radiation scheme as described above, and fed into the surface scheme. The albedo (α) of snow-covered surfaces is permitted to evolve as the snow ages according to the spectral albedo model of Wiscombe and Warren (1980). The absorption of SW$_{\downarrow}$ and LW$_{\downarrow}$ is related to surface temperature (T$_S$) and summed over i SW bands, making R$_{net}$ equal to:

$$R_{net} = \sum i(1-\alpha)SW_{\downarrow,i} + SW_{\downarrow,i} - \sigma T_S^4 \tag{3.6}$$

where σ is the Stefan-Boltzmann constant.

Turbulent fluxes are parameterised using the bulk aerodynamic formulae, with sensible heat flux defined as:

$$H_S = \rho \frac{C_p}{r_a} \{T_S - T_1 - \frac{g}{C_p} z_1\} \tag{3.7}$$

and latent heat flux defined as:

$$H_L = \psi \frac{\rho}{r_a} q_{sat}(T_S, p_S) - q_1 \tag{3.8}$$

where g is the acceleration due to gravity, C_p is the specific heat capacity of air, T_1 and q_1 are the atmospheric temperature and specific humidity at height z_1 above the surface, respectively, r_a is the aerodynamic resistance (which depends on roughness length, prescribed as 1.0×10^{-4} m for ice, wind speed and atmospheric stability), ρ is the surface air density, T_S is the surface temperature, ψ is a factor set to 1 for saturated surfaces including snow, and $q_{sat}(T_S, p_S)$ is the saturation specific humidity at temperature T_S and pressure p_S.

The conductive flux, G_S, from the surface into the (in this case single) sub-surface layer is parameterised as:

$$G_S = \frac{2\lambda}{\Delta z_S}(T_S - T_{sub}) \tag{3.9}$$

where Δz_S is the layer thickness, λ is the thermal conductivity (assumed to be 0.265 W m^{-1} K^{-1}) and T_S and T_{sub} are the temperatures of the surface and underlying layer, respectively.

The surface temperature, T_S is a diagnostic with the form:

$$T_S = T_{sub} + \frac{G_S \Delta z_S}{2\lambda} \tag{3.10}$$

The energy balance of the surface is calculated as in Equation 3.3, such that any residual energy ($E_{tot} > 0$) is available for melting. When there is snow, melt occurs whenever T_S or $T_{sub} > 0$. Enough melting must occur such that the Equation 3.3 is satisfied for $T_{sub} = T_S$ and other surface fluxes are adjusted accordingly.

This chapter has summarised the data and methods used throughout the thesis, including surface AWS and airborne microphysics observations and detailed the configuration and parameterisations used in the MetUM. The next chapter presents results of wintertime case studies of foehn events identified from AWS data, and simulated with the MetUM.

4

The influence of foehn winds on surface melting over Larsen C in non-summer seasons

Parts of the work on which this chapter is based have been published in: Kuipers Munneke, P., Luckman, A. J., Bevan, S. L., **Gilbert, E.**, Smeets, C. J. P. P., Van Den Broeke, M. R., Wang, W., Zender, C., Hubbard, B., Ashmore, D., Orr, A., King, J. C. (2018). "Intense winter surface melt on an Antarctic ice shelf." *Geophysical Research Letters*, 45, 7615–7623. https://doi.org/10.1029/2018GL077899, doi: https://doi.org/10.1029/2018GL077899 (reproduced in Appendix A).

My contribution to this paper was the modelling work, and figures 3 c) and d). Elements of this chapter that have been previously published are indicated.

4.1 Introduction

4.1.1 Aims and objectives

This chapter investigates the role of foehn winds in driving surface melting over Larsen C in non-summertime conditions (hereafter referred to as "wintertime melt" for convenience). It aims to determine whether foehn events have an effect on the SEB and surface melting by examining observations from AWS 18 and simulations with the MetUM during two case studies when foehn were suspected in Cabinet Inlet. As described in Chapter 3, AWS 18 is located at the foot of the peninsula mountains, adjacent to the Larsen C ice shelf (see Figure 3.1). The signatures of foehn events are strongest nearest the steep terrain that generates them, which also causes more frequent meltwater ponding here (Luckman et al., 2014), hence Cabinet Inlet is an appropriate location at which to study foehn-induced melt.

The two case studies identified are 9–13 May 2016 (CS1) and 25–30 May 2016 (CS2). CS2 is evaluated in Kuipers Munneke et al. (2018) and both cases were selected because they were associated with considerable temperature and wind speed increases and large decreases in relative humidity. These wintertime foehn tend to be intense, yet short-lived compared to summertime events (Kuipers Munneke et al., 2018). The MetUM was run as described in Chapter 3 for both case studies. Both were simulated at 4.4 and 1.5 km resolution as outlined in Table 3.2. For clarity, throughout the majority of this chapter, only results from the 1.5 km domain will be presented, except where comparison with 4.4 km results is informative.

4.1.2 Research questions

The influence of foehn winds on the SEB of Larsen C during CS1 and CS2 are examined by answering the following research questions:

1. Do foehn events occur on Larsen C during winter?
2. What is the effect of wintertime foehn on the SEB of Larsen C?
3. Do wintertime foehn events cause melting on Larsen C?

4.1.3 Novelty of research

As described in Chapter 2, foehn-related melt events have been documented in summer on Larsen C (Elvidge et al., 2015; Elvidge et al., 2016; Cape et al., 2015; King et al., 2017), supported by an array of observational data (for example from aircraft, modelling, radiosondes and AWS data). However, until 2018 there had been no definitive demonstration that foehn-driven surface melting also occurs during other seasons. This chapter builds on contributions to Kuipers Munneke et al. (2018), which showed for the first time that foehn-driven surface melt is occurring during winter on the Larsen C ice shelf. This has subsequently also been demonstrated by Datta et al. (2019) and Elvidge et al. (2020). This chapter will add to work published in Kuipers Munneke et al. (2018) by examining the effect of foehn on the SEB, and hence on melting, in detail. This has not yet been done for Larsen C during non-summer seasons, and exploring this connection is important to better understand the processes that connect atmospheric phenomena with the observed glaciological changes described in Chapter 2.

4.2 Research question 1: Do foehn events occur on Larsen C during winter?

First, it must be established whether foehn occurs during winter. As described in Chapter 2, leeside foehn conditions can occur when upstream $\hat{h}$, defined as in Equation 2.1, exceeds 1. In both CS1 and CS2, $\hat{h}$ derived from 4.4 km model output suggests that such conditions prevail ($\hat{h}$ = 1.89 and 1.61 for CS1 and CS2, respectively). Non-linear effects such as foehn events, wave breaking and hydraulic jumps occur when $\hat{h} > 1$ (Elvidge et al., 2016), suggesting that these conditions could establish a non-linear leeside foehn response during both cases.

4.2.1 Synoptic conditions

As described in Chapter 2, foehn events on Larsen C are generated by synoptic conditions favourable to their development, i.e. cross-peninsula (westerly) flow. Mean atmospheric circulation at 750 hPa at the start of CS1 and CS2 from ERA-5 reanalysis is shown in Figure 4.1a and b, respectively, and shows that synoptic flow is broadly cross-peninsula over Larsen C in both cases. Lower pressure east of the Antarctic Peninsula is shown in both cases, although the low pressure centre in the Weddell Sea in CS2 is deeper. A ridge of high pressure extends along the peninsula mountains in CS1, and to some extent in CS2, generating flow with a large westerly component. The approximately zonal flow at 750 hPa and upwind $\hat{h} > 1$ suggests that low-level flow blocking occurs during both cases, and that foehn is generated by the isentropic drawdown mechanism outlined in Chapter 2.

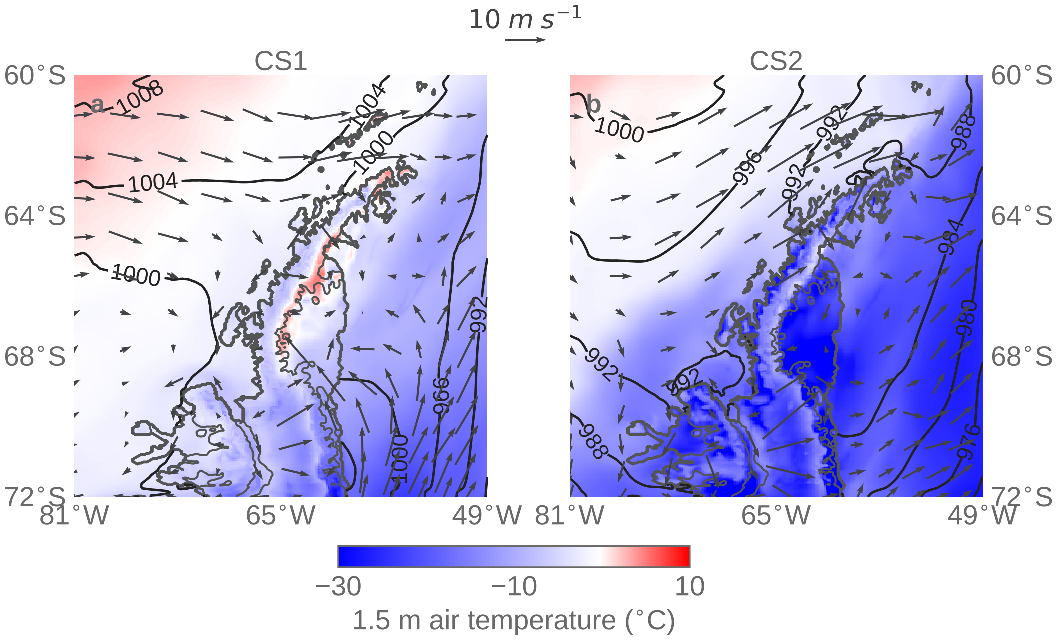

Figure 4.1.: Synoptic conditions over the Antarctic Peninsula at the onset of foehn conditions: a) 12:00 UTC on 9 May and b) 12:00 UTC on 25 May, derived from ERA-5 reanalysis at 31 km grid spacing. Colour contours show 1.5 m temperature in degrees celsius, unfilled contours show mean sea level pressure and overlaid vectors show 750 hPa winds in m s^{-1}. A 10 m s^{-1} scale vector is included at top left for reference.

4.2.2 Surface conditions

The classical fingerprint of foehn (warm, dry, windy conditions) can be seen in the surface meteorological observations from AWS 18 during CS1 and CS2 (Figures 4.2 and 4.3). The time series shown in Figures 4.2 and 4.3 show the signature of foehn beginning on both 9 May and

25 May, i.e. an abrupt rise in temperature and wind speed with a concurrent drop in relative humidity. Considerable temperature rise is observed at Cabinet Inlet during both foehn events: 2 m air temperatures (T_{air}) peak at 10°C and 14°C in Cabinet Inlet on the 9 (Figure 4.2) and 26 May (Figure 4.3), respectively. These temperatures represent a significant departure from temperatures usually observed over Larsen C during winter, which for March–May are around -20°C at AWS 14 and 15, both located closer to the edge of Larsen C (Kuipers Munneke et al., 2012). The 4.4 km and 1.5 km model output are almost indistinguishable, so the analysis in this section will focus on the 1.5 km results only. Modelled T_{air} rises across the whole ice shelf at the height of both cases, as shown in Figure 4.4. The surface temperature (T_S) rises abruptly to the melting point as T_{air} peaks, and does not fall below 0°C for most of the event (Figures 4.2 and 4.3). If E_{tot} is positive during the same time period, this will cause melt, according to Equation 3.4. Relative humidity falls by 40-50% in both cases, from fairly typical values of ~98% (Kuipers Munneke et al., 2012) to minima of ~40% and ~30% in CS1 and CS2, respectively. Wind speeds peak at approximately 20 m s^{-1} in both cases. Typical values at AWS 14 and 15 are 4 m s^{-1} during March–May (Kuipers Munneke et al., 2012), so this represents a significant increase. However, Cabinet Inlet might be expected to experience higher winds due to its location near the complex topography of the peninsula mountains, which can channel air and contribute to elevated wind speeds as described in Elvidge et al. (2015). This evaluation of observed time series supports the hypothesis that foehn events take place during winter.

Differences between the cases are evident, for instance CS2 is more intense than CS1. This may be because upstream flow is stronger at the start of CS2, which is indicated by the smaller $\hat{h}$ reported in section 4.2.1. ERA-5 analysis shows that T_{air} in Cabinet Inlet at the start of CS1 is warmer than at the start of CS2, and an area of warmer temperatures extends further south in CS1 from Cabinet Inlet across the Larsen C ice shelf (Figure 4.4). CS1 also appears to show two separate foehn events: the main event examined lasts from 9 May until 14 May, but another begins on 15 May. This is seen in the time series, where on 13 May relative humidity and temperatures (wind speeds) increase (die down), and then drop (pick up) again on 15 May (Figure 4.2).

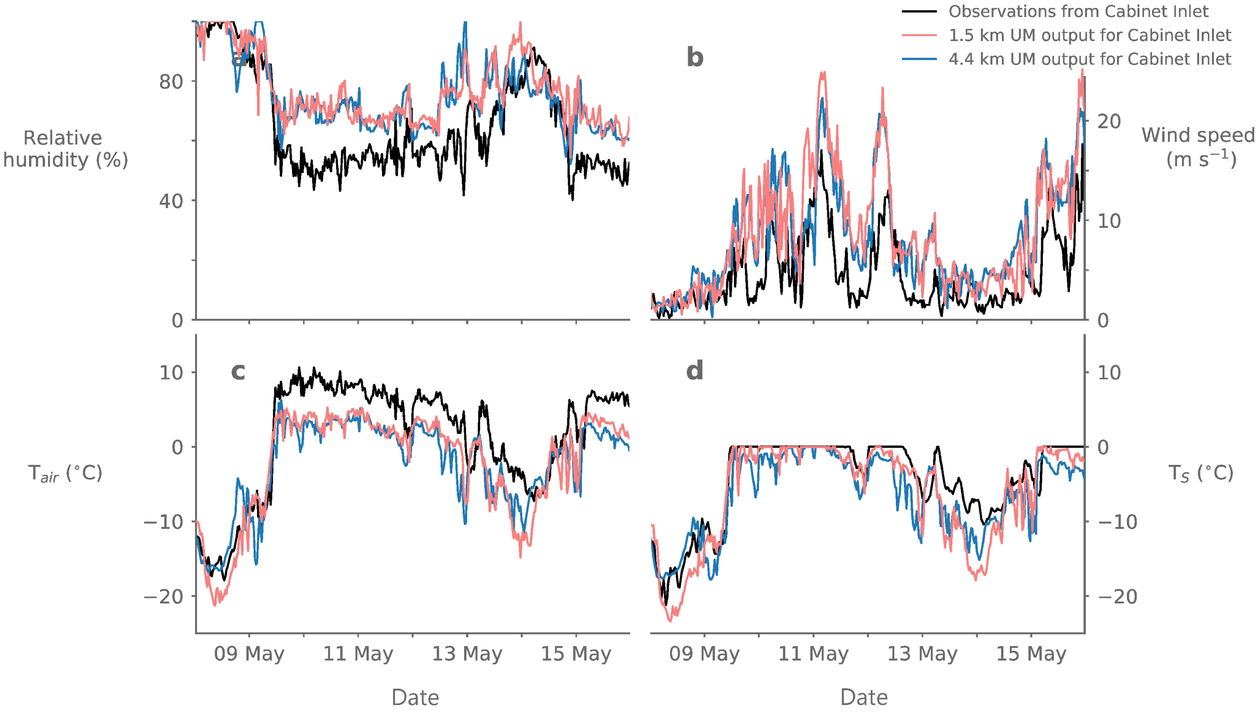

Figure 4.2.: Time series of near-surface meteorological variables during CS1: a) relative humidity, b) wind speed, c) 1.5 m air temperature, d) surface temperature. In all panels, the black line shows observations from the Cabinet Inlet AWS, while the blue and pink lines show the model output at 4.4 and 1.5 km resolution, respectively.

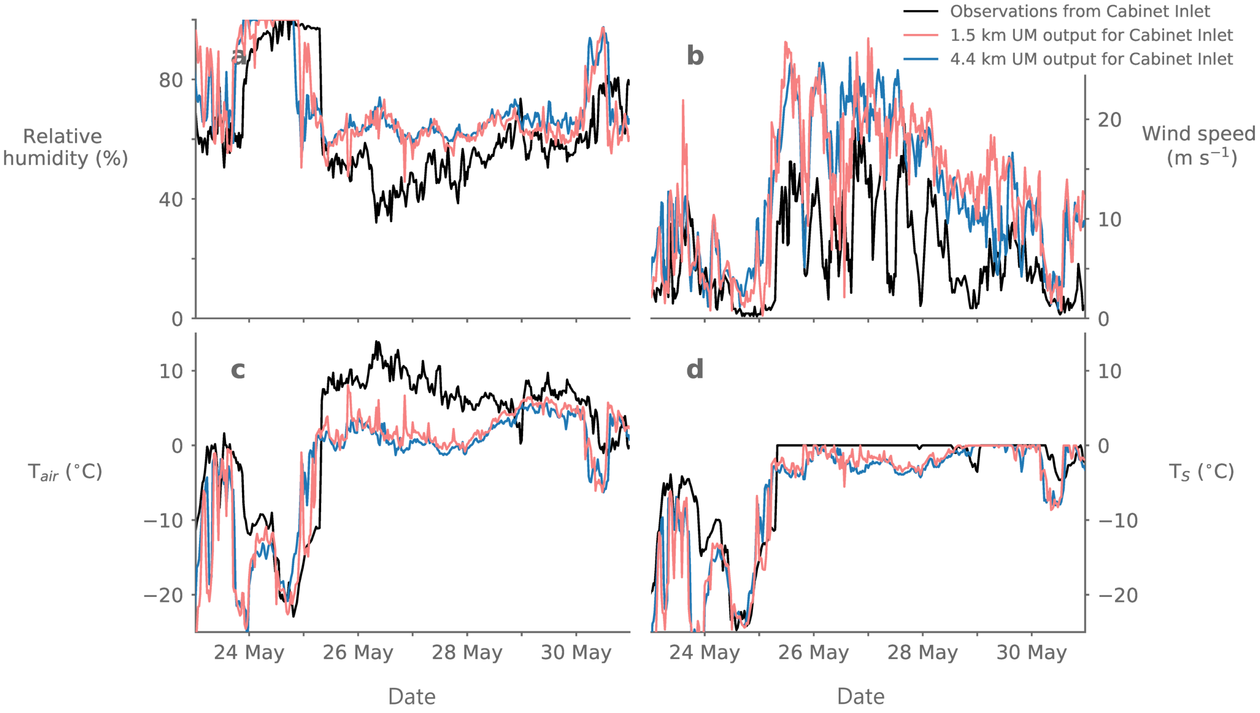

Figure 4.3.: Time series of near-surface meteorological variables during CS2: a) relative humidity, b) wind speed, c) 1.5 m air temperature, d) surface temperature, as in Figure 4.2.

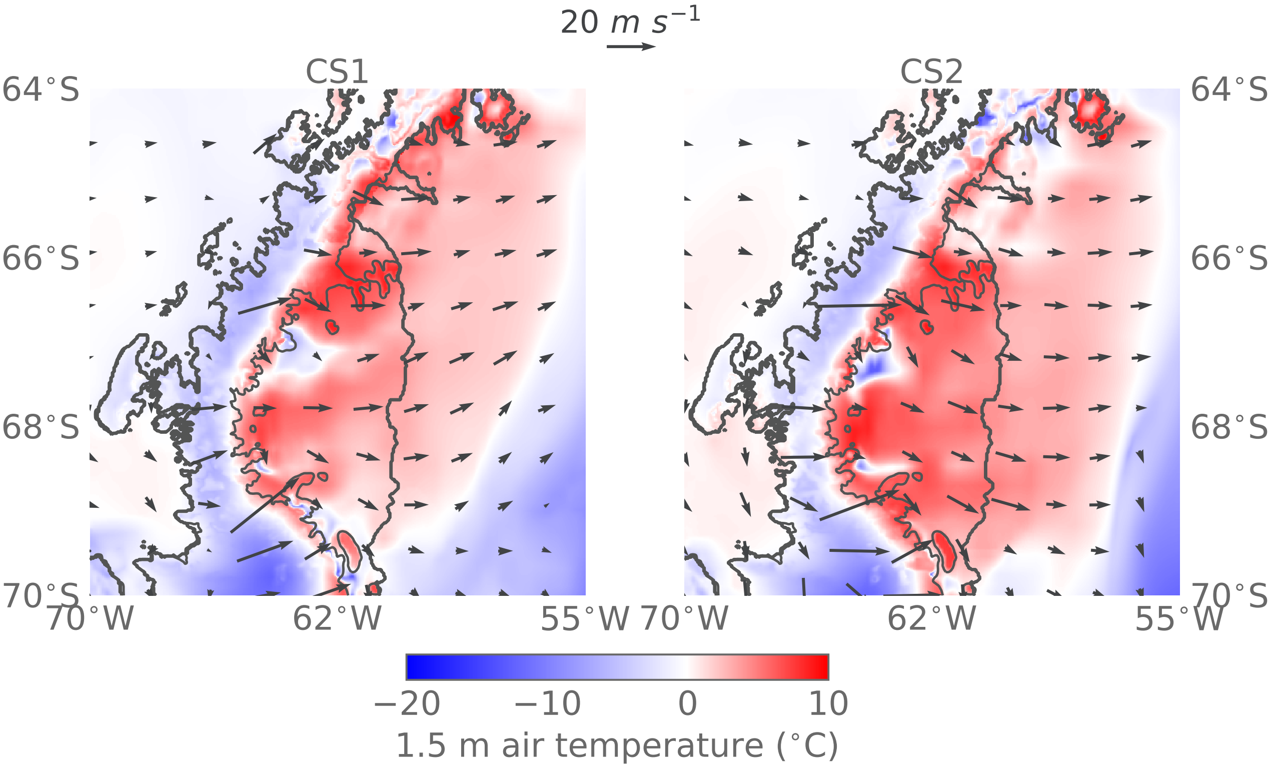

Figure 4.4.: Modelled near-surface conditions shortly after the onset of foehn conditions in a) CS1 at 12:00 UTC on 10 May and b) CS2 at 00:00 UTC on 26 May from the 1.5 km resolution model domain. Filled contours show 1.5 m air temperatures, while vectors indicate 10 m wind speeds. A scale vector of 20 m s^{-1} is shown top centre for reference.

Figures 4.2 and 4.3 show that the signature of foehn are modelled reasonably accurately, but that there are some disparities in the magnitude and timing of changes. Figure 4.4 shows a spatial snapshot of surface conditions at the onset of foehn, at 12:00 UTC on 10 May and 00:00 UTC on 26 May respectively, for CS1 and CS2. During both cases, simulated T_{air} rises above 0°C in the immediate lee of the mountains, and T_S reaches 0°C across much of the ice shelf. Modelled wind speeds are highest closest to steep terrain, consistent with the occurrence of foehn. In both cases, the extent and precise location of simulated warming differs, which could be due to differences in the MetUM's representation of foehn dynamics, wind direction or boundary layer stability. Models struggle to represent stable boundary layers, which develop frequently in winter.

Although overall the MetUM represents surface meteorological variables well, some biases are still evident. Table 4.1 and panels a – d in Figures 4.5 and 4.6 show correlations between observed and modelled surface meteorology during CS1 and CS2, respectively. Modelled T_{air} and T_S are both negatively biased, while relative humidity and wind speed are positively biased. The root mean square errors (RMSE) of the time series of modelled surface variables for CS1 and CS2 are shown in Table 4.1.

Table 4.1 shows that the cold bias and RMSE is larger for T_{air} than T_S. The RMSE of air (surface) temperature is 4.4°C (3.3°C), respectively, during CS1 and 6.9°C (4.8°C) during CS2. Model biases are larger in CS1 than CS2, which may be because CS1 is less intense. Figures 4.2 and 4.3 show that the MetUM under-estimates the maximum temperatures reached during both events by several degrees, and misses the smaller peak in temperatures observed on May 23–24 (CS2). This bias could result from several things. Firstly, the vertical structure of the atmosphere may not be modelled accurately. If the potential temperature of air sourced from higher altitudes during the foehn event is not warm enough, this will create a cold bias at the surface once it is adiabatically compressed and warmed as it descends down the lee slope. Secondly, over-estimated wind speeds may also push too much warm foehn air out over the ice shelf and away from Cabinet Inlet, contributing to the cold bias. Lastly, if the modelled boundary layer is too stable or too deep, the MetUM could struggle to represent the magnitude of temperature changes associated with foehn, which would influence the biases shown in Table 4.1. If the stable boundary layer does not erode correctly with time, warm temperatures may not penetrate to the surface and produce a surface effect, despite foehn occurring dynamically at higher levels. This process is described in Orr et al. (2008).

Relative humidity is also over-estimated by approximately 5-15% in the model compared with the observations, which suggests that the model under-estimates the intense drying associated with extreme wintertime foehn events such as these. However, this is because the simulated air temperature is too low, which means the air is more saturated with water vapour. This is illustrated in panels a and c of Figures 4.2 and 4.3, where the bias in relative humidity is highest when the bias in air temperature is highest and can be demonstrated using the Clausius Clapeyron equation[1].

Wind speed is over-estimated relative to observations in both cases. The model particularly over-estimates winds during strong wind periods, such as those seen on 11 and 12 May (CS1) and 26–28 May (CS2). The RMSE of wind speed is highest during CS2 at 1.5 km resolution when the correlation between observed and modelled values is also lowest. However, given the complex orography in this region, which can be extraordinarily difficult to represent in a model (King et al., 2017), wind speeds are reproduced very closely.

---

[1] The Clausius-Clapeyron equation takes the form $\mathrm{Ln}(e_s/6.11) = (L_v/R_v)(1/T_0)\text{-}(1/T)$, where L_v is the latent heat of vaporisation, 2.453×10^6 J kg^{-1}, R_v is the gas constant for dry air, 461 J kg^{-1} and T_0 is a reference temperature, taken to be 0°C or 273.15 K. For example, at the onset of CS2, modelled $T_{air} \approx 4.0$°C and RH $\approx 70.9\%$, making $e/e_s \approx 5.75/8.11$ hPa. At the observed $T_{air} \approx 8.4$°C and RH $\approx 52\%$, $e/e_s \approx 5.65/10.89$ hPa. The approximate equivalence of e between model and observations demonstrates that the model correctly simulates the absolute quantity of atmospheric water vapour, and that temperature biases are responsible for the RH bias.

Of the four surface variables considered, relative humidity is simulated best, particularly in CS1. However, minimum relative humidity is often over-estimated, especially in CS2, when observed relative falls to 32.1%, whereas the modelled low is 45.8%. However, the mean bias is around 10% during both cases, and RMSE is $< 25\%$. The statistics are poorer during CS2 because the model simulates the onset of foehn slightly too early, and because the temperature bias is more extreme during CS2.

4.2.3 Model representation of atmospheric vertical structure during foehn

The vertical structure of the atmosphere during the cases provides further evidence that foehn is occurring. Figure 4.7 shows a longitudinal cross-section through the peninsula during the peak of CS2. A similar structure is observed during CS1 (not shown). Cross-peninsula airflow causes high wind speeds and warm near-surface air temperatures in the lee of the mountains, consistent with the signature of foehn recorded at the surface and reproduced in model output (Figure 4.3). Enhanced downslope winds associated with the event are evident in Figure 4.7, accompanied by the drawdown of potentially warmer air from higher altitudes. This suggests that foehn is generated by the isentropic drawdown mechanism, described in Chapter 2. This warm air causes near-surface temperatures to rise above freezing across much of Larsen C (Figure 4.4). This is confirmed in the observations from Cabinet Inlet.

The vertical structures of the cases support the conclusion that CS2 is more extreme than CS1. Higher downslope wind speeds are observed during CS2, consistent with higher surface winds and warmer air temperatures at Cabinet Inlet shown in Figure 4.3.

The representation of the vertical structure of foehn events is important to understand the sources and mechanisms that generate surface conditions. Improved spatial resolution may therefore enhance the interpretation of plots like Figure 4.7. The next section will examine the effect of altering the model set-up on the representation of foehn.

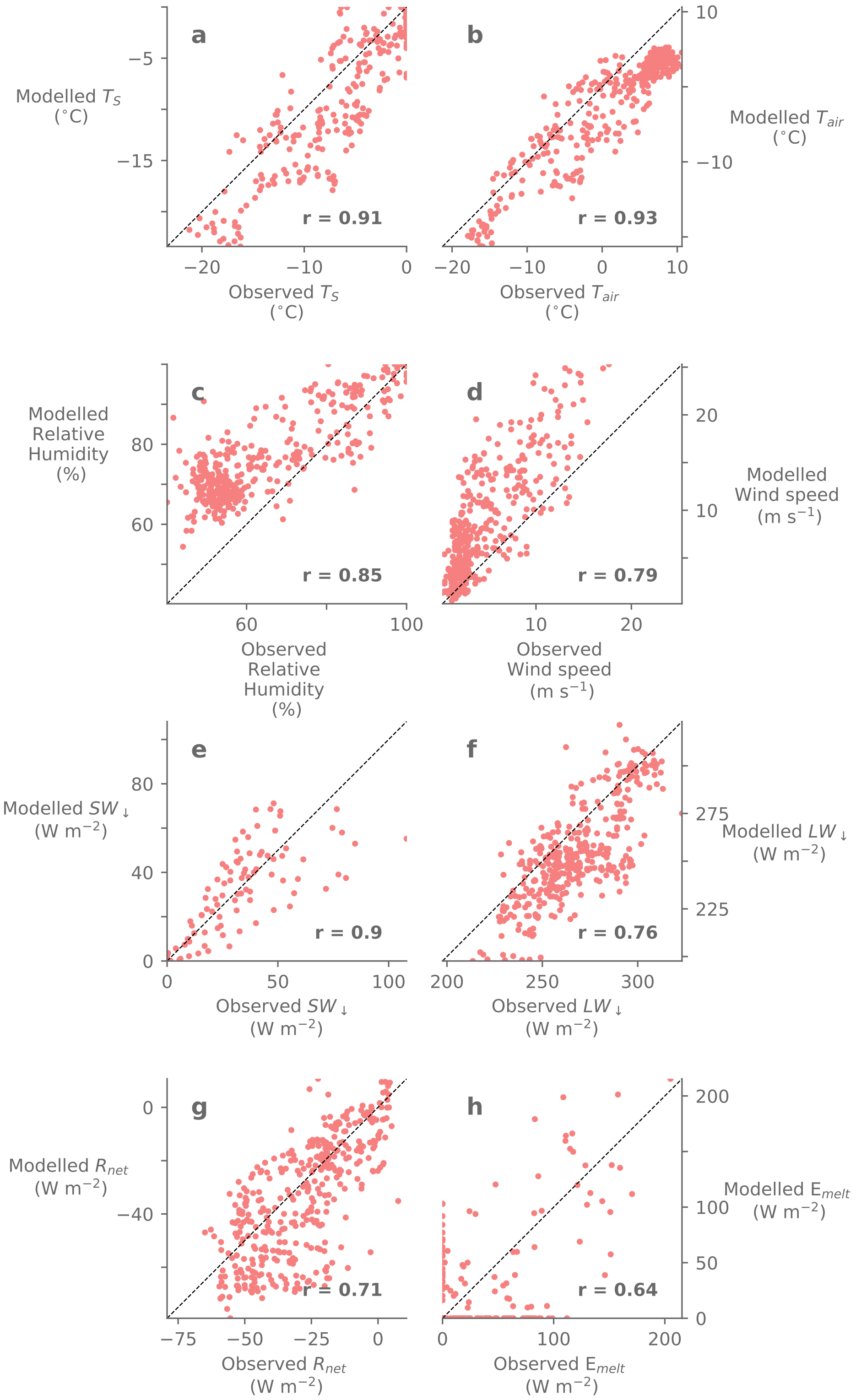

Figure 4.5.: Scatterplots of observed vs. modelled (1.5 km resolution) surface variables at the Cabinet Inlet AWS during CS1. Correlations (r values) are given in the top right hand corner of each panel: bold values indicate statistical significance at the 99% level. The dashed line in each plot indicates perfect agreement between model and observations. Panels a – d show surface meteorological variables: surface temperature, T_S; near-surface air temperature, T_{air}; relative humidity; and wind speed; and panels e – h show SEB terms: downwelling longwave, $LW_\downarrow$; downwelling shortwave, $SW_\downarrow$; net radiative, R_{net} and melt, E_{melt}, fluxes.

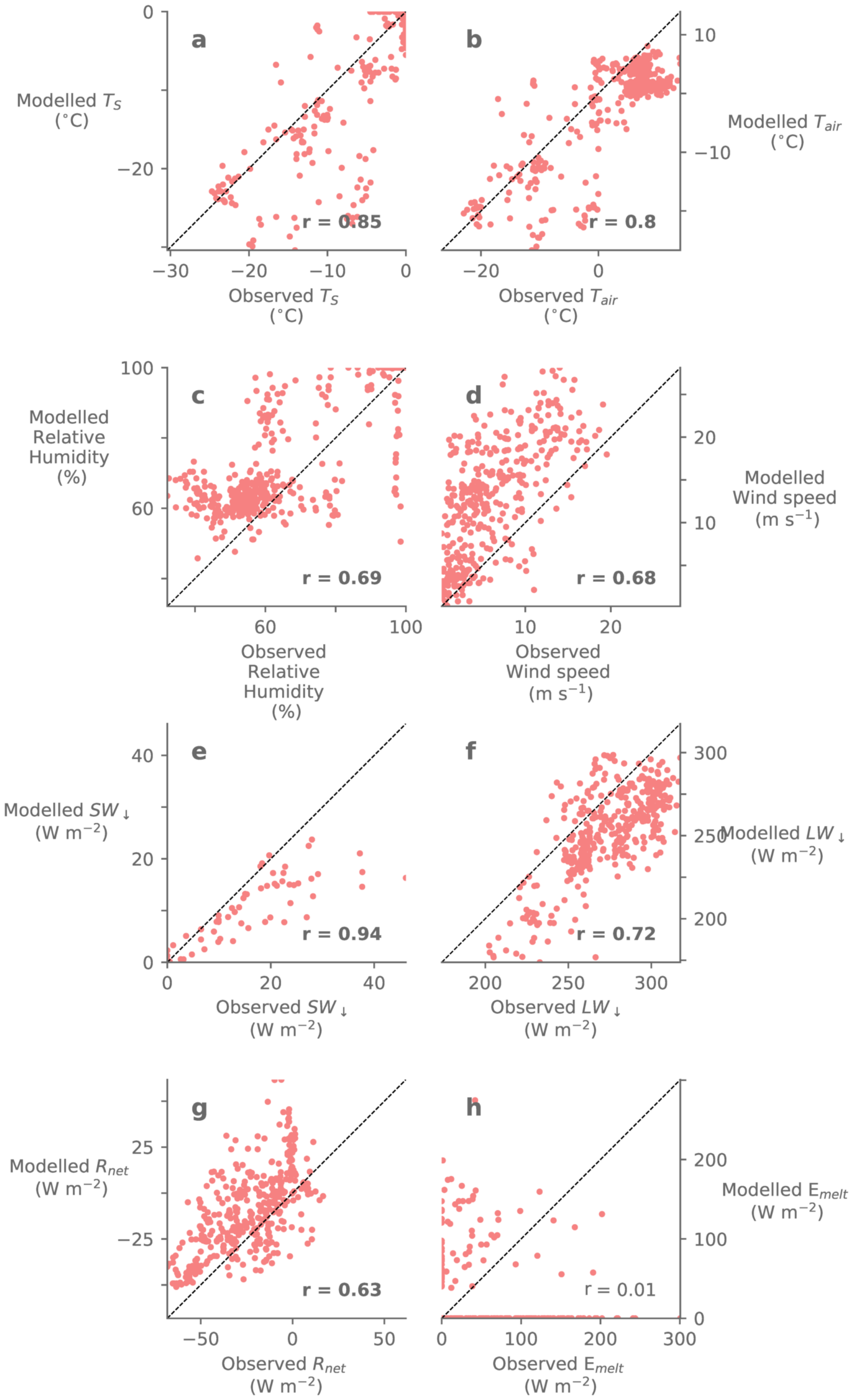

Figure 4.6.: Scatterplots of observed vs. modelled surface variables at the Cabinet Inlet AWS during CS2, with details as in Figure 4.5.

Table 4.1.: Observed and modelled means, plus biases, percent root mean square error ("% RMSE") and correlation coefficients ("Correlation (r)") during both cases at 1.5 km resolution for surface variables: surface temperature, T$_S$ (°C); near-surface air temperature, T$_{air}$ (°C); relative humidity, RH (%); wind speed, FF (m s^{-1}); and fluxes of downwelling and upwelling shortwave and longwave SW$_\downarrow$, SW$_\uparrow$, LW$_\downarrow$ and LW$_\uparrow$, respectively; net shortwave, SW$_{net}$; net longwave, LW$_{net}$; sensible heat, H$_S$; latent heat, H$_L$; total energy, E$_{tot}$; melt energy, E$_{melt}$ and melt energy with observed T$_S$ prescribed, E$_{melt,forced}$, all measured in W m^{-2}.

	Observed mean		**Model mean**		**Bias**		**% RMSE**		**Correlation (r)**	
	CS1	**CS2**	**CS1**	**CS2**	**CS1**	**CS2**	**CS1**	**CS2**	**CS1**	**CS2**
T_S	-4.49	-4.15	-6.24	-6.29	-1.74	-2.14	-73%	116%	0.91	0.85
T_{air}	1.14	1.89	-2.19	-2.27	-3.33	-4.16	384%	363%	0.93	0.80
RH	65.47%	62.94%	76.83%	70.72%	11.35%	7.78%	22%	24%	0.85	0.69
FF	4.63	6.13	8.57	12.72	3.94	6.59	115%	136.%	0.79	0.68
$SW_\downarrow$	7.95	2.48	7.59	1.59	-0.36	-0.89	96%	138%	0.90	0.94
$SW_\uparrow$	-7.44	-2.34	6.04	-1.20	1.14	-1.40	166%	102%	0.90	0.94
SW_{net}	0.51	0.14	1.55	0.39	1.04	0.25	516%	596%	0.89	0.89
$LW_\downarrow$	267.28	273.71	253.95	252.36	-13.33	-21.35	8%	11%	0.76	0.72
$LW_\uparrow$	-297.96	-296.13	-263.34	-289.69	34.63	6.44	13%	4%	0.86	0.91
LW_{net}	-28.84	-24.25	-35.73	-10.97	-6.89	13.28	-58%	-94%	0.71	0.63
H_S	44.23	65.97	65.92	98.55	21.70	32.59	96%	109%	0.77	0.53
H_L	-5.53	-9.03	-14.07	-32.97	-8.53	-23.94	-379%	-409%	0.72	0.64
E_{tot}	6.49	31.82	17.68	55.00	11.18	23.18	642%	236%	0.66	0.25
E_{melt}	18.14	34.90	15.28	20.01	-2.86	-14.88	174%	209%	0.64	0.01
$E_{melt,forced}$	18.14	34.90	16.70	33.52	-1.44	-1.38	160%	165.35%	0.69	0.38

4.2.4 The effect of higher resolution on the representation of foehn

In contrast to previous findings (Elvidge et al., 2015; Elvidge et al., 2016; Elvidge and Renfrew, 2016), the representation of surface variables appears insensitive to resolution (Figures 4.2 and 4.3). There is little difference between the 4.4 km and 1.5 km time series of surface variables and fluxes at Cabinet Inlet in either case. This may be because the newer version of the model used in this chapter (10.4) uses the improved ENDGame dynamical core, whereas version 7.6 used in Elvidge's work was still based on the older "New Dynamics". The 1.5 km domain represents surface meteorology slightly better, capturing peak wind speeds and minimum relative humidities better. Generally however, wind speeds are over-simulated more at 1.5 km than at 4.4 km, which also results in a larger sensible heat flux in the 1.5 km data. Temperature biases improve moderately between the 1.5 km and 4.4 km results, but wind speed and relative humidity biases are higher at 1.5 km resolution. Considering these limited differences, the 1.5 km results have been the focus of the preceding sections.

Figure 4.7 shows a snapshot of both foehn events at 4.4 km (left, panels a and c) and 1.5 km (right, panels b and d) grid spacing. The foehn event appears only slightly stronger at the finest resolution. Modelled wind speeds and temperatures are higher at 1.5 km spacing, likely

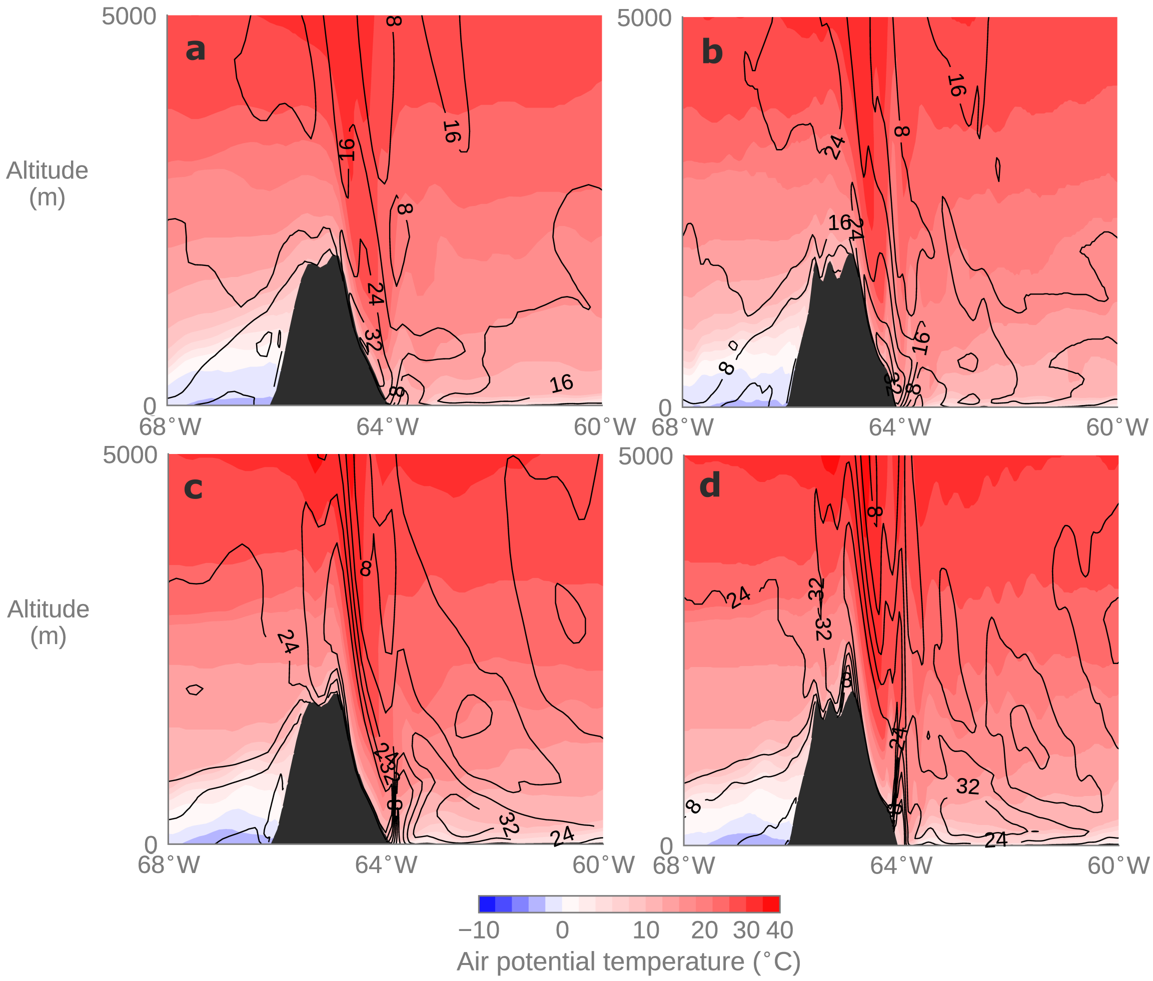

Figure 4.7.: Vertical cross-sections through the Antarctic Peninsula mountains into Cabinet Inlet at the onset of foehn during CS1 (top row, panels a and b) on 10 May at 12:00 UTC, and during CS2 (bottom row, panels c and d) on 26 May 2016 at 00:00 UTC. Filled colour contours show potential temperature (in degrees celsius) and contours show zonal wind velocity, in m s^{-1}. The first column (panels a and c) show 4.4 km MetUM output, and the second column (panels b and d) show 1.5 km MetUM output. A similar plot has been published in Kuipers Munneke et al. (2018).

due to the increased ability to represent the steep terrain, which generates higher downslope winds and thus greater isentropic drawdown and compressional heating.

Overall, there appears to be limited benefit to increasing model resolution from 4.4 km to 1.5 km or better in both CS1 and CS2, suggesting that foehn events are already suitably resolved at 4.4 km. This result suggests that, at least for wintertime cases, running the MetUM at 4.4 or 1.5 km resolution may be sufficient to resolve the dynamical and thermodynamical structure associated with foehn events at this particular AWS. However, spatial comparisons against observations are impossible because data is available only at a single grid point, which limits the conclusions. Further, this is in opposition to the findings of Elvidge et al. (2016) who showed that the boundary layer structure and foehn jets were better resolved at higher resolution. As previously discussed, this may be due to the improvements made to the MetUM's dynamical core. What may also be important is the resolution of the orography that is fed into the model, because foehn winds are generated by flow over steep terrain. The next section will explore this.

4.2.5 The effect of improved orography on the representation of foehn

Foehn winds are examples of orographic flows, hence the representation of orography in the model is of great significance. Because it was anticipated that increasing the resolution of the model orography would improve the representation of atmospheric conditions, model simulations using the default and updated orography datasets described in section 3.2.3 were compared. The effect on simulation quality using the two datasets are shown in Figure 4.8. During typical (non-foehn) winter conditions, near-surface conditions are very alike. It was originally hypothesised that wind speeds in the lee of the mountains during foehn events would be higher in simulations with more finely resolved orography, generating more extreme adiabatic warming and thus more intense foehn. However, this is not observed: the overall effect of using improved orography is minimal at Cabinet Inlet for the cases examined.

Ten metre winds appear largely unchanged compared to the default set-up in simulations with updated orography (Figure 4.8). Strong cross-peninsula flow is observed in both configurations during foehn conditions, and is strongest near mountain passes, which generate gap flows downwind. To some extent, jet and wake regions such as those identified by Elvidge et al. (2015) are more clearly visible and spatially constrained in the updated set-up, but this may just be for the cases examined. The spatial distribution of above-freezing 1.5 m temperatures also differs marginally between the set-ups. Warm air is advected by wind during foehn, so because the wind field is comparable between the simulations, patterns in 1.5 m temperatures are too.

The net effect on the surface at Cabinet Inlet of improving orographic resolution is negligible, as can be seen in the time series shown in Figure 4.9. Simulations with default and updated orography are almost indistinguishable for 10 m wind speed, 1.5 m humidity, 1.5 m air temperature and surface temperature during CS2 (Figure 4.9) and CS1 (not shown). Indeed, the model bias relative to observations is much larger than the difference between the two configurations. However, surface observations may be better represented at a nearby grid point if the MetUM simulates foehn conditions correctly, but in a slightly different location. This is examined in the following section.

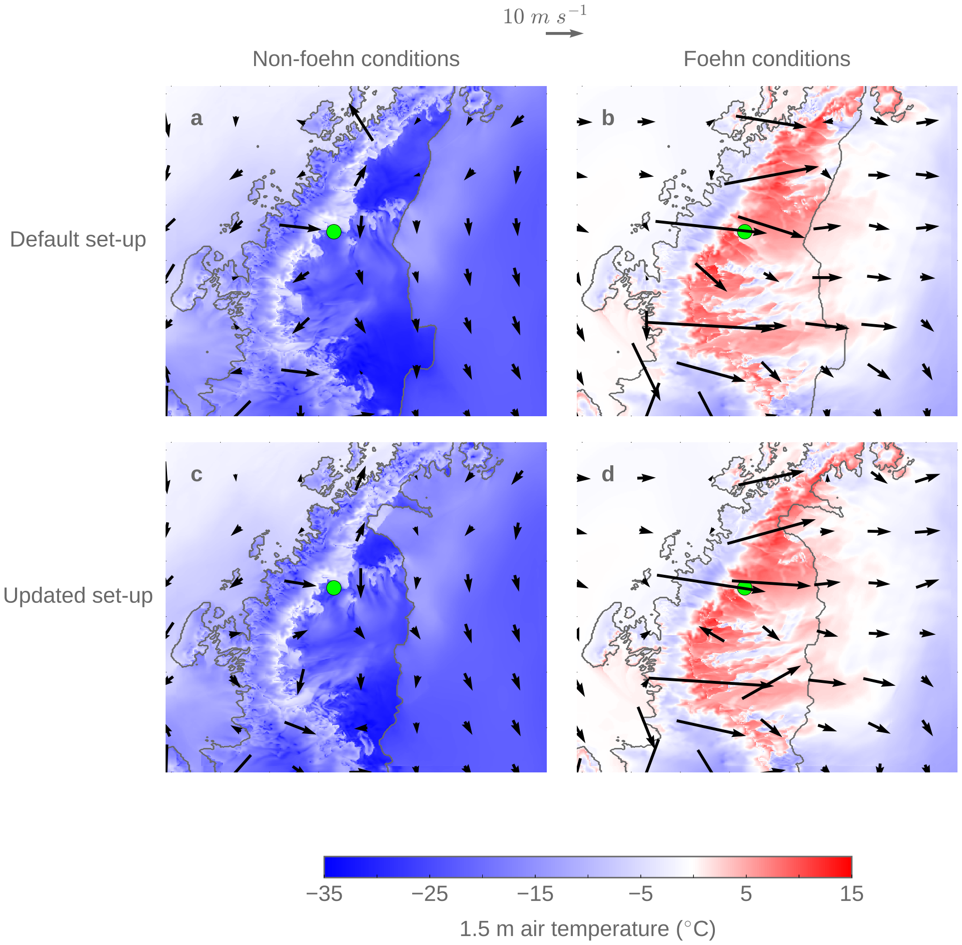
$10\ m\ s^{-1}$
Non-foehn conditions
Foehn conditions
Default set-up
Updated set-up
a
b
c
d
−35
−25
−15
−5
5
15
1.5 m air temperature (°C)

Figure 4.8.: Near-surface (1.5 m) air temperatures and 10 m wind speeds during non-foehn (left column; panels a and c) and foehn conditions (right column; panels b and d) during CS2 using the default MetUM orography and land-sea mask (top row; panels a and b) and updated orography and land-sea mask (bottom row; panels c and d). Non-foehn panels show hourly mean conditions for the period 23:00 UTC 22 May - 00:00 UTC 23 May and foehn panels show hourly mean conditions for the period 11:00 - 12:00 UTC 26 May. Filled contours show 1.5 m air temperatures, while vectors show 10 m wind speeds. A scale vector of 10 m s^{-1} is given at top centre for reference.

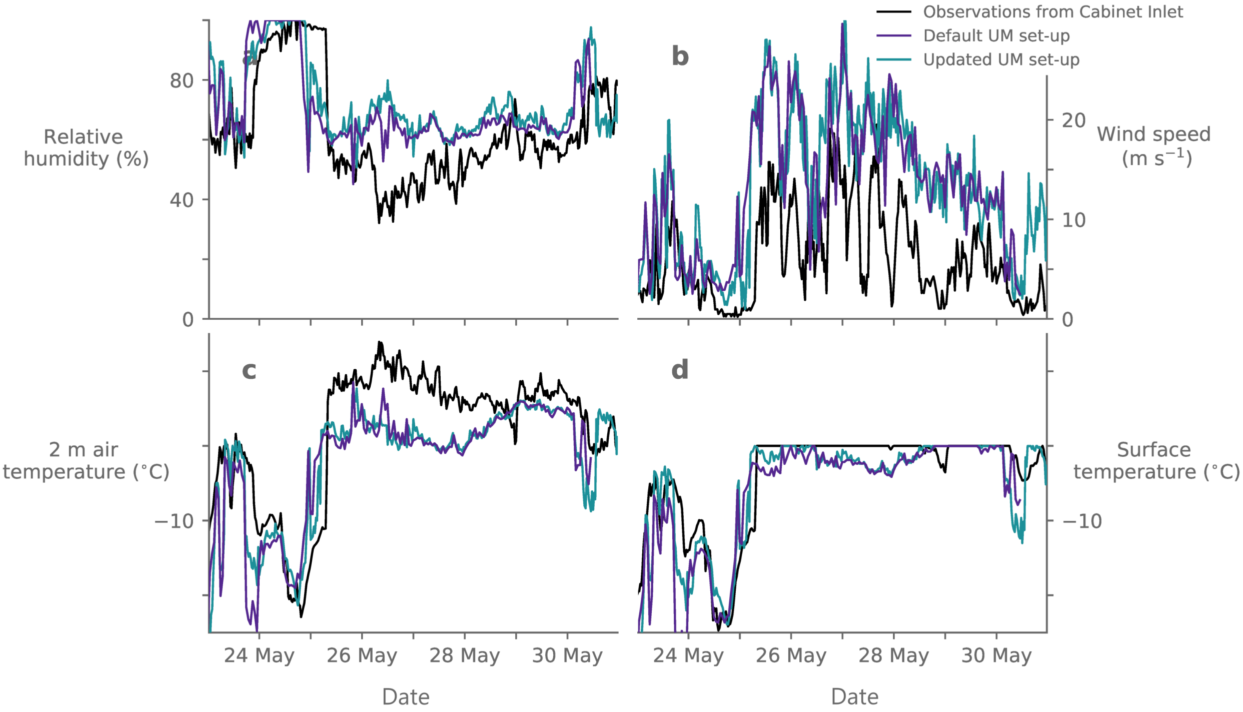

Figure 4.9.: Time series of surface meteorological variables during CS2 in AWS observations at Cabinet Inlet (black) and 1.5 km MetUM output using the default MetUM orography and land-sea mask (purple) and updated set-up (turquoise). Panel a) shows relative humidity; b) 10 m wind speed; c) near-surface air temperature; and d) surface temperature.

4.2.6 Can biases be improved by choosing a more representative grid point?

The effect of choosing a more representative grid point at which to calculate surface variables was examined (not shown). Because models may struggle to represent features precisely where they are observed, choosing a nearby grid box that more closely reproduces observations can be justifiable. Representation of surface meteorology was assessed in all grid boxes within 20 km of the Cabinet Inlet AWS's model location. MetUM temperature and wind speed biases shown in section 4.2.2 are larger during foehn conditions than non-foehn conditions, suggesting that the model may simulate foehn warming more accurately further east over the ice shelf, further away from the direct effect of leeside foehn warming. During the peak of both foehn events, modelled air temperatures do not reach those observed in any of the grid boxes on the ice shelf (not shown). Overall therefore, there is limited justification for choosing a different (nearby) grid point. The results of these sensitivity tests suggest that there may be more fundamental causes of the model biases in the representation of foehn, such as dynamics or other physical processes in the model like the surface or boundary layer schemes.

The first section of this chapter has demonstrated that foehn events occurred during winter 2016 at Cabinet Inlet. The classic signature of these events is evident in surface meteorology and the modelled vertical structure of the atmosphere suggests that foehn are produced via the isentropic drawdown mechanism. The next section will demonstrate the effect of wintertime foehn on the SEB.

4.3 Research question 2: What is the effect of wintertime foehn on the SEB of Larsen C?

The onset of foehn changes the sum of fluxes contributing to the SEB. In summer, radiative (SW and LW) fluxes dominate because of the near-24-hour daylight, which is reflected from the high-albedo ice surface. Daily mean $\mathrm{SW}_{\downarrow}$ fluxes can exceed 400 W m^{-2} in summer, and although almost all is reflected by the ice surface, the instantaneous SEB is dominated by SW fluxes. However, during polar night, the SW component of radiation is small and LW fluxes dominate the radiative component of the SEB. LW_{net} becomes negative at the beginning of both observed foehn events (Figures 4.10 and 4.11), meaning the surface is cooling. While this could indicate a reduction in $LW_{\downarrow}$ associated with foehn-induced cloud clearance, also implied by the lower humidity values shown in Figures 4.2 and 4.3 and expected from studies such as Elvidge et al. (2016) and Hoinka (1985), the decrease in LW_{net} is due mostly to the enhanced emission of LW radiation by the ice surface as the surface temperature increases. In both cases the model over-estimates LW_{net}, making it occasionally positive. This is because the model under-estimates surface temperature, so although $\mathrm{LW}_{\downarrow}$ is also under-estimated (Figures 4.12 and 4.13), LW_{net} is over-estimated because the compensating errors do not entirely cancel.

Biases in the modelled fluxes are evident in panels e – h of Figure 4.5 and 4.6. These scatterplots of observed vs. modelled surface fluxes exhibit the same negative biases in both downwelling radiative components as are reported in King et al. (2015), who considered summertime conditions. This indicates that cloud is optically too thin in the infrared part of the spectrum (likely because there is too little liquid), which reduces $LW_{\downarrow}$, while it is too thick in the SW, thereby preventing enough solar radiation from reaching the surface, even during winter. However, net radiation (R_{net}) is positively biased, due to a combination of factors: because surface temperatures are too low, not enough LW (SW) is emitted (reflected), meaning the surface does not cool enough and $\mathrm{LW}_{\uparrow}$ and $\mathrm{SW}_{\uparrow}$ are both too small to compensate for the downwelling fluxes, resulting in a positive R_{net} bias. Additionally, the mean model albedo, α ($SW_{\uparrow}/SW_{\uparrow}$) is 0.8 in CS1 and 0.75 in CS2, which is lower than the observed mean albedo of approximately 0.94 in both cases. This means that too little radiation is reflected, producing a positive bias.

Figures 4.12 and 4.13 show that during both cases, $LW_{\downarrow}$ remains quite high, even increasing slightly: from ~250 W m^{-2} pre-foehn to ~300 W m^{-2}. The model under-estimates $LW_{\downarrow}$, particularly in CS2 (Figure 4.13), suggesting that too little cloud, or cloud that is optically too thin, is present in the model run. This is consistent with the findings of King et al. (2015) who find negatively biased $LW_{\downarrow}$ at AWS 14 in summer 2011. Clouds that are cooler, higher, or have lower liquid water contents than observed will radiate less strongly in the infrared (LW) (Zhang et al., 1996). Several works (e.g. Field et al., 2014; Abel et al., 2017) have found that the MetUM under-estimates liquid water contents during relatively cold conditions, causing downwelling radiative fluxes to be negatively biased. A more detailed examination of this problem over Larsen C is conducted in the following chapter.

Turbulent fluxes, usually of the order of tens of W m^{-2}, become increasingly important during foehn. H_S becomes strongly positive in foehn periods because warm, dry air is brought to the surface by the high winds (Figures 4.12 and 4.13). Rapid H_S increases follow wind speed peaks, when much warmer air is advected into Cabinet Inlet. This produces a positive temperature gradient between the air and the surface, meaning energy is transferred from the overlying air mass into the ice surface. During both cases, H_S fluxes become the dominant source of energy available for melting, peaking at almost 350 Wm^{-2} during CS2.

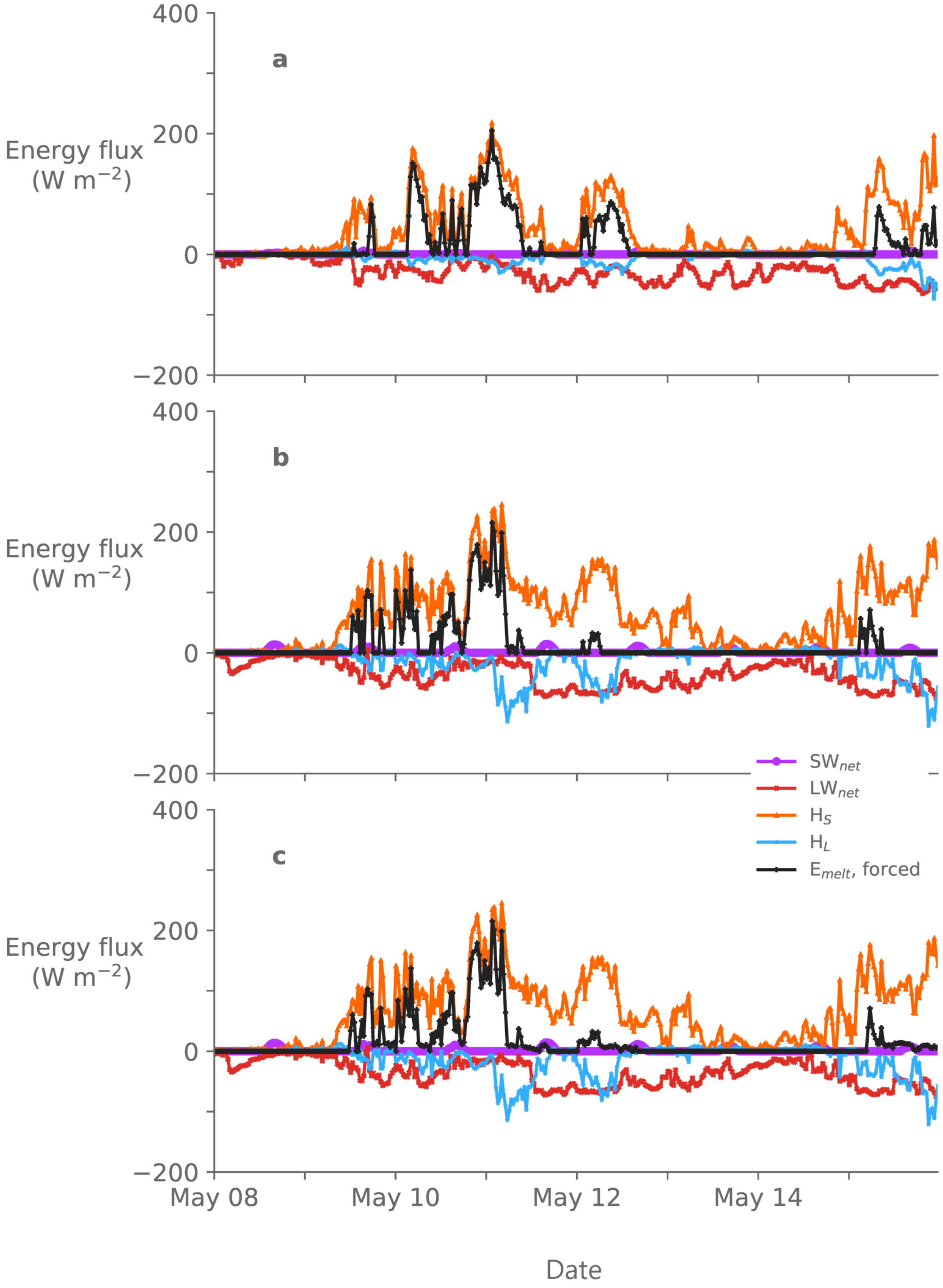

Figure 4.10.: Time series of total SEB during CS1, May 9-–15, in a) observations, and b) and c) 1.5 km model output. Panel b) includes directly modelled melt flux, while panel c) shows the melt flux calculated using observed surface temperatures (as discussed in main text). Net SW and LW fluxes are shown in purple and red, respectively, sensible and latent heat fluxes are shown in orange and blue, respectively, and melt flux is shown in dark grey. All fluxes are given in W m^{-2}.

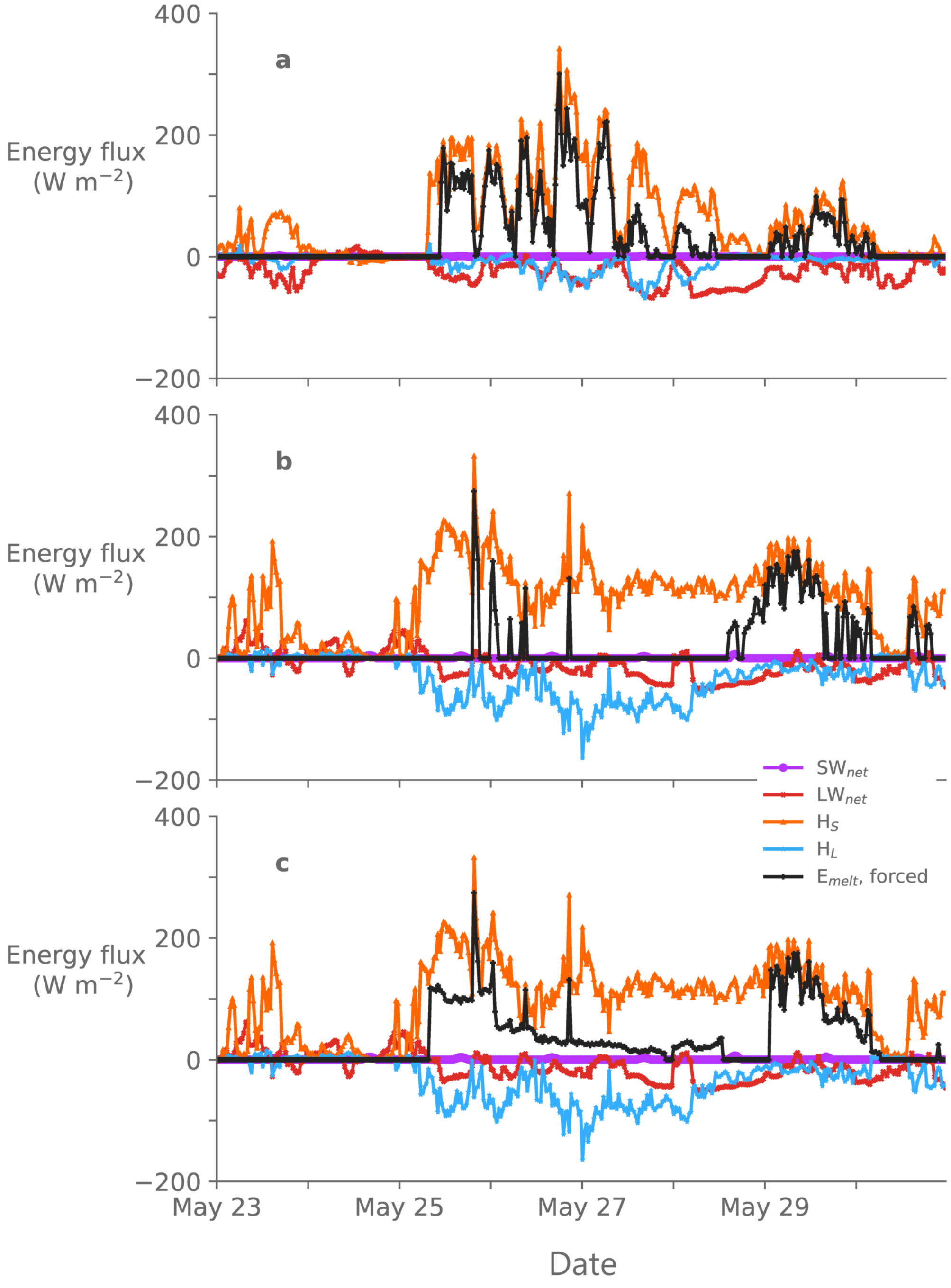

Figure 4.11.: Time series of total SEB during CS2, May 23–30, with details as in Figure 4.10.

Although the model represents patterns in H_S quite accurately, it generally over-predicts it, especially towards the end of CS2 (Figures 4.12 and 4.13). The MetUM fails to reproduce some of the rapid variation in H_S associated with wind speed because of its under-estimation of temperature. H_S is modelled far better in CS1 than in CS2, maybe because H_S fluxes during CS1 are smaller. The consistent over-estimation is probably because it over-estimates wind speed, which is used in the calculation of H_S (Equation 3.7). This means too much heat energy is mixed towards the surface by winds. Physically, over-estimated wind speeds mean too much warm air is advected to Cabinet Inlet, resulting in erroneously large H_S.

Modelled H_L is negatively biased relative to observations at AWS 18. This is seen in 1.5 km and 4.4 km output in Figures 4.12 and 4.13. Interestingly, the observed H_L (Figures 4.12 and 4.13) very occasionally becomes slightly positive during both foehn events, suggesting that condensation is occurring. This is unexpected: sublimation or evaporation would normally be expected as warm, dry foehn air is advected over a colder surface. This condensation is likely happening because the foehn air is so warm compared to the surface that it can "hold" more moisture; i.e. that its specific humidity at 1.5 m is higher than that at the surface, meaning the moisture gradient is directed towards the surface. These periods of positive H_L are short-lived however, so does not significantly affect the model mean bias, RMSE or correlation coefficient. Errors are larger during periods when the wind speed and humidity are more positively biased, and when temperature is most negatively biased, i.e. 10–13 and 26–29 May for CS1 and CS2, respectively.

Overall, this means the model over-estimates E$_{tot}$. E_{tot} is over-estimated by 11.18 Wm^{-2} in CS1 and 23.18 Wm^{-2} in CS2. The largest source of error is H_S, and to a lesser extent LW_{net}, which is not negative enough to offset modelled H_S as much as in observations. Errors in both H_S and LW_{net} originate from errors in key model variables: H_S is over-predicted because of positively biased wind speeds, while LW_{net} is positively biased because under-estimated surface temperatures reduce LW$_{\uparrow}$. Errors in fundamental model variables must therefore be addressed to improve the representation of surface fluxes.

In answer to the second research question, this section has shown that foehn alter the SEB. The observed effect on turbulent fluxes is pronounced: sensible heat fluxes increase significantly, and latent heat fluxes become negative. The MetUM simulates increased sensible heating, and decreased latent heating, but these are over- and under-estimated, respectively, resulting in biases. Effects on SW fluxes are minimal in the absence of significant solar heating, but under-estimated surface temperatures cause LW$_{\uparrow}$ to be too small. These effects cause E$_{tot}$ to become more positive in both observations and the model, and therefore could drive melting of the ice surface. This is the focus of the third research question, and of the following section.

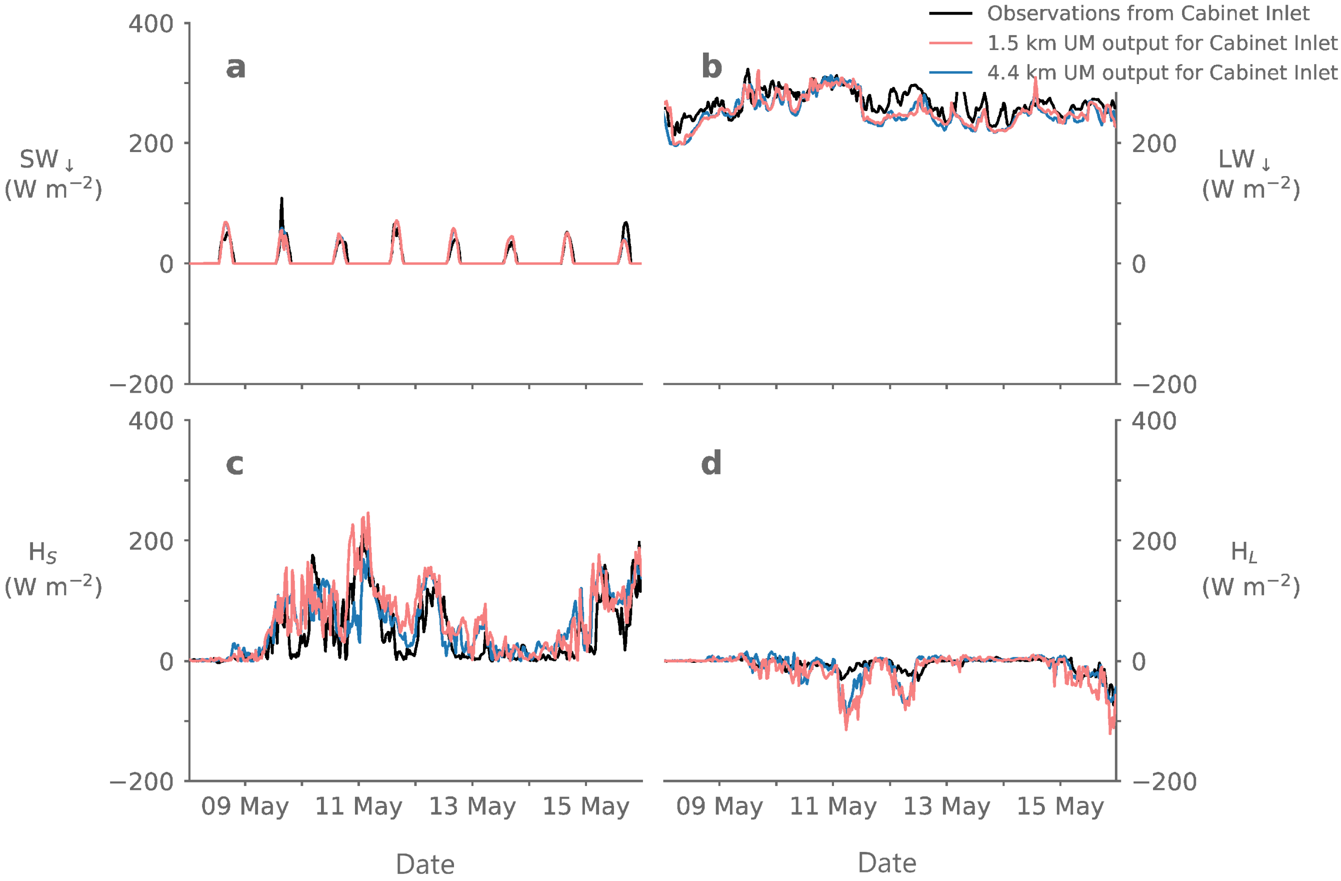

Figure 4.12.: Time series of surface energy fluxes at Cabinet Inlet during CS1, May 9 – 15, in observations (black line) and model output at 1.5 km (pink) and 4.4 km (blue) resolution. Panels show individual surface energy balance (SEB) components: a) downwelling shortwave, $SW_{\downarrow}$; b) downwelling LW, $LW_{\downarrow}$; c) sensible heat, H_S; and d) latent heat, H_L fluxes.

4.4 Research question 3: Do wintertime foehn events cause melting on Larsen C?

The significant effect of foehn on the SEB demonstrated above could be expected to influence the production of meltwater. Melting occurs when the SEB is positive, and when surface temperatures reach the melting point of 0°C as shown in Equation 3.4. As shown in section 4.3, the effect of wintertime foehn events is to increase the SEB and surface temperatures. To answer the third research question, this section will determine whether this results in an increased melt flux.

Observations suggest that foehn events may alter the ice shelf SEB enough to produce melt. During both cases studied in this chapter, surplus energy is available to melt the surface of the ice shelf (Figures 4.10 and 4.11) when surface temperatures reach the melting point

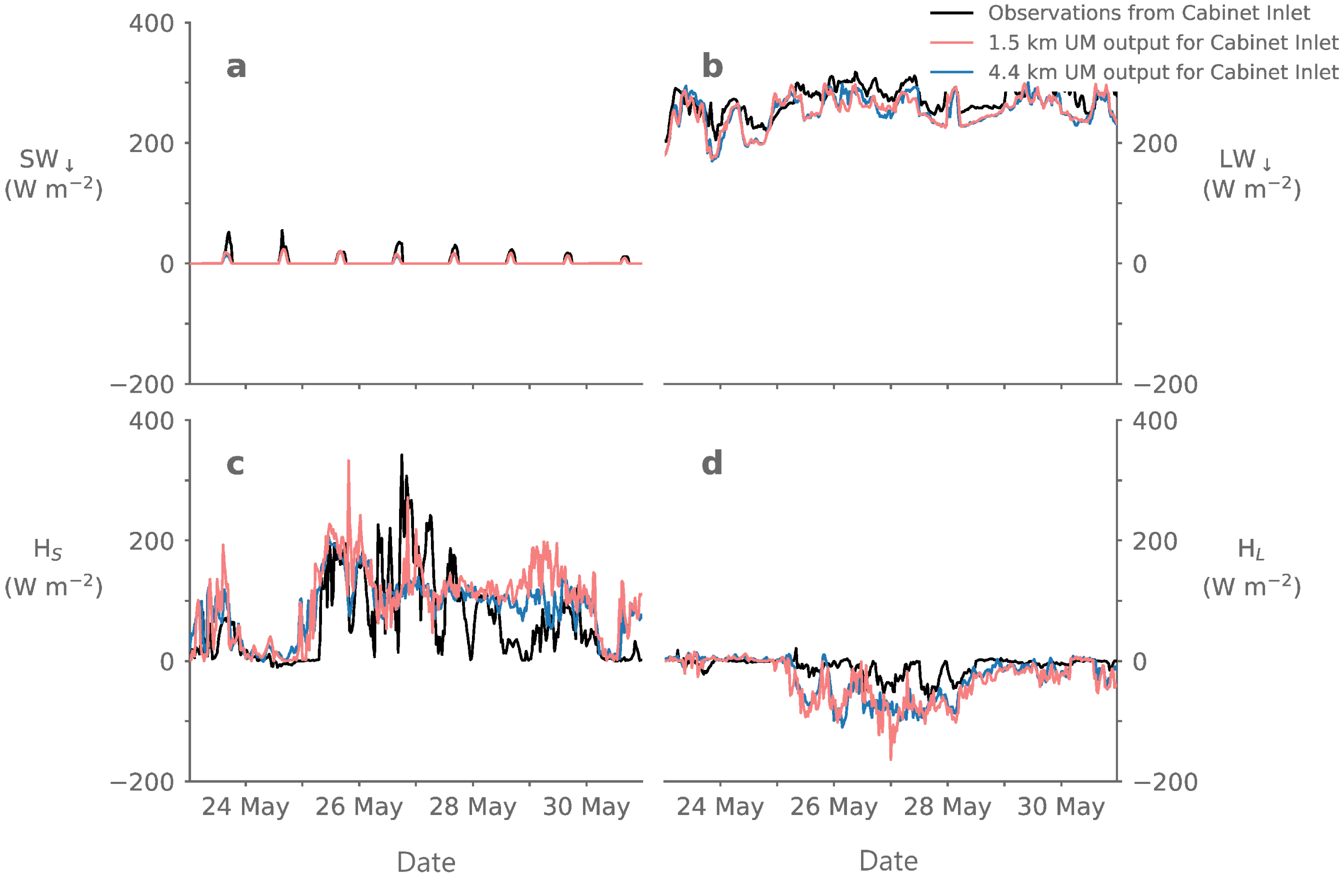

Figure 4.13.: Time series of surface energy fluxes at Cabinet Inlet during CS2, May 23 – 30, with details as in Figure 4.12.

(Figures 4.2 and 4.3). The observed melt flux closely follows H_S, indicating that the majority of the melting is driven by the advection of warmer air over the cold ice surface, generating extreme temperature gradients. Energy available for melting (E$_{melt}$) is converted to meltwater production, M, in mm w.e., using the latent heat of melting (L_m = 3.34 x 105 J kg^{-1}) and density of water (ρ_w = 999.7 kg m^{-3}), and Equation 4.1, after Krapp et al. (2017).

$$M = \frac{E_{melt}}{\rho_w L_m} \tag{4.1}$$

More melt is simulated during CS2 than CS1 (72 mm w.e. compared to 31.6 mm w.e.), as expected from the higher surface and air temperatures and H_S fluxes (Figures 4.3 and 4.13 and Table 4.2). Observed energy available for melting reaches a maximum of 300 W m^{-2} at the height of CS2 (Figure 4.11), and melting occurs almost continually from the onset of foehn at 08:24 on 25 May until 11:31 on the 28 May, producing 72.2 mm w.e. of meltwater (Table 4.2).

Despite E$_{tot}$ being positively biased in both cases, largely because H_S is over-estimated as discussed above, modelled E$_{melt}$ in CS2 is negatively biased, while it is positively biased in CS1. Mean observed E$_{melt}$ when the surface is at the melting point during CS1 (CS2) is 61.1 W m^{-2} (74.9 W m^{-2}), while the modelled melt flux for the same period is 71.6 W m^{-2} (69.2 W m^{-2}): a bias of 10.4 W m^{-2} (-16.4 W m^{-2}).

However, modelled meltwater production, M, is too low in both cases. This is because surface temperature is below the melting point for most of the foehn event, due to the cold bias shown in section 4.2.2 and Table 4.1. In CS1, modelled mean E$_{melt}$ is positively biased although the conditions for melting (T_S = 0°C) occur less frequently than observed due to this cold bias, but only because there is a large surplus of energy available for melting during periods when the modelled surface does reach the melting point. This means the model produces half the observed melt during CS2 (37.7 mm w.e. compared to 72.2 mm w.e.) and under-estimates meltwater production in CS1 by 15%. Particularly in CS2, this results in an extremely low correlation ($r < 0.02$) between observed and modelled E$_{melt}$ (Figure 4.6, panel h). Overall however, there is relatively good agreement between modelled and observed E$_{melt}$.

The effect of the cold T_S bias can be illustrated with the following example. Because the surface temperature is under-estimated, the surface is frequently too cold to melt despite a surplus of energy being available. However, due to the reasons listed in section 4.3, E_{tot} is modelled inaccurately. If model melt is calculated using observed T_S values rather than modelled T_S, as shown in panel c of Figures 4.10 and 4.11, then modelled mean E$_{melt}$ becomes 38.4 W m^{-2} and 33.3 W m^{-2} for CS1 and CS2, and meltwater production becomes 34.6 and 36.6 mm w.e., respectively. Both represent an improvement from the modelled values shown in Table 4.2, with r values increasing from 0.64 and 0.01 to 0.69 and 0.38 for CS1 and CS2, respectively.

Table 4.2.: Mean observed and modelled melt fluxes (top row, in W m^{-2}) during periods when the surface temperature is at melting point, and cumulative meltwater production (bottom row, in mm w.e.) for both case studies. Model results at 1.5 km resolution are shown.

	CS1		**CS2**	
	Observed	**Modelled**	**Observed**	**Modelled**
Energy available for melt ($T_S > 0$) (W m^{-2})	61.1	71.6	74.9	69.2
Meltwater produced (mm w.e.)	37.6	31.6	72.2	37.7

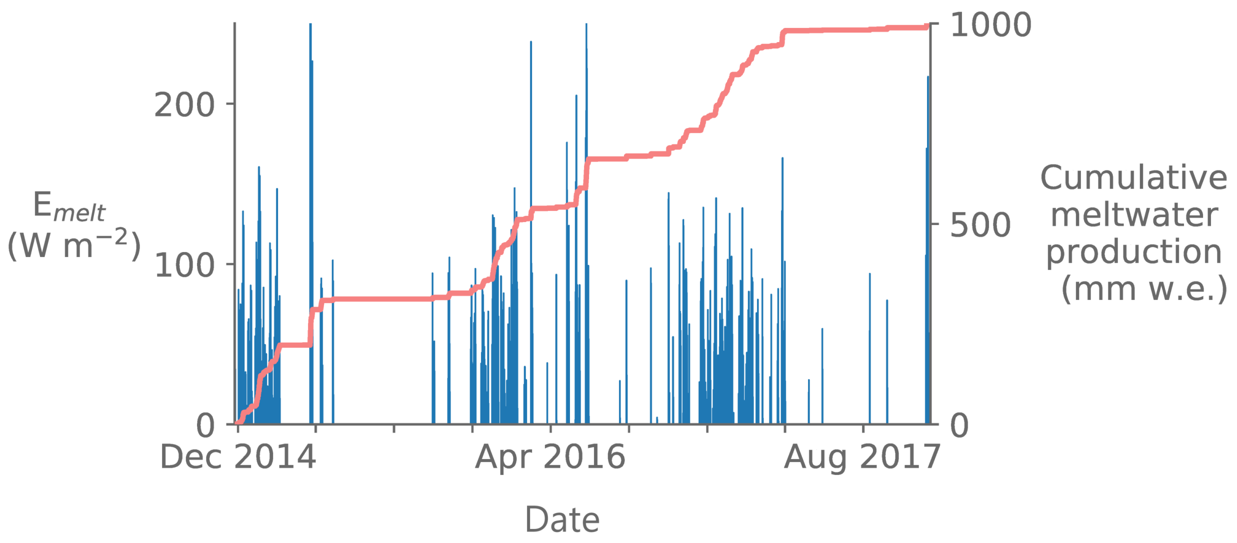

Figure 4.14.: Energy available for melting at the Cabinet Inlet AWS from November 2014 until September 2016. The blue lines show instantaneous melt fluxes (in W m^{-2}), while the pink line shows cumulative meltwater production over the entire time series in units of mm w.e..

Both the observations and model results show that melt is occurring as a result of foehn (Figures 4.10 and 4.11), although the modelled melt flux is lower than observations due to the cold surface temperature bias. However, if surface temperatures are set to observed values as described above and shown in Figures 4.10c and 4.11c, the over-estimated SEB causes modelled melt fluxes to be positively biased. Evidently, there are some errors in the representation of individual SEB components over Larsen C during foehn, but the model is still able to capture wintertime melting, which has not been shown before. These errors likely result from several problems. Firstly, errors in the representation of the stable boundary layer and its evolution, described above, may influence how surface variables are simulated. This may explain the large RMSE values for some variables. Secondly, the representation of cloud phase could produce errors in the LW flux, as also suggested in King et al. (2015). The representation of cloud phase, liquid and ice water path, and hence optical depth, alters how much radiation reaches the surface (Zhang et al., 1996). This is more important in summer though, when clouds can affect SW as well as LW radiation. The effect of cloud phase on the SEB of Larsen C is the subject of Chapter 5.

Both foehn cases examined are cases of vigorous winter melt. Winter foehn-driven melt events are intense, but short-lived, and cause large jumps in the cumulative melt flux (Figure 4.14). Such events were responsible for 23% of all melt in 2016 (Kuipers Munneke et al., 2018) in observations from the AWS 18 for the period November 2014 – November 2017 (and where "winter" is defined from 1 April – 31 October). This makes them important to represent accurately in order to improve estimations of ice shelf melt, which will be crucial for predicting future change and global sea level rise.

Although only two cases were examined, Figure 4.14 shows that these type of wintertime foehn events occur frequently. However, because 2016 was an exceptionally high melt year (Kuipers Munneke et al., 2018) and CS2 is the most intense event in a short observational record (since 2014), caution must be exercised when extrapolating to winter conditions generally. However, in a warming world - and given rising temperatures on the Antarctic Peninsula (as shown in Chapter 2) - foehn events could push surface temperatures above melting point more frequently, and therefore cause melting. This mechanism is hence likely to become more important in future.

4.5 Conclusion

This chapter, as well as Kuipers Munneke et al. (2018), has shown for the first time that observed wintertime melt over Larsen C is most likely due to foehn events. This work has shown firstly that foehn are occurring during winter, as is evident in observations and model output; secondly that these foehn events alter the SEB, again as seen in observations and the MetUM; and thirdly that this causes melting. Despite the shortcomings of the MetUM, particularly with respect to the SEB components, these findings are robust. Estimates of modelled melt rely on an accurate representation of surface temperature, however, which suggests that further work is necessary to improve the model physics. Further development will improve the representation of individual SEB components, consistent with the original premise of the thesis. Of particular interest is the representation of cloud phase, shown to be a significant source of error in the representation of radiative fluxes in the MetUM and other models (Chapter 2). This will be the subject of the next chapter. These findings have implications for the stability of the Larsen C ice shelf. If melt is occurring frequently in winter, Larsen C might be more susceptible to collapse than previously thought, and could make a larger contribution to future sea level rise than current estimates suggest.

The effect of summertime cloud phase on surface melting over Larsen C

5

Declaration: Much of this chapter has been adapted from **Gilbert, E.**, Orr, A., King, J. C., Renfrew, I. A., Lachlan-Cope, T., Field, P. F., Boutle, I. A. (2020). "Summertime cloud phase strongly influences surface melting on the Larsen C ice shelf, Antarctica." *Quarterly Journal of the Royal Meteorological Society*, 2020, 1–16, doi: https://doi.org/10.1002/qj.3753. The paper is reproduced in Appendix B.

5.1 Introduction

This chapter will investigate the effect of cloud properties, and particularly cloud phase, on the SEB of Larsen C. Microphysical data from an aircraft campaign conducted in January/February 2011 will be compared with surface meteorological and energy flux measurements at AWS 14 (see Figure 3.1). Specifically, this chapter will focus on two case studies during this period when microphysical data were collected.

5.1.1 Aims and objectives

The aim of this chapter is to determine the importance of the microphysics of Antarctic Peninsula summertime mixed phase clouds in influencing the SEB, and how accurately this is represented in the MetUM. This is a key topic of uncertainty because as described in Chapter 2, observations of Antarctic cloud microphysics are difficult to make, and our understanding of them is therefore limited. This means that models also struggle to represent Antarctic clouds. A further objective of this chapter is to optimise the MetUM to best represent summertime mixed phase clouds over Larsen C, which will inform the production of the hindcast configuration used in Chapter 6.

5.1.2 Research questions

To achieve this aim, several specific research questions will be explored. These are:

1. Is the MetUM able to represent observed cloud phase and microphysics?
2. How does cloud phase influence the SEB in observations and the MetUM?
3. Can a double-moment microphysics scheme improve simulations of cloud phase?
4. How does summertime cloud phase influence the SEB during the entire OFCAP period?

5.1.3 Novelty of research

Published studies, discussed in Chapter 2, have focused on individual components of this chapter, or different regions, for instance on: 1) observed microphysics in the Antarctic (Grosvenor et al., 2014; Lachlan-Cope et al., 2016); 2) model representation of cold mixed phase cloud microphysics in the Antarctic (Listowski and Lachlan-Cope, 2017) and mid-latitudes (Field et al., 2014; Abel et al., 2017); 3) the observed and modelled radiative effect of cloud microphysics in the Arctic (Stevens, 2017) and West Antarctica (Scott et al., 2017; Nicolas et al., 2017; Hines et al., 2019); and 4) the SEB of Antarctic Peninsula ice shelves like Larsen C (King et al., 2015). Until now, there has not been a study that brings together each of these components to understand how models represent mixed phase microphysics on the Antarctic Peninsula, and how this translates into the representation of the SEB. This chapter will address each of these elements specifically and draw them together to comprehensively address this knowledge gap.

5.2 Data, modelling and methods

5.2.1 Methods

Two instructive case studies are identified to examine cloud properties and surface fluxes: flights 150 and 152, hereafter referred to as f150 and f152, conducted on 15 January 2011 and 18 January 2011, respectively. The flight tracks and location of AWS 14 are shown in Figure 5.1. Cases were selected following inspection of AVHRR satellite imagery and ERA-Interim re-analysis data that showed cloud cover to be evenly distributed across Larsen C, with similar synoptic meteorological conditions across the whole ice shelf. Under these conditions, it is assumed that the cloud sampled by the aircraft is representative of cloud across the whole ice shelf. Case f150 was selected because the aircraft conducted several lateral transects at approximately constant latitude, sampling predominantly supercooled liquid-bearing mixed-phase cloud, which models are known to represent poorly (see Chapter 2 for a summary of the literature). Case f152 was selected because the aircraft conducted two vertical profiles between 100–5000 m near AWS 14.

Observed and modelled surface fluxes and in-cloud atmospheric profiles and transects are compared at AWS 14 during both cases. "In-cloud" is defined as per Lachlan-Cope et al. (2016) to be when the observed ice number concentration exceeds 1.0×10^{-8} cm^{-3} or droplet number concentration exceeds 1.0 cm^{-3}. Model in-cloud values are more complex to determine because single-moment microphysics schemes output only mass mixing ratios

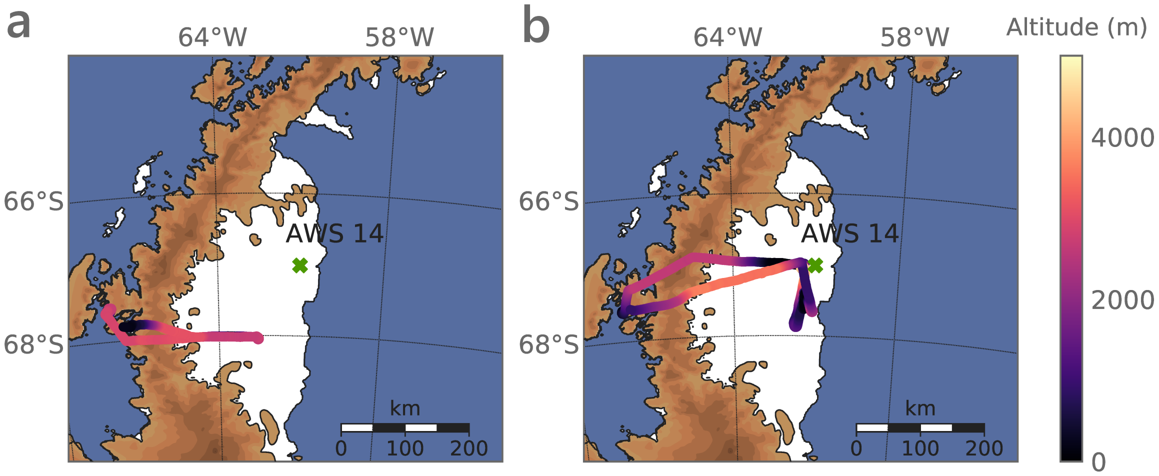

Figure 5.1.: The inner 1.5 km resolution MetUM model domain used in this chapter, centred on the Larsen C Ice Shelf. The model's surface elevation is indicated by shaded contours. The flight track of the f150 (a) and f152 (b) case studies is also shown, where the aircraft's altitude is indicated by the scale shown on the right, and the location of AWS 14 is marked with a cross.

of ice and liquid, not number concentrations. Thus, a mass mixing ratio threshold derived from the OFCAP observations is applied. Model in-cloud conditions are therefore diagnosed when mass mixing ratios exceed the minimum in-cloud mass mixing ratio observed during all OFCAP flights: 1.0×10^{-4} g kg^{-1} and 1.5×10^{-6} g kg^{-1} for ice and liquid, respectively.

Model output is taken from the closest gridpoint to AWS 14's location, plus the eight surrounding gridpoints: an area of approximately 4.5 km^2. Because AWS 14 is located on a flat, homogeneous ice surface, it can be reasonably assumed that conditions there are representative of a large area (King et al., 2015). Mean vertical profiles and transects are computed from observations and model output using in-cloud data only, during the period when the aircraft was sampling over the ice shelf (between approximately 17:15 and 19:45 UTC during f150 and 15:00 and 17:00 UTC during f152).

Case f152 was simulated with four single-moment model "Regional Atmosphere" (RA) configurations, which are summarised in Table 5.1 and described in detail in section 3.2. Case f152 is used to answer research questions 2, 3, and 4. Case f150 was simulated with the best-performing single-moment configuration and several variants of the CASIM double-moment configuration (described in Chapter 3) with differing ice nucleation parameterisations, shown in Table 5.1 and detailed in section 3.2.4. Case f150 is predominantly used to answer research question 4 and single-moment results are not presented for this case to avoid repetition. The best-performing configuration identified using case f152 was used to simulate the entirety of the Orographic Flows and Climate of the Antarctic Peninsula (OFCAP) campaign, which took place between January 1 and February 7, 2011 (see Elvidge et al., 2015; Elvidge et al., 2016; King et al., 2015). An additional sensitivity test is performed with amended representation of boundary layer mixing, and is described in Appendix C. During the whole OFCAP period, only the representation of surface fluxes is assessed because cloud phase measurements are not consistently available throughout the period. Initial tests showed modelled cloud phase to be sensitive to forecast length, so the first 12 hours of each 24-hour forecast were discarded as spin-up. Each case study simulation was initialised at 00:00 UTC on the day of interest to allow the model to spin up. For the longer OFCAP simulation, forecasts were re-initialised every 12 hours and the t+12 h to t+24 h hour part of each successive forecast was concatenated to form a continuous time series.

The aim of running multiple MetUM experiments with varying configurations is to optimise the simulation of summertime cloud phase and SEB, and inform the production of the hindcast setup for Chapter 6. There must be reasonable confidence in the model's ability to represent the fields of interest before it can be robustly relied upon to simulate conditions for which there is limited or no data, for instance during winter, when aircraft campaigns are impossible. This configuration is optimised for the Antarctic and includes processes and features that are not included by default in the MetUM, which is tuned to simulate conditions in northern mid-latitudes.

5.2.2 Data

Two observational datasets are used to validate MetUM-simulated cloud phase and SEB over Larsen C. Namely, airborne observations of cloud collected with the British Antarctic Survey's instrumented De Haviland Twin Otter aircraft and observations of near-surface meteorological variables and surface energy fluxes from the Larsen North AWS (AWS 14). Both datasets and their treatment are described in Chapter 3, and the SEB is computed as in Equation 3.3.

5.2.3 Model experiments

Regional atmosphere physics configurations

Two variants of RA physics are used in this chapter: RA1M and RA1T, configured for the mid-latitudes and tropics, respectively, and described in Bush et al. (2019). The primary difference between them is that RA1M uses the operational (diagnostic) large-scale cloud scheme based on Smith (1990a) whereas RA1T uses a prognostic scheme, PC2 (Wilson et al., 2008). Both are described in Chapter 3.

Table 5.1.: Configurations for model experiments used in this study. Varying model schemes and parameterisations used in each model experiment are summarised in the second column ("options"), and the cases that each experiment is used to simulate are indicated in the last column ("case").

Experiment name	**Options**	**Case**
RA1M	• RA1M physics, based on Smith (1990) large-scale cloud scheme • Heterogeneous nucleation temperature threshold set to -18°C (Field et al., 2014)	f152
RA1M_mod	As in RA1M, with the following modifications: • Shape-dependent riming (Furtado and Field, 2017) • Modified ice cloud fraction parameterisation (Abel et al., 2017)	all
RA1T	• RA1T physics, based on PC2 (Wilson et al., 2008) large-scale cloud scheme • Heterogeneous nucleation temperature threshold set to -18°C (Field et al., 2014)	f152
RA1T_mod	As in RA1T, with the following modifications: • Turbulent production of supercooled water (Furtado et al., 2016) • Shape-dependent riming (Furtado and Field, 2017)	f152
no ice	As in RA1M_mod, with ice processes switched off.	f150 & f152
Cooper	As in RA1M_mod, with the following modifications: • CASIM double-moment microphysics representing cloud particle mass mixing ratio and number concentration • Cooper (1986) ice nucleation parameterisation	f150 & f152
DeMott2010	As in Cooper, but using the DeMott et al. (2010) ice nucleation parameterisation	f150 & f152
DeMott2015	As in Cooper, but using the DeMott et al. (2015) ice nucleation parameterisation	f150 & f152
RH_{crit} = 0.85	As in Cooper, with RH_{crit} set to 0.85 throughout the profile (see description in main text)	f150

Configurations used in the second two experiments (RA1M_mod and RA1T_mod) include modifications to the base configurations shown to improve the simulation of cold mixed-phase clouds by increasing the supply of liquid water and reducing its conversion to ice (see Table 5.1 for a summary). These are: 1) the inclusion of shape-dependent riming (Furtado and Field, 2017), 2) the turbulent production of supercooled liquid (Furtado et al., 2016), and 3) modifications to the ice cloud fraction parameterisation described in Abel et al. (2017). Modification 1) is applied to both RA1M and RA1T, 2) is applied to RA1T only, and 3) is applied to RA1M only. Firstly, riming depletes liquid water, so limiting the efficiency of this process can sustain higher liquid fractions in mixed-phase clouds. Reducing riming efficiency has been shown to improve Southern Ocean $SW_{\downarrow}$ biases associated with the conversion of too much cloud liquid water to ice (Chapter 2, Furtado and Field, 2017). Secondly, cloud liquid water can also be produced by sub-grid scale variations in humidity that are related to unresolved turbulence. Because turbulent motions occur at finer scale than the MetUM can explicitly resolve, this can produce humidity distribution differences that are also not explicitly simulated. Furtado et al. (2016) demonstrated that increasing the supply of liquid in this manner can enhance the amount of cloud liquid. This modification is only compatible with the PC2 cloud scheme, on which RA1T is based. Finally, several studies show that ice cloud fractions are consistently over-estimated in mixed-phase clouds by the MetUM (e.g. Field et al., 2014; Abel et al., 2017) due to computational limitations that mean that the model cannot explicitly resolve small-scale spatial heterogeneity in cloud water phase. Abel et al. (2017) developed an adaptation to the ice cloud fraction parameterisation that limits the overlap between the liquid and ice fractions, thereby reducing the conversion of liquid to ice via vapour deposition and riming. This adaption mimics the real-world existence of spatially discrete (sub-grid scale) pockets of ice and liquid without explicitly resolving them. It is only compatible with the RA1M scheme.

In all experiments, the heterogeneous ice nucleation temperature threshold (representing an immersion freezing or condensation mechanism, whereby ice is permitted to form heterogeneously in the presence of liquid water) used by the microphysics scheme was changed from its default value of -10°C to -18°C, shown by Field et al. (2014) to improve the representation of mixed-phase cloud.

Double moment cloud microphysics

The newly developed Cloud AeroSol Interaction Microphysics scheme (CASIM: Shipway and Hill, 2012; Hill et al., 2015; Grosvenor et al., 2017) is a double-moment parameterisation with five hydrometeor classes that permits one- or two-way cloud-aerosol interactions. The size distribution of each hydrometeor class is described with a gamma distribution, and CASIM calculates prognostic mass mixing ratios and number concentrations (Miltenberger et al., 2018). Density, mass-diameter and fall speed relationships are prescribed. Further details on CASIM can be found in Miltenberger et al. (2018), Grosvenor et al. (2017) and Chapter 3. In the configuration used, two soluble modes of aerosol are represented (accumulation mode and coarse dust), with one-way coupling between cloud and aerosol, meaning that the cloud field is forced by aerosol, but that cloud development does not deplete aerosols during the simulation. The Abdul-Razzak and Ghan (2000) droplet activation scheme is used, and the default Cooper (1986), DeMott et al. (2010) and DeMott et al. (2015) ice nucleation schemes are all tested (the "Cooper", "DeMott2010" and "DeMott2015" experiments in Table 5.1, respectively), as well as an experiment with ice processes switched off ("no ice" in Table 5.1), and another with a constant profile of critical relative humidity ("$\mathrm{RH}_{crit} = 0.85$"). In the default MetUM configuration, RH_{crit} is higher nearer the surface because temperatures are warmer at lower altitudes, and so condensation can occur more readily. Hence, reducing RH_{crit} closer to the surface in this experiment should allow more cloud to form at lower levels.

The configurations used in this chapter are summarised in Table 5.1.

5.3 Results and discussion

A summary of cloud microphysics observed during the OFCAP campaign is given in Lachlan-Cope et al. (2016). Of the two cases selected, f150 has relatively higher liquid water contents and lower ice contents (mean mass mixing ratios of 8.76×10^{-2} g kg^{-1} (standard deviation, σ, = 1.56×10^{-2} g kg^{-1}) and 2.62×10^{-4} g kg^{-1} ($\sigma = 1.37 \times 10^{-4}$ g kg^{-1}), respectively, and number concentrations of 294.11 cm^{-3} (σ = 16.22 cm^{-3}) and 1.69×10^{-4} cm^{-3} ($\sigma = 5.72 \times 10^{-5}$ cm^{-3}), respectively), whereas f152 is a case with relatively lower liquid contents and higher ice contents (mean mass mixing ratios of 6.3×10^{-2} g kg^{-1} ($\sigma = 7.74 \times 10^{-2}$ g kg^{-1}) and 1.83×10^{-3} g kg^{-1} ($\sigma = 3.78 \times 10^{-3}$ g kg^{-1}), respectively, and number concentrations of 60.34 cm^{-3} (σ = 52.80 cm^{-3}) and 4.08×10^{-4} cm^{-3} ($\sigma = 6.02 \times 10^{-4}$ cm^{-3}), respectively). In comparison, using a larger sample of flights, Lachlan-Cope et al. (2016) report mean liquid and ice mass mixing ratios east of the peninsula mountains during OFCAP of 1.08×10^{-1} g kg^{-1} and 1.24×10^{-2} g kg^{-1}, respectively, and liquid and ice number concentrations of 191.68 cm^{-3} and 7.37×10^{-4} cm^{-3}, respectively. This suggests that droplets in f150 and ice particles in f152 were relatively smaller than the average of all flights: in f152 a comparable ice mass mixing ratio is divided between a larger number of particles, suggesting a source of INP, while in f150 the number concentration of droplets is similar to the average of Lachlan-Cope et al. (2016), but mass mixing ratio is approximately half.

5.3.1 Observed cloud phase during f150 and f152

Two cloud layers were present over Larsen C during f150: mid-level altostratus (between 2500 - 3100 m altitude) and low-level stratocumulus (< 750 m altitude) layers. The aircraft flew straight and level east-west transects across the Larsen C ice shelf between approximately 66.0°W and 62.5°W at a constant latitude of approximately 67.0°S (see Figure 5.1), sampling predominantly in the upper layer, where temperatures were between -11°C and -20°C (not shown). The lower layer contained mostly small liquid droplets, and temperatures were warmer than -5°C. Ice crystals were large, and showed evidence of riming. Pockets with much smaller ice crystals were observed in the mid-level layer at temperatures below -18°C. Maximum liquid droplet number concentrations and mass mixing ratios, peaking at 469.21 cm^{-3} and 1.45×10^{-1} g kg^{-1}, respectively, were observed closest to the ice shelf edge, suggesting marine sources of CCN.

During case f152, the aircraft performed a spiral ascent and descent to vertically profile the cloud layers (see Figure 5.1). A multi-layered cloud structure was observed (Figure 5.2), with many thin, tenuous layers between thicker layers. A higher altostratus layer was present at around 4 km altitude, while a stratocumulus deck was observed between approximately 400 m and 2200 m. This stratocumulus appeared in two distinct layers and contained higher mass mixing ratios of cloud ice and liquid than the upper level altostratus, reaching 1.6×10^{-2} g kg^{-1} and 3.4×10^{-1} g kg^{-1}, respectively, and exhibiting the "water-over-ice" structure typical of low-level polar mixed-phase clouds. Very large particles were observed at the base of the lowest layer (not shown), around 100 m above the surface, where temperatures were warmer (-2°C) and ice mass mixing ratios were high, while very little liquid was observed, which suggests that these particles were rimed ice crystals or precipitation-sized particles.

5.3.2 Research question 1: Is the MetUM able to represent observed cloud phase and microphysics?

To avoid repetition, only results from case f152 are presented in answer to research question 1. Results are broadly similar for f150. During f152, while the MetUM successfully captures the presence of altostratus and lower stratocumulus layers, all four model configurations

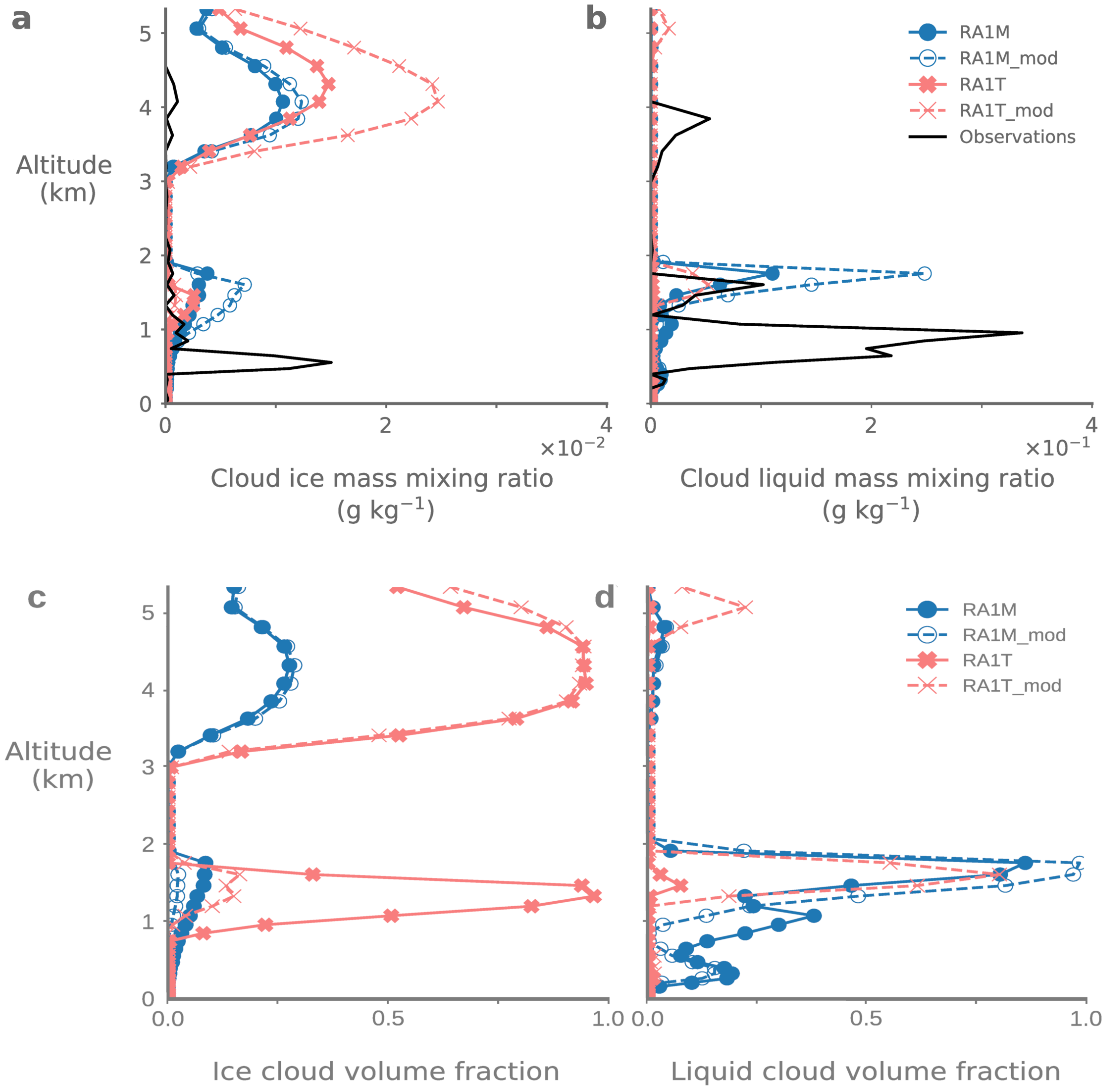

Figure 5.2.: Mean vertical profiles of cloud a) ice and b) liquid mass mixing ratios, in g kg^{-1}, and mean modelled cloud gridbox volume fractions of c) ice cloud and d) liquid cloud during f152 when the aircraft was sampling over Larsen C. Observations are shown in a) and b) with the solid black line and model output above AWS 14 is shown in all panels with coloured lines with markers. Solid lines with heavy markers indicate the two "base" configurations, while dashed lines with lighter markers show their modified counterparts. The experimental configurations are detailed in Table 5.1.

Table 5.2.: Mean observed surface energy fluxes, defined as in Equation 3.3, Chapter 3, and associated model biases of each experiment at AWS 14 during f152. All fluxes are given in W m^{-2}, and are abbreviated as in Chapter 3. Fluxes and biases are positive when directed towards the surface. The smallest biases are highlighted in bold text and standard deviations are given in brackets.

		Mean bias (W m^{-2})			
Flux	AWS 14 (observed)	RA1M	RA1M_mod	RA1T	RA1T_mod
$SW_{\downarrow}$	594.6 (76.2)	66.1 (12.6)	**30.3** (12.0)	195.4 (15.0)	114.8 (29.0)
$SW_{\uparrow}$	-501.3 (64.2)	-55.4 (8.7)	**-32.1** (8.7)	-135.1 (9.5)	-84.9 (18.5)
SW_{net}	93.2 (11.9)	10.7 (4.1)	**-1.8** (3.4)	60.3 (5.7)	30.0 (10.6)
$LW_{\downarrow}$	279.1 (12.2)	9.2 (3.0)	12.4 (1.6)	-41.1 (8.7)	**-5.1** (7.2)
$LW_{\uparrow}$	-315.6 (0.0)	0.3 (0.0)	**0.3** (0.0)	0.8 (0.1)	0.4 (0.1)
LW_{net}	-36.5 (12.2)	9.5 (3.0)	12.6 (0.0)	-40.3 (8.6)	**-4.7** (7.2)
H_S	-3.6 (3.5)	**-2.4** (0.6)	-3.5 (0.5)	-8.6 (0.4)	-6.6 (0.4)
H_L	-10.9 (8.1)	7.8 (1.3)	7.9 (1.5)	**1.4** (1.1)	6.2 (0.8)
E_{tot}	42.2 (12.5)	25.1 (3.0)	**13.2** (4.1)	15.3 (3.0)	23.4 (5.2)
E_{melt}	47.3 (9.5)	17.3 (5.1)	**6.1** (5.9)	9.6 (3.6)	16.5 (7.0)

simulate the lowest cloud layer around 1 km higher than is observed and produce just one layer below 2 km rather than the two indicated by the observations.

Figure 5.2a and b show that all model configurations (RA1M, RA1M_mod, RA1T and RA1T_mod) over-estimate ice mass mixing ratios, and under-estimate liquid mass mixing ratios above 2.5 km altitude, where virtually no liquid is present in any configuration. Ice cloud is concentrated in the upper layers (above ~3 km) because any supercooled liquid present is converted readily to ice below the ice nucleation temperature threshold of -18°C. At 4 km altitude, the largest positive bias in ice contents is in RA1T_mod, which produces an ice mass mixing ratio 22.7 times larger than observed, while RA1M shows the smallest bias (an over-estimate of 2.3 times compared to observations). All models except RA1T_mod produce negligible liquid mass mixing ratios above 4 km, although observed liquid mixing ratios reach 5.3×10^{-2} g kg^{-1} at 3.8 km. At lower altitudes modelled cloud generally contains less liquid and ice than observed. Between 1 and 2 km, ice mass mixing ratios in RA1M_mod peak at 7.2×10^{-3} g kg^{-1}, 1.9 times higher than RA1M, and 2.8 and 7.5 times larger than in RA1T and RA1T_mod, respectively. At the same heights, liquid mass mixing ratios peak in RA1M and RA1M_mod at 1.1×10^{-1} g kg^{-1} and 2.5×10^{-1} g kg^{-1}, respectively, and at 2.1×10^{-3} g kg^{-1} and 5.2×10^{-2} g kg^{-1} respectively in RA1T and RA1T_mod. Throughout the profile, ice mass mixing ratios are over-estimated (by between 1.7 times in RA1M and 5.1 times in RA1T_mod), while liquid mass mixing ratios are under-estimated (by 3.0 times in RA1M_mod to 64.9 times in RA1T) compared to observations. This is consistent with the results of Furtado et al. (2016) and Abel et al. (2017) who find that riming and vapour deposition occur too efficiently in modelled cold mixed-phase clouds, forming ice too readily at the expense of supercooled liquid.

RA1M simulates cloud ice and liquid mass mixing ratios that are closer to those observed than the tropical configuration, RA1T. RA1T produces little liquid cloud compared to observations, evident from Figure 5.2b, and compared to RA1M, shown in Figure 5.2b and d. Additionally, RA1T only simulates thin ice clouds over AWS 14. This is suggested by Figure 5.2c, which shows that ice cloud volume fraction reaches 100% at 1.2 km, and Figure 5.2a, which shows very low ice mass mixing ratios in this layer. Modelled "volume fractions" refer to the fraction of a gridbox occupied by cloud of each phase, and volume fractions in Figure 5.2c and d are shown as means for each model layer. Note that RA1T is designed for use in tropical, convective regions and is less suited to Antarctic conditions where convection is less vigorous, which may explain these differences.

Modifications to the "base" model configurations produce varying results. Observed liquid mass mixing ratios in the lowest simulated cloud layer peak at 3.4×10^{-1} g kg^{-1}. At 2.5×10^{-1} g kg^{-1}, RA1M_mod produces 2.3 times more liquid than RA1M in the lowest cloud layer, but the modifications to RA1M do not change its height, which is still approximately 1 km too high in RA1M_mod. RA1T_mod generates 1.7 times more cloud ice above 3 km than RA1T, but is the only configuration to simulate liquid at this height, as is observed (Figure 5.2d). Throughout the profile, it also produces almost ten times as much liquid than RA1T, but liquid mass mixing ratios in RA1T_mod are still around six times lower than in observations. Of all four experiments, RA1M_mod exhibits the lowest bias in liquid mass mixing ratios, while RA1M over-estimates ice mass mixing ratios by the smallest amount.

Water vapour mass mixing ratio is represented reasonably accurately (within 10-25% of observed values) in all experiments throughout the profile up to 2 km (Figure 5.3a). However, between 2 and 3.5 km, modelled water vapour mass mixing ratios are considerably lower than observed (by 63-65% at 2.6 km). This under-estimation of water vapour may be expected to negatively bias LW fluxes. However, all configurations are largely in agreement, so this effect should have the same effect on the SEB in all experiments. Similarly, all experiments show similar air temperature biases (Figure 5.3b), so these would not be expected to impact the formation of cloud differently between experiments.

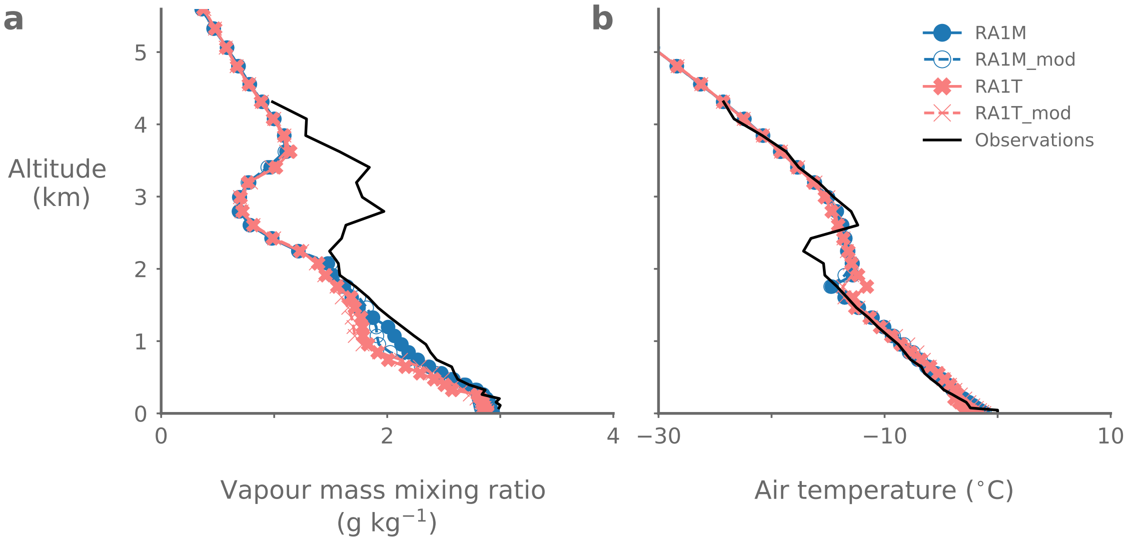

Figure 5.3.: As in Figure 5.2, observed and modelled vertical profiles of a) water vapour mass mixing ratio, in g kg^{-1}, and b) air temperature (in degrees celsius) during flight f152. Colours and markers are as indicated in Figure 5.2.

5.3.3 Research question 2: How does cloud phase influence the surface energy balance in observations and the MetUM?

Surface flux biases at AWS 14 for each model experiment during f152 are presented in Table 5.2. As in the previous section, biases are not shown for f150 to avoid repetition. E_{melt} is over-estimated by all configurations of the MetUM, but the bias is highest in RA1M at 17.3 W m^{-2}, causing modelled E_{melt} to be 37% too large compared to observations. Because the modelled and observed surface temperature are at melting point throughout the flight (not shown), this bias is solely driven by errors in the simulated surface fluxes. Additionally, the modelled surface albedo ($SW_{\uparrow}$ / $SW_{\downarrow}$) is within ± 2% of observed values in all simulations, suggesting that biases are driven almost entirely by downwelling radiative errors, and highlighting the importance of cloud phase in determining melt. SW_{net} is simulated better by RA1M and RA1M_mod, with the lowest bias produced by RA1M_mod (-1.8 W m^{-2}), while the smallest bias in LW_{net} (-4.7 W m^{-2}) is found in RA1T_mod. Both modified experiments produce lower SW flux biases than their respective "base" configurations, but RA1M produces smaller $LW_{\downarrow}$ and LW_{net} biases than RA1M_mod.

Between-experiment differences in downwelling fluxes are partly driven by the representation of cloud. Positive $SW_{\downarrow}$ biases in all experiments indicate that the simulated cloud is optically too thin in this part of the spectrum, thus allowing too much SW radiation to reach the surface (as also found by King et al., 2015). Conversely, over-estimated $LW_{\downarrow}$ indicates that the cloud is optically too thick in the infrared, which can be related to poorly simulated cloud liquid water content, temperature or altitude (Zhang et al., 1996). The lowest simulated cloud layer is approximately 1 km too high in all experiments, which would cause cloud base temperature to be lower than observed, while temperature profiles are represented well compared to observations (Figure 5.3b). A too-cold, too-high cloud base would be expected to contribute to negative LW$_\downarrow$ and LW$_{net}$ biases in all experiments, but this is only true of the two RA1T experiments, suggesting that other effects, such as biases in parameterised cloud particle size, influence biases in RA1M and RA1M_mod. RA1T_mod exhibits the smallest LW$_\downarrow$ bias, while RA1T has the largest. LW$_\downarrow$ biases are positive in the two RA1M experiments, and negative in the RA1T experiments, although LW$_\downarrow$ and LW$_\uparrow$ biases are both comparatively small in RA1T_mod. Positive LW$_\downarrow$ biases in RA1M and RA1M_mod are also likely a result of errors in simulated cloud phase, which are only partly offset by negative water vapour biases (Figure 5.3). Thick ice clouds can have a significant LW warming effect (Miller et al., 2015), so although water vapour and liquid contents - usually the dominant component of cloud LW radiative forcing – are under-estimated, the considerable over-estimation of ice contents at altitudes above 3 km likely explains this positive bias.

The RA1T experiment produces quite different cloud profiles, and consequently SEB biases, to the other three simulations. As shown in Figure 5.2, RA1T produces comparatively low liquid cloud fractions and liquid mass mixing ratios throughout the cloud profile, which likely explains the negative LW$_\downarrow$ (-41.13 W m^{-2}) and extremely positive SW$_\downarrow$ (195.38 W m^{-2}) biases shown in Table 5.2. The amount of SW radiation transmitted through ice clouds is relatively insensitive to ice cloud thickness (Miller et al., 2015), which means that although RA1T simulates an ice cloud gridbox volume fraction of 100% in two layers (5.2c and d), this has a limited effect on surface SW$_\downarrow$ because SW radiation can still reach the surface. RA1T produces a melt flux bias comparable to RA1M_mod because its large LW and SW biases cancel and biases in the turbulent fluxes are relatively minor.

RA1T_mod has the smallest (negative) LW$_\downarrow$ bias, but this may be due to errors in simulated cloud phase. An accompanying positive SW$_\downarrow$ bias indicates that too little (liquid) cloud is simulated (also suggested by the low liquid water contents and volume fractions in Figure 5.2), which would usually be associated with a large negative LW$_\downarrow$ bias. However, liquid cloud occupies up to 80% of the gridbox in the lowest layer, despite the liquid water contents being far too low, suggesting that the layer is extremely thin in RA1T_mod. Optically thin liquid clouds have been shown to cause greater warming than thicker liquid clouds in summer over the Greenland ice sheet because they are thin enough to allow SW radiation to penetrate, but thick, low and warm enough to radiate strongly in the infrared (Bennartz et al., 2013).

Overall, RA1M_mod is considered to be the best-performing single-moment configuration with respect to cloud and SEB properties. Erroneous cloud fields and large cancelling radiative flux errors remove RA1T and RA1T_mod from consideration. RA1M and RA1M_mod have comparable LW_{net} biases, and although cancelling $SW_{\downarrow}$ and $SW_{\uparrow}$ errors exist in both, these are smaller in RA1M_mod, which over-estimates $SW_{\downarrow}$ by just 5%. Further, RA1M_mod's E_{tot} and E_{melt} biases are the smallest of all configurations.

5.3.4 Research question 3: Can a double moment microphysics scheme improve simulations of cloud phase?

Several studies suggest that more sophisticated formulations of model microphysics can improve the representation of polar cloud phase and consequently SEB (e.g. Klein et al. (2009) in the Arctic; Listowski and Lachlan-Cope (2017); Hines et al. (2019) in the West Antarctic). RA1M_mod simulations of cases f152 and f150 are therefore compared to several experiments (shown in Table 5.1) using the MetUM's multi-moment microphysics scheme, CASIM, with varying ice nucleation schemes, plus an experiment with ice processes switched off ("no ice") and for f150 only, another with modified critical relative humidity ("RH_{crit} = 0.85"). Double-moment results from case f152 are presented for comparison with results shown in section 5.3.2, while results from f150 are evaluated to determine the MetUM's ability to simulate mixed-phase cloud with relatively higher liquid and lower ice contents. Each experiment is based on RA1M_mod physics for comparability, and all are summarised in Table 5.1. This section addresses the third research question with these experiments.

Double-moment model representation of case f152

Case f152 is simulated with three double-moment configurations (Cooper, DeMott2010 and no ice), which are summarised in Table 5.1. These are compared with profiles from RA1M_mod to determine how well they perform in relation to the improved single-moment configuration. Figure 5.4 shows mean vertical profiles of ice and liquid mass mixing ratio, as in Figure 5.2, with these four configurations. All three double-moment configurations perform poorly compared to observations, and worse than RA1M_mod. Cooper over-estimates ice mass mixing ratios above 3 km similarly to RA1M_mod, with the layer displaced slightly lower. Ice mass mixing ratios at this altitude are too large in Cooper by a median of 15.2 times, while RA1M_mod over-estimates by a median of 14.9 times. DeMott2010 reproduces observed ice mass mixing ratios above 3 km best, over-estimating the peak ice mass mixing ratio at 4.1 km of 1.09×10^{-3} g kg^{-1} by only 12%. By definition, the no ice configuration contains no ice throughout the profile, and neither Cooper nor DeMott2010 contain any ice below 2.5 km. All double-moment configurations produce virtually no liquid water throughout the profile, completely failing to simulate the observed peaks in liquid mass mixing ratios between 1 and 2 km altitude, and what liquid there is is confined to the lowest 150 m of the profile. The maximum liquid mass mixing ratios produced are 3.4×10^{-2} g kg^{-1}, 3.0×10^{-2} g kg^{-1} and 1.5×10^{-3} g kg^{-1} for DeMott2010, Cooper and no ice, respectively. All three under-estimate the amount of liquid in the profile by one or two orders of magnitude, and also considerably under-estimate cloud ice mass mixing ratios compared to observations. Overall, the double-moment experiments simulate f152 poorly, with DeMott2010 slightly out-performing Cooper and no ice. Inspection of time series of ice and liquid water paths (Figure 5.5a) reveals that cloud forms approximately five hours before the time of f152 in all model experiments listed in Table 5.1, with liquid converted steadily to ice as the cloud begins to glaciate, precipitate and dissipate. However, the rate at which the cloud dissipates varies between experiments (not shown). RA1M_mod glaciates less quickly, consistent with a slower rate of conversion of liquid to ice via vapour deposition, which prolongs the lifetime of modelled cloud.

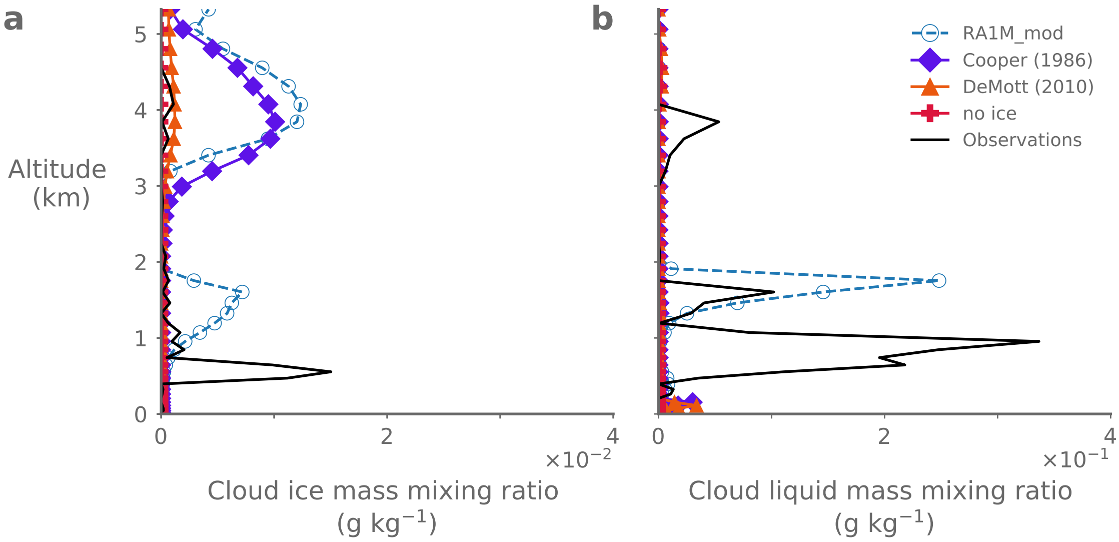

Figure 5.4.: As in Figure 5.2, but showing mean vertical profiles of cloud ice and liquid mass mixing ratios from double-moment experiments using CASIM (Cooper, DeMott2010 and no ice) during f152.

Double-moment model representation of case f150

As noted previously, the aircraft sampled predominantly liquid-bearing clouds in case f150. It has been demonstrated that the conversion of ice to liquid is a consistent problem in the configurations tested, particularly in double-moment configurations. This section evaluates model representation of cloud during a case with relatively lower ice and higher liquid mass mixing ratios than f152, to explore whether mass mixing ratio biases are related to over-active ice formation or the representation of cloud overall. Case f150 is simulated with the RA1M_mod, Cooper, DeMott2010 and no ice configurations detailed above, plus the DeMott2015 and RH$_{crit}$ = 0.85 experiments also detailed in Table 5.1. Initial tests showed that the DeMott2010 and DeMott2015 results were indistinguishable, so for the remainder of this section, only results from the DeMott2010 experiment are shown.

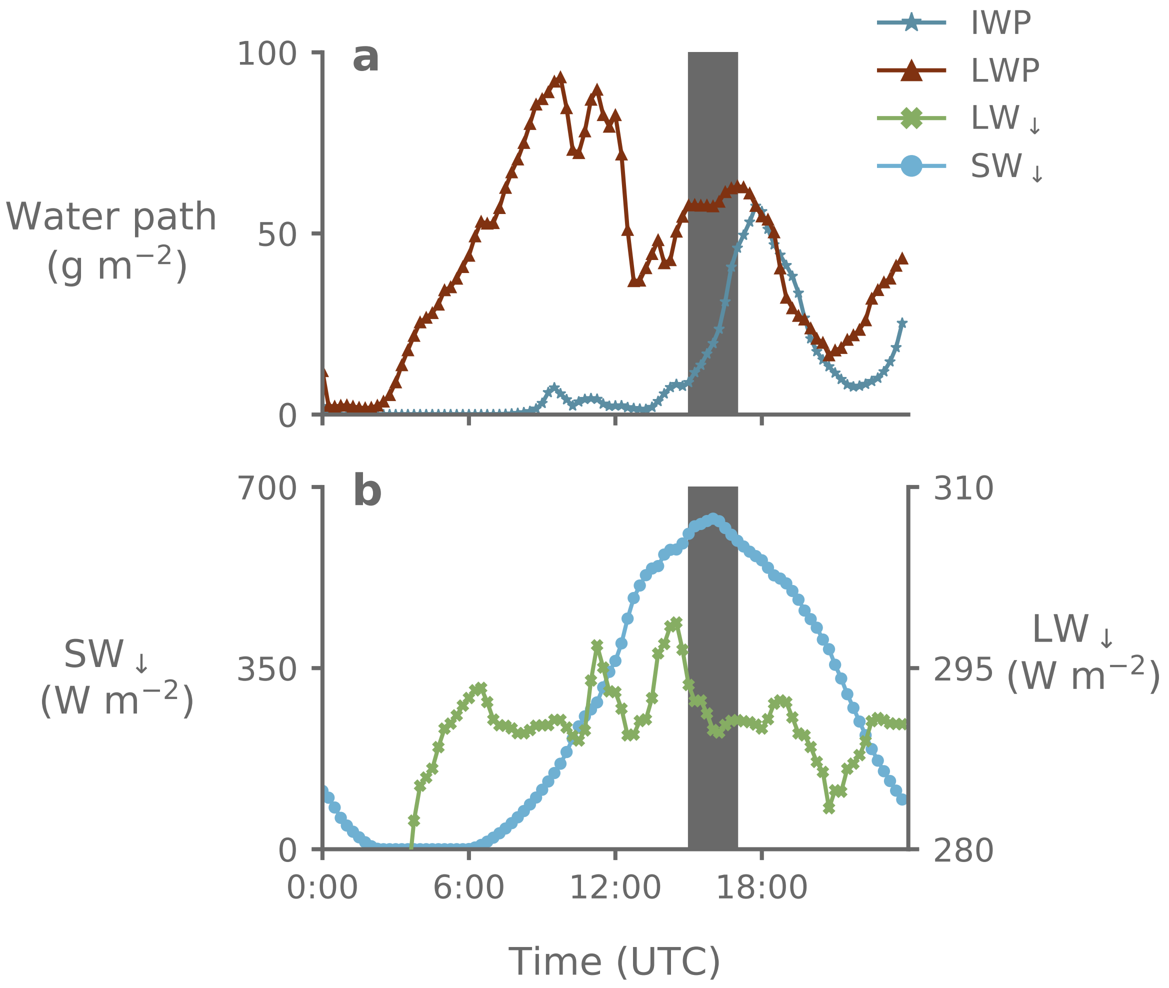

Figure 5.5.: Time series of modelled ice and liquid water paths, plus downwelling LW and SW radiation over AWS 14 during f152 on 18 January 2011 in RA1M_mod. Panel a) shows mean modelled ice (IWP) and liquid (LWP) water paths, both in g m^{-2}, and indicated with the blue line with starred markers, and brown line with triangle markers, respectively. Panel b) shows downwelling LW and SW radiation (LW$_{\downarrow}$ and SW$_{\downarrow}$, respectively, both in W m^{-2}) and indicated with the green line with crossed markers and blue line with circle markers, respectively. The approximate time during which the aircraft was sampling over Larsen C is indicated with the grey shading.

Figure 5.6 shows transects of in-cloud liquid mean mass mixing ratios during f150 along a line of constant latitude (approximately 67.0°S). Ice mass mixing ratios are not examined because they are not the focus of this section, and are low throughout the transect (observed mean values of 4.1 $\times$ 10^{-5} g kg^{-1}). The aircraft conducted longitudinal transects during f150, predominantly sampling low-level stratiform cloud with liquid mass mixing ratios of up to 1.3 $\times$ 10^{-1} g kg^{-1} and cloud droplet number concentrations of up to 469.2 cm^{-3}. The black line

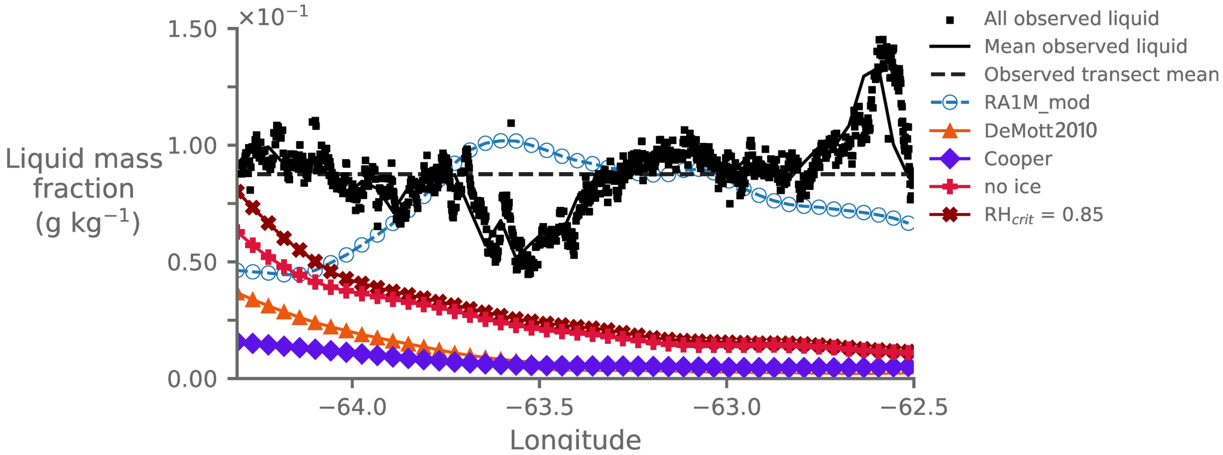

Figure 5.6.: Mean longitudinal transects (at ∼67.0°S) of in-cloud liquid mass mixing ratios, in g kg^{-1}, during f150 when the aircraft was sampling over Larsen C. Observations are shown in turquoise, with individual data points indicated with square markers and the transect mean given with the solid line. The total in-cloud observed mean liquid mass mixing ratio for the entire flight is shown as a dashed black line. Other coloured lines indicate the various experiments examined during f150: RA1M_mod, Cooper, DeMott2010, no ice and RH$_{crit}$ = 0.85 (details in Table 5.1).

and data points show that observed cloud liquid water contents mostly ranged between 5.0 $\times$ 10^{-2} g kg^{-1} and 1.5 $\times$ 10^{-1} g kg^{-1}, peaking at around 62.5°W, and with a minimum at 63.5°W, and a mean value of 8.8 $\times$10^{-2} g kg^{-1}. All double-moment experiments simulate liquid mass mixing ratios lower than observed, and exhibit a decline in liquid contents with increasing distance from the peninsula mountains that is not observed. The only experiment to successfully simulate the magnitude of liquid contents is RA1M_mod, which simulates mean in-cloud mass mixing ratios of up to 1.0 $\times$ 10^{-1} g kg^{-1}, peaking at 63.7°W, and a transect-mean in-cloud mass mixing ratio of 7.3 $\times$ 10^{-2} g kg^{-1}, an under-estimate of 17%. Although RA1M_mod simulates the peak in liquid water contents in a different location to the observed peak, this could be an artefact of the sampling strategy or due to the evolution of the observed cloud (which began to glaciate during the flight, not shown). Model transect-mean liquid mass mixing ratios in RA1M_mod are 2.9 times higher than the 2.5 $\times$ 10^{-2} g kg^{-1} simulated by RH$_{crit}$ = 0.85, the experiment with the next-highest liquid contents, and 10.8 times higher than the 6.7 $\times$ 10^{-3} g kg^{-1} simulated by Cooper, with the lowest liquid water contents.

The demonstrated failure of double moment experiments to represent cloud phase in cases f150 and f152 may be related to the aerosol inputs to CASIM, which parameterise the availability of CCN and INP, but it is beyond the scope of this chapter to investigate this further. The large errors in cloud phase shown above result in wildly inaccurate surface fluxes (not

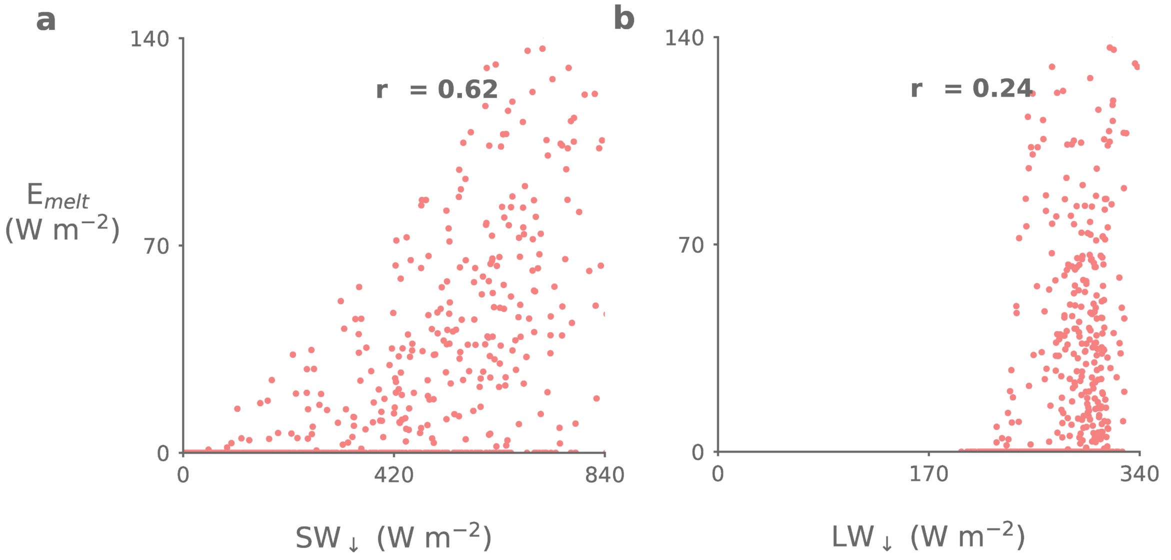

Figure 5.7.: Scatterplots of observed energy available for melting (E_{melt}) against a) downwelling shortwave ($SW_{\downarrow}$) and b) downwelling longwave ($LW_{\downarrow}$) at AWS 14. Data plotted are instantaneous values outputted at 30-minute intervals. Pearson correlation coefficients, significant at the 99% level, are given at top centre of each panel.

shown) that offer limited insight into processes on Larsen C. Consequently, the remainder of the chapter focuses on RA1M_mod, which was used to run a five-week simulation of the OFCAP period for a third evaluation of simulation quality.

Table 5.3.: Pearson correlation coefficients between cloud cover (CC), downwelling longwave ($LW_{\downarrow}$) and shortwave fluxes ($SW_{\downarrow}$), and melt flux (E_{melt}), at AWS 14 during 1 January – 7 February 2011. Correlation coefficients between observed components are shown in columns one to four, while modelled coefficients are given in columns five to eight. Correlation coefficients in bold text are significant at the 99% level.

	Observed correlations				**Modelled correlations**			
	CC	$LW_{\downarrow}$	$SW_{\downarrow}$	E_{melt}	CC	$LW_{\downarrow}$	$SW_{\downarrow}$	E_{melt}
CC	1.00		**-0.19**	**0.12**	1.00	**0.87**	**-0.14**	**0.05**
$LW_{\downarrow}$		1.00		**0.24**		1.00		**0.15**
$SW_{\downarrow}$			1.00	**0.62**			1.00	**0.65**
E_{melt}				1.00				1.00

5.3.5 Research question 4: How does summertime cloud phase influence the surface energy balance during the entire OFCAP period?

Sections 5.3.2 and 5.3.3 showed that errors in modelled cloud phase contribute to errors in modelled downwelling fluxes during case f152. However, single case studies may not be representative of mean summertime conditions on Larsen C, so conditions during the entire five-week OFCAP period (1 January – 7 February 2011) are simulated. Because there are very few aircraft observations over Larsen C of cloud properties during this period, comparison of cloud microphysics is not possible for OFCAP. Downwelling radiation fluxes and biases are therefore used to infer information about cloud phase in observations, and Pearson correlation coefficients are used to understand relationships between melting and observed or modelled fluxes.

Table 5.4.: Mean observed surface energy fluxes at AWS 14 ("AWS 14 (observed)") and mean model biases of the RA1M_mod simulation of the OFCAP period ("Mean bias"), as in Table 5.2. Mean biases reported by King et al. (2015) are given in the third column ("King et al. (2015) bias", and mean biases, RMSEs and Pearson correlation coefficients of the RA1M_mod OFCAP simulation are given in columns four to six, respectively. As in Table 5.2, the smallest biases are highlighted in bold, and fluxes and biases are positive when directed towards the surface.

			RA1M_mod			
Flux	AWS 14 (observed)	King et al. (2015) bias	Mean bias	RMSE	Correlation coefficient	Standard deviation
SW$_{\downarrow}$	277.9	-31.6	**-21.0**	105.0	0.91	12.0
SW$_{\uparrow}$	-232.7	41.0	**12.8**	87.8	0.91	8.7
SW$_{net}$	45.2	9.4	**-8.2**	24.9	0.9	3.4
LW$_{\downarrow}$	280.1	-7.0	**-0.3**	33.0	0.49	1.63
LW$_{\uparrow}$	-303.9	-2.0	**1.2**	14.1	0.63	0.0
LW$_{net}$	-23.8	-6.3	**0.8**	25.7	0.47	1.6
H$_{L}$	-5.1	**1.9**	4.6	8.7	0.71	0.5
H$_{S}$	-9.3	**5.9**	6.4	11.5	0.48	1.5
E$_{tot}$	-1.4	**10.5**	12.0	31.7	0.78	4.1
E$_{melt}$	13.5	7.6	**-1.7**	16.3	0.82	5.9

Table 5.3 and Figure 5.7 show positive correlations (significant at the 99% level) at AWS 14 between observed E$_{melt}$ and SW$_{\downarrow}$ ($r_{SW,melt}$ = 0.62) and LW$_{\downarrow}$ ($r_{LW,melt}$ = 0.24). This indicates that surface melt is most likely to occur when more SW radiation can reach the surface, but is also weakly associated with higher LW$_{\downarrow}$, which is strongly related to liquid water contents, especially at the relatively low liquid water paths ($<$ 40 g m^{-2}) typical of Antarctic clouds

(Grosvenor et al., 2017) and shown in f150 and f152. Observed E_{melt} is not strongly related to cloud cover ($r_{CC,melt}$ = 0.12), where "cloud cover" is defined as the portion of the sky above AWS 14 occupied by cloud, and the negative correlation between $SW_{\downarrow}$ and cloud cover shows that $SW_{\downarrow}$ is highest during clear conditions ($r_{CC,SW}$ = -0.19), which occur 11.5% of the time (defining "clear" as having cloud cover $<$ 0.31, as in Kay et al., 2008). Observed cloud cover is not compared with $LW_{\downarrow}$ because it is computed from the closure of the LW radiation budget using the energy balance model of Kuipers Munneke et al. (2009) and so is not independent.

Modelled relationships between radiative fluxes and E_{melt} (Table 5.3) compare well with observations, suggesting that the model is able to reproduce the observed drivers of surface melting. For example, modelled E_{melt} is positively correlated with $SW_{\downarrow}$ ($r_{SW,melt}$ = 0.65) and to a much lesser extent, $LW_{\downarrow}$ ($r_{LW,melt}$ = 0.15). Additionally, the large and significant (at the 99% level) correlation between modelled cloud cover and $LW_{\downarrow}$ ($r_{CC,LW}$ = 0.87) suggests that cloud cover affects LW fluxes most strongly in the MetUM. This is mostly due to the contribution of liquid clouds – the correlation between $LW_{\downarrow}$ and liquid water path is much higher ($r_{LWP,LW}$ = 0.63) than with ice water path ($r_{IWP,LW}$ = 0.21) (not shown). Moreover, modelled melting during OFCAP usually follows cloudy periods, during which liquid and then ice water paths increase and then rapidly decline as cloud glaciates and dissipates (as is shown for f152 in Figure 5.5). Higher modelled cloud cover (and especially clouds with high liquid water contents) increases $LW_{\downarrow}$ relative to clear-sky conditions, which can begin to increase surface temperature and E_{tot}. Melting first begins as $LW_{\downarrow}$ increases, but is then sustained as the cloud glaciates and more SW radiation can reach the surface. This process is partly illustrated for f152 in Figure 5.5, but the timing of the flight means that $SW_{\downarrow}$ begins to decline as the day progresses. This time-evolving process may partly explain the relatively low modelled correlations with E_{melt} of cloud cover and downwelling fluxes.

Biases in modelled SEB terms during the OFCAP period (Table 5.4) are broadly similar to those during f152 (Table 5.2). As in f152, OFCAP SW_{net} is negatively biased, but not for the same reasons. Whereas during f152 $SW_{\downarrow}$ is positively biased, during OFCAP it is negatively biased, indicating that cloud is optically too thick in the SW part of the spectrum during the OFCAP period, consistent with King et al. (2015). As shown in Table 5.4, mean OFCAP LW biases are all $\sim$1 W m^{-2} in magnitude, but $LW_{\downarrow}$ (and consequently LW_{net}) shows a poor correlation with observations, indicating that the model struggles to represent (liquid) clouds, atmospheric water vapour contents and/or that clouds are simulated at the wrong time. As previously noted, this may be because the model is unable to capture the exact timing of cloud formation, glaciation and dissipation. OFCAP LW biases are consistent with results from the case study, which indicates that the MetUM represents some cloud properties poorly. For example, errors in simulated cloud base height may explain the poor correlation during OFCAP with observed $LW_{\downarrow}$, as seen for the f152 case, when the MetUM-simulated cloud base was 1 km too high. The OFCAP E_{tot} and E_{melt} biases are smaller than during f152 (12.0 W m^{-2} and -1.7 W m^{-2} compared to 13.2 W m^{-2} and 6.1 W m^{-2}, respectively, in f152. OFCAP E_{melt} is under-estimated, whereas E_{melt} is over-estimated during f152.

King et al. (2015) validated the SEB over Larsen C during the OFCAP period in three regional climate models, including an earlier version of the MetUM, largely similar to the (unmodified) RA1M configuration. As noted in Chapter 2, they concluded that cloud microphysics, and likely cloud phase, were responsible for SEB biases. The MetUM model configuration used by King et al. contained the same dynamical core as the version in this chapter, but numerous incremental improvements have been implemented since. Additionally, King et al. used a model domain at 4 km resolution, compared to 1.5 km in this chapter. As shown in Table 5.4, modelled radiative biases during OFCAP are mostly of the same sign as King et al. (2015), but smaller in magnitude, suggesting that physics updates, higher resolution, and modifications applied in this chapter have improved the representation of cloud microphysics, and consequently surface energy fluxes.

The OFCAP E_{melt} bias is smaller than in King et al. (2015) (-1.7 W m^{-2} compared to 7.6 W m^{-2}, an under-estimate of just 12%), but of the opposite sign. This results in a 13% under-estimate of cumulative meltwater production throughout OFCAP, at 114 mm w.e.. King et al. (2015) found that the MetUM over-predicts the occurrence of melt, despite a cold bias that is particularly present at high latitudes where conditions are more stable (Lock, 2011). Although the OFCAP simulation also produces a small mean cold bias (-0.27°C), and exhibits considerable negative biases in surface temperature during night-time (Figure 5.8), it represents melt frequency well because errors in modelled surface temperature are mostly when it is already well below the melting point (Figure 5.8). For example, observed melting occurs 29.5% of the time during OFCAP, while the model simulates melting 33% of the time (Figure 5.9). E_{melt} biases are therefore smaller than E_{tot} biases because melt occurs only when the surface temperature is at melting point. Remaining model biases, for instance in the turbulent fluxes, may be explained by other sources of error, such as the land surface or boundary layer schemes.

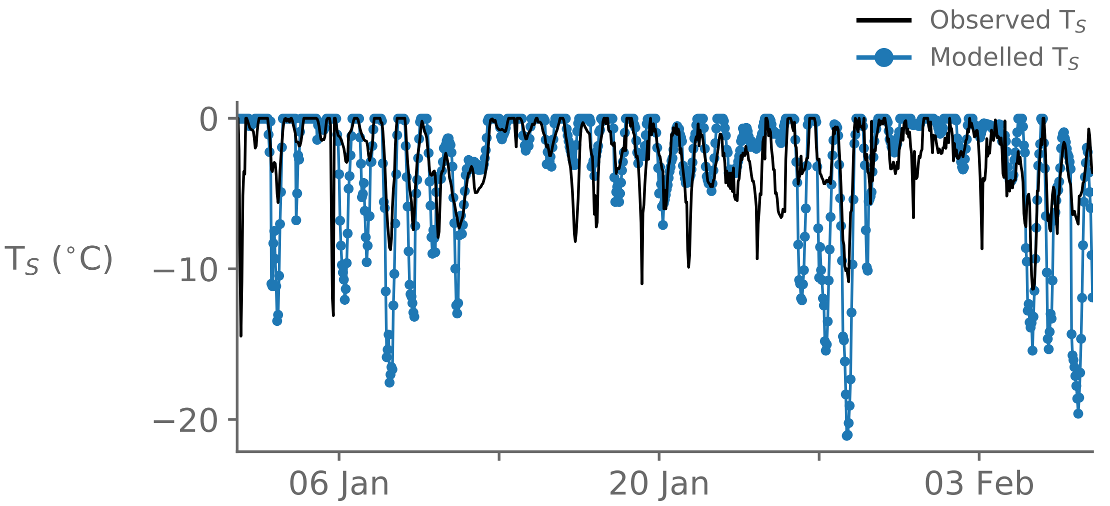

Figure 5.8.: Mean surface temperature, T_S during the OFCAP period in observations (black) and as modelled by the RA1M_mod simulation (blue, with circle markers).

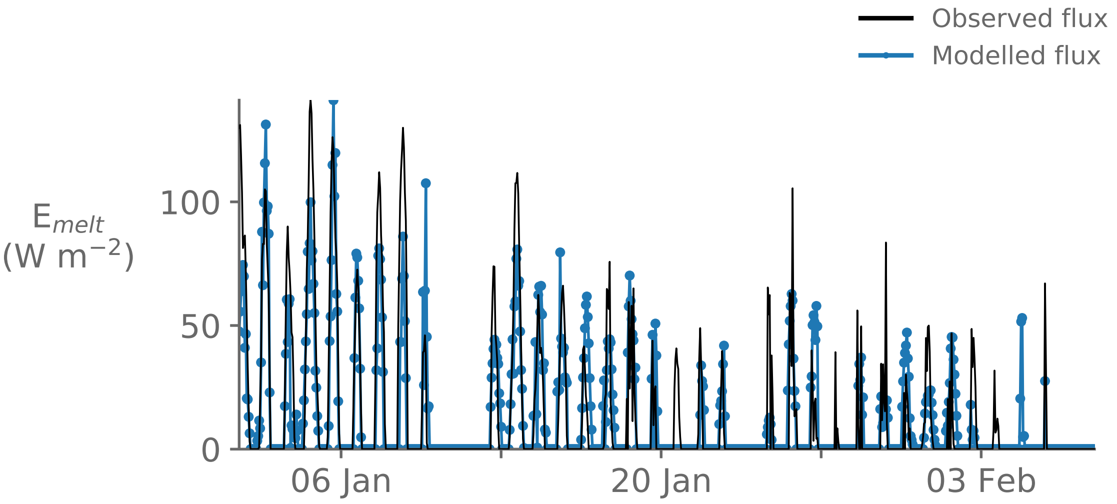

Figure 5.9.: As in Figure 5.8, but for mean modelled melt flux, E_{melt}, during the OFCAP period.

5.3.6 Summary of optimisations to the MetUM to better represent summertime mixed phase cloud and surface energy balance over Larsen C

Sections 5.3.2 to 5.3.5 have demonstrated, by testing the representation of summertime cloud microphysics and SEB in numerous model configurations, that the MetUM can be optimised to represent summertime mixed phase clouds and the SEB over Larsen C more accurately. Modifications proposed by Abel et al. (2017) and Furtado et al. (2016) reduced errors in simulated cloud phase and surface fluxes in two case studies, consistent with published results. However, contrary to the findings of Listowski and Lachlan-Cope (2017) and Hines et al. (2019) using WRF, the use of more sophisticated microphysics parameterisations did not improve the simulation of cloud phase in the MetUM during f152 or f150. This suggests that the implementation of CASIM in the MetUM requires further development before it is widely used for the Antarctic Peninsula. During OFCAP, the optimised RA1M_mod is shown to lessen SEB biases relative to previously published results using the MetUM.

5.4 Summary and conclusions

This chapter has demonstrated that summertime cloud phase strongly influences the SEB of Larsen C in observations and model output. An optimum MetUM configuration, RA1M_mod, is identified, which produces much better simulations of melt at AWS 14 during two case studies and the OFCAP period than the present default configurations and previous model versions. Because surface fluxes at AWS 14 are representative of a wider area (King et al., 2015) and the large-scale meteorological forcing producing cloud is similar across the ice shelf, these improvements will likely be seen across the whole of Larsen C. RA1M_mod uses single-moment microphysics and is based on the MetUM's mid-latitude regional atmosphere package, including modifications proposed by Furtado and Field (2017) and Abel et al. (2017). The quality of simulations using RA1M_mod was consistently higher than with double-moment configurations, in contrast to previous findings. This may be due to the aerosol data used as input to CASIM, which is derived from mid-latitude observations and may not be representative of the pristine Antarctic environment, although further investigation of the limitations of CASIM is beyond the scope of this thesis. The adaptations to improve simulated cloud phase applied in RA1M_mod have wider applications for other regional models and in other regions of Antarctica.

Visual inspection of vertical cloud profiles during case study f152 suggests that RA1M_mod reproduces the observed cloud vertical structure most closely. All single-moment model configurations over-estimate ice concentrations in a mid-level Altostratus layer (between ~3-5 km) and under-estimate liquid concentrations throughout the atmosphere, although this is especially visible at lower levels (below ~2 km). RA1M_mod produces the second lowest ice mass mixing ratios above 3 km and twice as much liquid as the next-best configuration in a lower cloud layer, bringing the modelled cloud liquid mass mixing ratio closer to observed values. Mean profile-integrated mass mixing ratios of liquid and ice in RA1M_mod are 2.8 and 2.3 times lower and higher, respectively, than observed.

The RA1M setup likely outperforms the RA1T configurations because it has been more extensively developed, and is designed for use in colder mid-latitude conditions that are more comparable to those observed in the Antarctic, and because it is based on the Smith (1990a) large-scale cloud scheme, which has been more extensively modified and tested than the prognostic PC2 scheme on which RA1T is based. RA1T probably requires further development if it is to be suitable for simulating the Antarctic environment. Additionally, the superior performance of RA1M_mod over the basic RA1M setup supports the findings of previous work that modifications to increase the amount of liquid and limit its conversion to ice improve the representation of cold mixed-phase clouds (Furtado and Field, 2017; Abel et al., 2017).

Double-moment configurations consistently produce too little ice and liquid throughout the profile in f152, with the best-performing configuration, DeMott2010, producing 4.9 and 16.8 times too little ice and liquid, respectively. By improving the MetUM's representation of cloud phase in f152, RA1M_mod restricts biases in downwelling radiative fluxes to around 5% of their observed values. The resultant net radiation bias of 10.8 W m^{-2} is almost half that of 20.2 W m^{-2} produced by the default RA1M configuration.

RA1M_mod performed better when simulating a case (f150) where observed clouds contained relatively more liquid water, representing cloud liquid water mass mixing ratios to within 17% of observed values. This suggests that the parameterisation of ice microphysics is still a large source of error in simulated cloud and SEB terms. Comparison of transects simulated by RA1M_mod and several experiments using the double-moment CASIM microphysics show that RA1M_mod out-performed all CASIM-based experiments. RA1M_mod produces 2.9 and 6.1 times more liquid water in cases f150 and f152, respectively, than the next-best simulation. The poor performance of CASIM-based experiments suggests that further development is required before it can be widely used in Antarctica. Future research should focus on ice microphysics and the aerosol inputs used to parameterise the availability of CCN and INP in CASIM, which may not be representative of Antarctic conditions.

During the whole OFCAP period, only the model's representation of surface fluxes was evaluated because continuous observations of cloud properties were not available. Cloud phase is shown to be important for mediating the onset and evolution of melting via its relationships with downwelling fluxes. Enhanced $LW_{\downarrow}$ associated with increased cloud cover and particularly liquid water contents raises T_S and initiates surface melting. As the cloud develops and glaciates, $SW_{\downarrow}$ increases and sustains melting. Biases in downwelling radiative fluxes during the OFCAP period were less than 8% of their observed values, which produced a net radiation bias of -7.3 W m^{-2} (11%). RA1M_mod is able to simulate the occurrence and magnitude of summertime surface melt better than the versions of the MetUM used in previous studies, such as King et al. (2015), which used the default Smith (1990a) large-scale cloud scheme without the modifications noted here. Over the entire OFCAP period, a mean bias of -1.7 W m^{-2} (-12%) is found in modelled melt flux at AWS 14, which represents a four-fold reduction on the bias of 7.6 W m^{-2} (+56%) reported by King et al. (2015). Despite this improvement, further developments in the representation of cloud phase are evidently still needed to reduce summertime biases in melt. Observed cumulative meltwater production of 114 mm w.e. during the OFCAP period is still underestimated by 13% due to errors in the modelled SEB. Biases of 4.6 W m^{-2} and 6.4 W m^{-2} in the latent and sensible heat fluxes, respectively, account for a large proportion of the overall biases in E_{tot} and are greater than those shown in King et al. (2015). Remaining sources of error likely include model schemes beyond the scope of this thesis, such as the land surface, snow or boundary layer schemes. The snow scheme is important for determining the ground heat flux, which is poorly represented during OFCAP (see Appendix C for details).

The following chapter presents results from a 20-year model hindcast to examine the role of foehn winds and cloud on the SEB and surface melting between 1998-2017.

6

Simulated surface melting on Larsen C in a 20-year hindcast of the Antarctic Peninsula

6.1 Introduction

6.1.1 Aims and objectives

This chapter aims to synthesise and build upon work from the preceding two results chapters (Chapters 4 and 5) and published studies to determine which conditions and atmospheric phenomena are responsible for causing surface melting on Larsen C. The effect of foehn winds, large-scale meteorology and cloud on the surface energy balance (SEB) will be evaluated to provide a comprehensive understanding of surface melting on the ice shelf.

An optimised configuration of the MetUM is used to run a high-resolution hindcast of the period 1998-2017. This configuration has been shown in Chapter 5 and Gilbert et al. (2020) to improve the representation of cloud and the SEB over Larsen C. The 20-year hindcast, with 4.0 km horizontal grid spacing (demonstrated in Chapter 4 to be sufficient to resolve foehn winds) and outputted at 3-hourly temporal resolution, is the highest resolution multi-year model dataset of the Antarctic Peninsula region to date, and includes a comprehensive list of variables to examine the role of various atmospheric features on the SEB and surface melt.

6.1.2 Research Questions

As outlined in Chapter 1, this chapter will evaluate the key atmospheric processes contributing to melting on Larsen C by answering the following research questions:

1. How does the SEB of Larsen C vary throughout the year?

a) How do surface fluxes and the mean SEB change between seasons?

2. How does cloud influence surface melting on Larsen C?

a) Can certain cloud types/conditions be related to specific SEB regimes/melting?

b) Does cloud phase influence the amount of melt?

3. Where and when do foehn events occur?

a) How frequently do foehn events occur?

b) Are there patterns in their occurrence (e.g. seasonal)?

c) How does this compare with published work?

4. Where and when does the most surface melting occur?

a) Does this match with satellite observations and previously published work?

b) How variable is melt spatially and temporally?

5. What is the current modelled ice shelf-integrated surface melt rate?

a) Are there seasonal patterns or trends?

b) What might be the effect on Larsen C's stability?

6. What are the most important drivers of surface melting on Larsen C?

a) Where does foehn exert the strongest influence on melting? Where is the correlation strongest between foehn occurrence and melt?

b) How do synoptic meteorology and large-scale circulation interact with the local weather and climate?

c) Are there specific conditions that enhance or dampen melt?

6.1.3 Novelty of research

Although some studies have been published on individual drivers of melt, no work has attempted to assess the relative roles of these different elements (e.g. cloud, foehn, large-scale meteorology) on melting together. Additionally, there has not been a thorough assessment of the effect of these drivers of melting on the SEB, i.e. how they contribute to melting. For example, several studies have assessed spatial and temporal patterns of melt over the ice shelf (e.g. Luckman et al. (2014) and Bevan et al. (2018) using satellite data; Hubbard et al. (2016) using borehole data; Kuipers Munneke et al. (2017) using snow stake records and radar data; Bevan et al. (2017) using firn models; Holland et al. (2011) using airborne geophysical surveys) and many have suggested atmospheric causes for observed patterns, but none have quantified this.

Similarly, many studies have looked at atmospheric conditions on Larsen C, but have not directly linked these to surface melting. For instance, Kuipers Munneke et al. (2012) evaluated the weather and climate of Larsen C with two years of observational data at AWS 14 and 15, though they caution against considering this a climatology due to the limited dataset used. van Wessem et al. (2018) produced a near-surface climatology using RACMO at 5.5 km resolution, but this dataset includes only temperature and wind speed and RACMO is a hydrostatic model, which may not be capable of adequately resolving foehn winds, especially at 5.5 km resolution. Wiesenekker et al. (2018) diagnose foehn wind occurrence between 1979-2016 at Cabinet Inlet, close to the foot of the mountains, from observations and RACMO model data, but do not relate this to the SEB. King et al. (2015) comprehensively evaluate three models' ability to reproduce observed meteorology and SEB during summer 2010/11, but the period is short – just one month. Similarly, Elvidge et al. (2020) use the MetUM at 1.5 km resolution to assess the role of various SEB regimes in driving melting on Larsen C during a six-month period, which includes a thorough investigation of the role of different types of foehn and the conditions that produce these. However, this study is also limited in its duration. Another relevant recent study is Datta et al. (2019), who use the MAR model at 7.5 km resolution to produce a climatology of an overlapping time period (1982-2017). They use this climatology to evaluate the effect of foehn events on surface melting of the ice shelf, and hence the evolution of the snowpack. Combining model output with satellite data, they find three regimes in which surface melting occurs, related to foehn winds and cloud occurrence. However, the focus of their study is on the evolution of firn and the snowpack, rather than quantifying the atmospheric processes that produce various SEB regimes and surface melting, which is the objective of this chapter.

Models have been increasingly used in recent years to assess melting on Larsen C. However, most struggle to reproduce observed patterns of melting. Luckman et al. (2014) and Bevan et al. (2018) used satellite measurements to show that annual meltwater production on Larsen C is highest in the north, where temperatures are closer to the melting point, and in inlets close to the mountains, where foehn winds are most intense and frequent. These patterns are also seen in borehole and air content measurements that indicate firn densification in inlets (Hubbard et al., 2016; Bevan et al., 2017; Holland et al., 2011). Many models successfully simulate the temperature and radiation-driven north-south gradient in melting, but most are unable to reproduce the east-west gradient in melt associated with foehn winds. This is largely a result of the modelling techniques used, which have been at insufficient resolution or complexity to simulate foehn winds, the SEB, and consequently melting. However, Datta et al. (2018) use MAR at 10 km horizontal resolution to show slightly enhanced surface melting in southern inlets, which they suggest is associated with foehn occurrence. A follow-up paper (Datta et al., 2019) showed higher melt totals and higher foehn occurrence nearest the mountains during March and May 2016 (using MAR at 7.5 km resolution). However, the east-west gradient in melting is much weaker than observed using satellites, is demonstrated only for the strongest cases, and is not replicated during their entire period of study.

Various models have also been used to simulate the surface mass balance (SMB) of the entire Antarctic ice sheet (e.g. RACMO, Lenaerts et al. (2017); COSMO-CLM, Souverijns et al. (2019); and MAR, Agosta et al. (2018)) as well as various regions, including West Antarctica

(Lenaerts et al., 2018) and the Antarctic Peninsula (van Wessem et al., 2018). Given the established role of surface melting in previous ice shelf disintegrations on the peninsula, quantifying surface melting is important for understanding SMB in the context of past, present and future change. However, although these studies have determined the role of surface melting on surface mass balance, none have evaluated the processes that cause surface melt.

This chapter will fill the gap identified in the literature. By bringing together many elements that are demonstrably important in the region, such as cloud phase, foehn and large-scale circulation, and comprehensively determining their impacts on the SEB and surface melting, it will bridge the gap between studies documenting dominant atmospheric phenomena and those examining the SMB. Understanding the drivers of melting on Larsen C will enhance scientific knowledge of present conditions and facilitate more accurate projections of future scenarios in a warming climate.

6.2 Hindcast model configuration

As described in Chapter 3, the model configuration consists of a nested inner domain at 4.0 km (0.036°) horizontal resolution containing 220 × 220 gridpoints, centred on the Larsen C ice shelf. The domain is slightly smaller than the 4.4 km domain used in Chapter 4 because the simulation is much longer and computationally expensive, but larger than the domain used in Chapter 5, which focused more specifically on Larsen C. This domain should therefore include synoptic-scale features. This domain is nested within the N512 global model, which is initialised with 12-hourly ERA-Interim data. ERA-Interim was selected because the full time series of forcing data was readily accessible and at adequate resolution for initialising the global model. As in previous chapters, 24-hour forecasts are run, with the model re-initialised every 12 hours. The first 12 hours of each forecast is discarded as spin-up and the t+12 h to t+24 h period of each forecast is concatenated into a single 20 year time series, in the same manner as the OFCAP simulation in Chapter 5. The model configuration is summarised in Table 3.2, Chapter 3.

The model physics are the same as in Chapter 5, using RA1M regional physics and adaptations to the large-scale cloud and microphysics presented there, plus a revised mixing length of 5 m (see Appendix C for details). The inner domain runs with a 100 second time step, as recommended in Bush et al. (2019) for simulations of this resolution. Surface (2D) variables are outputted 3-hourly and 3D variables are 6-hourly, considered sufficient temporal resolution to capture important processes such as cloud and foehn winds. Further details are given in Chapter 3.

6.3 Validation

Like many models, the MetUM exhibits biases associated with the representation of the stable boundary layer, which commonly develop at high latitudes. However, biases vary during specific conditions. As shown in Chapter 4, during two wintertime foehn case studies in 2016, the MetUM over-estimates wind speed and relative humidity, while under-estimating T_S and T_{air}. During these cases, modelled $LW_{\downarrow}$ and R_{net} are both under-estimated relative to observations (Figures 4.5 and 4.6). During the OFCAP period discussed in Chapter 5, relative humidity is also over-estimated, but wind speeds are under-estimated, in contrast to what is shown in Chapter 4. Coupled with a cold T_S bias and warm T_{air} bias, this enhances temperature and moisture gradients between the surface and near-surface, and produces positive biases in latent, H_L, and sensible, H_S, heat fluxes. During OFCAP, SW_{net} and LW_{net} are under- and over-estimated, respectively. Overall, the sum of fluxes, E_{tot}, is too large, while melt flux, E_{melt}, is under-estimated.

The MetUM hindcast is validated at all AWSs shown in Figure 3.1 using all available observations. Missing data are linearly interpolated for validation purposes. Initial inspection of time series at each station (not shown), reveals that AWS 17/18 and AWS 14/15 are similar enough to justify being grouped. The means of the time series at AWS 14/15 and AWS 17/18 are hereafter presented as "ice shelf" and "inlet" stations, respectively. Because the full SEB is not available at AWS 15, ice shelf values for T_S, H_L, H_S, E_{tot} and E_{melt} are taken from AWS 14 only. The full SEB is available at both inlet stations.

Table 6.1 shows observed and modelled annual mean values and the 5^{th} and 95^{th} percentiles for surface variables at inlet and ice shelf stations during the hindcast period. Observed statistics in Table 6.1 are given for the observational period available for each station (see Table 3.1 for details), while modelled statistics are shown for the entire period 1998-2017. Scatterplots of observed vs. modelled surface variables at AWS 14 during the entire observational period for that station (January 2009 - December 2017, Table 3.1) are shown in Figure 6.1. AWS 14 is shown because it has the longest observational record, and for brevity, only these results are shown in this chapter. Results at all stations are broadly similar, and scatterplots for AWS 17 and 18 are given in Figures D.4 and D.5 in Appendix D, which also contains further details of the hindcast validation.

Overall, the MetUM hindcast performs extremely well with respect to surface meteorological variables and surface fluxes. The seasonal cycle and timing of weather events (not shown) matches well between model and observations, which produces high correlation coefficients

(Figure 6.1) and low RMSEs for most parameters in Table 6.1. As shown in Figure 6.1 and Table 6.1, annual mean T_{air}, T_S, wind speed and relative humidity are positively biased by 2.1°C, 2.4°C, 0.91 m s^{-1} and 2.7%, respectively, at inlet stations and 2.1°C, 3.1°C, 0.81 m s^{-1} and 3.8%, respectively, at ice shelf stations (Table 6.1), making the MetUM on average warmer, windier and moister than observations. The slight warm bias in temperatures is likely related to the representation of boundary layer mixing in the MetUM and the warm bias in ERA-Interim discussed in Chapter 2. Because both T_{air} and T_S are positively biased, the near-surface temperature gradient is too large, which contributes to biases in H_S. Wind and relative humidity biases may be related to the representation of orography, as discussed in Chapter 4.

As shown in Table 6.1, annual mean downwelling radiative fluxes are simulated to within 10% of their observed values at all stations and the model SW albedo ($SW_{\downarrow}/SW_{\uparrow}$) is simulated to within 1% and 3% of observed values at inlet and ice shelf stations, respectively. Positive biases in T_S and T_{air} cause $LW_{\uparrow}$ to be over-estimated by 2.9% annually, generating an energy deficit at the surface (and negatively biased mean R_{net}, shown in Figure 6.1). This causes annual mean daily mean E_{melt} to be under-estimated by 17-31%, particularly at inlet stations. Negative E_{melt} biases are largest during DJF when the majority of melting occurs, and biases increase during 2015-17 (see Appendix D for further details), when exceptional foehn-driven melt events, such as those examined in Chapter 4 and in section 6.6.3 (this chapter) were observed. This may indicate that the MetUM under-predicts the magnitude of foehn-driven E_{melt} fluxes, consistent with the results of Chapter 4, which found that although the MetUM was able to capture the timing and duration of the foehn cases examined, the magnitude of E_{melt} was under-estimated.

To summarise, the hindcast is able to simulate observed surface meteorological variables and SEB components at all stations and in all seasons reliably. This is consistent with the validation results presented in Chapters 4 and 5, which demonstrated that the MetUM was able to accurately reproduce the events observed during case studies. Further discussion of the model validation can be found in Appendix D.

6.4 Research question 1: How does the surface energy balance vary throughout the year?

This section will answer the first research question and examine seasonal variations in the SEB. Figure 6.2 shows the mean modelled daily SEB for summer (DJF) and winter (JJA) at ice

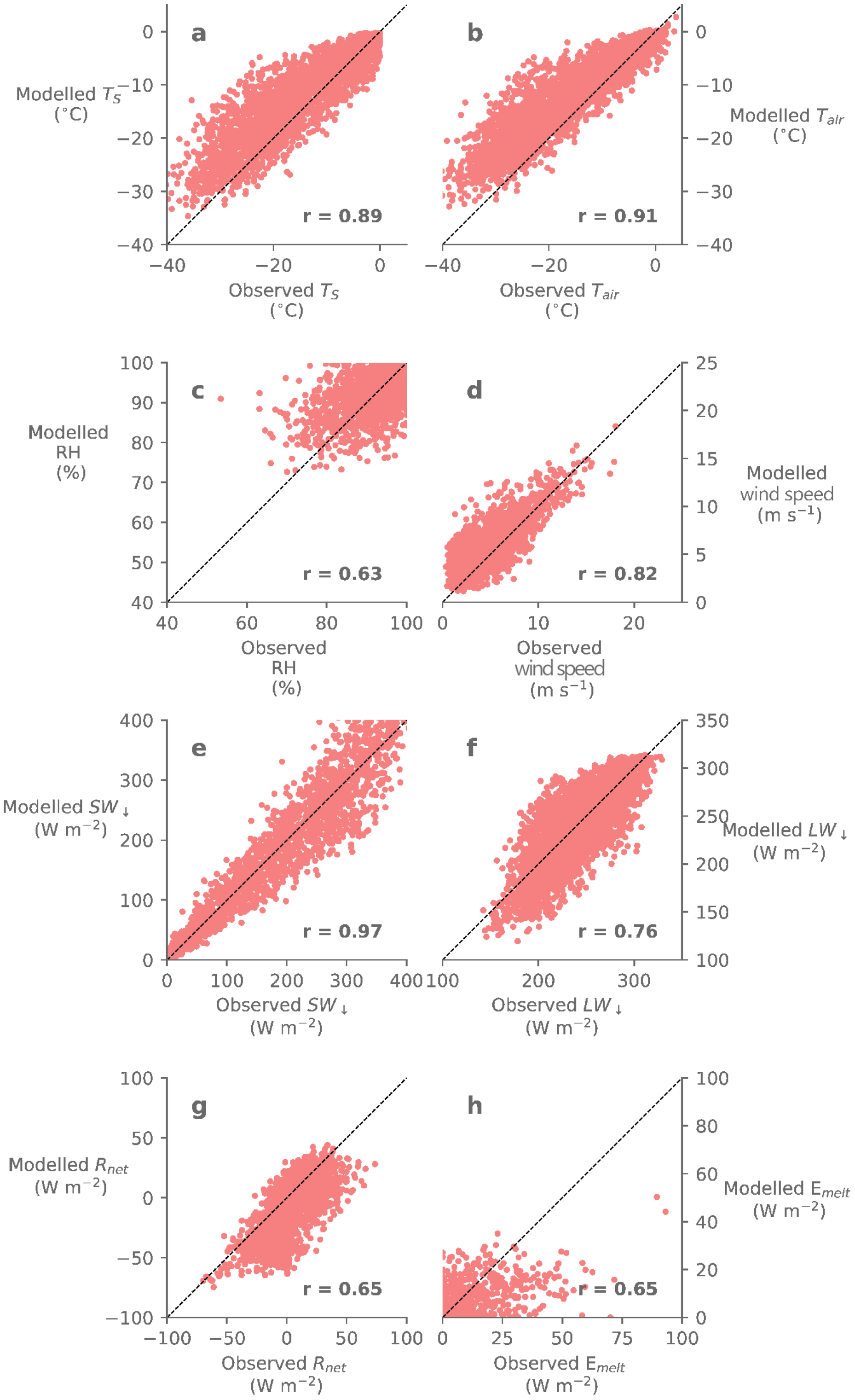

Figure 6.1.: Scatterplots of observed vs. modelled daily means of surface variables at AWS 14. Correlation coefficients (r values) are given in the bottom right hand corner of each panel: all values are statistically significant at the 99% level. The dashed line in each plot indicates perfect agreement between model and observations. Panels a – d show surface meteorological variables: surface temperature, T_S; near-surface air temperature, T_{air}; relative humidity; and wind speed; and panels e – h show surface energy budget terms: downwelling longwave, $LW_\downarrow$; downwelling shortwave, $SW_\downarrow$; net radiative, R_{net} and melt, E_{melt}, fluxes.

Table 6.1.: Summary statistics for inlet and ice shelf stations in observations and model output. Annual means (shown in bold), plus the fifth and ninety-fifth percentiles of surface variables are given, where abbreviations and units are as follows: T_S: surface temperature (°C); T_{air}: 1.5 m air temperature (°C); RH: relative humidity (%), FF: 10 m wind speed (m s^{-1}); P: surface pressure (hPa); u: 10 m zonal wind speed (m s^{-1}); v: 10 m meridional wind speed (m s^{-1}); $SW_{\downarrow}$: downwelling shortwave radiation (W m^{-2}), $SW_{\uparrow}$: upwelling shortwave radiation (W m^{-2}); SW_{net}: net shortwave radiation (W m^{-2}); $LW_{\downarrow}$: downwelling shortwave radiation (W m^{-2}); $LW_{\uparrow}$: upwelling shortwave radiation (W m^{-2}); LW_{net}: net shortwave radiation (W m^{-2}); H_S: sensible heat flux (W m^{-2}); H_L: latent heat flux (W m^{-2}); E_{tot}: sum of all fluxes (W m^{-2}); E_{melt}: melt flux (W m^{-2}). All fluxes are positive when directed towards the surface.

	Observed						**Modelled**					
	Inlet			**Ice shelf**			**Inlet**			**Ice shelf**		
	Mean	**5^{th}**	**95^{th}**	**Mean**	**5^{th}**	**95^{th}**	**Mean**	**5^{th}**	**95^{th}**	**Mean**	**5^{th}**	**95^{th}**
T_{air}	**-14.5**	-26.0	-2.5	**-14.7**	-26.7	-2.2	**-12.4**	-23.0	-2.4	**-12.6**	-23.4	-2.4
T_S	**-14.0**	-25.2	-3.0	**-15.2**	-27.1	-3.2	**-11.6**	-21.6	-2.3	**-12.1**	-22.4	-2.3
FF	**4.2**	2.6	6.2	**4.3**	2.9	5.6	**5.1**	3.4	6.8	**5.1**	4.0	6.3
u	**0.1**	-0.3	0.3	**0.0**	-0.2	0.2	**1.1**	-0.3	2.3	**0.4**	-1.4	2.2
v	**0.0**	-0.4	0.3	**0.0**	-0.2	0.2	**1.6**	-0.8	4.1	**0.9**	-1.0	2.8
P	**984.5**	975.3	995.0	**985.0**	977.1	994.2	**983.6**	974.1	993.5	**983.9**	974.4	993.4
RH	**90.9**	79.5	96.3	**93.3**	88.7	97.4	**93.6**	86.9	99.8	**97.1**	91.9	102.5
$SW_{\downarrow}$	**124.5**	2.9	302.2	**131.0**	0.7	323.2	**130.2**	0.1	319.2	**126.6**	0.0	320.3
$SW_{\uparrow}$	**-105.6**	-2.7	-255.0	**-113.4**	-0.4	-283.0	**-109.4**	-267.8	-0.1	**-106.6**	-268.4	0.0
SW_{net}	**18.9**	0.2	50.4	**19.2**	0.1	51.0	**20.9**	0.0	55.4	**20.0**	0.0	53.4
$LW_{\downarrow}$	**237.6**	205.8	280.9	**238.6**	203.9	283.7	**233.6**	191.0	276.3	**234.1**	188.2	278.8
$LW_{\uparrow}$	**-256.3**	-213.0	-304.4	**-255.5**	-210.2	-305.9	**-263.6**	-304.9	-222.7	**-262.8**	-304.7	-221.0
LW_{net}	**-18.7**	-33.1	-5.4	**-15.8**	-28.6	-2.4	**-30.0**	-43.9	-18.2	**-28.8**	-42.4	-16.2
H_S	**3.7**	-8.5	21.3	**-1.1**	-10.6	9.9	**6.9**	-4.0	23.9	**4.2**	-3.9	18.5
H_L	**-4.3**	-10.7	0.2	**-3.4**	-12.1	0.9	**-3.9**	-9.3	0.3	**-1.8**	-7.8	2.1
E_{tot}	**-3.6**	-12.0	4.8	**-3.4**	-12.0	7.4	**-6.1**	-22.5	11.3	**-6.3**	-22.0	10.8
E_{melt}	**3.4**	0.0	16.1	**2.9**	0.0	14.8	**2.9**	0.0	12.9	**2.2**	0.0	11.3

shelf and inlet stations averaged over the hindcast period. Similar patterns (not shown) are observed during spring (SON) and autumn (MAM), but are less pronounced. All fluxes are positive when directed towards the surface.

At all stations during DJF (Figure 6.2a and b), the SEB is dominated by SW_{net}, which peaks at local noon (around 16:00 UTC). Simultaneously, LW_{net}, H_L and H_S become more negative, cooling the surface. This is explained as follows. As the surface temperature rises, the surface emits more longwave radiation, increasing $LW_{\uparrow}$, making LW_{net} more negative. As the surface warms, the air-surface temperature gradient decreases, therefore reducing H_S so that it becomes negative, indicating that the surface is warmer than the overlying air and the H_S flux cools the surface. H_L falls from very slightly positive values during night-time to negative values during the day, suggestive of sublimation. These negative fluxes compensate (partly) for the positive SW_{net} flux, but overall the surface gains energy during the day in DJF.

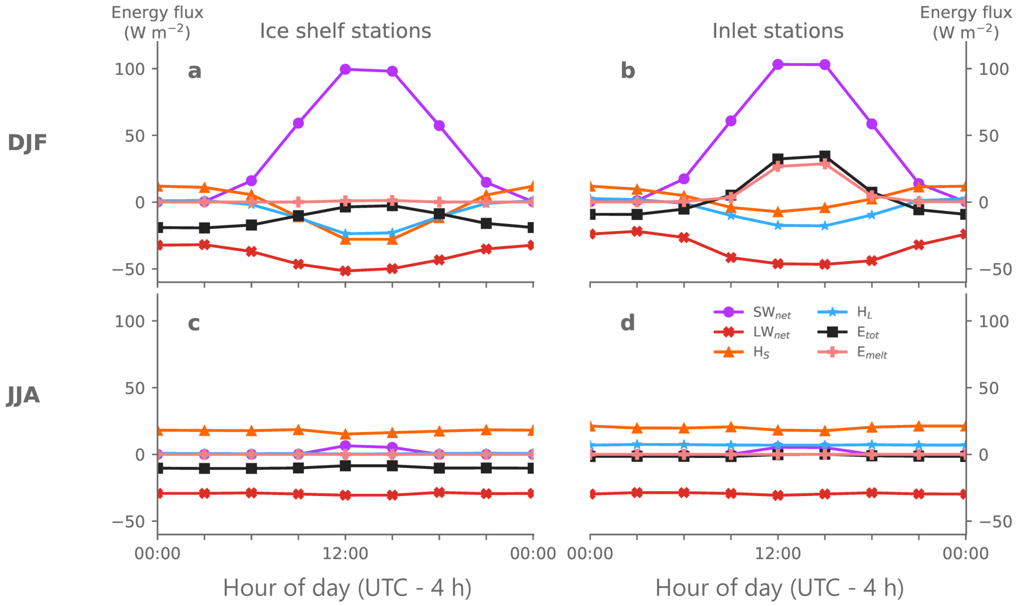

Figure 6.2.: Mean modelled diurnal cycle, averaged over each season, of SEB components during DJF (top row, panels a and b) and JJA (bottom row, panels c and d) at ice shelf (first column, panels a and c) and inlet stations (second column, panels b and d) during 1998-2017. The sum of all fluxes, E_{tot}, is shown in black. For ease of understanding, the diurnal cycle is presented in local time such that local noon is at 12:00 h (UTC -4 h), equivalent to 16:00 UTC.

During JJA (Figure 6.2c and d) when the amount of SW radiation reaching the surface is greatly reduced, there is a very minimal modelled diurnal cycle and a stable boundary layer develops. Mean fluxes stay relatively constant throughout the day, with negative LW_{net} fluxes dominating the SEB. This cooling effect is partially offset by a positive H_S flux, but overall the surface loses energy during JJA because the latent and SW fluxes are so close to zero.

While the modelled diurnal cycles are broadly similar between inlet and ice shelf stations, there are some noticeable differences. During DJF, daily mean E_{melt} is very close to zero at ice shelf stations, peaking at a maximum of 1.22 W m^{-2}. By contrast, E_{melt} reaches 28.73 W m^{-2} at inlet stations. As shown in Chapter 5, Grosvenor et al. (2014), Elvidge et al. (2016) and Gilbert et al. (2020), $SW_{\downarrow}$ is the primary source of energy available for melting during summer on Larsen C. However, because the ice shelf and inlet stations are at comparable latitudes, differences in the amount of solar radiation reaching the surface, and consequently SW_{net}, do not explain these differences in E_{melt}. Rather, contrasting diurnal cycles in the modelled turbulent fluxes produce an excess of energy available for melting at inlet stations, which produces a larger mean modelled melt flux than at ice shelf stations. At inlet stations, the sensible and latent heat fluxes do not become as negative during the day as at ice shelf stations. Consequently, H_L and H_S do not offset the positive SW_{net} flux as much as at ice shelf stations. This leads to a surplus of energy available, meaning that melting can take place if temperatures are warm enough. As shown in Chapter 4 and Elvidge et al. (2016), turbulent fluxes are extremely important for controlling melt during foehn events, and the difference between ice shelf and inlet stations is related to the increased occurrence of foehn in inlets. This will be investigated in section 6.6, this chapter.

6.5 Research question 2: How does cloud influence surface melting on Larsen C?

This section examines the role of cloud in determining the SEB and melting over Larsen C. The importance of cloud and its phase and microphysical composition has been demonstrated in Chapter 5. To understand the drivers of melting on Larsen C, modelled cloud properties must be assessed in the hindcast. Table 6.2 shows the percentage of time during which different cloud cover regimes are simulated, based on the criteria of Kay et al. (2008). Throughout the year, cloudy conditions occur 92.2% of the time, with seasonal mean cloud fractions of 0.75 in DJF and 0.72 in JJA, consistent with colder temperatures and thus lower moisture availability for cloud formation in JJA. Clear periods occur most frequently in JJA (10.6% of the time), while they occur 7.2% of the time during DJF. Overcast and broken cloud conditions (the second cloudiest category) are most common during SON (1.3% and 62.8% of the time, respectively).

Table 6.2.: Percentage of time during the hindcast period where simulated daily mean cloud fraction averaged over the Larsen C region (see Figure H.1) meets the criteria of Kay et al. (2008). The cloud regimes of Kay et al. are determined using cloud fraction thresholds, derived from Arctic cloud satellite observations. Standard deviations of the percentage of time each category is simulated are given in brackets.

	Percent of time category observed.				
Category	**ANN**	**DJF**	**MAM**	**JJA**	**SON**
"Overcast" = 1.	0.4 (0.4)	0.0 (0.0)	0.0 (0.0)	0.2 (0.4)	1.3 (1.5)
1. < "Broken" > 0.75	58.3 (3.8)	58.9 (7.5)	56.9 (8.5)	53.9 (7.5)	62.8 (7.2)
0.75 < "Scattered" > 0.31	33.5 (2.8)	33.9 (5.4)	36.6 (7.8)	35.3 (5.7)	28.8 (5.8)
"Cloudy" > 0.31	92.2 (2.2)	92.8 (5.1)	93.6 (4.2)	89.4 (4.8)	92.8 (4.0)
"Clear" < 0.31	7.8 (2.2)	7.2 (5.1)	6.4 (4.2)	10.6 (4.8)	7.2 (4.0)

6.5.1 The influence of cloud on the surface energy balance and surface melting

Cloudy and clear conditions are typified by high and low liquid water path (LWP $> 75^{th}$ percentile and $< 25^{th}$ percentile), respectively. To explore the impact of such conditions on the SEB, daily mean meteorological conditions during periods of high and low cloud fraction and LWP are averaged to produce a composite (Figure 6.3). The thresholds used to diagnose each regime are summarised in Table H.1, Appendix H. Synoptic conditions and SEB anomalies during the "cloudy" / "high LWP" and "clear"/ "low LWP" regimes are virtually indistinguishable from one another.

During JJA, cloudy, high LWP conditions, generated by cyclonic flow to the east and southerly winds over Larsen C, are associated with positive mean daily maximum temperature (T_{max}) anomalies (Figure 6.3c). Meanwhile, clear conditions (Figure 6.3g) are associated with very negative T_{max} anomalies caused by weak flow over Larsen C, which permits strong radiative cooling to occur - typical stable boundary layer conditions - and a zonal pressure gradient. Mean E_{melt} anomalies in JJA (Figure 6.3d and h) are almost zero in both regimes because melt occurs so infrequently in JJA, but 95% of the melting that does occur is associated with cloudy conditions (91% for high LWP).

Clear, low LWP summertime conditions, typically associated with westerly flow (Figure 6.3e), result in higher SW_{net} fluxes and T_{max} anomalies, which permits surface melting to occur closest to the mountains, although mean E_{tot} is lower than average because of the negative LW_{net} anomalies in clear conditions (not shown). Mean absolute values of E_{tot} during clear conditions are negative across Larsen C (-4.6 W m^{-2}), but an east-west gradient in E_{melt} anomalies is visible in Figure 6.3d, which suggests that foehn-induced cloud clearance may sometimes influence surface melting during DJF. These findings are consistent with Chapter 5, which shows that summertime melting is predominantly driven by SW fluxes.

During DJF, cloudy, high LWP conditions are associated with easterly flow of maritime air from the Weddell Sea and negative T_{max} anomalies on Larsen C (Figure 6.3a). Enhanced $LW_{\downarrow}$ produces positive E_{tot} anomalies and absolute values (9.3 W m^{-2} over ice shelf areas below 50 m), but because temperatures typically do not reach the melting point during cloudy periods (mean T_{max} = -1.13°C), melt anomalies are negative and despite occurring 59% of the time in DJF, cloudy conditions (cloud fraction > 0.75) are associated with just 50% of melt (Figure 6.3b, Table 6.10).

Because mean daily T$_{max}$ during cloudy, high LWP conditions during 1998-2017 is only slightly below the melting point and the large LW$_{\downarrow}$ fluxes associated with cloud produce positive E$_{tot}$ fluxes, this implies that cloud could become an important driver of surface melt in a warming climate. Surface air temperatures on the eastern Antarctic Peninsula are projected to warm by ~0.5-3°C by 2100 (van Oldenborgh et al., 2013), which would mean the melting point could be reached more frequently in DJF during cloudy periods. This could allow extensive low cloud-mediated melt events to occur such as were observed in Greenland in 2012 (Bennartz et al., 2013). As shown in Chapter 5, cloud initiates summertime melt by raising surface temperatures, which then persists as glaciation occurs and SW fluxes increase. Because low-level (liquid) cloud is typically extensive on Larsen C, this melting could occur across the entire ice shelf.

Correlations between melting, cloud properties and radiative fluxes over the ice shelf during the hindcast offer insight into the processes driving melting. These will be examined in section 6.8.1 below. The following section examines foehn winds in the hindcast.

6.6 Research question 3: Where and when do foehn events occur?

6.6.1 Diagnosis methods

The importance of foehn for determining the SEB and thus melting has been well established, for instance in Chapter 4, King et al. (2017) and Kuipers Munneke et al. (2018). King et al. (2017) find that foehn conditions over Larsen C occur ~20% of the time during summer 2010/11, which agrees well with other estimates, such as Wiesenekker et al. (2018), Turton et al. (2018) and Datta et al. (2019), who find that foehn conditions occur 14%, 15% and 6-15% of the time, respectively, at various locations on the ice shelf.

Foehn can be diagnosed from model output in several ways, which may affect the way foehn events are counted. These can be summarised as: the (1) surface, (2) Froude number and (3) isentrope methods. The surface method diagnoses foehn when near surface winds, temperature and relative humidity change by a threshold amount over a given time period, typically 6 hours. The Froude number method diagnoses foehn conditions based on the upstream Froude number, while the isentrope method diagnoses foehn by determining the change in height of an upstream isentrope on the lee side of orography. All three methods are

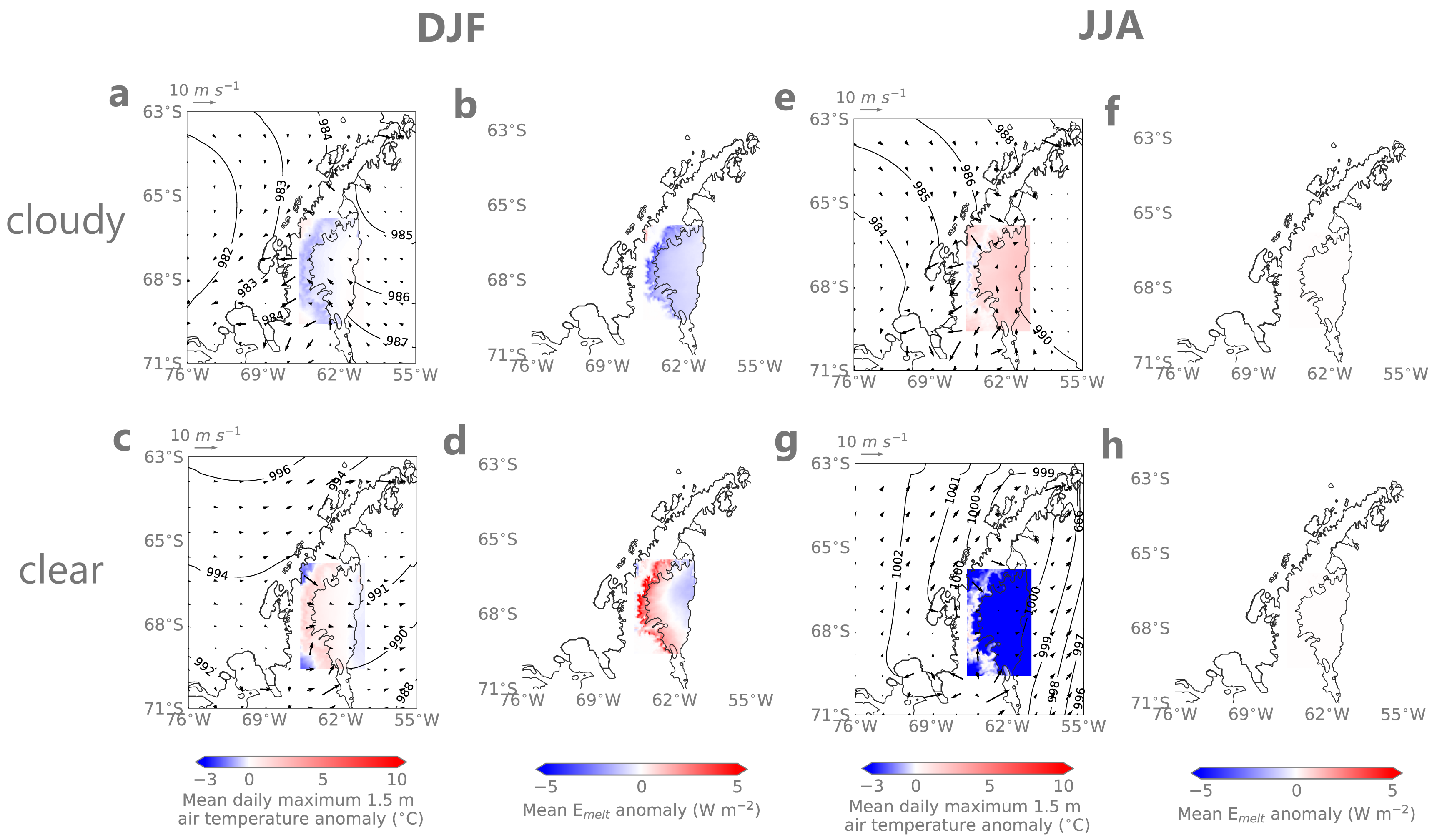
DJF
JJA
cloudy
clear
a
b
c
d
e
f
g
h
10 m s⁻¹
63°S
65°S
68°S
71°S
76°W
69°W
62°W
55°W
982
983
984
985
986
987
988
990
994
996
991
992
1002
1001
1000
999
998
997
−3 0 5 10
Mean daily maximum 1.5 m air temperature anomaly (°C)
−5 0 5
Mean E_melt anomaly (W m⁻²)

Figure 6.3.: Composited mean modelled meteorological conditions and melt flux anomalies during "cloudy" (top row, panels a-d) and "clear" (bottom row, panels e-h) periods in summer (DJF) and winter (JJA) over Larsen C during the hindcast period, using the thresholds of Kay et al. (2008) given in Table 6.2. Panels a, c, e and g show synoptic conditions, where coloured shading shows the mean daily maximum 1.5 m air temperature anomaly (in °C) during periods when each condition is diagnosed, while contours and vectors show the mean mean sea level pressure (in hPa) and 10 m winds (in m s^{-1}) during each regime, respectively. A wind speed scale vector of 10 m s^{-1} is given at top left for reference. Panels b, d, f and h show mean daily mean melt flux anomalies (in W m^{-2}) across Larsen C associated with each regime.

described in detail and assessed for use over Larsen C in Appendix E, alongside temperature and relative humidity thresholds for use in method 1.

Following initial evaluation of these three methods (see Appendix E), a combined "Goldilocks" foehn detection algorithm was devised. The Goldilocks detection algorithm is a combination of the isentrope method (3) with additional stipulations that concurrent surface effects must also be simulated at the location considered. An increase and decrease in temperature and relative humidity, respectively, must be simulated to detect foehn. This minimises the chance of diagnosing foehn conditions during periods of foehn flow at downstream locations where these are not experienced. For example, although isentropic drawdown may cause a foehn effect near the mountains, this may not be experienced at the surface further out on the ice shelf, particularly in the case of non-linear events that result in features like hydraulic jumps. Because the purpose of this section is to determine the overall effect of foehn on surface melting, if surface temperatures do not rise sufficiently to permit melt and drive positive sensible heat fluxes at a particular location, melt will not occur and foehn should not be diagnosed.

The algorithm is summarised as follows:

- Determine the mean westerly component of the wind, u_{Z1}, impinging on the peninsula. u_{Z1} is calculated at least one Rossby radius of deformation away from the barrier and as an average of the flow speed between the near-surface and an altitude, Z_1, equivalent to the peak height of orography. In this thesis, u_{Z1} was calculated as the mean u wind between 200-2000 m altitude in the region marked "X" in Figure H.1. If this westerly component, $u_{Z1} \geq 2$ m s^{-1} (and there is therefore a clear cross-barrier flow):
  - Find the potential temperature at Z_1, θ_{Z1}, and trace this isentrope across the mountain barrier
  - Determine the minimum elevation, Z_2, of θ_{Z1} on the lee side of the mountains over Larsen C
  - Determine the maximum change in height of the isentrope θ_{Z1} upwind and downwind of the barrier, i.e. $Z_3 = Z_1 - Z_2$.
  - If, over 6 hours, $Z_3 > 500$ m AND T_{air} increases AND RH decreases, then foehn conditions are detected.

A schematic illustration is given in Figure E.1.

Table 6.3.: Summary seasonal modelled foehn frequency statistics for ice shelf and inlet stations over the period 1998-2017. Means, medians and standard deviations ("SD") are given for each season and annual totals.

		Mean	**Median**	**SD**
Ice shelf	DJF	11.2 %	11.0 %	3.7 %
	MAM	12.1 %	11.3 %	3.9 %
	JJA	13.4 %	13.1 %	3.3 %
	SON	14.5 %	14.4 %	3.1 %
	ANN	12.7 %	12.5 %	2.4 %
		Mean	**Median**	**SD**
Inlet	DJF	15.4 %	15.8 %	4.0 %
	MAM	15.4 %	14.9 %	3.7 %
	JJA	16.1 %	16.8 %	3.0 %
	SON	18.5 %	18.5 %	2.7 %
	ANN	16.1 %	16.0 %	1.9 %

6.6.2 Modelled foehn frequency

Table 6.3 shows summary statistics for modelled foehn frequency at inlet and ice shelf stations during all seasons in the hindcast period. An equivalent table showing foehn frequencies at all stations and during all years is given in Table F.1, Appendix F. Foehn conditions are modelled 27% more frequently at inlet stations than at ice shelf stations, consistent with theory. Foehn are least likely to occur during DJF, especially at ice shelf stations, as has also been found by Datta et al. (2019). As is widely noted in the literature (e.g. Cape et al., 2015; Turton et al., 2018; Wiesenekker et al., 2018; Datta et al., 2019), modelled foehn on Larsen C are most frequent in SON, and modelled foehn frequencies compare favourably with figures reported in the studies cited (5-25% in Cape et al., 15% in Turton et al., 14% in Wiesenekker et al. and 21% in King et al., 2017 for summer 2010/11). Trends calculated with a Mann-Kendall test in annual and seasonal foehn frequency are small and insignificant at all stations. However, considerable inter-annual variability is seen, as shown by the large standard deviations in Table 6.3.

Particularly, MAM 2016 stands out as an extremely high foehn season. As shown in Table 6.4, foehn frequencies at all stations exceed one standard deviation, a result also found by Datta et al. (2019). Interestingly, this is also the period examined in Chapter 4 and Kuipers Munneke et al. (2018), which may indicate that the foehn-driven wintertime melting observed during that year was unusually high. To examine the causes of the unusually high foehn frequency during this period, the synoptic meteorology and surface fluxes are assessed in greater detail.

Table 6.4.: Mean modelled MAM foehn occurrence during the model hindcast period ("1998-2017 mean"), mean modelled MAM foehn occurrence during the hindcast period plus one standard deviation ("Mean + SD") and modelled foehn occurrence during MAM 2016 ("MAM 2016") at each station.

AWS	1998-2017 Mean (%)	Mean + SD (%)	MAM 2016 (%)
AWS 14	13.9	17.6	22.8
AWS 15	10.3	13.5	18.3
AWS 17	15.7	19.3	21.5
AWS 18	15.1	18.9	24.2

6.6.3 MAM 2016: a high-foehn season

In order to evaluate the causes of the unusually high foehn flow simulated in the hindcast during the second half of MAM 2016 (Table 6.4), mean meteorological conditions are examined during April 15 – May 31, when foehn occurrence and melting across Larsen C were both anomalously high (Figure 6.4a). Strong cross-peninsula flow is simulated and mean near-surface daily maximum air temperatures are 5.8°C warmer than climatology for the period, causing surface temperatures to frequently reach the melting point and climb as high as 12.6°C in Mill Inlet on the 25 May 2016 (the peak of CS2 in Chapter 4, the case identified as being strongest in the entire AWS record from Cabinet Inlet).

This synoptic situation creates optimum conditions for foehn to occur. Panels b – f in Figure 6.4 show mean anomalies for individual SEB components during April 15 – May 31. Increased surface temperature produces modest negative $LW_{\uparrow}$ and LW_{net} anomalies (Figure 6.4b) but the turbulent fluxes differ considerably from the climatology. Negative H_L anomalies leeward of the mountains (Figure 6.4c) indicate that the air is drier than the climatology, as foehn air is warmed and dried on its descent, and causes sublimation over Larsen C. Extremely positive sensible heat anomalies (Figure 6.4d) are modelled east of the mountain crest and extend across the ice shelf as foehn flow mixes warm, dry air towards the surface. This strong foehn effect generates mean E_{tot} anomalies (Figure 6.4e) of up to 76.8 W m^{-2} in the lee of the mountains. Mean E_{melt} anomalies (Figure 6.4f) of up to 61.1 W m^{-2} are simulated wherever E_{tot} is positive, as mean maximum air temperatures are above 0°C in almost all locations (Figure 6.4a).

E_{melt} anomalies result in anomalous cumulative meltwater production over Larsen C (Figure 6.5), with 29 times more melt (5.7 Gt) produced during the MAM 2016 season than in the 1998-2017 MAM climatology (0.2 Gt), representing 35.4% of the meltwater production for the 2015/16 melt year (August-July, 16.0 Gt). The mean modelled MAM 2016 meltwater production anomaly over Larsen C relative to the model MAM climatology is shown in Figure 6.5b, with maximum simulated melt along a transect shown in Figure 6.5a. Maximum melt fluxes along the transect are highest in the immediate lee of the mountains, and diminish rapidly with distance from the peak of orography as warm, dry foehn air is increasingly mixed into cold ambient air masses. Regions of elevated melt exist further out onto the ice shelf in some regions, with "streams" of higher melt emanating from the mouths of inlets. These may be the same foehn "jet" regions identified by Elvidge et al. (2015), which are typically cooler but experience higher wind speeds during foehn events. They are downstream of mountain passes which channel flow and enhance wind speeds, but cause air to be sourced from lower altitude, meaning that it is cooler when it reaches the surface than in adjacent "wake" regions. Because the events during MAM 2016 are so intense and ambient temperatures are so high, the relatively cooler jet temperatures do not limit melting, and the elevated wind speeds enhance the sensible heat flux enough to drive extremely intense melting in these jet regions.

6.6.4 Spatial patterns of foehn occurrence

Spatial patterns of foehn occurrence are important to understand surface melting. However, foehn cannot be diagnosed over the entire model domain using the isentrope or "Goldilocks" methods because of computational constraints. Therefore, to produce spatial maps of foehn frequency, the surface method of Turton et al. (2018) is used, with an additional requirement that there be an upwind westerly wind component ($u_{Z1} \geq 2.0$ m s^{-1}, as in King et al., 2017). Turton et al. (2018) diagnose foehn using RH-based criteria, when over 12 hours either: 1) RH falls below the 10^{th} percentile, 2) RH decreases below a defined threshold, or 3) a decline in RH below the 15^{th} percentile is accompanied by a temperature increase greater than 3°C.

The overall pattern shown in Figure 6.6, with foehn occurring most frequently in inlets in the immediate lee of steep orography and infrequently over the ice shelf, is consistent with theory and observations. Closest to the mountains, modelled foehn conditions prevail for 16.1% of the entire year on average, while further out on the ice shelf, foehn conditions occur less frequently (12.7%). The percentage of time when foehn conditions are diagnosed decreases rapidly with distance from the mountains. Airflow over the mountain range produces a larger foehn effect in inlets because warm, dry foehn air is increasingly mixed into the ambient air as it flows over the ice shelf and away from the mountain barrier. Therefore intense (non-linear) events have the largest surface effect nearest the mountains, particularly when non-linear features like hydraulic jumps mean foehn flow is deflected upwards away from the surface (cf. case study "A" in Elvidge et al., 2016).

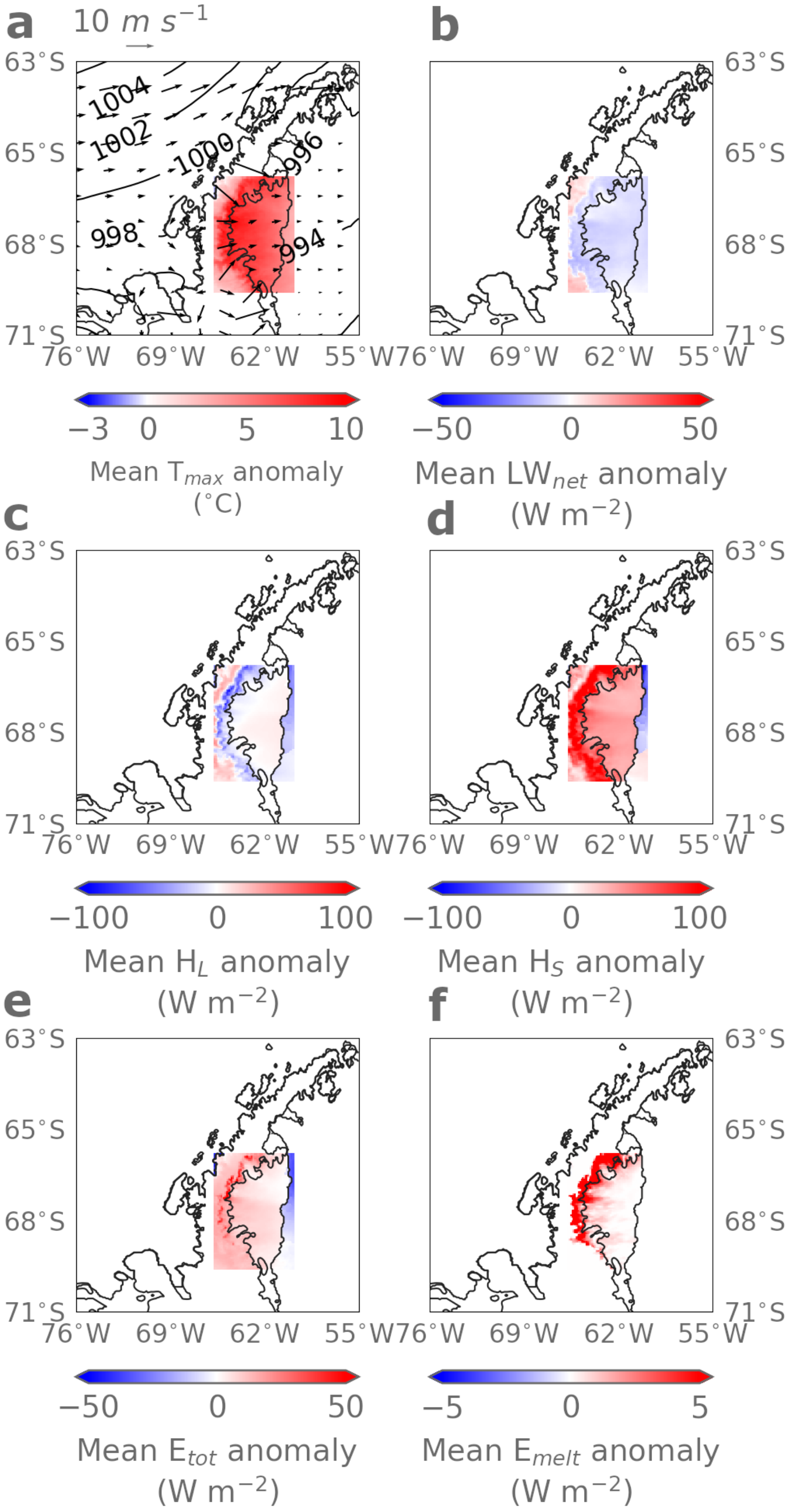
a
10 m s⁻¹
1004
1002
1000
996
998
994
b
63°S
65°S
68°S
71°S
76°W
69°W
62°W
55°W
−3
0
5
10
Mean T_max anomaly (°C)
−50
0
50
Mean LW_net anomaly (W m⁻²)
c
d
−100
0
100
Mean H_L anomaly (W m⁻²)
Mean H_S anomaly (W m⁻²)
e
f
−50
0
50
Mean E_tot anomaly (W m⁻²)
−5
0
5
Mean E_melt anomaly (W m⁻²)

Figure 6.4.: Mean modelled synoptic meteorological conditions and surface flux anomalies during 15 April – 31 May 2016. Panel a) shows mean modelled meteorological conditions, where colours indicate the mean daily maximum 1.5 m air temperature anomaly (in °C), contours show mean mean sea level pressure (hPa) and vectors show mean 10 m wind speed and direction. Panels b) to f) show flux anomalies, in W m^{-2}, relative to the 1998-2017 model climatology for 15 April – 31 May, of LW_{net}, H_L, H_S, E_{tot} and E_{melt}, respectively. In all panels, blue colours indicate negative anomalies while red colours show positive anomalies.

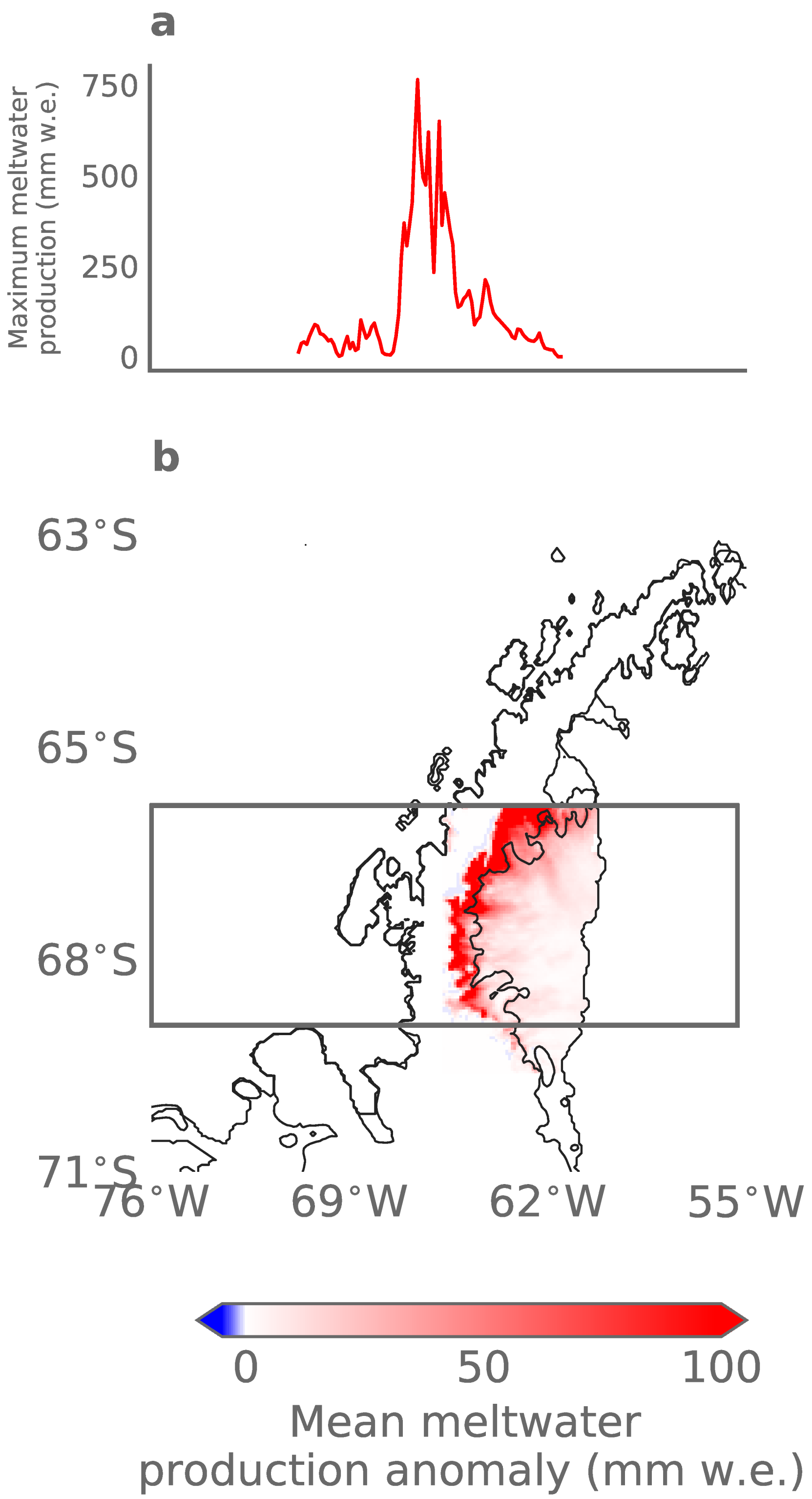
a
Maximum meltwater production (mm w.e.)
750
500
250
0
b
63°S
65°S
68°S
71°S
76°W
69°W
62°W
55°W
0
50
100
Mean meltwater production anomaly (mm w.e.)

Figure 6.5.: Mean meltwater production over Larsen C during 15 April – 31 May 2016. Panel a) shows the maximum cumulative melt produced along an east-west transect, indicated by the grey box in panel b). Panel b) shows the mean cumulative meltwater production anomaly with respect to the 1998-2017 model climatology for 15 April – 31 May.

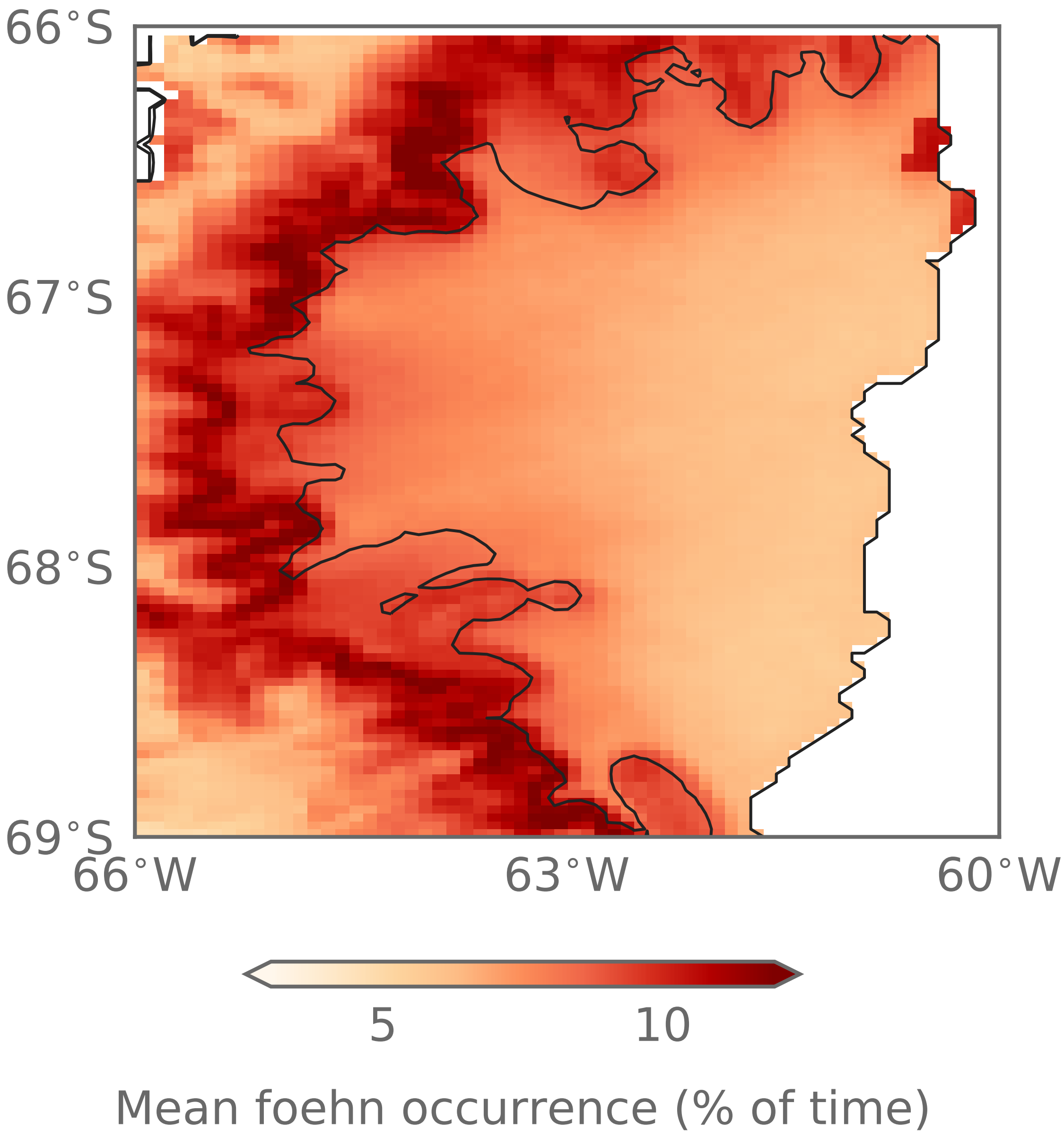
66°S
67°S
68°S
69°S
66°W
63°W
60°W
5
10
Mean foehn occurrence (% of time)

Figure 6.6.: Mean percentage of time over the period 1998-2017 where foehn conditions are diagnosed over the model domain, using the surface-based foehn diagnosis method of Turton et al. (2018) with an additional requirement, as in King et al. (2017), that there be a westerly wind component ($u_{Z1} \geq 2.0$ m s^{-1}). See text for more details. The 50 m elevation contour (approximately the height of the ice shelf at the grounding line), is shown.

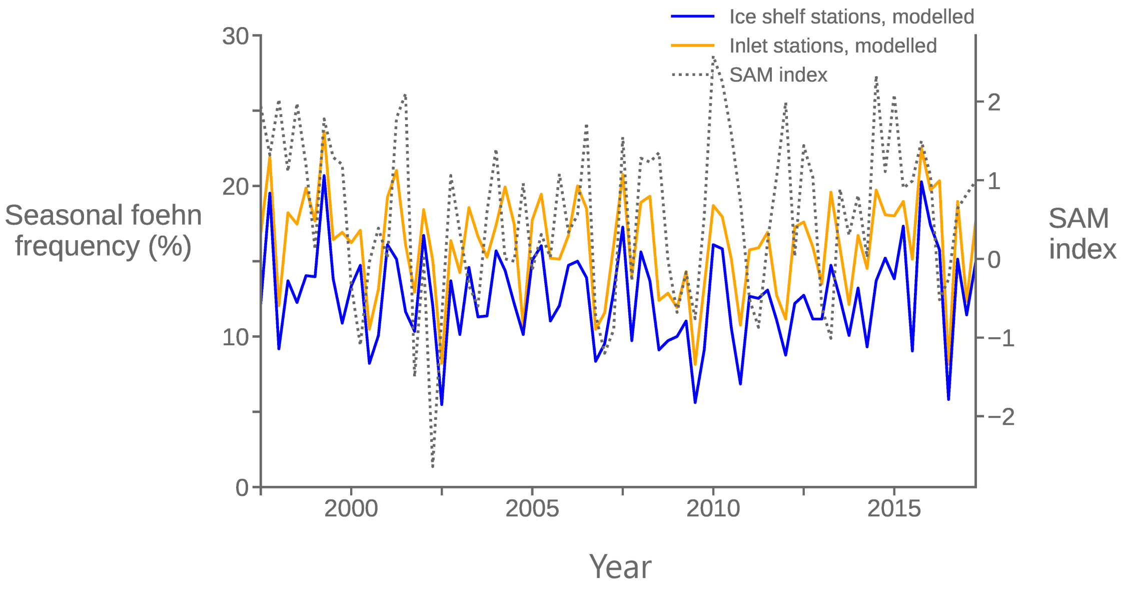

Figure 6.7.: Time series of total seasonal foehn frequency diagnosed from model output at inlet and ice shelf stations (coloured lines) against seasonally-averaged SAM index, after Marshall (2003). Foehn frequency and SAM index are both shown as seasonal means.

6.6.5 Correlations between modelled foehn and SAM index

As is well established in the literature (e.g. Orr et al., 2004; Orr et al., 2008; Marshall et al., 2006; van Lipzig et al., 2008, see Chapter 2 for a comprehensive review), a positive SAM index is associated with stronger westerly winds over the Antarctic Peninsula, which increase the frequency of foehn events, leading to increased surface temperatures to the east of the Peninsula. As shown in Figure 6.7, the time series of foehn frequency at inlet and ice shelf stations closely matches patterns in the time series of seasonally averaged SAM index. The number of foehn events diagnosed at inlet stations is systematically higher than ice shelf stations, consistent with theory. More positive SAM seasons are associated with a higher number of foehn events as a result of a more westerly wind pattern, while fewer foehn events are simulated during negative SAM seasons. Correlations between the seasonal mean SAM index and seasonal foehn frequency are strongest and most statistically significant during DJF and weakest (and insignificant) during JJA. As shown in Table 6.5, the Pearson correlation coefficient between annually averaged SAM index and annual mean foehn frequency is 0.52 in inlets and 0.54 at over the ice shelf (both significant at the 95% level). However, while statistics are relatively similar between AWS 17 and 18, there are differences between AWS 14 ($r = 0.46$) and AWS 15 ($r = 0.63$).

Table 6.5.: Pearson correlation coefficients between modelled foehn frequency at inlet and ice shelf stations with the observed SAM index of Marshall (2003). Correlations that are statistically significant at the 95% level are given in bold, while statistical significance of 99% is indicated with an asterisk.

	inlet	ice shelf
DJF	**0.66***	**0.62***
MAM	**0.55**	**0.54**
JJA	0.19	0.16
SON	**0.50**	**0.46**
ANN	**0.52**	**0.54**

6.7 Research questions 4 and 5: How does surface melting vary in time and space?

Determining the total amount of melt that occurs over Larsen C is a key objective of this work. This section will address the fourth and fifth research questions, which focus on where and when melting occurs during the hindcast, whether these patterns match published estimates, and current meltwater production on Larsen C.

6.7.1 Comparing hindcast- and satellite-derived estimates of melt

Observed annual melt duration (Bevan et al., 2018) is compared with simulated melt duration for all full melt seasons included in the hindcast period (a total of 18 melt years, starting 1999/2000 and ending 2016/2017), where melt seasons are defined as in Bevan et al. from August-July (Figure 6.8). Simulated melt duration (Figure 6.8b) agrees well with the results of Bevan et al. (2018) (Figure 6.8a) and Luckman et al. (2014) (not shown), with a clear north-south gradient across the ice shelf, and more melt days observed in inlets. The modelled east-west gradient in melt duration is weaker than observed, with longer melt duration simulated in the southeast of Larsen C (near the shelf edge) and shorter melt periods in the southwestern inlets than observed. However, the model's ability to reproduce the major patterns of melting, particularly the east-west gradient and concentration of meltwater production in inlets – which has not been shown before in any published model hindcast – is extremely encouraging and justifies the use of the MetUM for further study in this region.

6.7.2 Modelled meltwater production

Total meltwater production is more useful to simulate than melt duration because it is directly related to the surface mass balance of Larsen C. In contrast to Chapter 4, in the hindcast simulation meltwater production is outputted by the MetUM. Meltwater production

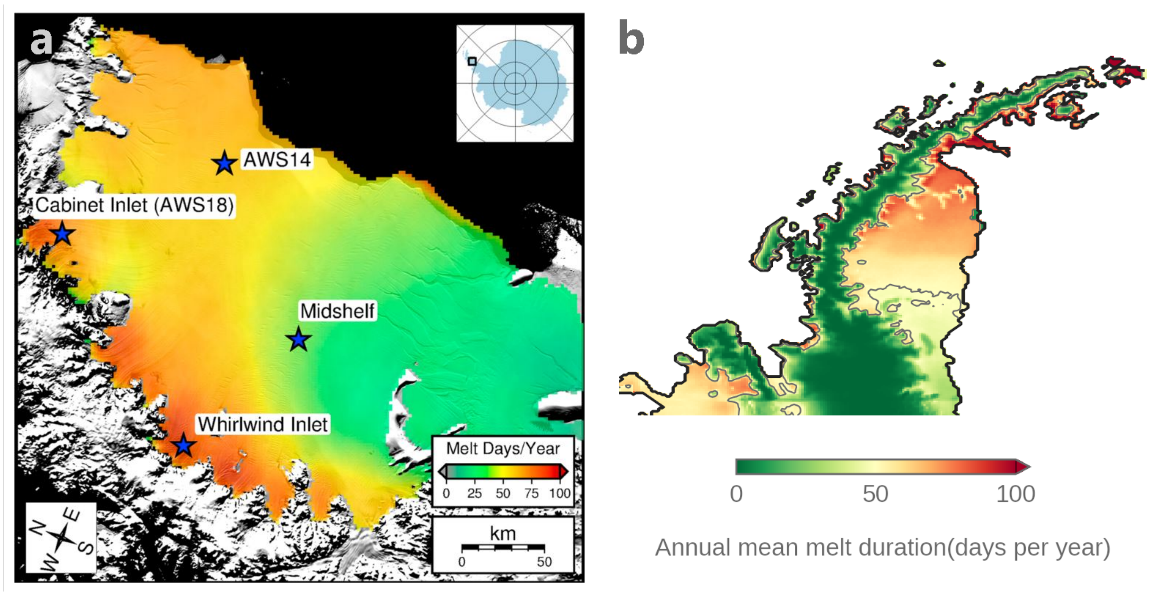
a
AWS14
Cabinet Inlet (AWS18)
Midshelf
Whirlwind Inlet
Melt Days/Year
0 25 50 75 100
km
0 50
N E S W
b
0 50 100
Annual mean melt duration(days per year)

Figure 6.8.: Mean melt duration (in number of melt days per melt season) over the Larsen C ice shelf in satellite observations and the hindcast. Panel a) shows the mean number of melt days per melt season calculated from QSCAT morning and ASCAT satellite retrievals during the period 1999/2000 to 2016/2017, and is reproduced from Bevan et al. (2018) "Decline in Surface Melt Duration on Larsen C Ice Shelf Revealed by The Advanced Scatterometer (ASCAT)" *Earth & Space Science* 5, doi: 10.1029/2018EA000421. Copyright (c) 2018, the authors, under Creative Commons CC BY-NC 3.0 license. Panel b) shows the annual mean number of days per melt year where melting is modelled during at least one 3-hour period over the Antarctic Peninsula model domain for the same period. The plot is designed for comparison with both Luckman et al. (2014) and Bevan et al. (2018) and uses the same colour scale. The grey contour shows where annual mean modelled melt duration is equal to 50 days per year.

is calculated by the surface scheme in a manner similar to Equation 4.1. Figure 6.10 shows simulated cumulative annual meltwater production in all complete melt years (August 1999 – July 2017). The spatial pattern of melt duration (Figure 6.8b) and meltwater production (Figure 6.10) closely matches the pattern of foehn occurrence (Figure 6.6), further emphasising the importance of foehn in driving melting on Larsen C, especially in inlets. A statistically significant difference (99% level) in modelled monthly mean melt amount is simulated at ice shelf stations compared to inlet stations.

Figures 6.9 and 6.10 show that ice-shelf averaged meltwater production was highest during the 1999/2000, 2006/07 and 2015/16 melt seasons and that maximum melt rates, which are always simulated in inlets, are highest in 2006/07, 2013/14 and 2015/16. These findings broadly agree with the high melt years identified in Bevan et al. (2018) and Luckman et al. (2014). As shown in Chapter 4, Kuipers Munneke et al. (2018), Datta et al. (2019) and this chapter, foehn-driven melting dominates in JJA, SON and MAM when solar radiation is less important, while in DJF melting is more strongly related to temperature and SW radiation (Chapter 5, Gilbert et al., 2020). The stronger relationship noted in Chapter 2 between ENSO and SAM (and therefore foehn occurrence) during SON and JJA accounts for the larger amount of melt modelled in inlets during El Niño melt seasons of 1999/2000, 2006/07 and 2015/16, and suggests an important role for foehn-driven melt in these years. Additionally, as shown above, the number of foehn events in MAM 2016 was more than one standard deviation above the annual mean, accounting for 35% of meltwater production during the 2015/16 melt season. The seasonally averaged SAM index in MAM 2016 was 1.5 (calculated after Marshall, 2003) – also outside one standard deviation of the MAM mean during the hindcast period. This suggests that the considerable melt rates observed during 2015/16 are related to the positive phase of the SAM, which dramatically increased the number of foehn events during MAM, and dominated the signal for the whole year. The mechanisms and drivers of melt, including the influence of large-scale climate variability, are examined further in section 6.8.

Simulated mean annual meltwater production amounts over Larsen C (Table 6.6, Figure 6.9) are comparable to those in Trusel et al. (2013), who use satellite data and modelling to find ice-shelf integrated mean meltwater production of 220 mm w.e. yr^{-1} over the period 1999-2009, exceeding 400 mm w.e. yr^{-1} in the northwestern inlets, and Trusel et al. (2015) who show contemporary melt rates over Larsen C of ∼300 mm w.e. yr^{-1} (see Chapter 2). Comparable hindcast-simulated values for 1998-2017 are 130 mm w.e. yr^{-1} for all of Larsen C, and 536 mm w.e. yr^{-1} for inlets only, taking maximum meltwater production rates as

Table 6.6.: Total and maximum modelled meltwater production over the Larsen C ice shelf and tributary glaciers (region marked "LCIS" in Figure H.1, Appendix H) plus the standard deviation of annual mean cumulative melt during each melt year (August-July) in the hindcast period. Annual ice-shelf integrated and maximum modelled meltwater production greater than one standard deviation above the mean are indicated with red-orange shading and bold text, while modelled meltwater production less than one standard deviation below the mean is indicated with green shading and italics. The standard deviation of annual cumulative mean melt across Larsen C, that is, a measure of the spatial variability of cumulative melt totals, is given in the final column.

Melt year	Ice shelf mean annual total meltwater production (mm w.e.)	Maximum annual total meltwater production (mm w.e.)	Standard Deviation (mm w.e.)
98-99	117.4	**761.9**	80.6
99-00	156.8	488.1	97.6
00-01	*98.6*	422.3	66.3
01-02	111.1	439.2	62.2
02-03	156.4	414.3	85.4
03-04	117.9	419.8	69.4
04-05	145.7	573.8	92.1
05-06	124.6	467.0	79.4
06-07	**187.9**	**779.6**	115.7
07-08	149.1	481.8	78.8
08-09	135.6	451.4	89.8
09-10	112.8	396.6	70.7
10-11	*86.4*	370.0	55.6
11-12	131.0	411.3	78.0
12-13	*103.4*	421.0	62.7
13-14	130.9	601.6	80.9
14-15	*93.9*	347.2	58.8
15-16	**157.1**	**796.5**	105.4
16-17	**161.0**	**1024.7**	124.1

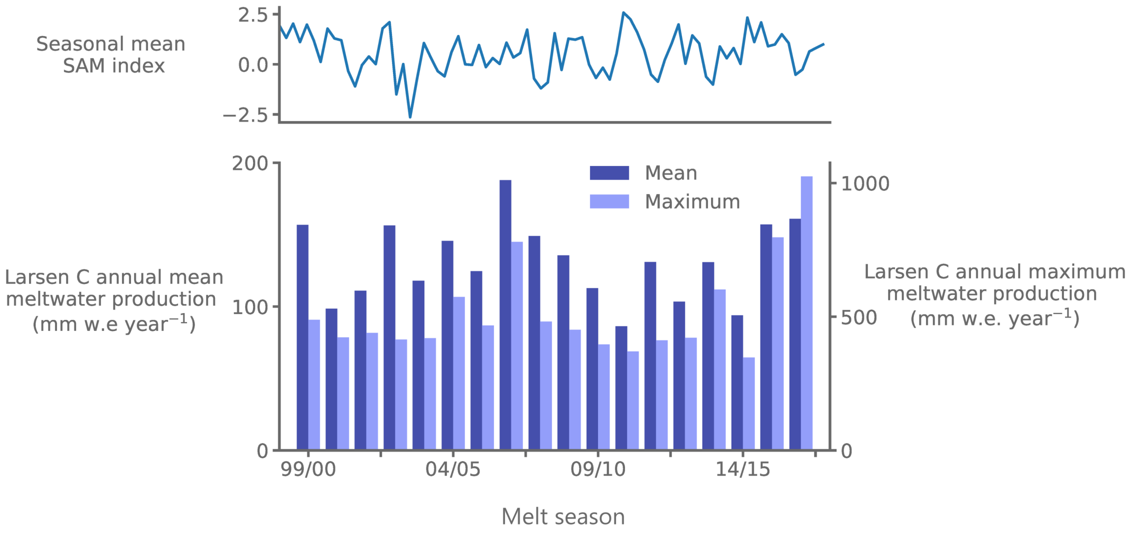

Figure 6.9.: Seasonal SAM index and annual mean and maximum cumulative meltwater production rates across the Larsen C ice shelf in each melt year during the hindcast simulation, in mm w.e. yr^{-1}. The seasonal mean SAM index is shown with the blue line in panel a and is calculated after Marshall (2003), while cumulative melt production is shown in panel b. The region over which the totals are calculated is shown in Figure H.1.

a proxy for inlet melting (maxima are always observed in inlets). This suggests that the MetUM may under-estimate surface melting, as was also shown in section 6.3 (Table 6.1 and Appendix D). Although caution should be used when evaluating the hindcast's absolute meltwater production totals, it is notable that maximum values simulated in the northwestern inlets during high melt years (up to 796.5 mm w.e., 601.59 mm w.e. and 1024.7 mm w.e. in Mill Inlet during 2013/14, 2015/16 and 2016/17, respectively, and up to 779.63 mm w.e. in Cabinet Inlet during 2006/07) exceed those observed over Larsen B before its collapse (~600 mm w.e. yr^{-1}, Trusel et al., 2015). If rising global temperatures increases the number of high melt years in future, or causes melt to extend across the entire ice shelf, this could compromise the stability of Larsen C. This impact would be compounded by the ongoing trend towards a positive SAM, which increases the frequency of foehn events.

Considerable inter-annual variability in simulated surface melting across Larsen C is evident in Table 6.6 and Figure 6.9b during 1998-2017. Considerable inter-seasonal variability is also visible in the SAM (Figure 6.9a), and no statistically significant correlation between SAM index and cumulative annual meltwater production is present, a finding also reported by Bevan et al. (2018) using satellite measurements. Similarly, as Bevan et al. also show, no statistically significant trends are seen in hindcast-modelled ice-shelf averaged meltwater production. Contrasting trends are reported in the literature, however. For example, Trusel et al. (2015) find an increase in Larsen C-averaged surface melting between 2000-2009, concurrent with rising temperatures (discussed in Chapter 2), while Bevan et al. (2018), show a decline in ice-shelf averaged surface melting between 2000-17 but an increase in melt duration in inlets over that period (Chapter 2). In the hindcast, more melting is simulated in inlets towards the end of the hindcast period (Table D.1, Figures 6.10 and 6.9), echoing the findings of Bevan et al. (2018). Maximum melt rates, which are a good proxy for inlet melting, are relatively stable throughout the period, except during the positive SAM, high foehn, high melt years of 2006/07, 2015/16 and 2016/17. The considerable meltwater production observed during 2015/16 and 2016/17, when mean melt rates were considerably higher than during the preceding seven years, coincide with a period of exceptional Antarctic sea ice decline, including in the Weddell and Bellingshausen Seas that sandwich the peninsula (Turner et al., 2016; Parkinson, 2019, Chapter 2). Reduced sea ice concentrations can increase turbulent heat fluxes and affect local atmospheric circulation, but are also caused by the same large-scale patterns, such as ENSO, SAM and the polar stratospheric vortex (Schlosser et al., 2018; Wang et al., 2019) that can enhance melting over Larsen C.

6.8 Research question 6: What are the most important drivers of surface melting on Larsen C 1998-2017?

This final section will answer some of the key questions posed during this thesis, and reveal some of the dominant atmospheric causes of surface melting on Larsen C. Specifically, it will answer the last research question, examining the relationships between variables, spatial correlations and composites to identify the most important factors contributing to surface melting on the Larsen C ice shelf.

6.8.1 Time series correlations

Tables 6.7 and 6.8 show Pearson correlation coefficients between daily mean modelled variables over the Larsen C ice shelf for the entire hindcast period (i.e. annual values, ANN) and for individual seasons, respectively. Correlations between E_{melt} and other variables are used to identify the most important atmospheric drivers of melting. The conclusions drawn here are broadly similar to the results of the process-based study of Elvidge et al. (2020).

Radiative fluxes are important in determining whether or not melt occurs. The largest correlation annually (ANN, Table 6.7), between E_{melt} and any flux is with SW_{net} ($r_{SW_{net},E_{melt}}$ = 0.56), and E_{melt} is (slightly) negatively related with cloud cover ($r_{E_{melt},CC}$ = -0.05). This pattern is also seen in DJF (Table 6.8), with a positive relationship between E_{melt} and SW_{net}

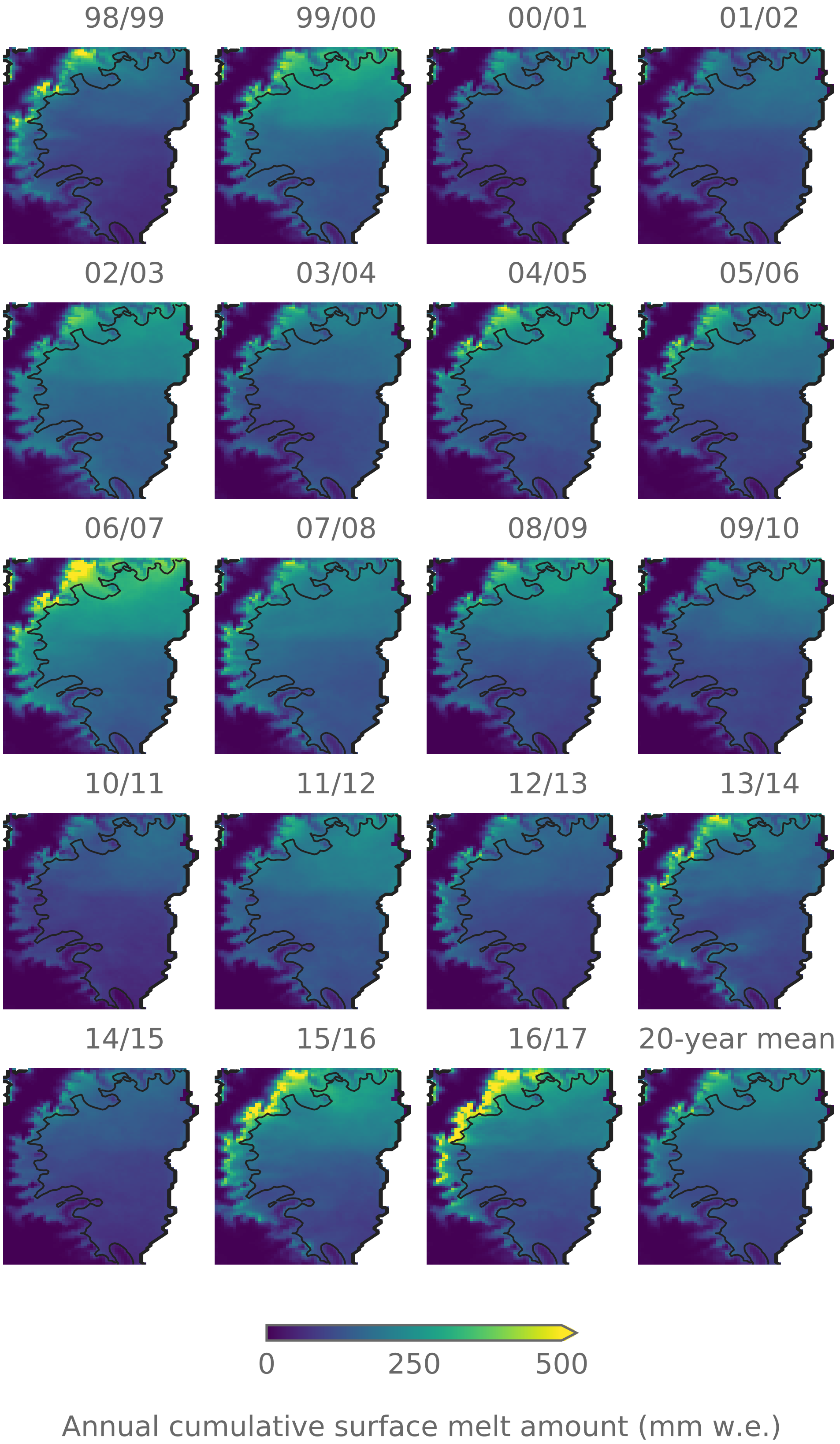
98/99
99/00
00/01
01/02
02/03
03/04
04/05
05/06
06/07
07/08
08/09
09/10
10/11
11/12
12/13
13/14
14/15
15/16
16/17
20-year mean
0
250
500
Annual cumulative surface melt amount (mm w.e.)

Figure 6.10.: Total annual cumulative snow melt amount (in mm meltwater equivalent per year, mm w.e. yr^{-1}) across the Larsen C ice shelf for each melt year (August - July, defined as in Luckman et al., 2014 and Bevan et al., 2018) in the period 1998-2017, plus the mean of all full melt years (bottom right panel). The 50 m elevation contour is given, approximately the height of the modelled ice shelf at the grounding line.

Table 6.7.: Pearson correlation coefficients between daily mean modelled variables over the Larsen C ice shelf during the entire hindcast period, for all months. Only values that are significant at the 99% level are given. Correlations between E$_{melt}$ and other variables are indicated in bold.

	SW$_{net}$	**LW**$_{net}$	**SW**$_{\downarrow}$	**LW**$_{\downarrow}$	**H**$_{L}$	**H**$_{S}$	**E**$_{melt}$	**CC**	**LWP**	**IWP**
SW$_{net}$	1	-0.41	0.99	0.34	-0.64	-0.26	**0.56**	-0.19		-0.20
LW$_{net}$		1	-0.34	0.62	0.40	-0.32	**-0.12**	0.83	0.60	0.57
SW$_{\downarrow}$			1	0.41	-0.63	-0.30	**0.52**	-0.12	0.17	-0.14
LW$_{\downarrow}$				1	-0.11	-0.27	**0.33**	0.63	0.77	0.42
H$_{L}$					1	0.13	**-0.19**	0.14		0.28
H$_{S}$						1	**-**	-0.26	-0.25	-0.18
E$_{melt}$							**1**		**0.17**	
CC								1	0.50	0.49
LWP									1	0.38
IWP										1

($r_{SW_{net},E_{melt}}$ = 0.45) and a negative correlation between E$_{melt}$ and cloud cover ($r_{melt,CC}$ = -0.2). This emphasises the conclusions of Chapter 5 that SW radiation is the dominant driver of surface melting. The strongest positive (negative) correlations between E$_{melt}$ and SW$_{\downarrow}$ (cloud cover) throughout the year are found closest to the mountains, in inlets (not shown), which may indicate that foehn-related cloud clearance can enhance melt, as found by Grosvenor et al. (2014).

Annually, E$_{melt}$ is negatively correlated with LW$_{net}$ ($r_{LW_{net},E_{melt}}$ = -0.12) but positively correlated with LW$_{\downarrow}$ ($r_{LW_{\downarrow},E_{melt}}$ = 0.33, Table 6.7), which is also seen in MAM and SON (Table 6.8). This suggests the importance of cloud liquid water contents and atmospheric water vapour, especially in the shoulder seasons of MAM and SON: when low-level liquid clouds are present they radiate strongly in the infrared, increasing LW$_{\downarrow}$ but also raise the surface temperature, which raises LW$_{\uparrow}$ and causes LW$_{net}$ to become negative. This process, whereby low-level liquid clouds warm the surface and initiate melt, has been observed in Greenland and other locations in Antarctica (Bromwich et al., 2012; Bennartz et al., 2013; van Tricht et al., 2016; Hines et al., 2019) and is also described in Chapter 5 and Gilbert et al. (2020). As cloud develops and begins to glaciate, particles grow and eventually reach precipitable size, so the cloud begins to dissipate, allowing more SW radiation to reach the surface. Because SW radiation is the dominant driver of melting, this sustains and intensifies melt. In months where SW radiation is not a significant contributor to the SEB, melting is driven by other fluxes, for example turbulent fluxes during foehn events.

Table 6.8.: As in Table 6.7, but for individual seasons.

DJF

	SW$_{net}$	**LW**$_{net}$	**SW**$_{\downarrow}$	**LW**$_{\downarrow}$	**H**$_L$	**H**$_S$	**E**$_{melt}$	**CC**	**LWP**	**IWP**
SW$_{net}$	1	-0.83	0.97	-0.7	-0.54	0.16	**0.45**	-0.73	-0.69	-0.52
LW$_{net}$	-0.83	1	-0.76	0.96	0.47	-0.39	**-0.19**	0.96	0.81	0.52
SW$_{\downarrow}$	0.97	-0.76	1	-0.63	-0.56	-	0.42	-0.65	-0.62	-0.45
LW$_{\downarrow}$	-0.7	0.96	-0.63	1	0.45	-0.32	-	0.93	0.81	0.49
H$_L$	-0.54	0.47	-0.56	0.45	1	-0.09	**0.15**	0.34	0.44	0.39
H$_S$	0.16	-0.39	-	-0.32	-0.09	1	**0.38**	-0.5	-0.23	-0.15
E$_{melt}$	**0.45**	**-0.19**	**0.42**	-	**0.15**	**0.38**	**1**	**-0.2**	**-0.17**	**-0.16**
CC	-0.73	0.96	-0.65	0.93	0.34	-0.5	**-0.2**	1	0.71	0.45
LWP	-0.69	0.81	-0.62	0.81	0.44	-0.23	**-0.17**	0.71	1	0.5
IWP	-0.52	0.52	-0.45	0.49	0.39	-0.15	**-0.16**	0.45	0.5	1

MAM

	SW$_{net}$	**LW**$_{net}$	**SW**$_{\downarrow}$	**LW**$_{\downarrow}$	**H**$_L$	**H**$_S$	**E**$_{melt}$	**CC**	**LWP**	**IWP**
SW$_{net}$	1	-0.28	0.99	0.17	-0.33	-0.1	**0.07**	-0.15	-	-0.17
LW$_{net}$	-0.28	1	-0.21	0.79	0.32	-0.42	-	0.91	0.69	0.57
SW$_{\downarrow}$	0.99	-0.21	1	0.24	-0.31	-0.13	-	-0.09	0.1	-0.11
LW$_{\downarrow}$	0.17	0.79	0.24	1	0.22	-0.08	**0.15**	0.77	0.78	0.5
H$_L$	-0.33	0.32	-0.31	0.22	1	0.09	**0.08**	0.15	0.22	0.3
H$_S$	-0.1	-0.42	-0.13	-0.08	0.09	1	**0.28**	-0.43	-0.16	-0.21
E$_{melt}$	**0.07**	-	-	**0.15**	**0.08**	**0.28**	**1**	-	**0.11**	**0.08**
CC	-0.15	0.91	-0.09	0.77	0.15	-0.43	-	1	0.6	0.52
LWP	-	0.69	0.1	0.78	0.22	-0.16	**0.11**	0.6	1	0.43
IWP	-0.17	0.57	-0.11	0.5	0.3	**-0.21**	0.08	0.52	0.43	1

JJA

	SW$_{net}$	**LW**$_{net}$	**SW**$_{\downarrow}$	**LW**$_{\downarrow}$	**H**$_L$	**H**$_S$	**E**$_{melt}$	**CC**	**LWP**	**IWP**
SW$_{net}$	1	-0.21	1	-0.21	-	0.09	-	-	-0.14	-0.14
LW$_{net}$	-0.21	1	-0.19	0.86	0.39	-0.43	-	0.75	0.67	0.63
SW$_{\downarrow}$	1	-0.19	1	-0.19	-	0.09	-	-	-0.12	-0.12
LW$_{\downarrow}$	-0.21	0.86	-0.19	1	0.3	-	**0.07**	0.75	0.73	0.62
H$_L$	-	0.39	-	0.3	1	-0.15	-	0.09	0.32	0.29
H$_S$	0.09	-0.43	0.09	-	-0.15	1	**0.11**	-0.16	-0.07	-0.23
E$_{melt}$	-	-	-	**0.07**	**0.11**	**1**	-	**0.12**	-	
CC	-	0.75	0	0.75	0.09	-0.16	-	1	0.46	0.52
LWP	-0.14	0.67	-0.12	0.73	0.32	-0.07	**0.12**	0.46	1	0.46
IWP	-0.14	0.63	-0.12	0.62	0.29	-0.23	-	0.52	0.46	1

SON

	SW$_{net}$	**LW**$_{net}$	**SW**$_{\downarrow}$	**LW**$_{\downarrow}$	**H**$_L$	**H**$_S$	**E**$_{melt}$	**CC**	**LWP**	**IWP**
SW$_{net}$	1	-0.51	0.98	0.08	-0.62	-0.23	**0.33**	-0.41	-0.09	-0.32
LW$_{net}$	-0.51	1	-0.43	0.74	0.37	-0.32	-	0.84	0.65	0.62
SW$_{\downarrow}$	0.98	-0.43	1	0.15	-0.61	-0.31	**0.29**	-0.35	-	-0.26
LW$_{\downarrow}$	0.08	0.74	0.15	1	-	-0.20	**0.22**	0.69	0.77	0.53
H$_L$	-0.62	0.37	-0.61	-	1	-	**-0.14**	0.17	0.08	0.28
H$_S$	-0.23	-0.32	-0.31	-0.20	-	1	**0.07**	-0.14	-0.19	-0.16
E$_{melt}$	**0.33**	-	**0.29**	**0.22**	**-0.14**	**0.07**	**1**	-	**0.14**	-
CC	-0.41	0.84	-0.35	0.69	0.17	-0.14	-	1	0.50	0.51
LWP	-0.09	0.65	-	0.77	0.08	-0.19	**0.14**	0.50	1	0.41
IWP	-0.32	0.62	-0.26	0.53	0.28	-0.16	-	0.51	0.41	1

SW and LW fluxes (both net and downwelling) are typically anti-correlated, suggesting LW fluxes are small during periods of high SW and vice versa – this, and the negative correlation between cloud cover and SW fluxes indicates the importance of cloud in controlling the SEB.

Cloud properties influence the radiative fluxes, and hence melting. A statistically significant correlation is only modelled between E_{melt} and cloud cover in DJF, when $r_{CC,E_{melt}}$ = -0.20 (Table 6.8). Annually there is a significant correlation, but it is very weak ($r_{CC,E_{melt}}$ = -0.05, Table 6.7). However, although the modelled cloud volume fraction appears unimportant in determining E_{melt}, cloud phase does influence melting. Cloud liquid contents are especially important: in all seasons except DJF (when melting is overwhelmingly driven by $SW_{\downarrow}$), correlation coefficients between E_{melt} and LWP are positive ($r_{LWP,E_{melt}}$ = 0.11, 0.12, 0.14 and 0.17 for MAM, JJA, SON and ANN, respectively, Tables 6.7 and 6.8). Correlations between E_{melt} and IWP are mostly very small and insignificant, likely because the LW effect of liquid dominates in mixed phase cloud and ice is relatively transparent to SW (Zhang et al., 1996, Chapter 5). The positive correlation between E_{melt} and LWP is consistent with the dominant role cloud liquid plays in determining the LW fluxes: the correlation coefficient of $LW_{\downarrow}$ with cloud cover and LWP, respectively, is $r_{CC,LW\downarrow}$ = 0.63 and $r_{LWP,LW\downarrow}$ = 0.77 through the whole period, but both are especially large in DJF when they rise to $r_{CC,LW\downarrow}$ = 0.93 and $r_{LWP,LW\downarrow}$ = 0.81, respectively.

Turbulent fluxes become important for driving melting in specific seasons. Positive correlations are modelled between E_{melt} and H_S and in all seasons, but annually it is only significant at the 95% level. The correlation is largest in DJF ($r_{H_S,E_{melt}}$ = 0.38) when temperature gradients are at their most extreme because air temperatures are warmest and surface temperatures do not rise above the melting point of 0°C. This correlation coefficient is almost as large as $r_{SW_{net},E_{melt}}$ in DJF, suggesting that foehn events are almost as important for driving melting as SW fluxes. In all seasons, foehn events are associated with higher H_S fluxes, which drive melting, so $r_{H_S,E_{melt}}$ is positive. The combined effect of foehn and warm air advection may explain why the correlation is higher in DJF and MAM. In contrast, H_L is negatively correlated with E_{melt} annually and in SON, which is consistent with melt occurring when the overlying air mass is drier than the surface, for example during foehn events or when drier air masses are advected over a melting surface. However, the correlation is positive during DJF and MAM ($r_{H_L,E_{melt}}$ = 0.15 and 0.08 in DJF and MAM, respectively, Table 6.8), suggesting that melting occurs when H_L fluxes are positive, indicative of condensation. This is likely because MAM and DJF are the only seasons when temperatures are warm enough for the air to hold more moisture than the surface, so when warmer air moves over the ice shelf,

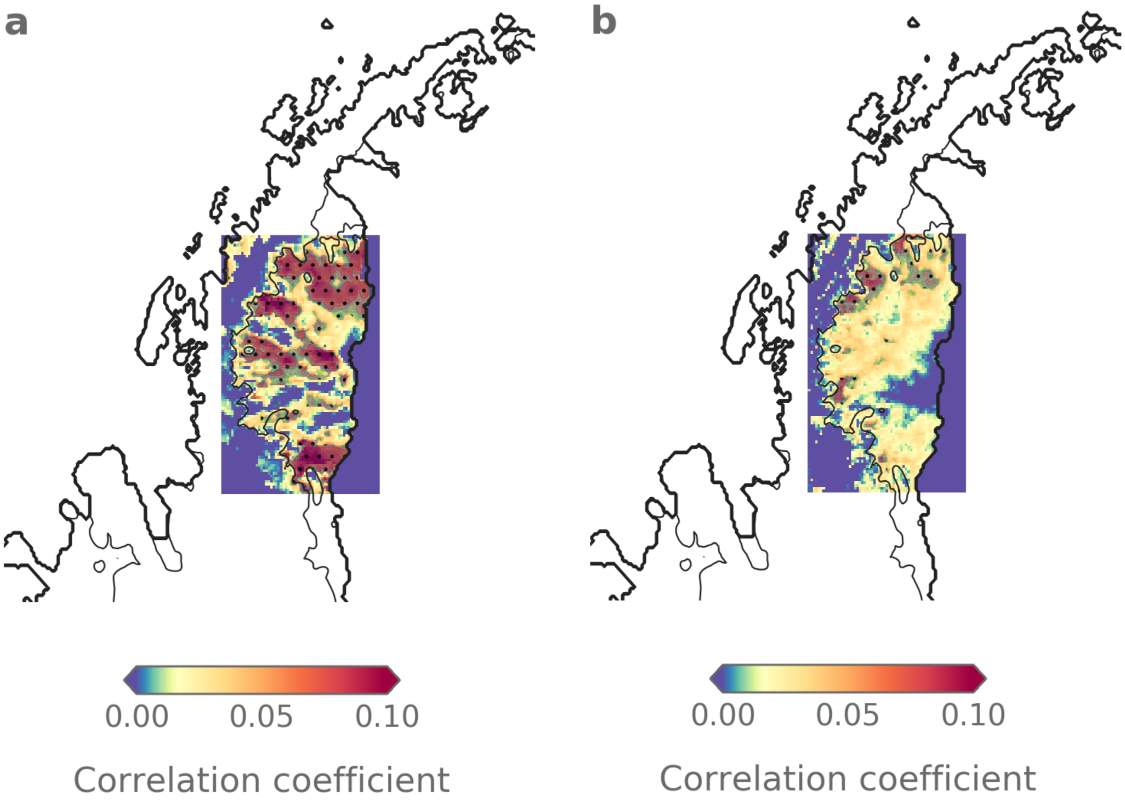

Figure 6.11.: Pearson correlation coefficient across the Larsen C ice shelf between derived foehn index, FI (see main text), and simulated melt amount during a) MAM and b) SON. Areas where the correlation is significant at the 90% level are indicated with shading and stippling.

condensation or freezing can occur. These warm conditions likely coincide with periods of melting.

6.8.2 Spatial correlations

In order to spatially correlate foehn frequency with melt amount, a "Foehn Index" is devised that describes the intensity of each event. The foehn index, FI, defined in Equation 6.1, combines the percent change in temperature and relative humidity when airflow impinging on the peninsula is westerly (i.e. $u_{Z1} \geq 2.0$ m s^{-1}). As described in section 6.6, u_{Z1} is calculated at each time step as the mean u wind between 200-2000 m (representative of the mean flow impinging on the peninsula) in the area marked region "X" in Figure H.1. At each time step that $u_{Z1} \geq 2.0$ m s^{-1}, the percentage change in air temperature and relative humidity over 6 hours, dT_{6hr} and dRH_{6hr}, respectively, is calculated for all gridboxes, and the change in relative humidity is subtracted from the change in air temperature such that a positive value indicates a foehn event and values are normalised such that changes in air temperature and relative humidity are equally important.

$$FI = \begin{cases} dT_{6hr} - dRH_{6hr} & u_{Z1} \geq 2.0ms^{-1} \\ 0 & u_{Z1} < 2.0ms^{-1} \end{cases} \tag{6.1}$$

The mean foehn index during each season is shown in Appendix G. Averaged across all of Larsen C, FI is highest during SON, consistent with greater overall frequency of foehn events in this season (Table 6.3), but higher in inlets during DJF, perhaps suggesting a role for more intense, rather than extensive foehn events in DJF than in SON. During all periods, the largest values of FI are found in the northwestern inlets, where the highest meltwater production rates and melt durations are found, yet again suggesting an important role for foehn in causing surface melting.

Correlations between FI and surface meltwater production across Larsen C are largest and most statistically significant in the inlets. Figure 6.11 shows the Pearson correlation coefficients between FI and melt amount during MAM and SON. The correlation is highest and most widely significant during MAM, suggesting that relatively more melt is caused by foehn in MAM, and in both seasons is most significant closest to high elevation. However, correlations are typically small (r $<$ 0.1) and not significant across the whole Larsen C ice shelf, which may indicate that foehn events are not the only driver of surface melting in these seasons, or that the foehn index does not capture all foehn events. During MAM, regions downstream of lower elevation topography - the "jet" regions identified by Elvidge et al. (2015) - exhibit negative correlations, suggesting that foehn events do not contribute to surface melting here because these regions are associated with cooler temperatures during foehn. This emphasises the role of foehn in driving surface melt downwind of steep topography, especially in MAM. Next, the dominant regimes associated with surface melting are evaluated using a composite approach.

6.8.3 Regimes influencing melt on Larsen C

To diagnose the dominant causes of surface melting in the hindcast, several regimes are determined. These are abbreviated as indicated in the caption of Table 6.10 and Appendix H. The seasonal mean frequency of occurrence and percentage of total meltwater production occurring during each regime throughout the whole hindcast period are given in Table 6.10. Table 6.10 shows that the cloudy regime is most common in all seasons, while the barrier wind regime occurs least frequently in most seasons. Some regimes, such as the ENSO, SAM and barrier wind regimes, are more common in certain seasons, whereas others vary relatively less between seasons. Daily means of surface meteorological variables and SEB components during each regime are averaged to produce composites, as in section 6.5.1 and Figure 6.3.

To diagnose each regime, various indicator variables, thresholds and regions are established. These are summarised in Table H.1. The regions used for averaging indicator variables are shown in Figure H.1 and data sources and treatments are described in detail in Appendix H. Large-scale circulation patterns (SAM and ENSO) are diagnosed using observed indices (NOAA's CPC index and the Nino3.4 index for SAM and ENSO, respectively). For the SAM, the threshold for positive and negative periods, respectively, is taken to be ± one standard deviation of the time series 1998-2017. The phase of ENSO is defined according to the World Meteorological Organization by taking the three-month running mean of sea surface temperature anomalies in the Nino3.4 region. Positive (negative) ENSO periods are diagnosed when three-month running mean anomalies exceed (fall below) +0.5°C (-0.5°C). Other regimes are determined from model output and diagnosed from "indicator variables". For example, the barrier wind regime is diagnosed when meridional wind speeds in the box indicated in Table H.1 and marked "B" in Figure H.1 exceed 5.0 m s^{-1}, while the "blocked" regime occurs during periods where u_{Z1} (as defined in section 6.6) $\geq$ 2.0 m s^{-1} and Fr $<$ 0.5. For further details, please refer to Appendix H.

Figure 6.12 shows synoptic meteorological conditions (panels a-d) and E_{melt} anomalies (panels e-h) during periods of significant melting (melt amount $> 75^{th}$ percentile) in all seasons. As shown in Table 6.9, 90% of melting occurs during DJF, with 4% and 5% occurring in MAM and SON, respectively. Throughout the year, significant melting occurs during periods of north-westerly flow, which produces cross-peninsula winds and establishes foehn conditions, and/or during warm air advection events. As shown in Chapter 4 and above, foehn increase H_S fluxes and significantly raise E_{tot} fluxes, driving surface melting. Table 6.9 shows seasonal mean meltwater production throughout the hindcast period. During JJA because melting is so rare ($<$ 0.1% of the time, Table 6.9), cross-peninsula flow must be exceptionally strong ($\sim$7 m s^{-1} and $\sim$20 m s^{-1} at 10 m upwind and in inlets, respectively), causing T_{max} anomalies of $\sim$20°C. During DJF when high SW fluxes cause temperatures to be at the melt point more frequently, much weaker cross-peninsula flow and very minimal T_{max} anomalies produce melt above the 75^{th} percentile, and significant melt events can also occur during clear periods (this is also seen in Figure 6.3d, which shows positive E_{melt} anomalies during clear conditions in DJF). Summertime melting is less intense, with 63% of DJF meltwater production occurring in "high melt" periods, which occur 25% of the time (Table 6.10). This differs from SON, MAM and JJA, when melting occurs almost exclusively during intense, confined melt events associated with cross-peninsula flow, with 93%, 100% and 100% of seasonal meltwater production occurring in just 9%, 25% and 3% of the time, respectively.

Table 6.9.: Percentage of modelled cumulative meltwater produced during each season.

Season	**Relative meltwater production**
JJA	<0.1%
SON	5.3%
DJF	90.4%
MAM	4.2%

Conversely, low melt periods (melt amount $< 25^{th}$ percentile) are associated in DJF with the development of a southerly barrier jet that delivers cold air from high on the Antarctic plateau, typically established by cyclones in the Weddell Sea that produce coastal easterlies or southeasterlies, resulting in cold T_{max} anomalies over Larsen C (Figure 6.13). DJF is shown because this is when the majority of melting occurs. The similarities between panels a) and b) of Figures 6.13 and 6.14 suggest that this barrier jet regime is the dominant circulation pattern during low melt periods over Larsen C in DJF. Figure 6.14 shows three regimes that suppress surface melting over Larsen C in DJF. The barrier wind regime (panels a and b) has the largest effect on E_{melt} during DJF. Although E_{tot} is affected minimally (anomalies are small, not shown), E_{melt} anomalies are negative across the entire Larsen C ice shelf because of the negative T_{max} anomaly (Figure 6.14). SAM- (panels c and d) and ASL (panels e and f) regimes also suppress melting relative to DJF climatology.

As noted in Chapter 2 and above, SAM+ and ENSO- are associated with cross-peninsula flow that promotes foehn occurrence (Figure 6.15). Cross-peninsula flow (both flow-over and blocked regimes) is important for controlling surface melting on Larsen C, particularly outside DJF, when melting is more strongly associated with high SW (Chapter 5, section 6.8.1). ENSO- has a very minimal effect on E_{melt} anomalies in all seasons except MAM, when ENSO- conditions are associated with greater melting in inlets (Figure 6.15h). Positive and negative SAM regimes produce positive and negative E_{melt} anomalies (Figures 6.16b and 6.14b), respectively, especially in the immediate lee of steep terrain, consistent with the importance of SAM in producing foehn winds demonstrated in section 6.6.5 and Figure 6.7. As seen in Figure 6.15, mean synoptic meteorological conditions during SAM+ and ENSO- during MAM (panels b and d, respectively) are characterised by cross-peninsula winds, positive T_{max}

anomalies and positive H_S anomalies (not shown), which results in positive E_{melt} anomalies in inlets (Figure 6.15f and h). In DJF, SAM+ and ENSO- are associated with much weaker cross-peninsula flow (Figure 6.15a and c), but small positive E_{melt} anomalies are still modelled because surface temperatures are at the melting point and melt is driven primarily by $SW_{\downarrow}$.

As shown in section 6.6.5 and Figure 6.7, modelled foehn occurrence is correlated with observed SAM index. During MAM, when foehn is most common, 36% of surface melting occurs when SAM is positive (17% of the time, Table 6.10), which suggests that SAM is an important driver of inlet surface melting via its effect on foehn occurrence. During MAM and JJA, 100% and 97%, respectively, of the melting that occurs is associated with cross-peninsula flow (defined as above and in King et al., 2017, to be when $u_{Z1} \geq 2.0$ m s^{-1} - see Appendix E for details), despite these conditions occurring just 61% and 59% of the time (the sum of values cited in Table 6.10 for the flow-over and blocked regimes). In DJF and SON, 47% and 20%, respectively, of the melting that occurs is caused by other processes, such as warm air advection events or clear conditions leading to enhanced SW fluxes.

The second column of Figure 6.16 shows E_{melt} anomalies associated with regimes that enhance surface melting: b) flow-over, d) SAM+ and f) ENSO- conditions. Anomalies are shown for DJF, when their influence on E_{melt} is strongest, but similar spatial patterns are observed in all seasons with the exception of ENSO- in SON, which is associated with negative T_{max} and E_{melt} anomalies. These regimes are non-independent and the similarities between them suggest that SAM+ and ENSO- patterns produce flow-over conditions that result in foehn, which this chapter has conclusively demonstrated to exert a considerable influence on surface melting.

The composites presented in Figures 6.14, 6.15 and 6.16 demonstrate the importance of large-scale atmospheric circulation patterns, which establish local and regional atmospheric conditions that either promote or suppress surface melting on Larsen C.

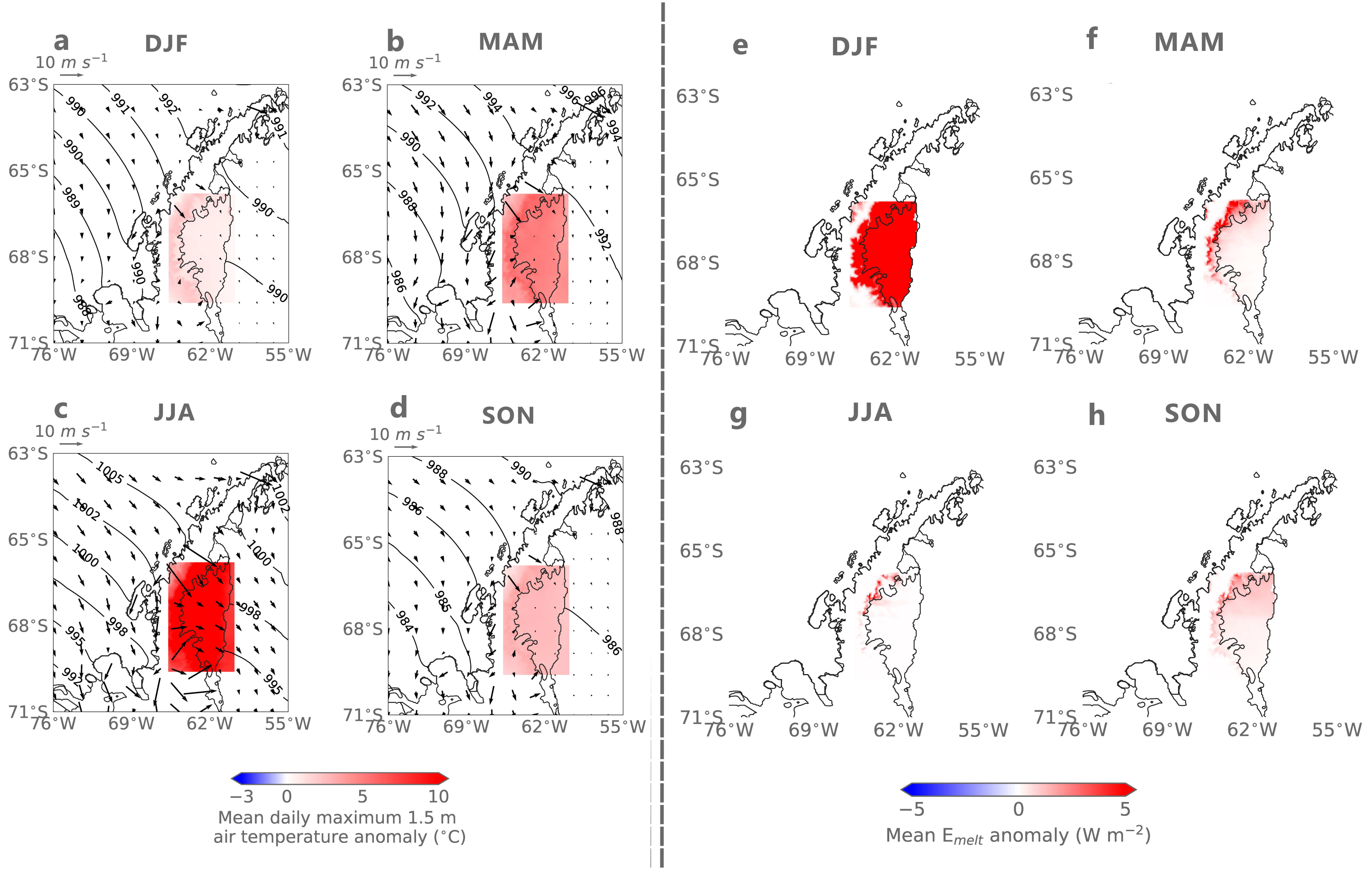
a
DJF
b
MAM
c
JJA
d
SON
e
DJF
f
MAM
g
JJA
h
SON
10 $m\,s^{-1}$
63°S
65°S
68°S
71°S
76°W
69°W
62°W
55°W
−3
0
5
10
Mean daily maximum 1.5 m air temperature anomaly (°C)
−5
0
5
Mean E_{melt} anomaly (W m^{-2})

Figure 6.12.: Composited mean conditions during the "high melt" regime (melt amount > 75^{th} percentile) for all seasons in the hindcast. Panels a) to d) show mean synoptic meteorological conditions, where coloured shading shows the mean daily maximum 1.5 m air temperature throughout this period, and contours and vectors give mean mean sea level pressure and 10 m winds, respectively. Panels e) to h) show seasonal mean melt flux anomalies relative to the 1998-2017 model climatology.

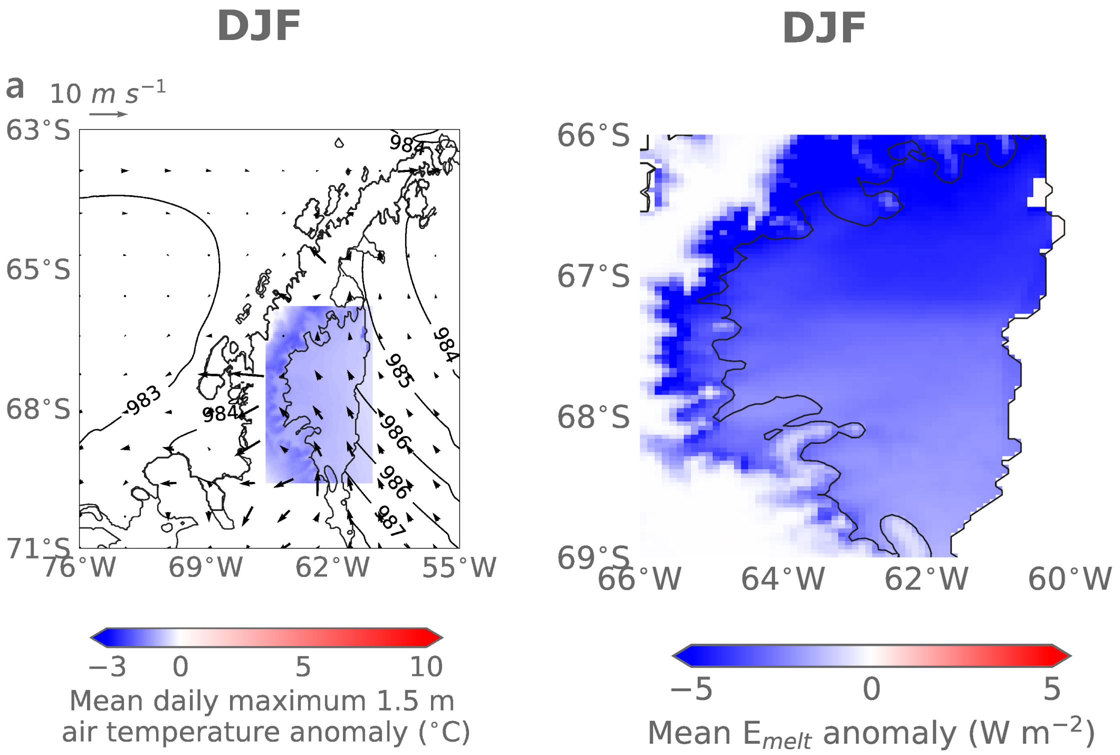
DJF
DJF
a
10 m s−1
63°S
65°S
68°S
71°S
76°W
69°W
62°W
55°W
983
984
984
985
986
986
987
984
−3
0
5
10
Mean daily maximum 1.5 m air temperature anomaly (°C)
66°S
67°S
68°S
69°S
66°W
64°W
62°W
60°W
−5
0
5
Mean E_melt anomaly (W m−2)

Figure 6.13.: Composited mean conditions during the "low melt" regime (melt amount < 25^{th} percentile) during DJF in the hindcast. Panel a) shows synoptic meteorological conditions, with colours, vectors and contours as in panels a - d of Figure 6.12. Panel b) shows seasonal mean melt flux anomalies, as in panels e - h of Figure 6.12.

Table 6.10.: Percentage of modelled meltwater production associated with each regime during each season, and the frequency at which they occur. Standard deviations are given in brackets next to each value. Regimes are abbreviated as defined in the main text, and as follows. "SAM+": positive SAM; "SAM-": negative SAM; "ENSO+" positive ENSO (La Niña conditions); "ENSO-": negative ENSO (El Niño conditions); "ASL": deep Amundsen Sea Low; "barrier": low-level southerly barrier jet over Larsen C; "blocked": blocked flow conditions; "flow-over": flow-over conditions; "LWP25": mean LWP < 25^{th} percentile; "LWP75": mean LWP > 75^{th} percentile; "melt25": mean meltwater production < 25^{th} percentile; "melt75": mean meltwater production > 75^{th} percentile; "cloudy": mean cloud fraction > 0.75; and "clear": mean cloud fraction < 0.31.

	DJF		**MAM**		**JJA**		**SON**	
	Melt amount	Regime frequency	Melt amount	Regime frequency	Melt amount	Regime frequency	Melt amount	Regime frequency
SAM+	25.0 (17.3)	21.9 (12.3)	38.9 (35.6)	17.4 (10.4)	21.9 (45.0)	22.2 (17.1)	24.5 (24.8)	16.9 (15.4)
SAM-	8.5 (11.3)	9.3 (9.7)	0.5 (21.9)	10.7 (11.4)	0.1 (17.0)	15.6 (13.6)	10.9 (20.9)	16.4 (14.3)
ENSO+	38.1 (34.6)	40.0 (36.0)	17.1 (44.5)	35.5 (40.5)	1.5 (35.5)	15.3 (30.6)	34.7 (46.7)	27.3 (38.6)
ENSO-	34.6 (28.7)	33.5 (31.0)	65.6 (42.6)	23.2 (40.0)	3.8 (20.7)	15.2 (25.6)	29.5 (44.1)	28.1 (42.8)
ASL	21.7 (11.8)	28.9 (9.1)	14.4 (26.4)	34.1 (10.8)	0.7 (32.0)	38.8 (14.3)	19.4 (20.2)	36.6 (14.3)
barrier	3.8 (2.4)	10.8 (5.4)	<0.1 (0.3)	15.9 (6.5)	0.0 (0.0)	19.3 (4.5)	1.4 (3.7)	18.3 (6.2)
blocked	44.4 (14.6)	40.5 (10.2)	33.4 (32.6)	44.1 (8.7)	22.9 (42.1)	43.1 (8.4)	55.7 (22.9)	46.7 (6.6)
flow-over	9.3 (7.7)	6.3 (4.0)	64.4 (32.9)	14.5 (7.3)	76.9 (44.6)	18.2 (5.8)	24.5 (22.6)	16.9 (6.9)
LWP25	32.0 (12.5)	25.0 6.6)	4.2 (20.2)	25.0 (6.5)	<0.1 (0.0)	25.0 (9.6)	8.4 (12.5)	25.0 97.6)
LWP75	15.2 (7.6)	25.0 (9.4)	44.4 (27.7)	25.0 (5.1)	90.7 (45.7)	25.0 (8.3)	35.7 (21.8)	25.0 (7.2)
melt25	0.8 (0.3)	24.5 (4.0)	<0.1 (0.2)	7.1 (2.9)	<0.1 (29.7)	0.6 (0.9)	<0.1 (0.2)	9.1 (3.6)
melt75	63.0 (13.1)	24.5 (8.7)	97.6 (8.8)	7.2 (5.3)	96.7 (44.4)	0.7 (1.0)	92.5 (20.4)	9.1 (4.5)
cloudy	50.2 (12.1)	58.9 (8.7)	69.1 (32.9)	56.9 (7.6)	95.5 (37.4)	54.1 (9.5)	56.6 (21.2)	64.1 (6.8)
clear	9.8 (6.9)	7.8 (4.0)	2.4 (6.3)	9.2 (4.0)	0.0 (0.0)	10.8 (5.9)	4.2 (6.4)	6.9 (3.9)

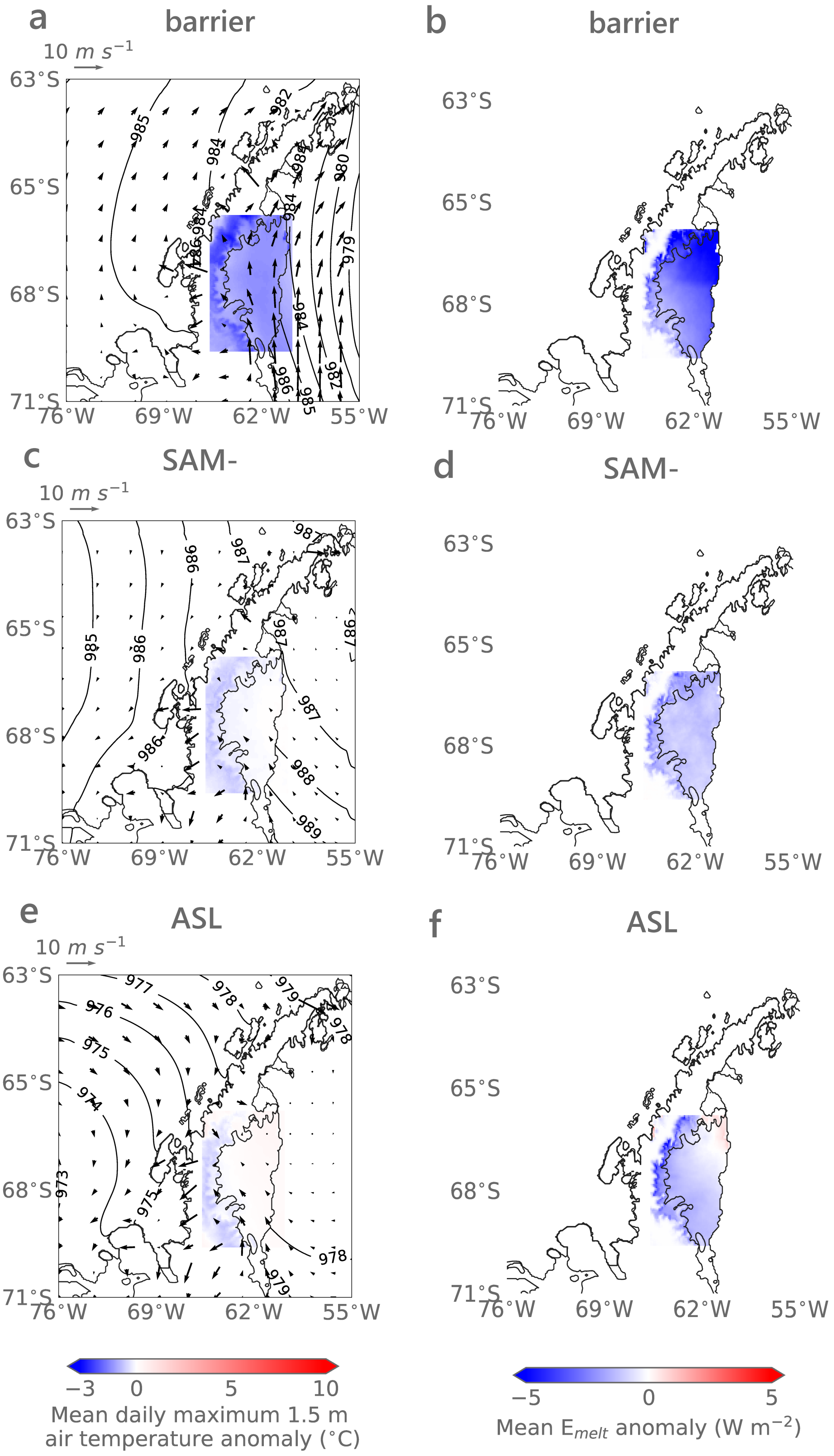
a
barrier
b
barrier
c
SAM-
d
SAM-
e
ASL
f
ASL
10 $m\ s^{-1}$
63°S
65°S
68°S
71°S
76°W
69°W
62°W
55°W
985
984
982
980
979
986
987
988
989
977
978
976
975
974
973
−3
0
5
10
Mean daily maximum 1.5 m air temperature anomaly (°C)
−5
0
5
Mean E_{melt} anomaly (W m^{-2})

Figure 6.14.: Composited mean synoptic meteorological conditions and mean E_{melt} anomalies in DJF associated with three regimes that reduce E_{melt} relative to climatology: the barrier wind ("barrier", panels a and b), negative SAM ("SAM-", panels c and d) and deep ASL ("ASL", panels e and f) regimes. Colours, contours and vectors are as in previous plots.

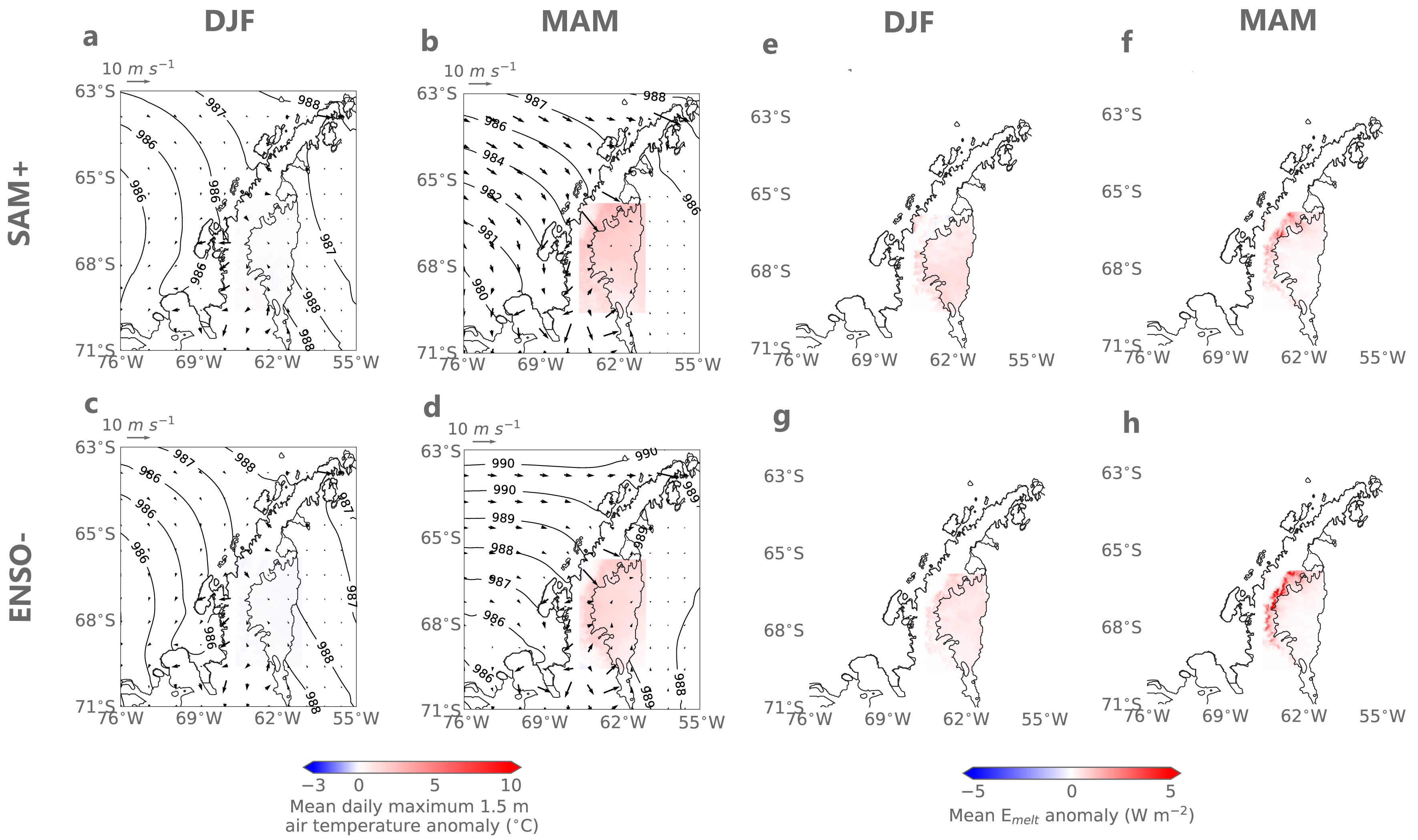
DJF
MAM
DJF
MAM
SAM+
ENSO-
a
b
c
d
e
f
g
h
10 $m\ s^{-1}$
63°S
65°S
68°S
71°S
76°W
69°W
62°W
55°W
986
987
988
984
982
981
980
989
990
−3
0
5
10
Mean daily maximum 1.5 m air temperature anomaly (°C)
−5
0
5
Mean E_{melt} anomaly (W m^{-2})

Figure 6.15.: Composited mean conditions modelled during positive and negative phases of SAM and ENSO (SAM+ and ENSO-, respectively) during DJF and MAM. As in Figure 6.12, panels a to d show synoptic near-surface meteorological conditions associated with each regime, while panels e to h show mean E_{melt} anomalies associated with each regime. The upper and lower rows show composites for SAM+ and ENSO- regimes, respectively.

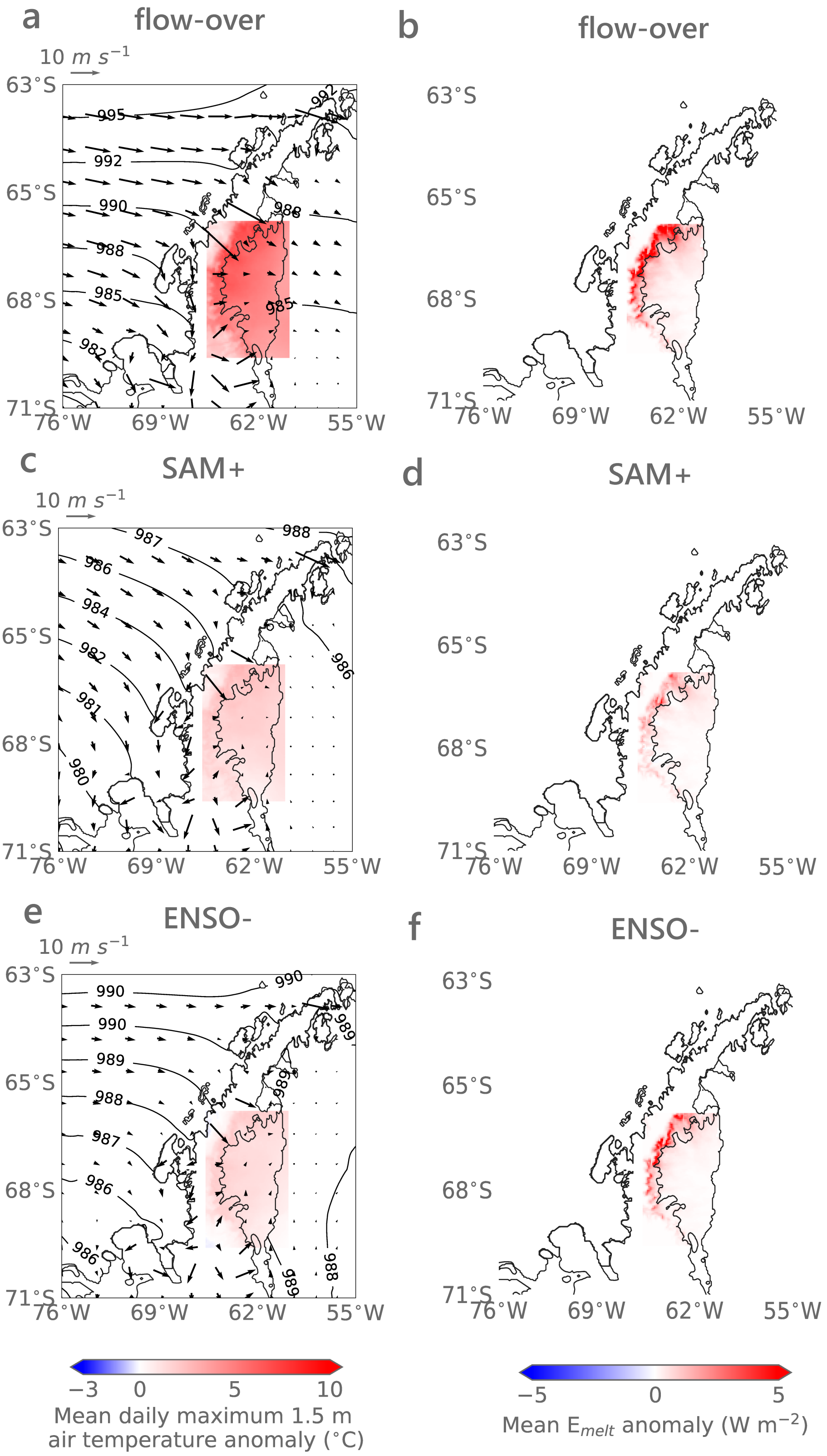
a
flow-over
10 $m\ s^{-1}$
995
992
990
988
986
985
982
b
flow-over
c
SAM+
987
988
986
984
982
981
980
d
SAM+
e
ENSO-
990
989
988
987
986
f
ENSO-
63°S
65°S
68°S
71°S
76°W
69°W
62°W
55°W
−3
0
5
10
Mean daily maximum 1.5 m air temperature anomaly (°C)
−5
0
5
Mean E_{melt} anomaly (W m^{-2})

Figure 6.16.: Composited mean synoptic meteorological conditions and mean E_{melt} anomalies in MAM associated with three regimes that increase E_{melt} relative to climatology: the flow-over ("flow-over", panels a and b), positive SAM ("SAM+", panels c and d) and negative ENSO ("ENSO-", panels e and f) regimes. Colours, contours and vectors are as in previous plots.

6.9 Summary and conclusions

This chapter has evaluated the drivers of melting on the Larsen C ice shelf and parts of the Antarctic Peninsula using an original MetUM model hindcast of the period 1998-2017, by focusing on synoptic meteorology, cloud, the SEB and large-scale circulation. Model validation at four AWSs show that the model performs well with respect to observations, although the annual mean daily mean melt flux is under-estimated by 17-31%. E_{melt} biases are largest in DJF, when the majority (90%) of melting occurs, and are positive at AWS 14, but negative at inlet stations, suggesting that the model may be struggling to entirely represent foehn-driven melt, or stable boundary layers. The warm temperature bias causes $LW_{\uparrow}$ to be over-estimated, leading to a LW cooling of the surface, especially in JJA when stable conditions dominate. This energy deficit means that there is sometimes too little energy available for melting despite the surface reaching melting point, which causes the melt flux to be under-estimated.

Seasonal differences are apparent in the modelled SEB, and in the SEB at inlet vs. ice shelf stations. In DJF, SW fluxes dominate the SEB and melting frequently occurs across the ice shelf, while during JJA, the turbulent fluxes become more important, and melting is occasionally modelled at inlet stations, associated with foehn events. As also shown in Chapter 5, cloud phase influences radiative fluxes, and consequently the SEB, during DJF. Larsen C is cloudy 92% of the time throughout the year, although this varies seasonally, with cloudy conditions dominating in DJF (93% of the time) and less common in JJA (89%). The effects of cloud on the SEB are explored using a composite approach, comparing "clear" vs. "cloudy" conditions. Cloudy conditions on Larsen C tend to be associated with warmer mean daily maximum air temperatures, and circulation patterns that advect moist air onto the ice shelf from either the west or southeast. Mean daily maximum temperatures above the melting point are commonly observed in DJF, supporting the findings of Chapter 5 that clouds can initiate or sustain surface melting on Larsen C. In DJF, cloudy conditions are associated with negative melt anomalies because they reduce $SW_{\downarrow}$, while clear conditions promote surface melting. The opposite is true in other seasons because cloudy conditions raise E_{tot} relative to clear-sky periods. However, because temperatures are typically below melting point in this scenario, melting rarely occurs. This suggests that cloud-mediated melting, whereby clouds warm the surface and initiate melting via the process described in Chapter 5, could become more important in future as climate change pushes mean temperatures higher. Such cloud-mediated melting would likely be most important at the beginning and end of the melt season, when SW is a less dominant driver of surface melting.

Foehn have been consistently identified in the literature and in this thesis as an important factor in determining the weather and climate of Larsen C, and of causing surface melting that could potentially have implications for glaciological processes like hydrofracturing and ice shelf destabilisation. Simulated spatial patterns of foehn occurrence are consistent with theory and exhibit an east-west gradient, declining in frequency with distance from the peninsula mountains. This matches the pattern of surface melting observed using satellite measurements and other in situ methods, supporting the hypothesis that foehn exert an important influence on melting over Larsen C. To understand the role of foehn in driving melt, a single, high-melt, high-foehn season is examined as a case study. This analysis shows that strong cross-peninsula flow produces foehn conditions in MAM 2016, which results in large positive temperature anomalies, and dramatically enhances the turbulent heat fluxes. During this season the SEB becomes dominated by H_S and melting occurs frequently, resulting in E_{melt} anomalies of up to 10 W m^{-2} in the lee of the mountains because foehn events raise temperatures high enough to reach the melting point. This results in much greater meltwater production than typically occurs outside DJF, accounting for 35% of meltwater production for the entire melt season, eight times greater than the simulated MAM average of 4% for the entire hindcast period. Modelled foehn frequency is shown to be strongly correlated with observed SAM index (r = 0.62), which suggests that more foehn, and therefore more melting, could result from the trend towards a more positive SAM that has been recorded over recent decades. However, no trends in foehn frequency are evident over the hindcast period, although this is a relatively short amount of time and the signal may be complicated by other factors.

Meltwater production rates, which are more useful for quantifying the surface mass balance of the ice shelf, and hence predicting Larsen C's future, compare well with the few values found in the literature, although caution should be used when interpreting absolute melt totals. This represents an advance in our understanding of meltwater production over the Larsen C ice shelf in recent decades because observations of meltwater production are difficult to make.

The final part of this chapter examined the causes of melting in more specific terms. Ice-shelf integrated correlations show that radiative fluxes, especially SW, are strongly related to surface melting, and that cloud properties have a small but important influence. Specifically, cloud liquid water content is more important for melt than cloud fraction or ice contents, underlining the conclusions of Chapter 5 that correctly simulating cloud phase is vital for constraining the SEB and hence surface melting. As demonstrated in Chapter 4 and above, turbulent fluxes are important during foehn events and so are correlated with E_{melt}. A composite approach is used to explore the importance of several different regimes in causing melting. Large-scale patterns such as SAM and ENSO and regional features such as the ASL and barrier winds influence atmospheric circulation in the region, and can affect the surface meteorology and SEB. Annually, flow-over conditions, which are associated with SAM+ and ENSO-, produce large mean daily maximum air temperatures, and are associated with SEB anomalies that drive melting on the lee of the mountains. SAM+, ENSO- and flow-over regimes account for 27.4%, 25% and 43.8% of annual melting over the hindcast period, despite occurring only 19.6%, 33.4% and 14.0% of the time, respectively. Conversely, barrier wind and deep ASL regimes are associated with comparatively less melting (1.3% and 14.1%, despite occurring 16.1% and 34.6% of the time, respectively).

The most important drivers of surface melting on Larsen C can be summarised as follows. Firstly, foehn winds are the most important driver of melt in non-summer seasons, especially MAM, but this only accounts for 10% of annual meltwater production. SW radiation is the most important driver of melting in DJF, when 90% of melting occurs, although foehn winds are also important because they enhance already high melt fluxes and can cause cloud clearance. Foehn events are associated with 63% of meltwater production during DJF.

Secondly, in DJF cloud reduces surface melting by reducing E_{tot} (reflecting incoming SW radiation and therefore reducing $SW_{\downarrow}$). The opposite is true in other seasons - cloud warms the surface and increases E_{tot}. Because temperatures in SON/MAM can hover just below 0°C, this suggests that as temperatures on the peninsula rise, as is projected to occur as climate changes (van Oldenborgh et al., 2013), cloud-mediated melting could become more important. This effect would likely extend the melt season because surface temperatures would reach/remain at the melting point earlier/later in the year, permitting the enhanced $LW_{\downarrow}$ and E_{tot} fluxes associated with cloud to warm the surface and initiate melt via the same processes outlined in Chapter 5. Warmer, more humid conditions could also be expected to produce thicker clouds with higher liquid water contents, which may also enhance $LW_{\downarrow}$ fluxes.

Thirdly, large-scale circulation influences local and regional meteorology by establishing dominant flow regimes. SAM+ and ENSO- promote melting, while a deep ASL (associated with negative MSLP anomalies to the west of the Antarctic Peninsula) and barrier winds suppress surface melting on Larsen C. The high correlation between modelled foehn frequency and SAM, alongside the importance of foehn in driving surface melting that has been demonstrated in this chapter, suggest that if trends towards a more positive SAM continue, then foehn-related surface melting on Larsen C could increase.

Fourthly, the characteristics of airflow in cross-peninsula regimes (i.e. blocked/flow-over conditions) determines the intensity and extent of the leeside foehn effect and therefore its impact on surface melting over Larsen C.

Finally, although meltwater production rates on Larsen C have not yet reached the values observed on Larsen B before its collapse, higher foehn frequency and rising temperatures associated with a more positive SAM and global climate change could contribute to greater meltwater production by allowing melt to occur more frequently, and for that melt to be more intense. This could lead to the eventual destabilisation of Larsen C via hydrofracturing, with far-reaching implications for global sea level rise. Quantifying the future fate of the Larsen C ice shelf is beyond the scope of this chapter, but should be a focus of research to determine change on the Antarctic Peninsula.

7

Summary and conclusions

The objective of this thesis was to identify the primary atmospheric causes of surface melting on Larsen C. This was done in three sections (Chapters 4 to 6), examining the role of specific atmospheric processes and properties in case studies and a multi-decadal hindcast. The primary analysis tool used throughout was the MetUM: model output was compared with observations from AWSs and aircraft during case studies to understand the processes driving surface melting under specific conditions, and AWS data alone was compared with model output when airborne observations were not available. Finally, to achieve a longer-term perspective, and to address the dearth of observational information on Larsen C, the MetUM was used to produce a multi-decadal hindcast that was validated using AWS data. The results presented in this thesis are novel and advance scientific understanding of the dominant processes and atmospheric drivers of melt on Larsen C.

Firstly, the importance of warm, dry foehn winds in driving elevated surface melting observed at Cabinet Inlet (AWS 18) during May 2016 was demonstrated in Chapter 4. Model simulations of two case studies confirmed that foehn occurred, and showed that foehn was produced via the isentropic drawdown mechanism. The sourcing of potentially warmer air from higher altitudes and the non-linearity of the flow led to high wind speeds and significant surface warming in the immediate lee of the mountains, and non-linear features like hydraulic jumps were simulated. In both cases, foehn events were associated with greatly increased turbulent fluxes, especially of sensible heat, which increased by almost ten times to $\sim$350 W m^{-2} in the stronger case. The delivery of large amounts of sensible heat to the surface produced a surplus of energy (large E_{tot} fluxes) and brought surface temperatures to the melting point, which allowed intense surface melting to occur. During this case, surface melt fluxes reached $\sim$310 and $\sim$280 W m^{-2} and cumulative meltwater production totalled 72.2 and 37.7 mm w.e. in observations and model output, respectively. This was the first time that considerable wintertime surface melting on Larsen C had been identified and attributed to foehn events. The results of Chapter 4 demonstrate that foehn can considerably alter the SEB and suggest that foehn events may be an extremely important driver of melting in seasons where there is little or no solar radiation. This has implications for estimates of surface melting, which may be under-estimated if these events are not taken into consideration. Some of these findings have been published in Kuipers Munneke et al. (2018) (Appendix A).

Secondly, Chapter 5 examined the link between summertime cloud phase and the SEB on Larsen C. Much of this work has been published in Gilbert et al. (2020) (Appendix B). Cloud phase was shown to strongly influence the SEB by controlling the radiative fluxes received at the surface. Cloud vertical structure was shown to be an important factor governing the surface radiative effect of summertime clouds and therefore to influence the amount of melting that occurs. The parameterisation of cloud properties in models like the MetUM is relatively simplified, and can introduce errors. An assessment of cloud vertical profiles during summertime case studies demonstrated that more accurately representing cloud phase can reduce biases in SEB terms, including surface melt. An optimised model configuration, RA1M_mod, was developed by comparing several configurations with varying parameterisations of cloud. RA1M_mod is based on the MetUM's mid-latitude physics package, and uses single-moment microphysics with adaptations designed to limit the conversion of liquid to ice via vapour deposition and riming, two processes that are known to contribute to model cloud and SEB biases.

Several double-moment configurations were also tested for two case studies, f150 and f152, conducted on the 15 and 18 January 2011, during which relatively more liquid and more ice were observed, respectively. Contrary to studies that use other high-resolution regional atmospheric models (such as WRF) to explore the link between modelled cloud phase and SEB, Chapter 5 found that several variants of the MetUM's double-moment cloud microphysics scheme, CASIM, were unable to simulate observed cloud fields as well as this optimised single-moment configuration. CASIM's poor performance may be related to the aerosol data used as input to the scheme, which may be uncertain and generated from mid-latitude observations. Developing CASIM for use in the Antarctic would be a promising area of future research, which could enable the study of microphysical processes such as secondary ice formation. Comparison of cases f150 and f152 reveals that ice microphysics (likely vapour deposition and riming processes) are still a considerable source of model error. During f150, the case with comparatively less ice, RA1M_mod simulated liquid water mass fractions more comparable to those observed – a bias of just -17%, compared with -64% during f152, the case with higher ice contents. The presence of ice enhanced the formation of further ice particles at the expense of supercooled liquid.

The optimised RA1M_mod configuration was then tested in a longer (five-week) simulation during the OFCAP period in summer 2011. Observed correlations between surface melting and radiative fluxes were modelled reasonably accurately, and showed that incoming solar radiation is the primary control on summertime surface melting. Cloud was demonstrated to influence the onset and persistence of surface melting by controlling the evolution of the SEB. The presence of cloud, particularly low-level, liquid-bearing mixed phase cloud, increases downwelling LW radiation and raises the surface temperature to the melting point, which permits melting to begin. As the cloud develops and glaciates, LW fluxes decline but relatively more SW radiation can penetrate to the surface of Larsen C, which sustains melting until the surface temperature falls below zero again. The evolution of cloud phase and microphysics, and consequently their influence on cloud radiative effects, are therefore extremely important in determining the extent, duration and intensity of melting on Larsen C.

Finally, the role of foehn, cloud phase and large-scale atmospheric circulation regimes were examined in a hindcast simulation of the period 1998-2017 using the RA1M_mod MetUM configuration. Validation suggested that the hindcast performs well in all seasons at the four AWS sites where meteorological and SEB data are available. A warm bias was present at all stations, which creates an energy deficit at the surface by causing excessive LW cooling throughout the year, although this was especially pronounced in winter and at ice shelf stations when the boundary layer is strongly stably stratified. In summer especially, this energy deficit resulted in negative melt biases.

The hindcast showed that cloudy conditions dominate over Larsen C, occurring 92% of the time annually, with a peak (94%) in MAM and minimum (89%) in JJA. Clouds are typically mixed-phase, with liquid contents having a dominant effect on radiative fluxes and hence the SEB, as suggested by the notable similarities between radiative effects of the "cloudy" and "high LWP" regimes, and stronger correlations between LWP and radiative fluxes than for IWP. Cloudy, high LWP conditions are associated with negative temperature and E_{tot} anomalies in summer because they prevent incoming SW radiation reaching the surface, consistent with the findings of Chapter 5. Conversely, these regimes result in positive E_{tot} and temperature anomalies during winter because they increase $LW_{\downarrow}$. Clouds in all seasons except DJF increase E_{tot}, but do not generally result in surface melting because the surface temperature does not reach 0°C. However, this could change if, as projected, rising temperatures continue over Larsen C, causing temperatures to reach the melting point even in cloudy periods. This would make conditions over Larsen C more comparable to those in Greenland, where cloud-driven melting is important throughout much of the year, and has been linked to extensive melting events.

As also demonstrated in Chapter 4, foehn events were shown to have a considerable influence on the SEB in the hindcast. The spatial pattern of modelled foehn occurrence, with increased foehn frequency nearest the steep mountains that generate them, followed the same pattern as observed and modelled melt. Alongside the conclusions drawn from the assessment of processes occurring during case studies in Chapter 4 - that foehn greatly increase turbulent fluxes and strongly perturb the SEB - this provided comprehensive evidence that foehn-driven surface melting is extremely important on Larsen C. For example, MAM 2016 was identified by Datta et al. (2019) as a season with anomalously high foehn occurrence and intensity, a finding also replicated in the hindcast. This period is the same season evaluated in Kuipers Munneke et al. (2018) and Chapter 4. Further evaluation of MAM 2016 showed that synoptic meteorological conditions established conditions that promoted foehn, such as were also seen during the strong foehn season of summer 2001/02 that triggered the collapse of the Larsen B ice shelf. The synoptic meteorological conditions, with persistent cross-peninsula winds, resulted in large turbulent heat flux anomalies throughout the season, which strongly affected the SEB and drove melting above one standard deviation of the climatological MAM mean across the whole ice shelf. Modelled foehn occurrence is positively correlated with observed SAM index, so if the trend towards a positive SAM noted in Chapter 2 continues, then these types of extreme foehn-driven melt events could occur more frequently in future because synoptic meteorological conditions would be more favourable to their development.

Composite analysis of the hindcast shows that large-scale atmospheric circulation patterns are important for controlling surface melting on Larsen C via their influence on synoptic meteorology. Circulation modes that favour cross-peninsula airflow and thus foehn conditions, such as SAM+ and ENSO-, are associated with positive E_{melt} anomalies in all seasons, though this effect is especially pronounced outside DJF. A deep ASL and barrier winds both suppress melting on Larsen C, and have the largest impact on surface meltwater production during DJF, when 90% of melting occurs.

Observed spatial patterns of surface melt duration were simulated well compared to satellite-based observations, and Chapter 6 built on existing studies by also simulating melt amount, which cannot be observed with satellites and is a more useful parameter for constraining the surface mass balance of Larsen C. No previous model hindcast has captured the observed east-west gradient in surface melt, but the hindcast shows melting concentrated in inlets, and at the north of the shelf where temperatures are warmer and more solar radiation reaches the surface throughout the year. This is the first time this pattern has been captured by a model hindcast and thus demonstrates its value for quantifying past, present and future change on Larsen C. Modelled meltwater production rates have not yet reached the values observed over Larsen B before its collapse, but trends toward warmer temperatures and a more positive SAM both suggest that meltwater production could increase over Larsen C in future.

To extend this work, future efforts should focus on improving the simulation of stably stratified boundary layers in the MetUM, which likely contributed to the aforementioned positive surface temperature and therefore $LW_{\uparrow}$ bias, and which is beyond the scope of this thesis to investigate. Further development of the CASIM double-moment cloud microphysics scheme would also be useful to advance the work presented in Chapter 5 and improve model simulations of cloud phase over Larsen C. One potentially fruitful avenue of enquiry may be to better constrain atmospheric aerosol concentrations in the Antarctic which can then be used with CASIM. Finally, the hindcast presented in Chapter 6 could be used as a baseline of present and recent historical conditions. Using the hindcast to produce future projections would provide novel insight into likely future atmospheric conditions over Larsen C. The understanding of atmospheric processes influencing surface melting presented in this thesis will be instrumental in determining future melt rates on Larsen C, and consequently its long-term fate.

In conclusion, this thesis has demonstrated that:

- Foehn events strongly perturb the SEB of Larsen C ice shelf by dramatically increasing sensible heat fluxes, and can drive surface melting in all seasons, including winter. Excepting SW radiation, foehn events are the most important driver of surface melting in the model hindcast, and summertime foehn events occur when SW radiation is already high.
- Clouds play a critical role in mediating the SEB by impacting radiative fluxes. Cloud phase influences the intensity, extent and duration of surface melting by affecting cloud lifetime and optical thickness, and therefore the amount of SW radiation that reaches the surface. This process may become more important in a warming climate, extending the melt season further into MAM/SON.
- Large-scale circulation influences the drivers of melting on Larsen C by producing synoptic conditions conducive to melt. Specifically, the positive phase of the SAM increases foehn occurrence and therefore melting. The ongoing trend towards a positive SAM index discussed in Chapter 2 suggests that foehn-driven melting may become even more important over Larsen C in future.

Present and future surface melting on Larsen C is governed by the combined impacts of large-scale circulation, foehn and cloud on the SEB. The rate of ongoing climate change suggests that these drivers will continue to exert a dominant influence on the SEB into the future, which will have profound impacts for the stability of the Larsen C ice shelf, and therefore for global sea level rise.

Appendices

A

Appendix: Kuipers Munneke et al. (2018)

In accordance with University of East Anglia regulations, this appendix reproduces published work, to which I contributed. As a co-author, I was responsible for the modelling work used in the paper, and particularly Figures 3c and 3d. The full citation is: P. Kuipers Munneke et al. (2018). "Intense winter surface melt on an Antarctic ice shelf". In: *Geophysical Research Letters* 45, pages 7615–7623, doi: https://doi.org/10.1029/2018GL077899.

This work is reproduced under Creative Commons Attribution license CC BY 4.0. Copyright [c] 2018, the authors.

Geophysical Research Letters

RESEARCH LETTER
10.1029/2018GL077899

Intense Winter Surface Melt on an Antarctic Ice Shelf

P. Kuipers Munneke[1], A. J. Luckman[2], S. L. Bevan[2], C. J. P. P. Smeets[1], E. Gilbert[3,4], M. R. van den Broeke[1], W. Wang[5], C. Zender[5], B. Hubbard[6], D. Ashmore[7], A. Orr[3], J. C. King[3], and B. Kulessa[2]

[1]Institute for Marine and Atmospheric research Utrecht, Utrecht University, Utrecht, Netherlands, [2]Department of Geography, Swansea University, Swansea, UK, [3]British Antarctic Survey, Natural Environment Research Council, Cambridge, UK, [4]School of Environmental Sciences, University of East Anglia, Norwich, UK, [5]Department of Earth System Science, University of California, Irvine, CA, USA, [6]Centre for Glaciology, Department of Geography and Earth Sciences, Aberystwyth University, Aberystwyth, UK, [7]School of Environmental Sciences, University of Liverpool, Liverpool, UK

Key Points:
- Wintertime surface melt occurs frequently in the Antarctic Peninsula
- Winter melt heats the firn to a depth of about 3 m, retarding or reversing winter cooling
- Increased greenhouse gas concentrations could increase the occurrence of winter surface melt

Correspondence to:
P. Kuipers Munneke,
p.kuipersmunneke@uu.nl

Citation:
Kuipers Munneke, P., Luckman, A. J., Bevan, S. L., Smeets, C. J. P. P., Gilbert, E., van den Broeke, M. R., et al. (2018). Intense winter surface melt on an Antarctic ice shelf. *Geophysical Research Letters*, *45*, 7615–7623. https://doi.org/10.1029/2018GL077899

Received 12 MAR 2018
Accepted 21 APR 2018
Accepted article online 2 MAY 2018
Published online 15 MAY 2018

Abstract The occurrence of surface melt in Antarctica has hitherto been associated with the austral summer season, when the dominant source of melt energy is provided by solar radiation. We use in situ and satellite observations from a previously unsurveyed region to show that events of intense surface melt on Larsen C Ice Shelf occur frequently throughout the dark Antarctic winter, with peak intensities sometimes exceeding summertime values. A regional atmospheric model confirms that in the absence of solar radiation, these multiday melt events are driven by outbreaks of warm and dry föhn wind descending down the leeside of the Antarctic Peninsula mountain range, resulting in downward turbulent fluxes of sensible heat that drive sustained surface melt fluxes in excess of 200 W/m^2. From 2015 to 2017 (including the extreme melt winter of 2016), ~23% of the annual melt flux was produced in winter, and spaceborne observations of surface melt since 2000 show that wintertime melt is widespread in some years. Winter melt heats the firn layer to the melting point up to a depth of ~3 m, thereby facilitating the formation of impenetrable ice layers and retarding or reversing autumn and winter cooling of the firn. While the absence of a trend in winter melt is consistent with insignificant changes in the observed Southern Hemisphere atmospheric circulation during winter, we anticipate an increase in winter melt as a response to increasing greenhouse gas concentration.

Plain Language Summary Around the coast of Antarctica, it gets warm enough in summer for snow to start melting, and the sun provides most of the energy for that melt. Almost all meltwater refreezes in the snowpack, but especially on floating glaciers in Antarctica, it has been observed that meltwater forms large ponds. The pressure exerted by these ponds may have led to ice shelves collapsing into numerous icebergs in recent decades. It is therefore important to understand how much meltwater is formed. To find out, we installed an automatic weather station on a glacier in Cabinet Inlet, in the Antarctic Peninsula in 2014. The station recorded temperatures well above the melting point even in winter. The occurrence of winter melt is confirmed by satellite images and by thermometers buried in the snow, which measured a warming of the snow even at 3 m depth. Between 2014 and 2017, about 23% of all melt in Cabinet Inlet occurred in winter. Winter melt is due to warm winds that descend from the mountains, known as föhn. We have not seen the amount of winter melt increasing since 2000. However, we expect winter melt to happen more frequently if greenhouse gas continues to accumulate in the atmosphere.

1. Surface Melt in Antarctica

Current mass loss of the Antarctic Ice Sheet is made up almost entirely of ice shelf basal melting and iceberg calving (Depoorter et al., 2013). Although supraglacial and englacial runoff has been widely observed, especially in regions of low albedo such as blue ice and bare rock (Bell et al., 2017; Kingslake et al., 2017; Lenaerts et al., 2016), models suggest that only a small fraction (<1%) of the ~115 Gt (1 Gt = 10^{12} kg) of surface meltwater produced annually (Trusel et al., 2013; Van Wessem et al., 2017) runs off directly into the ocean. Instead, it is refrozen within underlying snow and firn layers (Kuipers Munneke, Picard, et al., 2012). The indirect impact of meltwater is profound, however, as an important role for meltwater-induced fracturing is implicated in the collapse of coastal ice shelves (Banwell et al., 2013; Scambos et al., 2000). Observed collapse following

©2018. The Authors.
This is an open access article under the terms of the Creative Commons Attribution License, which permits use, distribution and reproduction in any medium, provided the original work is properly cited.

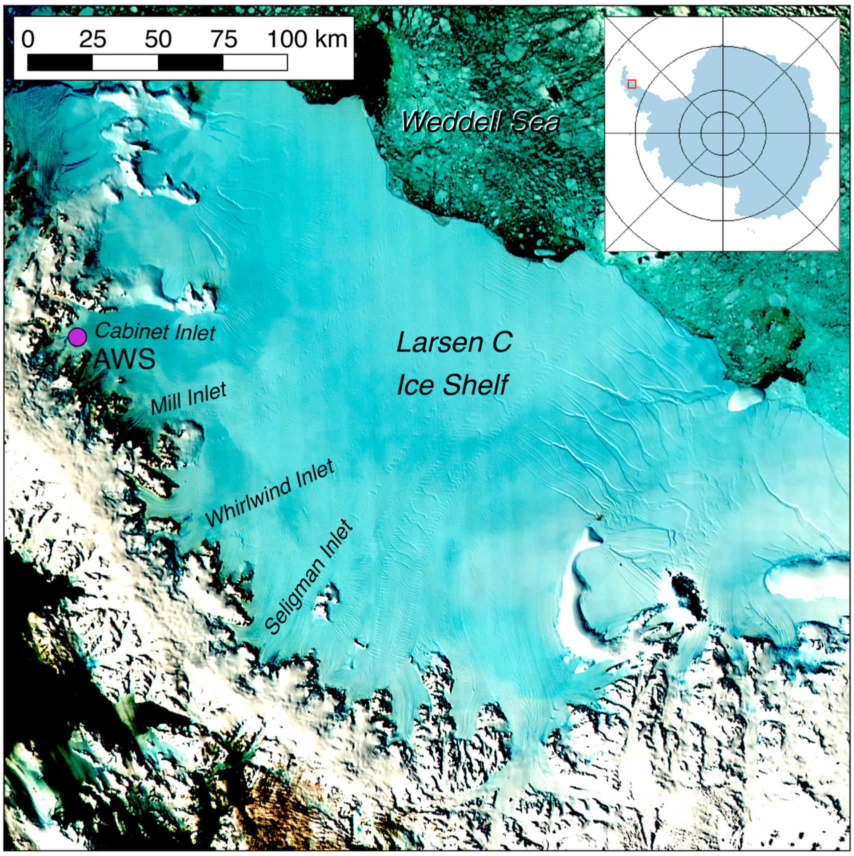

Figure 1. False-color Moderate Resolution Imaging Spectroradiometer image of Larsen C Ice Shelf in 2016. The magenta circle indicates the location of the automatic weather station (AWS) in Cabinet Inlet.

atmospheric warming (Abram et al., 2013) led to a manifold acceleration of grounded-ice flow (De Angelis & Skvarça, 2003; Rott et al., 2011), explaining part of the increased dynamic ice loss witnessed in the Antarctic Peninsula in recent decades (Harig & Simons, 2015). Further loss of ice shelves may induce rapid retreat by mechanical failure of grounded-ice cliffs (Bassis & Walker, 2012; DeConto & Pollard, 2016). Ice shelves may become more vulnerable to breakup due to sustained high rates of surface meltwater refreezing, which warms and softens the ice englacially (Hubbard et al., 2016; Phillips et al., 2010) and ultimately removes the layer of snow and firn (Kuipers Munneke et al., 2014).

Model- and satellite-derived surface melt rates range from less than 20 mm w.e./year on ice shelves in Dronning Maud Land and the Amundsen Sea sector to ~250 mm w.e./year on average over Larsen C Ice Shelf, with certain sectors of Larsen C peaking at 400 mm w.e./year (Trusel et al., 2013). In summer, the bulk of the energy for snowmelt in Antarctica is provided by solar radiation, which is only partly offset by turbulent fluxes of sensible and latent heat directed away from the surface (Van den Broeke et al., 2005). In winter, the sensible heat flux is directed toward the surface, to compensate for the absence of solar radiation and consequent surface cooling. Winter temperatures above the melting point of snow have been reported in the Antarctic Peninsula (e.g., Cape et al., 2015; Kuipers Munneke, Picard, et al., 2012; Leeson et al., 2017), in conjunction with warm and dry downslope winds known as föhn. In particular, Leeson et al. (2017) discuss that strong, likely föhn-related autumnal melting led to high surface melt fluxes 2 years before collapse of the Larsen B Ice Shelf in 2002. Föhn-induced melt is also observed in spring (King et al., 2017). Overall, however, the inventory of winter surface melt has been very sparse. Here we report peak annual melt fluxes in the austral winter, derived from measurements from an automatic weather station (AWS) located in Cabinet Inlet, a climatologically unsurveyed area of Larsen C Ice Shelf in the Antarctic Peninsula (Figure 1 and Appendix A), and for the first time discuss the occurrence, significance, context, and impact of wintertime surface melt in Antarctica.

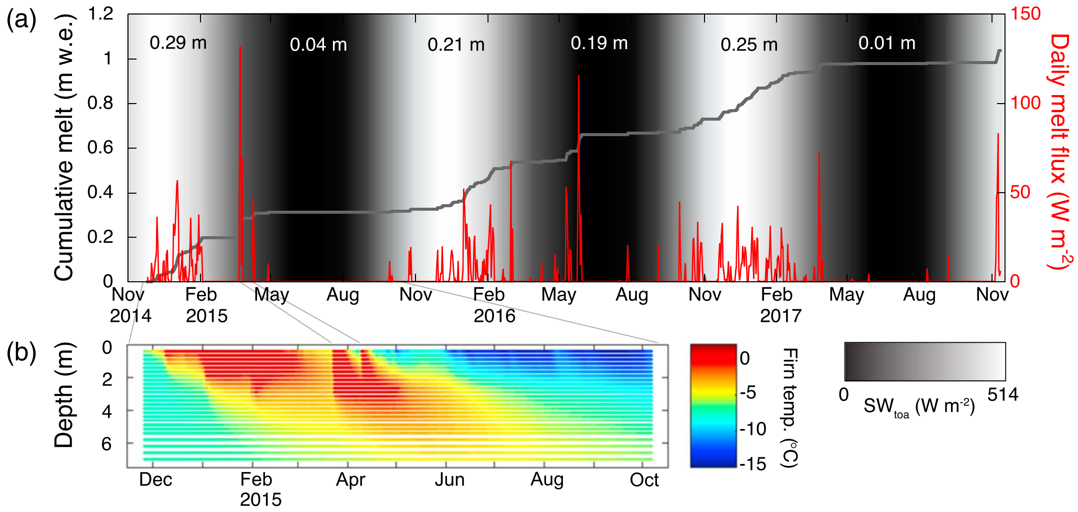

Figure 2. (a) Daily mean melt flux (W/m^2, red) and cumulative melt (m w.e., gray) for November 2014 to November 2017, computed from automatic weather station observations. Background gradient shows daily mean top-of-atmosphere incoming solar radiation, SW_{toa}: black is 0, white is 514 W/m^2. Text labels in the top of the panel denote cumulative melt (m w.e.) for austral summer (1 November to 31 March) and winter (1 April to 31 October) seasons. (b) Thermistor string observations of firn temperature (°C) as a function of depth (m), in 2015.

2. In Situ Observation of Winter Melt

Almost 3 years of AWS observations (25 November 2014 to 13 November 2017) were used to drive a model of the snow surface energy budget (Appendix B; Kuipers Munneke, van den Broeke, et al., 2012). It simulates a cumulative melt of 1,040 mm w.e. in Cabinet Inlet (Figure 2), equating to a melt rate of 350 mm w.e./year. We find that only 77% of the cumulative melt (800 mm w.e.) occurs in the austral summer season, which we define here to last from 1 November to 31 March. This summer melt mostly occurs in prolonged episodes of days to weeks, with peak daily melt fluxes of 40–60 W/m^2. Melt energy in these conditions is supplied by absorbed solar radiation (Kuipers Munneke, van den Broeke, et al., 2012). Thus, 23% of the surface melt in the period under consideration (240 mm w.e.) is generated in the winter season, here defined from 1 April to 31 October. Most of the observed wintertime melt occurred in the austral winter of 2016 (190 mm w.e.), with smaller fractions in 2015 (50 mm w.e.) and 2017 (10 mm w.e.). Over the three years recorded, wintertime surface melt took place in all months except July. In contrast to summer melt, the winter melt episodes are usually shorter (at most a few days) and more intense, with daily mean melt fluxes ranging from 25 to over 120 W/m^2 (equating to a melt rate of 6–31 mm w.e./day).

The strongest wintertime melt episode in the record occurred on 25–30 May 2016 (Figure 3) and featured observed melt fluxes that greatly exceeded those seen during summer. A combination of high observed wind speed (5–18 m/s) and warm air (5–13°C at 2 m above the surface) resulted in a large turbulent flux of sensible heat downward to the surface. Negative fluxes of longwave radiation (longwave cooling and under clear skies) and latent heat (sublimation) offset some of this sensible heat flux. Still, the resulting melt flux is dominated by sensible heat transfer, which frequently reaches up to 200 W/m^2 with sustained extremes of >300 W/m^2 lasting for up to 30 min (the recording resolution of the AWS data). In total, 71 mm of meltwater was produced as a consequence of this föhn event. During melt, the strong winds advect air that is dried by adiabatic warming, with relative humidity between 35% and 65%.

3. Cause and Consequence

The combination of strong wind, high temperature, and low relative humidity is common to all wintertime melt events. These are fingerprints for föhn winds that sometimes occur over the Antarctic Peninsula mountain range. Such föhn winds are caused by flow across a topographic barrier, whereby the downslope winds on the leeward side are heated adiabatically (Kuipers Munneke, van den Broeke, et al., 2012; Luckman et al., 2014). Additional heating can occur due to the drawdown of potentially warm and dry air from aloft when the flow is blocked at lower levels on the windward side and due to entrainment of potentially warm and dry air from upper levels into the flow over the mountains (Orr et al., 2008). The vertical cross section (Figure 3d) over

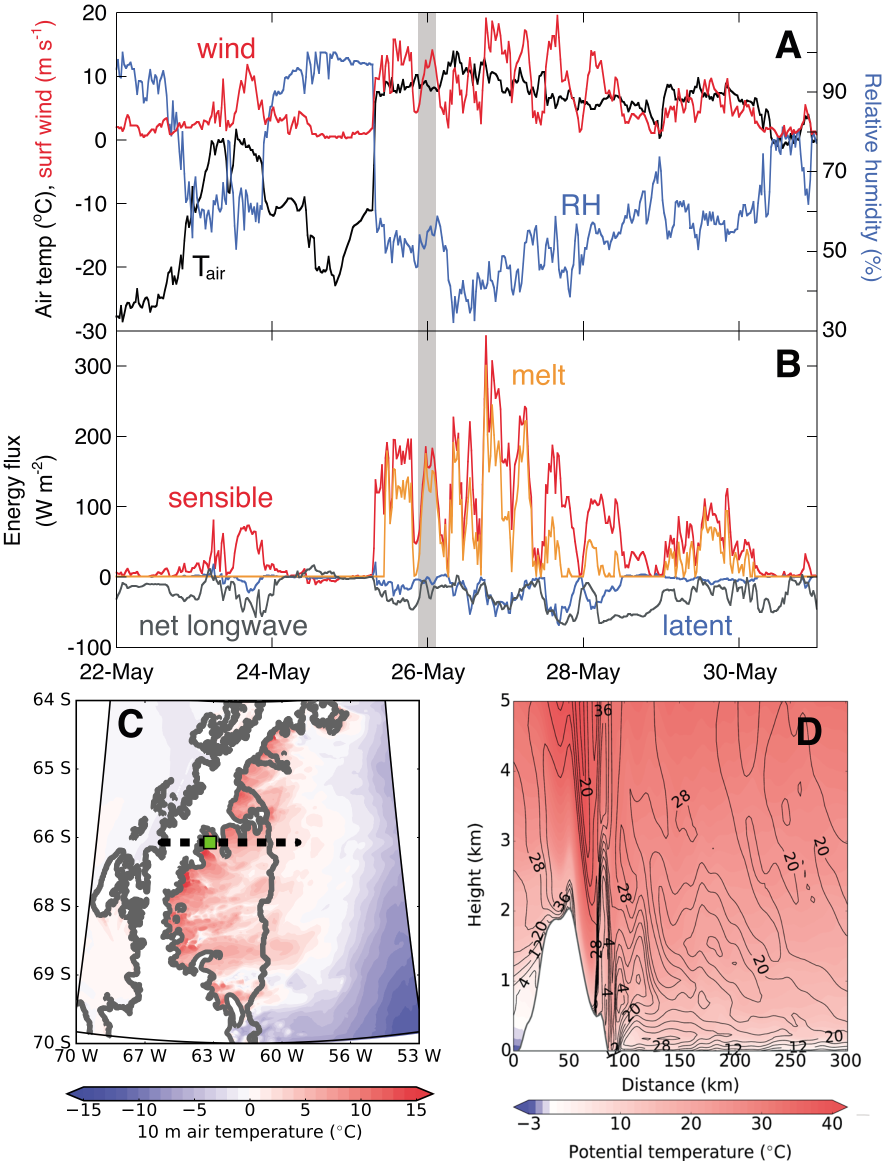

Figure 3. Hourly values of observed meteorological conditions and surface energy balance in Cabinet Inlet, 22–31 May 2016. (a) Air temperature (at 2 m above the surface, °C, black), wind speed (at 10 m above the surface, m/s, red), relative humidity (at 2 m above the surface, %, blue). The vertical gray bar indicates the time of the model snapshots in panels (c) and (d). (b) Net longwave radiation (gray), turbulent fluxes of sensible (red) and latent (blue) heat, and melt flux (orange). All fluxes in W/m^2. (c) Map showing modeled temperature (in °C) at 10 m above sea level over Larsen C, on 26 May 2016 at 00:00 UTC. The dashed line indicates the location of the transect shown in panel (d), and the green square shows the location of the Cabinet Inlet automatic weather station. (d) Modeled vertical cross section through the Antarctic Peninsula mountains into Cabinet Inlet on 26 May 2016 at 00:00 UTC. Filled color contours show potential temperature (in °C), and black open contours show wind speed (in m/s).

the Antarctic mountain range through Cabinet Inlet from a high-resolution regional atmospheric model (the UK MetOffice Unified Model, see Appendix C) confirms the occurrence of föhn during 25–30 May 2016, with moist air rising on the windward side of the mountains and relatively dry, adiabatically warmed air descending on its leeside. In the lee of the mountains, a hydraulic jump is apparent in the vertical wind component (at about 70 km on the horizontal axis in Figure 3d), characteristic of föhn (Elvidge & Renfrew, 2016).

The regional atmospheric model further shows that during this event, temperature at 10 m above the surface was above the melting point for most of the ice shelf, indicative of widespread surface melt not restricted

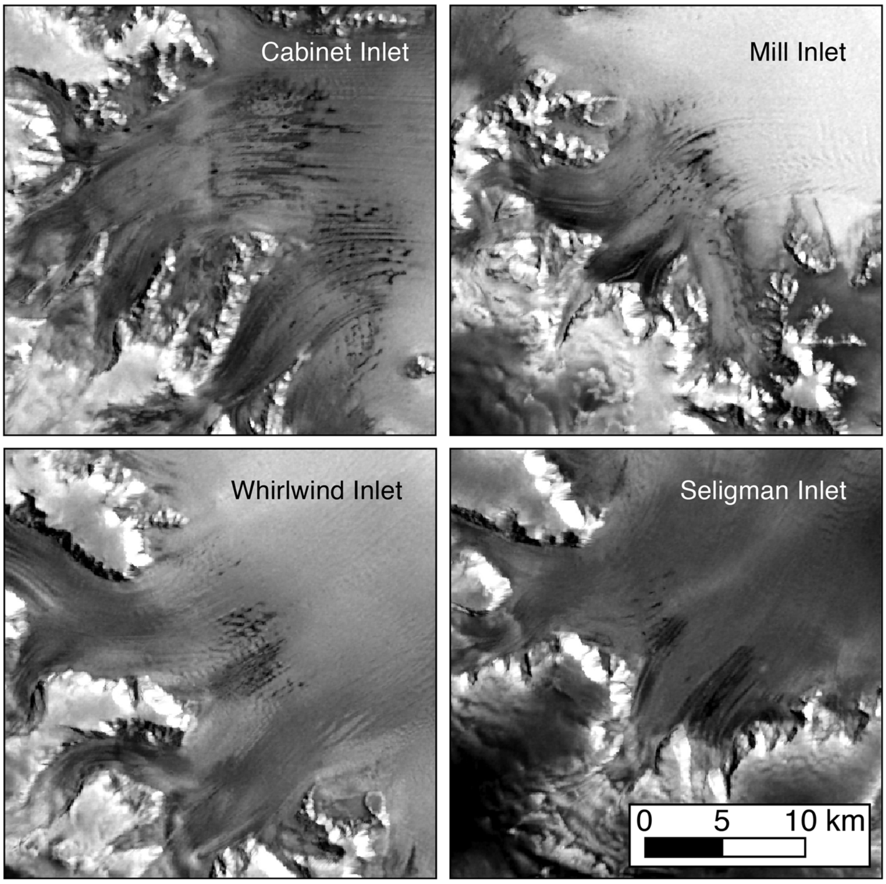

Figure 4. Sentinel 1A C-band synthetic aperture radar imagery from locations near the grounding line of Larsen C Ice Shelf. Elongated black features on the ice shelf indicate meltwater lakes and ponds. See Figure 1 for locations of the inlets.

to Cabinet Inlet (see Figure 3c). A collection of synchronous Sentinel-1A synthetic aperture radar images of a part of Larsen C Ice Shelf (Figure 4), taken near the end of the May 2016 föhn event, confirms that surface melt was occurring beyond Cabinet Inlet. It shows extensive snow melt across the northwestern and western inlets of the shelf (apparent in the satellite images as dark-hued areas), along with a large number of meltwater lakes collected in local depressions of the ice shelf (shown as black elongated features in the images of Figure 4). The elongated depressions express channels in the basal topography, possibly arising from buoyant basal meltwater generated at the grounding line (Sergienko, 2013) or from the grounded ice being extruded over a strongly undulating grounding line (Gladish et al., 2012).

Wintertime meltwater is able to percolate deeply into the snowpack, bringing snow temperatures to the melting point up to a depth of about 3 m (Figure 2b) when latent heat is released as the meltwater refreezes. Observations from thermistor-instrumented boreholes (Appendix D) suggest that effective pathways for this major source of latent energy are available year-round, as even during winter melt, the warming of near-surface layers is almost instantaneous (e.g., in two episodes of melt during end of March and April 2015, apparent in Figure 2b, percolation to 3 m depth occurred in about 12 hr). As a consequence, winter melt warms the snowpack, allowing for an earlier start of the main melt season in spring and summer and heating of the deeper ice layers. Also, it forms relatively impermeable infiltration ice (Hubbard et al., 2016) that can act as a runoff surface for meltwater (Bell et al., 2017).

4. Past, Present, and Future Winter Melt

To put the occurrence of wintertime surface melt into a longer-term perspective, we use satellite-borne Quik Scatterometer (QuikSCAT) (2000–2009) and Advanced Scatterometer (ASCAT) (2009–2016) scatterometer

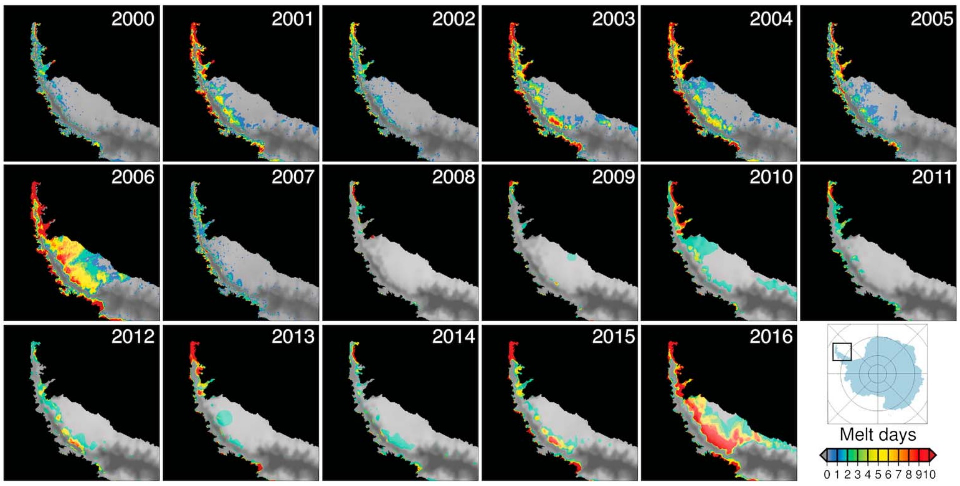

Figure 5. Maps over the Antarctic Peninsula showing annual number of melt days per winter (1 April to 31 October) between 2000 and 2016, observed by QuikSCAT (2000–2009) and ASCAT (2010–2016).

sensors to estimate the number of melt days over the Antarctic Peninsula for each winter season (Figure 5 and Appendix E). Radar scatterometry is an active remote sensing technique that is sensitive to the presence of liquid water in snow or firn. While the presence of liquid water does not necessarily imply the occurrence of surface melt, the two are highly correlated (Van den Broeke et al., 2010). In some years, little or no meltwater is present during winter, whereas in other years, the number of days with liquid water present on Larsen C approaches 10. In all years, we see enhanced melt over the Larsen C Ice Shelf near the base of the eastern slopes of the Antarctic Peninsula mountain range, which is consistent with föhn-driven warming (Luckman et al., 2014). Near the calving front of Larsen C, wintertime melt occurred in the extreme melt winter of 2006 and to a lesser extent in 2016. These stand out in our records as the most intense winter melt seasons since 2000.

No trend in the occurrence of winter melt over Larsen C is evident over the 17-year record of satellite scatterometry, which implies that there have been no contemporaneous changes in the frequency or duration of westerly föhn events in winter over the Antarctic Peninsula. This is consistent with the absence of any statistically significant winter trends in the Southern Annular Mode (SAM), which is the principal mode of Southern Hemisphere extratropical climate variability, during the scattermometry period considered or even since 1958 (Marshall, 2003). By contrast, the SAM has shifted toward a more positive phase in summer in recent decades (Marshall, 2003), resulting in increased westerly flow over the Antarctic Peninsula and associated föhn events (Marshall et al., 2006; Orr et al., 2008). These led to anomalous warming and melt due to föhn (Cape et al., 2015). As the winter SAM is projected to trend toward its positive phase during the 21st century because of increased greenhouse gas concentrations (Simpkins & Karpechko, 2012), we can thus expect an enhancement of winter melt in this century, from atmospheric circulation changes alone. The magnitude of this effect increases with the atmospheric concentration of greenhouse gases (Zheng et al., 2013).

Ice shelf collapse by hydrofracturing is implicated in future scenarios of rapid Antarctic ice discharge and sea level rise (DeConto & Pollard, 2016). For these processes to be understood and predicted, a reliable estimate of future surface melt and its impact on the state of the firn layer on ice shelves is required. Such estimates can only be achieved if subtle processes like the formation of impermeable ice layers, winter warming, and densification of firn, due to meltwater percolation, ponding, and refreezing, are appropriately taken into account.

Appendix A: Automatic Weather Station

An AWS was installed in Cabinet Inlet (66°24.1′S, 63°22.3′W) in November 2014. Data were recorded at half-hourly resolution. Instrument height was monitored and usually between 1.7 and 2.4 m above the surface. Reported quantities are at a nominal levels of 2 m for temperature and humidity and 10 m for wind speed. Shortwave radiation was tilt corrected using a Moderate Resolution Imaging Spectroradiometer satellite-guided procedure (Wang et al., 2016). Air temperature observations were unventilated, leading to overestimation during calm, sunny days. A correction function was derived from concurrent thermocouple observations during November 2014 through January 2015. Observations of relative humidity were corrected for solar heating of the housing of the humidity sensor and for hysteresis effects due to a long response time of the sensor.

Appendix B: Surface Energy Balance Model

The surface energy balance was computed using a model that includes a multilayer snowpack. The model forces the energy budget to close by iterating to a surface temperature for which all the terms balance (Kuipers Munneke, Picard, et al., 2012). If that temperature is above the freezing point, all excess energy is used for melting, and the surface temperature (and associated outgoing longwave radiation) is set to the melting point. The model is evaluated by comparing computed surface temperature with observed values (computed from the outgoing longwave radiation with the Stefan-Boltzmann law). The difference between these is 0.21 K on average (RMS = 1.85 K; RMS = root-mean-square). Further, the timing of melt is corroborated with surface height lowering observed by a sonic height ranger attached to the AWS mast and by observations of outgoing longwave radiation indicating the surface temperature to be at the melting point.

Appendix C: Regional Atmospheric Model

Version 10.4 of the UK Met Office Unified Model (Orr et al., 2014) is used to downscale operational analysis data to a horizontal grid spacing of 1.5 km, a resolution sufficient to represent föhn over the Antarctic Peninsula reasonably well (Elvidge et al., 2014). The 1.5 km inner domain, encompassing the Larsen C Ice Shelf and the adjacent region of the Antarctic Peninsula (see Figure 3C) is nested within a 4 km outer domain that includes the entire Antarctic Peninsula. Boundary and surface conditions for the outer domain are provided by a global, 25 km version of the Unified Model, which is driven by Met Office operational data. Only results from the 1.5 km domain are examined here.

Appendix D: Borehole Thermistor Strings

Firn temperatures were measured using a string of NTC thermistors in a Wheatstone half-bridge and recorded every 30 min using a Campbell Scientific data logger. Resistances were converted to temperatures using a Steinhart-Hart equation (Steinhart & Hart, 1968) and the manufacturer calibration data. A second calibration was performed by using a well-mixed distilled water/ice bath, assumed to be 0°C, to derive the zero offset for each thermistor. After-correction sensors gave an RMS error of ±0.03°C in an identical ice bath. In total, 26 sensors were spaced between 0.25 and 0.40 m apart, along 7 m of the thermistor string. The string was installed in a borehole drilled with pressurised hot water which was then backfilled with fine surface snow. The borehole drilling introduces a minor thermal disturbance to the firn, and so data from the first 5 days were discarded as a precaution.

Appendix E: Radar Scatterometry

Radar scatterometry is an active remote sensing technique that is sensitive to the presence of liquid water in snow or firn. To estimate the number of melt days for each winter, we use SeaWinds QuikSCAT Ku-band (2000–2009) and ASCAT C-band (2010–2016) enhanced resolution (4.45 km effective) backscatter products (ftp://ftp.scp.byu.edu/pub/). To maximize consistency in melt detection between the two sensors, we chose the morning overpass, vertical-polarization QuikSCAT product and the "all-pass" ASCAT product, also vertically polarized. This may underestimate the number of melt days for the QuikSCAT era, as more overpasses are available per day. A melt day was recorded if backscatter dropped more than a chosen threshold below the mean backscatter of the previous winter season. For QuikSCAT, the threshold was 3 dB (Luckman et al., 2014; Trusel et al., 2012). A lower threshold of 2.7 dB was chosen for ASCAT due to the reduced sensitivity of C-band microwaves.

Acknowledgments
We would like to thank the British Antarctic Survey logistics team. Funding of this research was through the Netherlands Earth System Science Centre (NESSC), the Netherlands Organization for Scientific Research (NWO), and NERC grant NE/L006707. E. G. and A. O. acknowledge use of the MONSooN system, supplied by the Joint Weather and Climate Research Programme (Met Office and NERC). The SAR data used in this study are modified Copernicus Sentinel data (2016), processed by the European Space Agency (ESA). All observational data are available at the NERC Polar Data Centre: http://doi.org/10.5285/e3616d28-759e-4cca-8fae-fe398f9552ba, and http://doi.org/10.5285/05c9124b-7119-4d99-8e17-ab754eb3f51c. The authors declare no conflict of interest.

References

Abram, N. J., Mulvaney, R., Wolff, E. W., Triest, J., Kipfstuhl, S., Trusel, L. D., et al. (2013). Acceleration of snow melt in an Antarctic Peninsula ice core during the twentieth century. *Nature Geoscience*, *6*, 404–411. https://doi.org/10.1038/ngeo1787

Banwell, A. F., MacAyeal, D. R., & Sergienko, O. V. (2013). Breakup of the Larsen B Ice Shelf triggered by chain reaction drainage of supraglacial lakes. *Geophysical Research Letters*, *40*, 5872–5876. https: //doi.org/10.1002/2013GL057694

Bassis, J. N., & Walker, C. C. (2012). Upper and lower limits on the stability of calving glaciers from the yield strength envelope of ice. *Proceedings of the Royal Society*, *468*, 913–931. https://doi.org/10.1098/rspa.2011.0422

Bell, R. E., Chu, W., Kingslake, J., Das, I., Tedesco, M., Tinto, K. J., et al. (2017). Antarctic ice shelf potentially stabilized by export of meltwater in surface river. *Nature*, *544*, 344–348. https://doi.org/10.1038/nature22048

Cape, M. R., Vernet, M., Skvarca, P., Marinsek, S., Scambos, T., & Domack, E. (2015). Foehn winds link climate-driven warming to ice shelf evolution in Antarctica. *Journal of Geophysical Research: Atmospheres*, *120*, 11,037–11,057. https://doi.org/10.1002/2015JD023465

De Angelis, H., & Skvarça, P. (2003). Glacier surge after ice shelf collapse. *Science*, *299*, 1560–1562.

DeConto, R. M., & Pollard, D. (2016). Contribution of Antarctic to past and future sea-level rise. *Nature*, *531*, 591–597. https://doi.org/10.1038/nature17145

Depoorter, M. A., Bamber, J. L., Griggs, J. A., Lenaerts, J. T. M., Ligtenberg, S. R. M., van den Broeke, M. R., & Moholdt, G. (2013). Calving fluxes and basal melt rates of Antarctic ice shelves. *Nature*, *502*, 89–92. https://doi.org/10.1038/nature12567

Elvidge, A. D., & Renfrew, I. A. (2016). The causes of foehn warming in the lee of mountains. *Bulletin of the American Meteorological Society*, *97*(3), 455–466.

Elvidge, A. D., Renfrew, I. A., King, J. C., Orr, A., Lachlan-Cope, T. A., Weeks, M., & Gray, S. L. (2014). Föhn jets over the Larsen C Ice Shelf, Antarctica. *Quarterly Journal of the Royal Meteorological Society*, *141*, 698–713. https://doi.org/10.1002/qj.2382

Gladish, C. V., Holland, D. M., Holland, P. R., & Price, S. F. (2012). Ice shelf basal channels in a coupled ice-ocean model. *Journal of Glaciology*, *58*(252), 1227–1244. https://doi.org/10.3189/2012JoG12J003

Harig, C., & Simons, F. J. (2015). Accelerated West Antarctic ice mass loss continues to outpace East Antarctic gains. *Earth Planet Science Letters*, *415*, 134–141. https://doi.org/10.1016/j.epsl.2015.01.029

Hubbard, B., Luckman, A., Ashmore, D., Bevan, S., Kulessa, B., Kuipers Munneke, P., et al. (2016). Massive subsurface ice formed by refreezing of ice-shelf melt ponds. *Nature Communications*, *7*, 11897. https://doi.org/10.1038/ncomms11897

King, J. C., Kirchgaessner, A., Bevan, S., Elvidge, A. D., Kuipers Munneke, P., Luck, A., et al. (2017). The impact of föhn winds on surface energy balance during the 2010–2011 melt season over Larsen C Ice Shelf, Antarctica. *Journal of Geophysical Research: Atmospheres*, *122*, 12,062–12,076. https://doi.org/10.1002/2017JD026809

Kingslake, J., Ely, J. C., Das, I., & Bell, R. (2017). Widespread movement of meltwater onto and across Antarctic ice shelves. *Nature*, *544*, 349–352. https://doi.org/10.1038/nature22049

Kuipers Munneke, P., Ligtenberg, S. R. M., van den Broeke, M. R., van Angelen, J. H., & Forster, R. R. (2014). Explaining the presence of perennial liquid water bodies in the firn of the Greenland Ice Sheet. *Geophysical Research Letters*, *41*, 476–483. https://doi.org/10.1002/2013GL058389

Kuipers Munneke, P., Picard, G., van den Broeke, M. R., Lenaerts, J. T. M., & Meijgaard, E. (2012). Insignificant change in Antarctic snowmelt volume since 1979. *Geophysical Research Letters*, *39*, L01501. https://doi.org/10.1029/2011GL050207

Kuipers Munneke, P., van den Broeke, M. R., King, J. C., Gray, T., & Reijmer, C. H. (2012). Near-surface climate and surface energy budget of Larsen C ice shelf, Antarctic Peninsula. *The Cryosphere*, *6*, 353–363. https://doi.org/10.5194/tc-6-353-2012

Leeson, A. A., van Wessem, J. M., Ligtenberg, S. R. M., Shepherd, A., van den Broeke, M. R., Killick, R., et al. (2017). Regional climate of the Larsen B embayment 1980–2014. *Journal of Glaciology*, *63*(240), 683–690. https://doi.org/10.1017/jog.2017.39

Lenaerts, J. T. M., Lhermitte, S., Drews, R., Ligtenberg, S. R. M., Berger, S., Helm, V., et al. (2016). Meltwater produced by wind-albedo interaction stored in an East Antarctic ice shelf. *Nature Climate Change*, *7*, 58–62. https://doi.org/10.1038/nclimate3180

Luckman, A., Elvidge, A., Jansen, D., Kulessa, B., Kuipers Munneke, P., King, J., & Barrand, N. E. (2014). Surface melt and ponding on Larsen C Ice Shelf and the impact of föhn winds. *Antarctic Science*, *26*(6), 625–635. https://doi.org/10.1017/S0954102014000339

Marshall, G. J. (2003). Trends in the Southern Hemisphere Annular Mode from observations and reanalyses. *Journal of Climate*, *16*, 4134–4143.

Marshall, G. J., Orr, A., van Lipzig, N., & King, J. C. (2006). The impact of a changing Southern Hemisphere Annular Mode on Antarctic Peninsula summer temperatures. *Journal of Climate*, *19*, 5399–5405. https://doi.org/10.1175/Jcli3844.1

Orr, A., Marshall, G. J., Hunt, J. C. R., Sommeria, J., Wang, C.-G., van Lipzig, N. P. M., et al. (2008). Characteristics of summer airflow over the Antarctic Peninsula in response to recent strengthening of westerly circumpolar winds. *Journal of the Atmospheric Sciences*, *65*, 1396–1413. https://doi.org/10.1175/2007JAS2498.1

Orr, A., Phillips, T., Webster, S., Elvidge, A., Weeks, M., Hosking, S., & Turner, J. (2014). Met Office Unified Model high-resolution simulations of a strong wind event in Antarctica. *Quarterly Journal of the Royal Meteorological Society*, *140*(684), 2287–2297.

Phillips, T., Rajaram, H., & Steffen, K. (2010). Cryo-hydrologic warming: A potential mechanism for rapid thermal response of ice sheets. *Geophysical Research Letters*, *37*, L20503. https://doi.org/10.1029/2010GL044397

Rott, H., Müller, F., Nagler, T., & Floricioiu, D. (2011). The imbalance of glaciers after disintegration of Larsen-B ice shelf, Antarctic Peninsula. *The Cryosphere*, *5*, 125–134. https://doi.org/10.5194/tc-5-125-2011

Scambos, T. A., Hulbe, C., Fahnestock, M., & Bohlander, J. (2000). The link between climate warming and break-up of ice shelves in the Antarctic Peninsula. *Journal of Glaciology*, *46*, 516–530.

Sergienko, O. V. (2013). Basal channels on ice shelves. *Journal of Geophysical Research: Earth Surface*, *118*, 1342–1355. https://doi.org/10.1002/jgrf.20105

Simpkins, G. R., & Karpechko, A. Y. (2012). Sensitivity of the Southern Annular Mode to greenhouse gas emission scenarios. *Climate Dynamics*, *38*, 563–572. https://doi.org/10.1007/s00382-011-1121-2

Steinhart, J. S., & Hart, S. R. (1968). Calibration curves for thermistors. *Deep Sea Research and Oceanographic Abstracts*, *15*, 497–503.

Trusel, L. D., Frey, K. E., & Das, S. B. (2012). Antarctic surface melting dynamics: Enhanced perspectives from radar scatterometer data. *Journal of Geophysical Research*, *117*, F02023. https://doi.org/10.1029/2011JF002126

Trusel, L. D., Frey, K. E., Das, S. B., Kuipers Munneke, P., & van den Broeke, M. R. (2013). Satellite-based estimates of Antarctic surface meltwater fluxes. *Geophysical Research Letters*, *40*, 6148–6153. https: //doi.org/10.1002/2013GL058138

Van den Broeke, M. R., König-Langlo, G., Picard, G., Kuipers Munneke, P., & Lenaerts, J. (2010). Surface energy balance, melt and sublimation at Neumayer station (East Antarctica). *Antarctic Science*, *22*(1), 87–96. https://doi.org/10.1017/S0954102009990538

Van den Broeke, M. R., Reijmer, C. H., van As, D., van de Wal, R. S. W., & Oerlemans, J. (2005). Seasonal cycles of Antarctic surface energy balance from automatic weather stations. *Annals of Glaciology*, *41*, 131–139.

Van Wessem, J. M., van de Berg, W. J., Noël, B. P. Y., van Meijgaard, E., Birnbaum, G., Jakobs, C. L., et al. (2017). Modelling the climate and surface mass balance of polar ice sheets using RACMO2, part 2: Antarctica (1979–2016). *The Cryosphere*, *12*, 1479–1498. https://doi.org/10.5194/tc-12-1479-2018

Wang, W., Zender, C. S., van As, D., Smeets, C. J. P. P., & van den Broeke, M. R. (2016). A Retrospective, Iterative, Geometry-Based (RIGB) tilt-correction method for radiation observed by automatic weather stations on snow-covered surfaces: Application to Greenland. *The Cryosphere*, *10*, 727–741. https://doi.org/10.5194/tc-10-727-2016

Zheng, F., Li, J., Clark, R. T., & Nnamchi, H. C. (2013). Simulation and projection of the Southern Hemisphere Annular Mode in CMIP5 models. *Journal of Climate*, *26*, 9860–9879. https://doi.org/10.1175/JCLI-D-13-00204.1

Appendix: Gilbert et al. (2020)

B

In accordance with University of East Anglia regulations, this appendix reproduces published work, to which I contributed. As lead author, I was responsible for the experimental design, modelling work, analysis, and writing of the paper, but other co-authors contributed ideas, analytical insight and assisted with drafting and editing the paper. The full citation is: E. Gilbert et al. (2020). "Summertime cloud phase strongly influences surface melting on the Larsen C ice shelf, Antarctica". In: *Quarterly Journal of the Royal Meteorological Society*, pages 1–16, doi: https://doi.org/10.1002/qj.3753.

This work is reproduced under Creative Commons Attribution license CC BY 4.0. Copyright [c] 2020, the authors.

Received: 16 September 2019 | Revised: 3 December 2019 | Accepted: 20 January 2020

DOI: 10.1002/qj.3753

Quarterly Journal of the Royal Meteorological Society

RMetS

RESEARCH ARTICLE

Summertime cloud phase strongly influences surface melting on the Larsen C ice shelf, Antarctica

E. Gilbert[1,2] | A. Orr[1] | J. C. King[1] | I. A. Renfrew[2] | T. Lachlan-Cope[1] | P. F. Field[3,4] | I. A. Boutle[3]

[1]British Antarctic Survey, Cambridge, UK

[2]School of Environmental Sciences, University of East Anglia, Norwich, UK

[3]Met Office, Exeter, UK

[4]University of Leeds, Leeds, UK

Correspondence
E. Gilbert. British Antarctic Survey, Madingley Road, Cambridge CB3 0ET, UK
Email: ellgil82@bas.ac.uk

Funding information
Natural Environment Research Council, NE/L002582

Abstract

Surface melting on Antarctic Peninsula ice shelves can influence ice shelf mass balance, and consequently sea level rise. We show that summertime cloud phase on the Larsen C ice shelf on the Antarctic Peninsula strongly influences the amount of radiation received at the surface and can determine whether or not melting occurs. While previous work has separately evaluated cloud phase and the surface energy balance (SEB) during summertime over Larsen C, no previous studies have examined this relationship quantitatively. Furthermore, regional climate models frequently produce surface radiation biases related to cloud ice and liquid water content. This study uses a high-resolution regional configuration of the UK Met Office Unified Model (MetUM) to assess the influence of cloud ice and liquid properties on the SEB, and consequently melting, over the Larsen C ice shelf. Results from a case-study show that simulations producing a vertical cloud phase structure more comparable to aircraft observations exhibit smaller surface radiative biases. A configuration of the MetUM adapted to improve the simulation of cloud phase reproduces the observed surface melt most closely. During a five-week simulation of summertime conditions, model melt biases are reduced to $<2\ \mathrm{W{\cdot}m^{-2}}$: a four-fold improvement on a previous study that used default MetUM settings. This demonstrates the importance of cloud phase in determining summertime melt rates on Larsen C.

KEYWORDS

Antarctic Peninsula, cloud phase, Larsen C ice shelf, regional climate modelling, surface energy balance, surface melt

This is an open access article under the terms of the Creative Commons Attribution License, which permits use, distribution and reproduction in any medium, provided the original work is properly cited.

© 2020 The Authors. *Quarterly Journal of the Royal Meteorological Society* published by John Wiley & Sons Ltd on behalf of the Royal Meteorological Society.

1 INTRODUCTION

Despite their importance in the polar climate system, Antarctic clouds are among the most under-sampled in the world because of the difficulties of *in situ* data collection in this harsh, remote environment (Lachlan-Cope, 2010; Bromwich *et al.*, 2012). The effect of Antarctic clouds on the amount of energy at the surface (the surface energy balance, SEB) can determine whether the ice surface remains frozen or melts (Kalesse *et al.*, 2016; Nicolas *et al.*, 2017), with consequent implications for ice sheet mass balance and, potentially, for global sea level rise. Cloud impacts on SEB are most important in warmer regions like the Antarctic Peninsula, where surface temperatures can rise above freezing in summer and cause melting, and where fractional cloud cover is typically 80–90% (Lachlan-Cope, 2010). The recent surface temperature rise and the loss of ice mass on more than half of the Peninsula's ice shelves further motivates investigation of cloud in this region (Turner *et al.*, 2005; 2016; Cook and Vaughan, 2010).

Larsen C is the largest remaining ice shelf on the Antarctic Peninsula, occupying ~47,000 km^2 (Bevan *et al.*, 2017). Previously neighbouring ice shelves, Larsen A and B, collapsed in 1995 and 2002, respectively, largely as a result of atmospherically driven surface melting (van den Broeke, 2005). Surface melting can destabilise ice shelves via “hydrofracturing”, whereby meltwater percolates into pre-existing rifts and expands, causing crevasses to propagate (Scambos *et al.*, 2000; 2003). Because melt rates are controlled by the balance of surface fluxes, understanding the influence of clouds on the SEB is of great importance to help establish whether Larsen C is likely to suffer the same fate.

Cloud phase strongly influences cloud radiative properties. Mixed-phase clouds dominate in summer over coasts and ice shelves like Larsen C (Lachlan-Cope, 2010; Listowski *et al.*, 2019) and have a complex vertical profile, with multiple thin layers in a “water-over-ice” structure of supercooled liquid droplets above heavier ice crystals (Barrett *et al.*, 2017). Clouds with higher liquid water paths, composed of many small droplets, are less transmissive to incoming short-wave radiation, and more emissive in the infrared, so radiate more long-wave radiation back to the surface (Zhang *et al.*, 1996). However, the vertical position of liquid within the cloud is important: for instance, the supercooled liquid upper layer of mixed-phase clouds can reflect lots of short-wave radiation, but has little effect on long-wave emission (Barrett *et al.*, 2017).

Atmospheric models typically struggle to represent cloud phase or vertical structure correctly, especially at high latitudes. For example, Klein *et al.* (2009) find that models cannot usually simulate enough liquid water in Arctic stratocumulus because too much ice is formed at the expense of supercooled liquid. Many atmospheric models, including the UK Met Office Unified Model (MetUM) used in this study, exhibit this bias in cloud phase and structure because their microphysical parametrizations are developed for the midlatitudes and are relatively simple. For example, poor representations of processes like riming (Furtado *et al.*, 2016) and vapour deposition (Furtado and Field, 2017), as well as large-scale cloud phase partitioning (Abel *et al.*, 2017) have been shown to cause the MetUM to overestimate cloud ice and underestimate cloud liquid contents. In many models, errors in cloud phase produce significant SEB biases, most notably over the Southern Ocean (Bodas-Salcedo *et al.*, 2012; Hyder *et al.*, 2018). This is because subgrid-scale spatial variability in temperature and humidity are necessarily parametrized in the model by large-scale cloud schemes, which compute liquid and ice cloud fractions that are then fed into the microphysics scheme. In reality, ice and liquid can coexist in spatially segregated pockets (Tan and Storelvmo, 2016), but in the MetUM it is difficult to sustain a separation between the phases. When total cloud fraction exceeds 100%, ice and liquid phases are assumed to overlap within a homogeneously mixed mixed-phase region. In this mixed-phase region, ice forms preferentially because of the lower saturation vapour pressure over ice than liquid.

Modelled cloud has been implicated as a primary driver of surface radiation biases over Antarctica (Bromwich *et al.*, 2013; Lenearts *et al.*, 2017) and specifically over Larsen C (King *et al.*, 2015; Listowski and Lachlan-Cope, 2017). King *et al.* (hereafter K15) find that three different regional atmospheric models simulate either too little cloud, or cloud that is optically too thin over the ice shelf. Summertime clouds over Larsen C in the MetUM are optically too thick in the short-wave part of the spectrum, while being too thin in the infrared, which results in negative downwelling short-wave ($SW_{\downarrow}$) and long-wave ($LW_{\downarrow}$) biases. Overall, they find positive (negative) net short-wave (long-wave) fluxes that do not entirely cancel, which produces a positive net energy flux at the surface and can cause the MetUM to overestimate melt on Larsen C. High-resolution regional climate models are typically able to represent the radiative effects of mixed-phase cloud more accurately than global models (Vergara-Temprado *et al.*, 2018). However, computational constraints still necessitate parametrizations that approximate subgrid-scale cloud properties, which produce errors in the SEB. Both Listowski and Lachlan-Cope (2017) and Hines *et al.* (2019) use the Polar-WRF model (and AMPS, in the case of Hines *et al.*) to show that more sophisticated parametrizations produce more accurate simulations of cloud microphysical properties, and consequently surface radiative fluxes, over Larsen C and the West Antarctic, respectively. Both find that double-moment parametrizations of liquid water represent cloud and SEB properties most accurately.

Over the entire continent, the widely varying representations of cloud phase between models and re-analyses still produce considerable errors in radiative fluxes: generally, CMIP5 models underestimate downwelling short-wave and overestimate downwelling long-wave (Lenaerts *et al.*, 2017). A better understanding of phase in Antarctic mixed-phase clouds, particularly the occurrence of supercooled liquid water (e.g. Listowski *et al.*, 2019), is essential to address this problem. For example, an improved cloud scheme was shown to reduce Antarctic-wide SEB biases in RACMO2 (Van Wessem *et al.*, 2014), and to increase modelled melt and precipitation rates over the Antarctic Peninsula (Van Wessem *et al.*, 2018). Melt and precipitation are both key inputs to surface mass balance (SMB) calculations, so improving simulated cloud phase and radiative effects contributes to a better understanding of SMB and consequently sea level rise. This is particularly important in coastal Antarctica (including the peninsula), where melt and precipitation rates are high, and model SEB biases are largest (Lenaerts *et al.*, 2017). Antarctic SMB has been estimated using regional models like MAR (Agosta *et al.*, 2018), COSMO-CLM^2 (Souverijns *et al.*, 2019) and RACMO2 (Lenaerts *et al.*, 2018; Van Wessem *et al.*, 2018), but further work is still required to better constrain modelled SMB. For instance, RACMO2 still overestimates coastal orographic precipitation rates near the grounding line of West Antarctic glaciers partly due to its representation of cloud (Lenaerts *et al.*, 2018).

There is currently a gap in scientific understanding on the influence of cloud phase on the SEB and melting over Antarctic Peninsula ice shelves. This has wider implications for model estimates of SMB across Antarctica, and therefore sea level rise. K15 conclude that cloud properties are a likely cause of observed SEB biases. However, although observed cloud phase on the peninsula has been assessed by Grosvenor *et al.* (2012) and Lachlan-Cope *et al.* (2016) and modelled by Listowski and Lachlan-Cope (2017), no work has been done to explicitly connect these properties to the SEB. This study will address this gap by investigating the sensitivity of the SEB to simulated cloud phase in a high-resolution regional climate configuration of the MetUM.

2 | DATA AND METHODS

2.1 | Study area

The study focuses on Larsen C, an ice shelf with a flat, homogenous surface on the eastern side of the mountains that extend approximately north–south along the Antarctic Peninsula (Figure 1). During summer, the shelf is characterised by relatively low wind speeds, high relative humidity and cloudy conditions (Kuipers Munneke *et al.*, 2012).

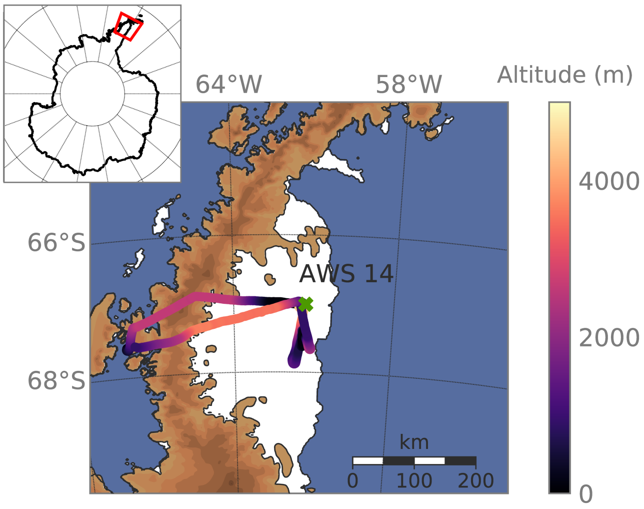

FIGURE 1 The inner 1.5 km resolution MetUM model domain used in this study, centred on Larsen C ice shelf. The model's surface elevation is indicated by shaded contours. The flight track of the f152 case-study is also shown, where the aircraft's altitude is indicated by the scale shown on the right, and the location of AWS14 is marked with a cross. The inset map shows the location of the model domain in a wider Antarctic context

2.2 | Data

Two observational datasets are used to validate MetUM-simulated cloud phase and SEB over Larsen C, namely, airborne observations of cloud collected with the British Antarctic Survey's instrumented Twin Otter aircraft and observations of surface meteorology and energy fluxes from an automatic weather station (AWS14), located at 67°00.8′S 61°28.8′W at 40 m above sea level. These data are from the Orographic Flows and Climate of the Antarctic Peninsula (OFCAP) campaign which took place between 1 January and 7 February 2011 (Elvidge *et al.*, 2015; 2016; K15).

The aircraft measures standard meteorological variables like temperature, pressure and humidity, three-dimensional winds and up- and downwelling radiation. A DMT Cloud, Aerosol and Precipitation Spectrometer (CAPS probe: Baumgardner *et al.*, 2001) containing three separate instruments to sample cloud particles of different sizes was also fitted. A full description of aircraft observations and data treatment can be found in Grosvenor *et al.* (2012), Lachlan-Cope *et al.* (2016) and Appendix A.

AWS14 measures near-surface meteorology and radiation components directly. Turbulent fluxes are computed using the bulk aerodynamic method to retrieve the full SEB, and the energy balance model of van den Broeke *et al.* (2005) calculates the SEB of the snowpack. Further details of weather station measurements and data treatment are given in Kuipers Munneke *et al.* (2009; 2012) and Appendix B.

The SEB of the ice surface is defined as per K15 and summarised as:

$$E_{\mathrm{tot}} = SW_{\mathrm{net}} + LW_{\mathrm{net}} + H_{\mathrm{L}} + H_{\mathrm{S}}, \quad (1)$$

where SW_{net} and LW_{net} are the net (downwelling minus upwelling) short-wave and long-wave fluxes, respectively; and H_{L} and H_{S} are the surface latent and sensible heat fluxes, respectively. Melting occurs when the sum of fluxes, E_{tot}, is positive, and the surface temperature, T_{s}, is at the melting point: 0 °C. Energy available for melting (or melt flux, E_{melt}) is therefore equal to E_{tot} when $T_{\mathrm{s}} = 0$ °C, as described in K15. All fluxes, including E_{melt} and E_{tot}, are measured in $\mathrm{W{\cdot}m^{-2}}$ and are positive when directed towards the surface.

2.3 | Model description

The MetUM (Walters *et al.*, 2017) is a non-hydrostatic numerical weather prediction model that uses semi-implicit time-stepping and semi-Lagrangian advection. A regional configuration using RA1 science settings was run in atmosphere-only forecast mode, with a set-up adapted from Orr *et al.* (2014) and forecast length of 24 hours. It was run in a nested configuration with a 1.5 km resolution inner domain centred on the Larsen C ice shelf, shown in Figure 1. This domain is positioned within a global domain that has ~17 km resolution at midlatitudes (N768) and was initialised with global UK Met Office operational analyses. The MetUM radiation scheme is based on Edwards and Slingo (1996) and all experiments used the operational single-moment cloud microphysics scheme based on Wilson and Ballard (1999), with extensive modifications as described in Bush *et al.* (2019). The heterogeneous ice nucleation temperature threshold (representing an immersion freezing or condensation mechanism, whereby ice is permitted to form heterogeneously in the presence of liquid water) used by the microphysics scheme was changed from its default value of −10 °C to −18 °C, shown by Field *et al.* (2014) to improve the representation of mixed-phase cloud. Additional details of model parametrizations are given in Appendix C.

2.4 | Method

Cloud properties and surface fluxes are examined in detail during one instructive case-study (flight 152, hereafter referred to as f152, conducted on 18 January 2011). This flight was selected because the aircraft conducted two vertical profiles between 100 and 5,000 m near AWS14. The flight track and location of AWS14 are shown in Figure 1. Observed and modelled surface fluxes and in-cloud vertical profiles are compared at AWS14 during f152. Model output is taken from the closest grid point to AWS14's location, plus the eight surrounding grid points: an area of approximately 4.5 km^2. Because AWS14 is located on a flat, homogeneous ice surface, it can be reasonably assumed that conditions there are representative of a large area (K15). Mean vertical profiles are computed from observations and model output using in-cloud data only, during the period when the aircraft was sampling over the ice shelf (approximately 1500–1700 UTC). Further detail is given in the appendices.

Four model experiments were run with varying "Regional Atmosphere" (RA) configurations (Table 1). Two sets of RA physics were tested: RA1M and RA1T, configured for the midlatitudes and Tropics, respectively, and described in Bush *et al.* (2019). These two experiments are the "base" configurations. The primary differences between them is that RA1M uses the operational (diagnostic) large-scale cloud scheme based on Smith (1990), whereas RA1T uses a prognostic scheme, PC2 (Wilson *et al.*, 2008). Smith (1990) parametrizes subgrid-scale variations in humidity and temperature to calculate cloud fractions using a triangular probability distribution function. Condensation within a grid box occurs when relative humidity reaches a critical value, RH_{crit}, which is specified for each model layer. Cloud liquid and ice fractions (that is, the fraction of the grid box occupied by liquid or ice cloud) are calculated by the scheme from the liquid and ice contents, before this information is fed into the microphysics for further calculation of cloud properties. The PC2 scheme is prognostic and computes liquid, ice and mixed-phase cloud fractions, which are advected in space and time after updating them by calculating sources and sinks of condensate. Incremental condensate fractions are outputted following each physical process represented by the model, such that each scheme (convection, radiation etc.) must produce an effect on condensate fractions. The connection to the microphysics scheme is slightly adapted compared to Smith (1990), so that autoconversion does not affect liquid cloud fractions. In practice, this permits the existence of extensive, optically thin liquid clouds, with high liquid cloud fraction but low liquid water contents.

TABLE 1 Configurations for model experiments used in this study

Experiment name	Options
RA1M	• RA1M physics, based on Smith (1990) large-scale cloud scheme • Heterogeneous nucleation temperature threshold set to −18 °C (Field *et al.*, 2014)
RA1M_mod	As in RA1M, with the following modifications: • Shape-dependent riming (Furtado and Field, 2017) • Modified ice cloud fraction parametrization (Abel *et al.*, 2017)
RA1T	• RA1T physics, based on PC2 (Wilson *et al.*, 2008) large-scale cloud scheme • Heterogeneous nucleation temperature threshold set to −18 °C (Field *et al.*, 2014)
RA1T_mod	As in RA1T, with the following modifications: • Turbulent production of supercooled water (Furtado *et al.*, 2016) • Shape-dependent riming (Furtado and Field, 2017)

The second two experiments (RA1M_mod and RA1T_mod) applied modifications to the base configurations shown to improve the simulation of cold mixed-phase clouds by increasing the supply of liquid water and reducing its conversion to ice (see Table 1 for a summary). These are: (a) the inclusion of shape-dependent riming (Furtado and Field, 2017), (b) the turbulent production of supercooled liquid (Furtado *et al.*, 2016, RA1T only), and (c) modifications to the ice cloud fraction parametrization described in Abel *et al.* (2017) (RA1M only). Firstly, riming depletes liquid water, so limiting the efficiency of this process can sustain higher liquid fractions in mixed-phase clouds. Reducing riming efficiency has been shown to improve Southern Ocean downwelling short-wave radiation biases associated with the conversion of too much cloud liquid water to ice (Furtado and Field, 2017). Secondly, cloud liquid water can also be produced by subgrid-scale variations in humidity that are related to unresolved turbulence. Because turbulent motions occur at finer scale than the MetUM can explicitly resolve, this can produce humidity distribution differences that are also not directly simulated. Furtado *et al.* (2016) demonstrated that increasing the supply of liquid in this manner can enhance the amount of cloud liquid. This modification is only compatible with the PC2 cloud scheme, on which RA1T is based. Finally, several studies show that ice cloud fractions are consistently overestimated in mixed-phase clouds by the MetUM (e.g. Field *et al.*, 2014; Abel *et al.*, 2017) due to computational limitations that mean that the model cannot explicitly resolve small-scale spatial heterogeneity in cloud water phase. Abel *et al.* (2017) develop an adaptation to the ice cloud fraction parametrization that limits the overlap between the liquid and ice fractions, thereby reducing the conversion of liquid to ice via vapour deposition and riming. This adaption mimics the real-world existence of spatially discrete (subgrid-scale) pockets of ice and liquid without explicitly resolving them. It is only compatible with the RA1M scheme.

The case-study was simulated with all four model configurations, then the best-performing configuration was used to simulate the entire five-week OFCAP period. During OFCAP, only the representation of surface fluxes is assessed because cloud phase measurements are not consistently available throughout the period. Initial tests showed modelled cloud phase to be sensitive to forecast length, so the first 12 hr of each 24 hr forecast were discarded as spin-up. The case-study simulation was initialised at 0000 UTC on 18 January 2011 to allow the model to spin up. For the longer OFCAP simulation, forecasts were re-initialised every 12 hr and the t + 12 to t + 24 hr part of each successive forecast was concatenated to form a continuous time series.

3 | RESULTS AND DISCUSSION

3.1 | Model representation of case-study f152

Observed ice and liquid mass mixing ratios during case f152 (18 January 2011) over AWS14 indicate that many thin cloud layers are present, with clouds below 2 km exhibiting the "water-over-ice" structure typical of low-level polar mixed-phase clouds (Figure 2). A higher altostratus layer is present at around 4 km altitude, while a stratocumulus deck is observed between approximately 400 and 2,200 m. This stratocumulus appears in two distinct layers and contains higher mass mixing ratios of cloud ice and liquid than the upper-level altostratus, reaching 1.6×10^{-2} g·kg^{-1} and 3.4×10^{-1} g·kg^{-1}, respectively. While the MetUM successfully captures the presence of altostratus and lower stratocumulus layers, all four model configurations simulate the lowest cloud layer around 1 km higher than is observed and produce just one layer below 2 km rather than the two indicated by the observations.

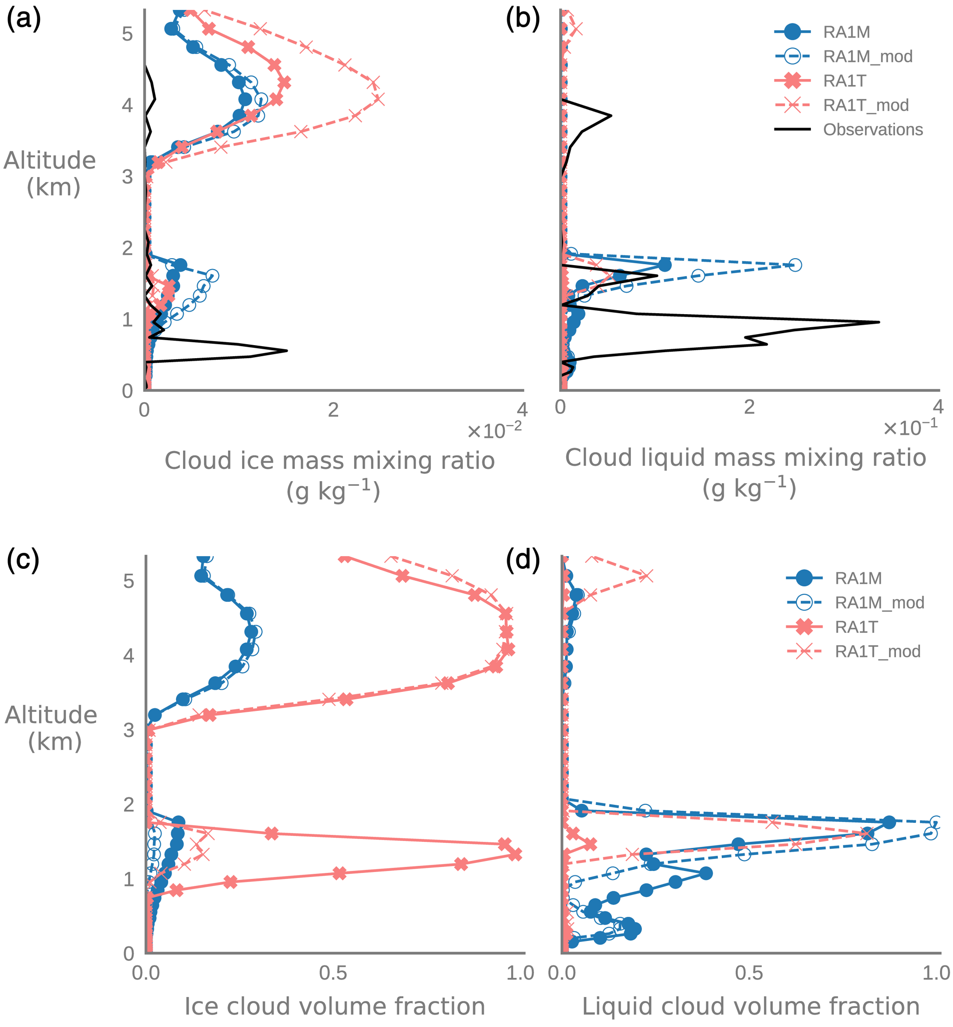

FIGURE 2 Mean vertical profiles of cloud (a) ice and (b) liquid mass mixing ratios, in g·kg^{-1}, and mean modelled cloud grid-box volume fractions of (c) ice cloud and (d) liquid cloud during f152 when the aircraft was sampling over Larsen C. Observations are shown in (a) and (b) with the solid black line and model output above AWS14 is shown in all panels by lines with markers. Solid lines with heavy markers indicate the two "base" configurations, while dashed lines with lighter markers show their modified counterparts. The experimental configurations are detailed in Table 1

Figure 2 shows that all model configurations (RA1M, RA1M_mod, RA1T and RA1T_mod) overestimate ice mass mixing ratios, and underestimate liquid mass mixing ratios above 2.5 km altitude, where virtually no liquid is present in any configuration. Ice cloud is concentrated in the upper layers (above ~3 km) because any supercooled liquid present is converted readily to ice below the ice nucleation temperature threshold of −18 °C. At 4 km altitude, the largest positive bias in ice contents is in RA1T_mod, which produces an ice mass mixing ratio 22.7 times larger than observed, while RA1M shows the smallest bias: an overestimate of 2.3 times. All models except RA1T_mod produce liquid mass mixing ratios of less than 5.0×10^{-4} g·kg^{-1} above 4 km, although liquid mixing ratios are observed to reach 5.3×10^{-2} g·kg^{-1} at 3.8 km. At lower altitudes modelled cloud generally contains less liquid and ice than observed. Between 1 and 2 km, ice mass mixing ratios in RA1M_mod peak at 7.2×10^{-3} g·kg^{-1}, 1.9 times higher than RA1M, and 2.8 and 7.5 times larger than in RA1T and RA1T_mod, respectively. At the same height, liquid mass mixing ratios peak in RA1M and RA1M_mod at 1.1×10^{-1} g·kg^{-1} and 2.5×10^{-1} g·kg^{-1}, respectively, and at 2.1×10^{-3} g·kg^{-1} and 5.2×10^{-2} g·kg^{-1} respectively in RA1T and RA1T_mod. Overall, ice mass mixing ratios are overestimated (by between 1.7 times in RA1M and 5.1 times in RA1T_mod), while liquid mass mixing ratios are underestimated (by 3.0 times in RA1M_mod to 64.9 times in RA1T). This is consistent with the results of Furtado *et al.* (2016) and Abel *et al.* (2017) who find that riming and vapour deposition occur too efficiently in modelled cold mixed-phase clouds, forming ice too readily at the expense of supercooled liquid.

The midlatitude configuration of the model, RA1M, simulates cloud ice and liquid mass mixing ratios that are closer to those observed than the tropical configuration, RA1T. RA1T produces little liquid cloud compared to observations, evident from Figure 2b, and compared to RA1M, shown in Figure 2b,d. Additionally, RA1T only simulates thin ice clouds over AWS14. This is suggested by Figure 2c, which shows that ice cloud volume fraction reaches 100% at 1.2 km, and Figure 2a, which shows very low ice mass mixing ratios in this layer.

Modelled "volume fractions" refer to the fraction of a grid box occupied by cloud of each phase; volume fractions in Figure 2 are shown as means for each model layer. RA1T is designed for use in tropical, convective regions and is less suited to Antarctic conditions where convection is less vigorous, which may explain these differences.

Modifications to the "base" model configurations produce varying results. Observed liquid mass fractions in the lowest simulated cloud layer peak at 3.4×10^{-1} g·kg^{-1}. At 2.5×10^{-1} g·kg^{-1}, RA1M_mod produces 2.3 times more liquid than RA1M in the lowest layer, but the modifications to RA1M do not change its height, which is still approximately 1 km too high in RA1M_mod. RA1T_mod generates 1.7 times more cloud ice above 3 km than RA1T, but is the only configuration to simulate liquid at this height, as is observed (Figure 2d). Throughout the profile, it also produces almost 10 times as much liquid than RA1T, but liquid mass fractions in RA1T_mod are still around six times lower than in observations. Of all four experiments, RA1M_mod exhibits the lowest bias in liquid mass fractions, while RA1M overestimates ice mass fractions by the smallest amount.

Specific humidity, that is, water vapour mass fraction, is represented reasonably accurately (within 10–25% of observed values) in all experiments throughout the profile up to 2 km (not shown). However, between 2 and 3.5 km, modelled water vapour mass fractions are considerably lower than observed (by 63–65% at 2.6 km). This underestimation of water vapour may be expected to negatively bias long-wave fluxes. However, very few differences are detectable between configurations, so this effect should have the same effect on the SEB in all experiments.

Surface flux biases at AWS14 for each model experiment during f152 are presented in Table 2. Energy available for melting, E_{melt}, is overestimated by all configurations of the MetUM, but the bias is highest in RA1M at 17.33 W·m^{-2}, causing modelled E_{melt} to be too large by 37%. Because the modelled and observed surface temperature are at melting point throughout the flight (not shown), this bias is solely driven by errors in the simulated surface fluxes. Additionally, the modelled surface albedo ($SW_{\uparrow}$ / $SW_{\downarrow}$) is within ±2% of observed values in all simulations, suggesting that biases are driven almost entirely by downwelling radiative errors, and highlighting the importance of cloud phase in determining melt. Net short-wave fluxes (SW_{net}) are simulated better by the two midlatitude experiments, with the lowest bias produced by RA1M_mod (−1.80 W·m^{-2}), while the smallest bias in net long-wave (−4.68 W·m^{-2}) is found in RA1T_mod. Both modified experiments produce lower short-wave flux biases than their respective "base" configurations, but RA1M produces smaller $LW_{\downarrow}$ and LW_{net} biases than RA1M_mod.

Between-experiment differences in downwelling fluxes are partly driven by the representation of cloud. Positive $SW_{\downarrow}$ biases in all experiments indicate that the cloud is optically too thin in this part of the spectrum, thus allowing too much solar radiation to reach the surface (as also found by K15). Conversely, overestimated $LW_{\downarrow}$ indicates that the cloud is optically too thick in the infrared, which can be related to cloud liquid water content, temperature or altitude (Zhang *et al.*, 1996). The lowest simulated cloud layer is approximately 1 km too high in all experiments, while temperature profiles are represented well compared to observations (not shown). A higher cloud base would be expected to contribute to negative $LW_{\downarrow}$ and LW_{net} biases in all experiments, but this is only true of the two RA1T experiments, suggesting a role for other effects, such as biases in parametrized cloud particle size. RA1T_mod exhibits the smallest $LW_{\downarrow}$ bias, while RA1T has the largest. $LW_{\downarrow}$ biases are positive in the two RA1M experiments, and negative in the RA1T experiments, although $LW_{\downarrow}$ and $LW_{\uparrow}$ biases are both comparatively small in RA1T_mod. Positive $LW_{\downarrow}$ biases in RA1M and RA1M_mod are also likely a result of errors in simulated cloud phase, which are only partly offset by negative water vapour biases (not shown). Thick ice clouds can have a significant long-wave warming effect (Miller *et al.*, 2015), so although specific humidity and liquid contents – usually the dominant component of cloud long-wave radiative forcing – are underestimated, the considerable overestimation of ice contents at altitudes above 3 km likely explains this positive bias.

The RA1T experiment produces quite different cloud profiles, and consequently SEB biases, to the other three simulations. As shown in Figure 2, RA1T produces very low liquid cloud fractions and virtually no liquid water throughout the cloud profile, which likely explains the negative $LW_{\downarrow}$ (−41.13 W·m^{-2}) and extremely positive $SW_{\downarrow}$ (195.38 W·m^{-2}) biases shown in Table 2. The amount of short-wave radiation transmitted through ice clouds is relatively insensitive to ice cloud thickness (Miller *et al.*, 2015), which means that although RA1T simulates an ice cloud grid-box volume fraction of 100% in two layers (Figure 1c,d), this has a limited effect on surface $SW_{\downarrow}$ because solar radiation can still penetrate. RA1T produces a melt flux bias comparable to RA1M_mod because its large radiative biases cancel and biases in the turbulent fluxes are relatively minor.

RA1T_mod has the smallest $LW_{\downarrow}$ bias, but this may be due to errors in simulated cloud phase. A positive $SW_{\downarrow}$ bias indicates that too little (liquid) cloud is simulated (also suggested by the low liquid water contents and volume fractions in Figure 2), which would usually be associated

TABLE 2 Time mean observed surface energy fluxes and model biases of each experiment at AWS14 during f152

		Mean bias			
	AWS14 (observed)	**RA1M**	**RA1M_mod**	**RA1T**	**RA1T_mod**
$SW_{\downarrow}$	594.58	66.14	**30.26**	195.38	114.84
$SW_{\uparrow}$	−501.34	−55.39	**−32.06**	−135.05	−84.90
SW_{net}	93.24	10.73	**−1.80**	60.33	29.95
$LW_{\downarrow}$	279.11	9.21	12.37	−41.13	**−5.11**
$LW_{\uparrow}$	−315.64	0.28	**0.25**	0.79	0.43
LW_{net}	−36.53	9.50	12.63	−40.34	**−4.68**
H_S	−3.63	**−2.37**	−3.49	−8.62	−6.62
H_L	−10.85	7.78	7.87	**1.40**	6.21
E_{tot}	42.23	25.05	**13.15**	15.29	23.35
E_{melt}	47.31	17.33	**6.09**	9.63	16.52

All fluxes are given in $\text{W}\cdot\text{m}^{-2}$, and are abbreviated as in Equation 1. Fluxes and biases are positive when directed towards the surface. The smallest biases are highlighted in bold text.

with a large negative $LW_{\downarrow}$ bias. However, cloud occupies up to 80% of the grid box in the lowest layer, despite the liquid water contents being far too low, suggesting that the layer is extremely thin. Optically thin liquid clouds have been shown to cause greater warming than thicker liquid clouds in summer over the Greenland ice sheet because they are thin enough to allow short-wave radiation to penetrate, but thick, low and warm enough to radiate strongly in the infrared (Bennartz *et al.*, 2013). Errors in simulated cloud phase may therefore produce small biases for the wrong reasons.

Overall, RA1M_mod is considered to be the best-performing experimental configuration with respect to cloud and SEB properties. Erroneous cloud fields and large cancelling radiative flux errors remove RA1T and RA1T_mod from consideration. RA1M and RA1M_mod have comparable net long-wave biases, and although cancelling $SW_{\downarrow}$ and $SW_{\uparrow}$ errors exist in both, these are smaller in RA1M_mod, which overestimates $SW_{\downarrow}$ by just 5%. Further, RA1M_mod's E_{tot} and E_{melt} biases are the smallest of all configurations. RA1M_mod is therefore used to run a five-week simulation of the OFCAP period for a second evaluation of simulation quality.

3.2 | Model representation of the OFCAP period

Errors in cloud phase have been shown to contribute to errors in downwelling fluxes during flight 152. However, because aircraft observations of cloud properties are not available for the entire period, a similar analysis is not possible for OFCAP. Downwelling fluxes are therefore used to infer information about cloud phase during OFCAP. Pearson correlation coefficients are used to understand relationships between melting and observed fluxes (Table 3, Figure 3).

Table 3a and Figure 3 show positive correlations (significant at the 99% level) between observed E_{melt} and $SW_{\downarrow}$ ($r_{\text{SW, melt}} = 0.62$, Figure 3a) and $LW_{\downarrow}$ ($r_{\text{LW, melt}} = 0.24$, Figure 3b). This indicates that melt is most likely to occur when more short-wave radiation can reach the surface, but is also weakly associated with higher $LW_{\downarrow}$, which is strongly related to liquid water contents, especially at the relatively low liquid water paths ($<40\,\text{g}\cdot\text{m}^{-2}$) typical of Antarctic clouds (Grosvenor *et al.*, 2017). Observed melt is not strongly related to cloud cover ($r_{\text{CC, melt}} = 0.12$), where "cloud cover" is defined as the portion of the sky above AWS14 occupied by cloud, and the negative correlation between $SW_{\downarrow}$ and cloud cover shows that $SW_{\downarrow}$ is highest during clear conditions ($r_{\text{CC, SW}} = -0.19$), which occur 11.5% of the time (defining "clear" as having cloud cover <0.31, as in Kay *et al.* (2008)). The low observed correlation between cloud cover and melt may be explained by the competing effects of cloud long-wave (positive correlation) and short-wave (negative correlation) radiative effects on melt. Observed cloud cover is not compared with $LW_{\downarrow}$ because it is computed from the closure of the long-wave radiation budget using the energy balance model of Kuipers Munneke *et al.* (2009) and so is not independent. Modelled relationships (Table 3b) compare well with observations, suggesting that the model is able to reproduce the observed drivers of melting. For example, modelled E_{melt} is positively correlated with $SW_{\downarrow}$ ($r_{\text{SW, melt}} = 0.65$) and to a much lesser extent, $LW_{\downarrow}$ ($r_{\text{LW, melt}} = 0.15$). Additionally, the large and significant (at the 99% level) correlation between modelled cloud cover and $LW_{\downarrow}$ ($r_{\text{CC, LW}} = 0.87$) suggests that cloud cover affects

TABLE 3 Pearson correlation coefficients between cloud cover, downwelling long-wave ($LW_{\downarrow}$) and short-wave fluxes ($SW_{\downarrow}$), and melt flux, (E_{melt}), at AWS14 during 1 January–7 February 2011

	(a) Observed correlations				**(b) Modelled correlations**			
	Cloud cover	$\boldsymbol{LW_{\downarrow}}$	$\boldsymbol{SW_{\downarrow}}$	$\boldsymbol{E_{\mathrm{melt}}}$	**Cloud cover**	$\boldsymbol{LW_{\downarrow}}$	$\boldsymbol{SW_{\downarrow}}$	$\boldsymbol{E_{\mathrm{melt}}}$
Cloud cover	1.00	—	**−0.19**	**0.12**	1.00	**0.87**	**−0.14**	**0.05**
$LW_{\downarrow}$		1.00	—	**0.24**		1.00	—	**0.15**
$SW_{\downarrow}$			1.00	**0.62**			1.00	**0.65**
E_{melt}				1.00				1.00

Correlation coefficients between observed components are shown in panel (a), while modelled coefficients are given in panel (b). Correlation coefficients in bold text are significant at the 99% level.

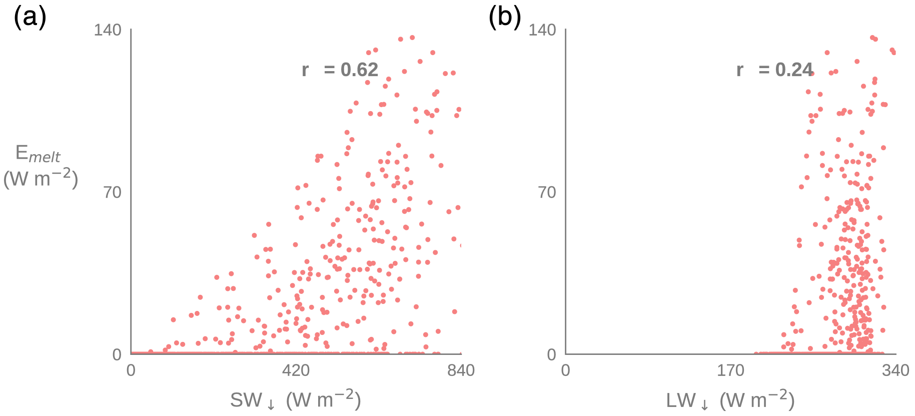

FIGURE 3 Scatterplots of observed energy available for melting (E_{melt}) against (a) downwelling short-wave ($SW_{\downarrow}$) and (b) downwelling long-wave ($LW_{\downarrow}$) at AWS14. Data plotted are instantaneous values outputted at 30 min intervals. Pearson correlation coefficients, significant at the 99% level, are given at top centre of each panel

long-wave fluxes most strongly in the MetUM. This is mostly due to the contribution of liquid clouds – the correlation between $LW_{\downarrow}$ and liquid water path is much higher ($r_{\mathrm{LWP,\,LW}} = 0.63$) than with ice water path ($r_{\mathrm{IWP,\,LW}} = 0.21$) (not shown). Modelled melting during OFCAP usually follows cloudy periods, during which liquid and then ice water paths increase and then rapidly decline as cloud glaciates and dissipates (not shown). Higher cloud liquid water contents increase $LW_{\downarrow}$ and begin to increase surface temperature and E_{tot}. Melting first begins as $LW_{\downarrow}$ increases, but is then sustained as the cloud glaciates and more short-wave radiation can reach the surface. This time-evolving process may partly explain the relatively low modelled correlations with melt of cloud cover and downwelling fluxes.

Biases in modelled SEB terms during the OFCAP period (Table 4) are smaller than those reported by K15, who use an earlier version of the default MetUM configuration, and broadly similar to those during f152 (Table 2). As in f152, SW_{net} is negatively biased, but not for the same reasons: whereas during f152 $SW_{\downarrow}$ is positively biased, during OFCAP it is negatively biased, indicating that cloud is optically too thick in the short-wave part of the spectrum during the OFCAP period. This finding is consistent with K15. Mean long-wave biases are all ~1 W·m^{-2} in magnitude, but $LW_{\downarrow}$ (and consequently LW_{net}) shows a poor correlation with observations, indicating that the model struggles to represent (liquid) clouds, atmospheric water vapour contents and/or that clouds are simulated at the wrong time. This is consistent with results from the case-study, which shows that the MetUM represents some cloud properties poorly. For example, errors in simulated cloud base height may explain the poor correlation with observed $LW_{\downarrow}$, as seen for the f152 case, when the MetUM-simulated cloud base was 1 km too high.

As shown in Table 4, modelled radiative biases during OFCAP are mostly of the same sign as K15, but smaller in magnitude, suggesting that the MetUM physics updates since 2015 and modifications made in this work have improved the representation of cloud microphysics, and consequently surface energy fluxes. The melt flux bias is smaller than in K15 and during f152 (−1.7 W·m^{-2} compared to 7.6 W·m^{-2} in K15 and 6.09 W·m^{-2} in f152, an underestimate of just 12%), but of the opposite sign. This results in a 13% underestimate of cumulative meltwater production throughout OFCAP, at 114 mm (water equivalent). K15 found that the MetUM overpredicts the occurrence of melt, despite a cold bias that is particularly present at high latitudes where conditions are more stable (Lock,

TABLE 4 Mean observed surface energy fluxes at AWS14 and mean model biases of each experiment during the OFCAP period, as in Table 2

		Mean bias			
	AWS14 (observed)	**K15**	**RA1M_mod**	**RMSE**	**Correlation coefficient**
$SW_{\downarrow}$	277.86	−31.6	**−20.95**	105.03	0.91
$SW_{\uparrow}$	−232.69	41.0	**12.78**	87.78	0.91
SW_{net}	45.17	9.4	**−8.16**	24.88	0.85
$LW_{\downarrow}$	280.10	−7.0	**−0.33**	33.01	0.49
$LW_{\uparrow}$	−303.88	−2.0	**1.17**	14.12	0.63
LW_{net}	−23.79	−6.3	**0.84**	25.70	0.47
H_{L}	−5.11	**1.9**	4.59	8.70	0.71
H_{S}	−9.34	**5.9**	6.35	11.46	0.48
E_{tot}	−1.43	**10.5**	11.98	31.71	0.78
E_{melt}	13.53	7.6	**−1.72**	16.26	0.82

Mean biases reported by K15 are given in the third column, and mean biases, root-mean-square errors and Pearson correlation coefficients of the OFCAP simulation are given in columns four to six. As in Table 2, the smallest biases are highlighted in bold, and fluxes and biases are positive when directed towards the surface.

2011). Although the OFCAP simulation also produces a small mean cold bias (−0.27 °C), and exhibits considerable negative biases in surface temperature during night-time, it represents melt frequency well because errors in modelled surface temperature are mostly when it is already well below the melting point (Figure 4). Observed melting occurs 29.5% of the time during OFCAP, while the model simulates melting 32% of the time. E_{melt} biases are therefore smaller than E_{tot} biases because melt occurs only when the surface temperature is at melting point. Remaining biases, for instance in the turbulent fluxes, may be explained by other sources of error, such as the land surface or boundary-layer schemes. Improvements made in the RA1M_mod configuration produce much better simulations of melt at AWS14 than the present default configurations and previous model versions. Because surface fluxes at AWS14 are representative of a wider area (K15) and the large-scale meteorological forcing producing cloud is similar across the ice shelf, these improvements will likely be seen across the whole of Larsen C.

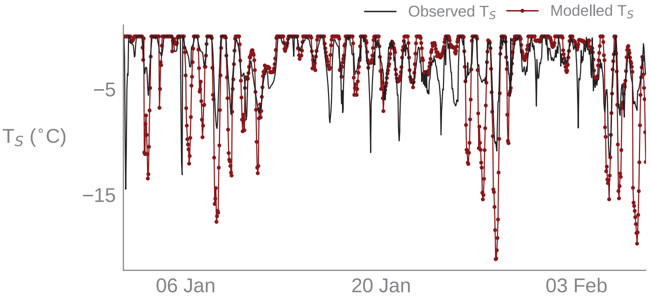

FIGURE 4 Hourly surface temperature (T_{s}) at AWS14 during the OFCAP period. Observations are given in black, while model output is shown with filled markers

4 | CONCLUSIONS

This study has shown that the representation of cloud phase in the MetUM strongly influences modelled summertime surface energy fluxes and melt over the Larsen C ice shelf. An optimum configuration, RA1M_mod, is identified and recommended for future work examining cloud properties and surface energy fluxes over the Antarctic Peninsula. RA1M_mod uses single-moment microphysics and is based on the MetUM's midlatitude regional atmosphere package, including modifications proposed by Furtado and Field (2017) and Abel *et al.* (2017). These adaptations to improve simulated cloud phase have wider applications for other regional models and in other regions of Antarctica.

Visual inspection of vertical cloud profiles during a case-study suggests that RA1M_mod reproduces the observed cloud vertical structure most closely. All model configurations overestimate ice concentrations in a mid-level altostratus layer (between ~3 and 5 km) and underestimate liquid concentrations throughout the atmosphere, although this is especially visible at lower levels (below ~2 km). RA1M_mod produces the second lowest ice mass mixing ratios above 3 km and twice as much liquid as the next-best configuration in a lower layer, bringing the modelled cloud liquid mass mixing ratio closer to observed values.

By improving the MetUM's representation of cloud phase in a case-study, RA1M_mod restricts biases in downwelling radiative fluxes to around 5% of their observed values. The resultant net radiation bias of 10.83 $W \cdot m^{-2}$ is almost half that of 20.23 $W \cdot m^{-2}$ produced by the default RA1M configuration. During the whole OFCAP period, only the model's representation of surface fluxes was evaluated because continuous observations of cloud properties were not available. Biases in downwelling radiative fluxes during the OFCAP period were less than 8% of their observed values, which produced a net radiation bias of -7.32 $W \cdot m^{-2}$ (11%). RA1M_mod is able to simulate the occurrence and magnitude of summertime melt better than the versions of the MetUM used in previous studies, such as K15, which used the default Smith (1990) large-scale cloud scheme without the modifications noted here. Over the entire OFCAP period, we find a mean bias of -1.72 $W \cdot m^{-2}$ in modelled melt flux at AWS14, which represents a four-fold reduction on the bias of 7.6 $W \cdot m^{-2}$ reported by K15. Despite this improvement, further developments in the representation of cloud phase are evidently still needed to reduce summertime biases in melt. Observed cumulative meltwater production of 114 mm (water equivalent) during the OFCAP period is still underestimated by 13% due to errors in the modelled SEB. Biases of 4.59 and 6.35 $W \cdot m^{-2}$ in the latent and sensible heat fluxes, respectively, account for a large proportion of the overall biases in E_{tot} and are greater than those shown in K15. Remaining sources of error likely include model schemes beyond the scope of this article, such as the land surface, snow or boundary-layer schemes.

The RA1M set-up likely outperforms the RA1T configurations because it has been more extensively developed, and is designed for use in colder midlatitude conditions, that are more comparable to those observed in the Antarctic, and because it is based on the Smith (1990) large-scale cloud scheme, which has been more extensively modified and tested than the prognostic PC2 scheme on which RA1T is based. RA1T probably requires further development before it is suitable for use in the Antarctic environment. Additionally, the superior performance of RA1M_mod over the basic RA1M set-up supports the findings of previous work that modifications to increase the amount of liquid and limit its conversion to ice improve the representation of cold mixed-phase clouds (Furtado and Field, 2017; Abel *et al.* 2017). These modifications may also be compatible with the MetUM's double-moment microphysics scheme, which is currently in development, although this requires further investigation. The RA1M_mod configuration will improve simulations of surface melting and ice shelf change in this rapidly changing environment, and, in future work, we will use RA1M_mod to produce a multi-decadal hindcast to investigate atmospheric processes influencing the SEB and hence melting of Antarctic Peninsula ice shelves.

ACKNOWLEDGEMENTS

The authors confirm that they have no conflicts of interest to declare. This work was supported by the Natural Environment Research Council through the EnvEast Doctoral Training Partnership (grant number NE/L002582/1). The authors also acknowledge use of the MONSooN system, a collaborative facility supplied under the Joint Weather and Climate Research Programme, a strategic partnership between the Met Office and the Natural Environment Research Council. The authors gratefully acknowledge the comments of two anonymous reviewers, which considerably strengthened the study.

DATA AVAILABILITY STATEMENT

Model data are available from the UK Met Office Managed Archive Storage System (MASS). AWS data can be retrieved from https://www.projects.science.uu.nl/iceclimate/aws/. Aircraft data are available from the British Atmospheric Data Centre, which can be cited as: Natural Environment Research Council; Lachlan-Cope, T.; Elvidge, A.D.; Smith, V.; Kirchgaessner, A.; King, J.C.; Ladkin, R. (2014): British Antarctic Survey Twin Otter aircraft Meteorological Airborne Science INstrumentation (MASIN) core data from the Orographic Flows and the Climate of the Antarctic Peninsula (OFCAP) project (2011). NCAS British Atmospheric Data Centre, 24 September 2014. doi:10.5285/2f53b18d-49fc-4477-b994-f1719d6f6dbe.

ORCID

E. Gilbert https://orcid.org/0000-0001-5272-8894
I. A. Renfrew https://orcid.org/0000-0001-9379-8215

REFERENCES

Abel, S.J., Boutle, I.A., Waite, K., Fox, S., Brown, P.R.A., Cotton, R., Lloyd, G., Choularton, T.W. and Bower, K.N. (2017) The role of precipitation in controlling the transition from stratocumulus to cumulus clouds in a Northern Hemisphere cold-air outbreak. *Journal of the Atmospheric Sciences*, 74(7), 2293–2314. https://doi.org/10.1175/JAS-D-16-0362.1.

Agosta, C., Amory, C., Kittel, C., Orsi, A., Favier, V., Gallée, H., van den Broeke, M.R., Lenaerts, J.T.M., van Wessem, J.M. and Fettweis, X. (2018) Estimation of the Antarctic surface mass balance using the regional climate model MAR (1979–2015) and identification of dominant processes. *The Cryosphere Discussions* 2018, (D), 1–22. https://doi.org/10.5194/tc-2018-76.

Baran, A.J., Hill, P., Furtado, K., Field, P. and Manners, J. (2016) A coupled cloud physics–radiation parameterization of the bulk optical properties of cirrus and its impact on the Met Office Unified Model Global Atmosphere 5.0 configuration. *Journal of Climate*, 27(20), 7725–7752. https://doi.org/10.1175/JCLI-D-13-00700.1.

Barrett, A.I., Hogan, R.J. and Forbes, R.M. (2017) Why are mixed-phase altocumulus clouds poorly predicted by large-scale models? Part 1. Physical processes. *Journal of Geophysical Research: Atmospheres*, 122(18), 9903–9926. https://doi.org/10.1002/2016JD026321.

Baumgardner, D., Jonsson, H., Dawson, W., O'Connor, D. and Newton, R. (2001) The cloud, aerosol and precipitation spectrometer: a new instrument for cloud investigations. *Atmospheric Research*, 59–60, 251–264. https://doi.org/10.1016/S0169-8095(01)00119-3.

Bennartz, R., Shupe, M.D., Turner, D.D., Walden, V.P., Steffen, K., Cox, C.J., Kulie, M.S., Miller, N.B. and Pettersen, C. (2013) July 2012 Greenland melt extent enhanced by low-level liquid clouds. *Nature*, 496(7443), 83–86. https://doi.org/10.1038/nature12002.

Bevan, S., Luckman, A., Hubbard, B., Kulessa, B., Ashmore, D., Kuipers Munneke, P., O'Leary, M., Booth, A., Sevestre, H. and McGrath, D. (2017) Centuries of intense melt on Larsen C Ice Shelf. *The Cryosphere*, 11(6), 2743–2753. https://doi.org/10.5194/tc-2017-81.

Bodas-Salcedo, A., Williams, K.D., Field, P.R. and Lock, A.P. (2012) The surface downwelling solar radiation surplus over the Southern Ocean in the Met Office model: the role of midlatitude cyclone clouds. *Journal of Climate*, 25(21), 7467–7486. https://doi.org/10.1175/JCLI-D-11-00702.1.

van den Broeke, M. (2005) Strong surface melting preceded collapse of Antarctic Peninsula ice shelf. *Geophysical Research Letters*, 32(12), 2–5. https://doi.org/10.1029/2005GL023247.

van den Broeke, M.R., Reijmer, C., Van As, D., Van de Wal, R. and Oerlemans, J. (2005) Seasonal cycles of Antarctic surface energy balance from automatic weather stations. *Annals of Glaciology*, 41, 131–139. https://doi.org/10.3189/172756405781813168.

Bromwich, D.H., Nicolas, J.P., Hines, K.M., Kay, J.E., Key, E.L., Lazzara, M.A., Lubin, D., McFarquhar, G.M., Gorodetskaya, I.V., Grosvenor, D.P., Lachlan-Cope, T. and van Lipzig, N.P.M. (2012) Tropospheric clouds in Antarctica. *Reviews of Geophysics*, 50(1), 1–40. https://doi.org/10.1029/2011RG000363.

Bromwich, D.H., Otieno, F.O., Hines, K.M., Manning, K.W. and Shilo, E. (2013) Comprehensive evaluation of polar weather research and forecasting model performance in the Antarctic. *Journal of Geophysical Research: Atmospheres*, 118(2), 274–292. https://doi.org/10.1029/2012JD018139.

Brown, P.R.A. and Francis, P.N. (1995) Improved measurements of the ice water content in cirrus using a total-water probe. *Journal of Atmospheric and Oceanic Technology*, 12(2), 410–414. https://doi.org/10.1175/1520-0426(1995)012<0410:IMOTIW>2.0.CO;2.

Bush, M., Allen, T., Bain, C., Boutle, I., Edwards, J., Finnenkoetter, A., Franklin, C., Hanley, K., Lean, H., Lock, A., Manners, J., Mittermaier, M., Morcrette, C., North, R., Petch, J., Short, C., Vosper, S., Walters, D., Webster, S., Weeks, M., Wilkinson, J., Wood, N. and Zerroukat, M. (2019) The first Met Office Unified Model/JULES regional atmosphere and land configuration, RAL1. *Geoscientific Model Development Discussions*, in review , 1–48. https://doi.org/10.5194/gmd-2019-130.

Cook, A.J. and Vaughan, D.G. (2010) Overview of areal changes of the ice shelves on the Antarctic Peninsula over the past 50 years. *The Cryosphere Discussions*, 3(2), 579–630. https://doi.org/10.5194/tcd-3-579-2009.

Crawford, T.L. and Dobosy, R.J. (1992) A sensitive fast-response probe to measure turbulence and heat flux from any airplane. *Boundary-Layer Meteorology*, 59(3), 257–278. https://doi.org/10.1007/BF00119816.

Crosier, J., Bower, K.N., Choularton, T.W., Westbrook, C.D., Connolly, P.J., Cui, Z.Q., Crawford, I.P., Capes, G.L., Coe, H., Dorsey, J.R., Williams, P.I., Illingworth, A.J., Gallagher, M.W. and Blyth, A.M. (2011) Observations of ice multiplication in a weakly convective cell embedded in supercooled mid-level stratus. *Atmospheric Chemistry and Physics*, 11(1), 257–273. https://doi.org/10.5194/acp-11-257-2011.

Edwards, J.M. and Slingo, A. (1996) Studies with a flexible new radiation code. I: Choosing a configuration for a large-scale model. *Quarterly Journal of the Royal Meteorological Society*, 122, 689–719. https://doi.org/10.1002/qj.49712253107.

Elvidge, A.D., Renfrew, I.A., King, J.C., Orr, A., Lachlan-Cope, T.A., Weeks, M. and Gray, S.L. (2015) Foehn jets over the Larsen C ice shelf, Antarctica. *Quarterly Journal of the Royal Meteorological Society*, 141(688), 698–713. https://doi.org/10.1002/qj.2382.

Elvidge, A.D., Renfrew, I.A., King, J.C., Orr, A. and Lachlan-Cope, T.A. (2016) Foehn warming distributions in nonlinear and linear flow regimes: a focus on the Antarctic Peninsula. *Quarterly Journal of the Royal Meteorological Society*, 142(695), 618–631. https://doi.org/10.1002/qj.2489.

Field, P.R., Cotton, R.J., McBeath, K., Lock, A.P., Webster, S. and Allan, R.P. (2014) Improving a convection-permitting model simulation of a cold air outbreak. *Quarterly Journal of the Royal Meteorological Society*, 140, 124–138. https://doi.org/10.1002/qj.2116.

Furtado, K. and Field, P. (2017) The role of ice microphysics parametrizations in determining the prevalence of supercooled liquid water in high-resolution simulations of a Southern Ocean midlatitude cyclone. *Journal of the Atmospheric Sciences*, 74, 2001–2021. https://doi.org/10.1175/JAS-D-16-0165.1.

Furtado, K., Field, P.R., Boutle, I.A., Morcrette, C.J. and Wilkinson, J.M. (2016) A physically based subgrid parameterization for the production and maintenance of mixed-phase clouds in a general circulation model. *Journal of the Atmospheric Sciences*, 73(1), 279–291. https://doi.org/10.1175/JAS-D-15-0021.1.

Grosvenor, D.P., Choularton, T.W., Lachlan-Cope, T., Gallagher, M.W., Crosier, J., Bower, K.N., Ladkin, R.S. and Dorsey, J.R. (2012) *In-situ* aircraft observations of ice concentrations within clouds over the Antarctic Peninsula and Larsen Ice Shelf. *Atmospheric Chemistry and Physics*, 12(23), 11275–11294. https://doi.org/10.5194/acp-12-11275-2012.

Grosvenor, D.P., Field, P.R., Hill, A.A. and Shipway, B.J. (2017) The relative importance of macrophysical and cloud albedo changes for aerosol-induced radiative effects in closed-cell stratocumulus: insight from the modelling of a case study. *Atmospheric Chemistry and Physics*, 17(8), 5155–5183. https://doi.org/10.5194/acp-17-5155-2017.

Hines, K.M., Bromwich, D.H., Wang, S.H., Silber, I., Verlinde, J. and Lubin, D. (2019) Microphysics of summer clouds in central

West Antarctica simulated by the Polar Weather Research and Forecasting model (WRF) and the Antarctic Mesoscale Prediction System (AMPS). *Atmospheric Chemistry and Physics*, 19(19), 12431–12454. https://doi.org/10.5194/acp-19-12431-2019.

Hyder, P., Edwards, J.M., Allan, R.P., Hewitt, H.T., Bracegirdle, T.J., Gregory, J.M., Wood, R.A., Meijers, A.J.S., Mulcahy, J., Field, P.R., Furtado, K., Bodas-Salcedo, A., Williams, K.D., Copsey, D., Josey, S.A., Liu, C., Roberts, C.D., Sanchez, C., Ridley, J., Thorpe, L., Hardiman, S.C., Mayer, M., Berry, D.I. and Belcher, S.E. (2018) Critical Southern Ocean climate model biases traced to atmospheric model cloud errors. *Nature Communications*, 9(1), 3625. https://doi.org/10.1038/s41467-018-05634-2.

Kalesse, H., de Boer, G., Solomon, A., Oue, M., Ahlgrimm, M., Zhang, D., Shupe, M.D., Luke, E. and Protat, A. (2016) Understanding rapid changes in phase partitioning between cloud liquid and ice in stratiform mixed-phase clouds: an Arctic case study. *Monthly Weather Review*, 144(12), 4805–4826. https://doi.org/10.1175/MWR-D-16-0155.1.

Kay, J.E., L'Ecuyer, T., Gettelman, A., Stephens, G., and O'Dell, C. (2008) The contribution of cloud and radiation anomalies to the 2007 Arctic sea ice extent minimum. *Geophysical Research Letters*, 35(8), 1–5. https://doi.org/10.1029/2008GL033451.

King, J.C., Lachlan-Cope, T.A., Ladkin, R.S. and Weiss, A. (2008) Airborne measurements in the stable boundary layer over the Larsen Ice Shelf, Antarctica. *Boundary-Layer Meteorology*, 127(3), 413–428. https://doi.org/10.1007/s10546-008-9271-4.

King, J.C., Gadian, A., Kirchgaessner, A., Kuipers Munneke, P., Lachlan-Cope, T.A., Orr, A., Reijmer, C., van den Broeke, M.R., Van Wessem, J.M. and Weeks, M. (2015) Validation of the summertime surface energy budget of Larsen C Ice Shelf (Antarctica) as represented in three high-resolution atmospheric models. *Journal of Geophysical Research: Atmospheres*, 120(4), 1335–1347. https://doi.org/10.1002/2014JD022604.

Klein, S.A., McCoy, R.B., Morrison, H., Ackerman, A.S., De Boer, G., Chen, M., Cole, J.N.S., Genio, D.D., Foster, M.J., Fridlind, A., Golaz, J.-C., Hashino, T., Jerry, Y., Hoose, C., Khairoutdinov, M.F., Larson, V.E., Liu, X., McFarquhar, G.M., Menon, S., Neggers, R.A.J., Park, S., Michael, R., Schmidt, J.M., Sednev, I., Shipway, B.J., Shupe, M.D., Spangenberg, D.A., Sud, Y.C., Turner, D.D., Veron, D.E., Von, K., Walker, G.K., Wang, Z., Wolf, A.B. and Xie, S. (2009) Intercomparison of model simulations of mixed-phase clouds observed during the ARM Mixed-Phase Arctic Cloud Experiment. I: Single-layer cloud. *Quarterly Journal of the Royal Meteorological Society*, 135, 979–1002. https://doi.org/10.1002/qj.416.

Kuipers Munneke, P., van den Broeke, M.R., Reijmer, C.H., Helsen, M.M., Boot, W., Schneebeli, M. and Steffen, K. (2009) The role of radiation penetration in the energy budget of the snowpack at Summit, Greenland. *The Cryosphere*, 3(1), 155–165. https://doi.org/10.5194/tcd-3-277-2009.

Kuipers Munneke, P., van den Broeke, M.R., King, J.C., Gray, T. and Reijmer, C.H. (2012) Near-surface climate and surface energy budget of Larsen C ice shelf, Antarctic Peninsula. *The Cryosphere*, 6(2), 353–363. https://doi.org/10.5194/tc-6-353-2012.

Lachlan-Cope, T. (2010) Antarctic clouds. *Polar Research*, 29(2), 150–158. https://doi.org/10.1111/j.1751-8369.2010.00148.x.

Lachlan-Cope, T., Listowski, C. and O'Shea, S. (2016) The microphysics of clouds over the Antarctic Peninsula – Part 1: Observations. *Atmospheric Chemistry and Physics*, 16, 15605–15617. https://doi.org/10.5194/acp-16-15605-2016.

Lenaerts, J.T.M., Van Tricht, K., Lhermitte, S. and L'Ecuyer, T.S. (2017) Polar clouds and radiation in satellite observations, reanalyses, and climate models. *Geophysical Research Letters*, 44(7), 3355–3364. https://doi.org/10.1002/2016GL072242.

Lenaerts, J.T.M., Ligtenberg, S.R.M., Medley, B., Van de Berg, W.J., Konrad, H., Nicolas, J.P., Van Wessem, J.M., Trusel, L.D., Mulvaney, R., Tuckwell, R.J., Hogg, A.E. and Thomas, E.R. (2018) Climate and surface mass balance of coastal West Antarctica resolved by regional climate modelling. *Annals of Glaciology*, 59(76, part 1), 29–41. https://doi.org/10.1017/aog.2017.42.

Listowski, C. and Lachlan-Cope, T. (2017) The microphysics of clouds over the Antarctic Peninsula – Part 2: Modelling aspects within Polar WRF. *Atmospheric Chemistry and Physics*, 17, 10195–10221. https://doi.org/10.5194/acp-17-10195-2017.

Listowski, C., Delanoë, J., Kirchgaessner, A., Lachlan-Cope, T. and King, J. (2019) Antarctic clouds, supercooled liquid water and mixed phase investigated with DARDAR: geographical and seasonal variations. *Atmospheric Chemistry and Physics*, 19(10), 6771–6808. https://doi.org/10.5194/acp-19-6771-2019.

Lock, A. (2011) Stable boundary layer modelling at the Met Office. In: *ECMWF GABLS Workshop on Diurnal cycles and the stable boundary layer*, 7–10 November 2011, 137–148.

Miller, N.B., Shupe, M.D., Cox, C.J., Walden, V.P., Turner, D.D. and Steffen, K. (2015) Cloud radiative forcing at Summit, Greenland. *Journal of Climate*, 28(15), 6267–6280. https://doi.org/10.1175/JCLI-D-15-0076.1.

Nicolas, J.P., Vogelmann, A.M., Scott, R.C., Wilson, A.B., Cadeddu, M.P., Bromwich, D.H., Verlinde, J., Lubin, D., Russell, L.M., Jenkinson, C., Powers, H.H., Ryczek, M., Stone, G. and Wille, J.D. (2017) January 2016 extensive summer melt in West Antarctica favoured by strong El Niño. *Nature Communications*, 8(May), 1–10. https://doi.org/10.1038/ncomms15799.

Orr, A., Phillips, T., Webster, S., Elvidge, A., Weeks, M., Hosking, S. and Turner, J. (2014) Met Office Unified Model high-resolution simulations of a strong wind event in Antarctica. *Quarterly Journal of the Royal Meteorological Society*, 140(684), 2287–2297. https://doi.org/10.1002/qj.2296.

Scambos, T.A., Hulbe, C., Fahnestock, M. and Bohlander, J. (2000) The link between climate warming and break-up of ice shelves in the Antarctic Peninsula. *Journal of Glaciology*, 46(154), 516–530. https://doi.org/10.3189/172756500781833043.

Scambos, T., Hulbe, C. and Fahnestock, M. (2003) Climate-induced ice shelf disintegration in the Antarctic Peninsula. In: Domack, E., Levente, A., Burnet, A., Bindschadler, R., Convey, P. and Kirby, M. (Eds.) *Antarctic Peninsula Climate Variability: Historical and Paleoenvironmental Perspectives, Antarctic Research Series*, Washington, DC: American Geophysical Union, Vol. 79, pp. 79–92. https://doi.org/doi:10.1029/AR079p0079.

Smith, R.N.B. (1990) A scheme for predicting layer clouds and their water content in a general circulation model. *Quarterly Journal of the Royal Meteorological Society*, 116, 435–460. https://doi.org/10.1002/qj.49711649210.

Souverijns, N., Gossart, A., Demuzere, M., Lenaerts, J.T.M., Medley, B., Gorodetskaya, I.V., Vanden Broucke, S. and van Lipzig, N.P.M. (2019) A new regional climate model for POLAR-CORDEX: evaluation of a 30-year hindcast with COSMO-CLM 2 over

Antarctica. *Journal of Geophysical Research: Atmospheres*, 124(3), 1405–1427. https://doi.org/10.1029/2018JD028862.

Tan, I. and Storelvmo, T. (2016) Sensitivity study on the influence of cloud microphysical parameters on mixed-phase cloud thermodynamic phase partitioning in CAM5. *Journal of the Atmospheric Sciences*, 73(2), 709–728. https://doi.org/10.1175/JAS-D-15-0152.1.

Turner, J., Colwell, S.R., Marshall, G.J., Lachlan-Cope, T.A., Carleton, A.M., Jones, P.D., Lagun, V., Reid, P.A. and Iagovkina, S. (2005) Antarctic climate change during the last 50 years. *International Journal of Climatology*, 25(3), 279–294. https://doi.org/10.1002/joc.1130.

Turner, J., Lu, H., White, I., King, J.C., Phillips, T., Hosking, J.S., Bracegirdle, T.J., Marshall, G.J., Mulvaney, R. and Deb, P. (2016) Absence of 21st century warming on Antarctic Peninsula consistent with natural variability. *Nature*, 535(7612), 411–415. https://doi.org/10.1038/nature18645.

Van Wessem, J.M., Reijmer, C.H., Lenaerts, J.T.M., Van de Berg, W.J., van den Broeke, M.R. and Van Meijgaard, E. (2014) Updated cloud physics in a regional atmospheric climate model improves the modelled surface energy balance of Antarctica. *The Cryosphere*, 8(1), 125–135. https://doi.org/10.5194/tc-8-125-2014.

Van Wessem, J.M., van de Berg, W.J., Noël, B.P., van Meijgaard, E., Birnbaum, G., Jakobs, C.L., Krüger, K., Lenaerts, J.T.M., Lhermitte, S., Ligtenberg, S.R.M., Medley, B., Reijmer, C.H., van Tricht, K., Trusel, L.D., van Ulft, L.H., Wouters, B., Wuite, J. and van den Broeke, M.R. (2018) Modelling the climate and surface mass balance of polar ice sheets using RACMO2. Part 2: Antarctica (1979–2016). *The Cryosphere*, 12(4), 1479–1498. https://doi.org/10.5194/tc-2017-202.

Vergara-Temprado, J., Miltenberger, A.K., Furtado, K., Grosvenor, D.P., Shipway, B.J., Hill, A.A., Wilkinson, J.M., Field, P.R., Murray, B.J. and Carslaw, K.S. (2018) Strong control of Southern Ocean cloud reflectivity by ice-nucleating particles. *Proceedings of the National Academy of Sciences*, 115(11), 2687–2692. https://doi.org/10.1073/pnas.1721627115.

Walters, D., Boutle, I., Brooks, M., Melvin, T., Stratton, R., Vosper, S., Wells, H., Williams, K., Wood, N., Allen, T., Bushell, A., Copsey, D., Earnshaw, P., Edwards, J., Gross, M., Hardiman, S., Harris, C., Heming, J., Klingaman, N., Levine, R., Manners, J., Martin, G., Milton, S., Mittermaier, M., Morcrette, C., Riddick, T., Roberts, M., Sanchez, C., Selwood, P., Stirling, A., Smith, C., Suri, D., Tennant, W., Luigi Vidale, P., Wilkinson, J., Willett, M., Woolnough, S. and Xavier, P. (2017) The Met Office Unified Model Global Atmosphere 6.0/6.1 and JULES Global Land 6.0/6.1 configurations. *Geoscientific Model Development*, 10(4), 1487–1520. https://doi.org/10.5194/gmd-10-1487-2017.

Wilson, D.R. and Ballard, S.P. (1999) A microphysically based precipitation scheme for the UK Meteorological Office Unified Model. *Quarterly Journal of the Royal Meteorological Society*, 125(557), 1607–1636. https://doi.org/10.1002/qj.49712555707.

Wilson, D.R., Bushell, A.C., Kerr-Munslow, A.M., Price, J.D. and Morcrette, C.J. (2008) PC2: a prognostic cloud fraction and condensation scheme. I: Scheme description. *Quarterly Journal of the Royal Meteorological Society*, 134(637), 2093–2107. https://doi.org/10.1002/qj.333.

Zhang, T., Stamnes, K. and Bowling, S.A. (1996) Impact of clouds on surface radiative fluxes and snowmelt in the Arctic and subarctic. *Journal of Climate*, 9(9), 2110–2123. https://doi.org/10.1175/1520-0442(1996)009<2110:IOCOSR>2.0.CO;2.

How to cite this article: Gilbert E, Orr A, King JC, *et al.* Summertime cloud phase strongly influences surface melting on the Larsen C ice shelf, Antarctica. *Q J R Meteorol Soc.* 2020;1–16. https://doi.org/10.1002/qj.3753

APPENDIX A: AIRCRAFT INSTRUMENTATION AND DATA TREATMENT

Cloud microphysics are observed using the British Antarctic Survey's instrumented De Haviland Twin Otter aircraft, which measures standard meteorological variables: total temperature is measured with Rosemount probes, static pressure is measured using in-built aircraft sensors, humidity is observed by a Vaisala humicap sensor and cooled mirror hygrometer, and three-dimensional winds are measured using a Best Aircraft Turbulence (BAT) probe (Crawford and Dobosy, 1992), mounted on a boom fitted to the nose of the aircraft. Upwelling and downwelling radiative fluxes (short-wave and long-wave) are measured using Eppley pyranometers and pyrgeometers mounted to the belly and roof of the aircraft, respectively. Surface temperatures are measured using a downward-looking infrared thermometer (Heitronics KT19.82). A full description of the aircraft's instrumentation can be found in King *et al.* (2008). The aircraft can be adapted to measure specific areas of interest, and during the OFCAP campaign was fitted with a Droplet Measurement Technologies Cloud, Aerosol and Precipitation Spectrometer (CAPS probe: Baumgardner *et al.*, 2001) to sample cloud properties. The probe contains three separate instruments: a Cloud and Aerosol Spectrometer (CAS) which measures the diameter of small cloud particles 0.5–50 μm, a Cloud Imaging Probe (CIP) which images larger cloud and precipitation-sized particles of 25 μm – 1.5 mm diameter using a charge-coupled device array, and a hotwire liquid water contents (LWC) sensor, which is used to validate CAS data.

In-cloud particles observed by the CAS instrument are all assumed to be liquid droplets, whereas those observed by the CIP must be post-processed to determine their phase. After data are quality controlled and processed using the method of Crosier *et al.* (2011), cloud particles are segregated into ice and liquid using the technique of Lachlan-Cope *et al.* (2016) by determining their circularity, C, defined as:

$$C = P^2/4\,\pi\,A, \tag{A1}$$

where P is the particle perimeter as measured by the instrument and A is the particle area, which must be a minimum of 50 pixels (or ~200 μm) to be detected. Particles with $0.9 \leq C \leq 1.2$ are considered to be circular and are thus classified as drops, while those with $C \geq 1.4$ are classified as ice. Following visual inspection of the data from the flights considered, particles with intermediate circularity $1.2 \leq C \leq 1.4$ are classified as ice, as in Lachlan-Cope *et al.* (2016). Ice water contents are then calculated with the mass-dimensional relationship of Brown and Francis (1995).

Only in-cloud data are used to compute mean profiles, where cloud is defined as in Lachlan-Cope *et al.* (2016) when the CAS instrument measures either number concentrations above 1 cm^{-3} of droplet-sized particles greater than 1 μm in diameter or when the CIP instrument measures number concentrations of ice particles above 1.0×10^{-8} cm^{-3}.

APPENDIX B: AUTOMATIC WEATHER STATION (AWS) DATA

Observations of surface energy fluxes and meteorology are retrieved from the Larsen North automatic weather station (AWS14), which is set up as described in Kuipers Munneke *et al.* (2009). Observations of air temperature, pressure, relative humidity, wind speed and direction, and radiative fluxes (up- and downwelling components of long-wave and short-wave) are made directly, while the sensible and latent heat fluxes are calculated using the bulk aerodynamic method. An energy balance model (van den Broeke *et al.*, 2005) is applied to compute the energy balance of the snowpack after the raw data have been corrected using the method of Kuipers Munneke *et al.* (2012).

APPENDIX C: NUMERICAL WEATHER PREDICTION MODEL DESCRIPTION AND PARAMETRIZATION SCHEMES

The Met Office Unified Model (MetUM) is a numerical weather prediction model used for operational and research purposes. Its dynamical core is non-hydrostatic and uses semi-implicit time-stepping and semi-Lagrangian advection (Walters *et al.*, 2017). Model equations are solved on a staggered Arakawa-C grid in the horizontal and with Charney–Phillips staggering in the vertical, with a hybrid height vertical coordinate that is terrain-following near the surface. It is run in atmosphere-only mode and configured similarly to Orr *et al.* (2014), although in contrast to that work, this study uses just one nested domain at 1.5 km horizontal grid spacing with a 60 second time step. This inner nest takes input from a global model that has ~17 km resolution in the midlatitudes, which is forced at the boundaries with Met Office global operational analyses.

Simulations are run in forecast mode as described in the main text: re-initialisations occur at 0000 UTC and 1200 UTC, with only the t + 12 to t + 24 part of the forecast retained. The case-study is initialised 12 hours prior to the flight, while the OFCAP simulation comprises a series of forecasts concatenated together. All quantities of interest are outputted as instantaneous values every 15 min, except meteorological variables, which are outputted hourly. During the OFCAP period, all variables are outputted as hourly instantaneous values.

The radiation scheme (SOCRATES) is based on Edwards and Slingo (1996), which calculates surface radiative fluxes prognostically using six short-wave and nine long-wave absorption bands. Absorption and scattering by cloud particles are treated by applying “thick averaging” to calculate droplet effective radius from number concentrations computed by the microphysics, and ice crystals are parametrized according to Baran *et al.* (2014).

The operational single-moment microphysics scheme used in all experiments is based on Wilson and Ballard (1999) and represents condensate mass mixing ratios only, with prescribed number concentrations over land (including ice shelves) and open water. The scheme is three-phase, representing cloud liquid water, rain and snow (which encompasses all ice in the grid box) prognostically. Microphysical processes produce or deplete condensate in each layer as follows: liquid droplets are formed via condensation, and are removed by droplet settling, autoconversion to rain drops, freezing during the ice nucleation process and riming. Rain droplets form from cloud water via autoconversion, from cloud water or other rain droplets via sedimentation or accretion, and from ice by melting. Rain is depleted by sedimentation or evaporation, or converted into ice during homogeneous ice nucleation or ice crystal capture. Ice is produced directly from the vapour phase via vapour diffusion (the Wegener–Bergeron–Findeisen process), or from the liquid phase via rain droplet capture or riming, and is lost due to sedimentation, sublimation and melting. Heterogeneous ice nucleation occurs when the temperature is below a specified threshold and liquid water is present in a grid box, representing an immersion freezing or condensation mechanism. All experiments use a modified threshold of −18 °C rather than the default −10 °C, as this modification was shown by Field *et al.* (2014) to improve the representation of mixed-phase cloud because it forces supercooled liquid to remain liquid at colder temperatures.

Appendix: Additional sensitivity testing of the RA1M_mod model configuration for use in the model hindcast

C

This appendix summarises additional sensitivity tests performed to optimise the RA1M_mod model configuration used in Chapter 5 to run the model hindcast presented in Chapter 6. Work presented in this appendix has been adapted from a report submitted in June 2019 in compliance with UEA's formal reporting procedure.

C.1 RA1M_mod model sensitivity testing

C.1.1 Sensitivity tests with amended boundary layer mixing length

In addition to the RA1M_mod OFCAP simulation presented in Chapter 5, a further simulation of the OFCAP period was conducted using the "lambda" configuration. This configuration uses exactly the same physics settings as RA1M_mod, but with the mixing length, λ, revised from its default value of 40 m to 5 m. Initial tests showed positive biases in the turbulent fluxes and too-cold night-time surface temperatures, consistent with a poor representation of the stable boundary layer, a consistent problem in the MetUM and many other models (Lock, 2011; Sandu et al., 2011; Beljaars et al., 2011). During night-time and/or winter, which is included in the hindcast presented in Chapter 6, turbulent mixing is too vigorous during stable conditions (Lock, 2011), which leads to a warm bias because too much heat is mixed towards the surface. This is related to the way the boundary layer mixing scheme represents diffusivity, which is a function of the mixing length, λ^2. This means mixing is more strongly affected by changing λ than by changing the tails distribution function, which preliminary work (Andrew Orr, pers. comm.) has shown to make a negligible difference to the quality of simulations. Hence, amending the mixing length should improve the representation of mixing, particularly in stable and neutral boundary layers.

Table C.1 shows observed and modelled mean values for key meteorological variables and SEB components during OFCAP, as in Table 5.3, but comparing the control RA1M_mod and lambda runs. As shown in Table C.1 the amended mixing length makes minor differences to the representation of surface meteorology, most notably reducing T_S biases. The time series of surface temperature (Figure C.1) and melt flux (Figure C.2) show that both experiments simulate melt too frequently. T_S is observed to be at the melting point for 4.38 days during the whole 37.5 day period (12% of the time), while the RA1M_mod (control) model estimates T_S = 0°C for 12.2 days (33% of the time) and the lambda run estimates a slightly lower frequency at 11.9 days (32%). Modifying the mixing length does not alter the significant negative T_S bias, but it does reduce the magnitude of the most negative temperature biases. The lambda run has a marginally improved representation of turbulent heat fluxes (reducing the RMSE of H_L from 11.5 W m^{-2} to 10.4 W m^{-2}, and increasing correlation coefficients from 0.71 and 0.48 to 0.72 and 0.51, respectively, for H_S and H_L. Mean E_{tot} biases across the whole period are reduced from 12.0 to 11.5 W m^{-2}, although RMSE is slightly increased and r values decrease from 0.78 to 0.77. Mean E_{melt} biases increase from -1.8 W m^{-2} to -2.2 W m^{-2} however, meaning the improvements cause melt to be underestimated slightly more.

As shown in Figure C.3, both model simulations fail to represent negative E_{tot} fluxes of the order -100 W m^{-2} for instance between 6-9 January or 5-7 Feb, which explains the positive E_{tot} mean biases in Table C.1. Changing λ has virtually no effect, although mean E_{tot} bias is reduced from 11.98 W m^{-2} to 11.54 W m^{-2}. This bias arises for two reasons. Firstly, on two occasions (6-9 January and 5-7 Feb), modelled $SW_\downarrow$ drops by ~200 W m^{-2}, and $LW_\downarrow$ increases by ~100 W m^{-2}, producing R_{net} of -100 W m^{-2}. The concurrent increase and decrease of $SW_\downarrow$ and $LW_\downarrow$, respectively, results from a dramatic drop in modelled cloud cover (not shown), which causes $LW_\downarrow$ to decline considerably (Figure C.4). However, an increase and decrease, respectively, in $SW_\downarrow$ and $LW_\downarrow$, is not observed during these periods, suggesting that cloudy conditions persist despite both experiments simulating clear-sky conditions. This bias in downwelling fluxes, and inferred bias in cloud cover, is consistent with modelled cloud ice contents being too high, causing the cloud to glaciate, precipitate and dissipate too quickly via the process described in Chapter 5. Biases in downwelling fluxes, and by inference cloud cover, during 6-9 January and 5-9 February 2011, are less extremely biased in the lambda run.

C.1.2 The importance of ground heat flux, G_S

The MetUM configurations used in this thesis do not include an accurate representation of the ground heat flux, G_S, which is observed to reach a minimum during OFCAP of -28 W m^{-2}, conducting energy away from the surface. G_S is most important during the night when SW_{net} is smallest and E_{tot} is most negative. If modelled E_{tot} and E_{melt} are calculated using observed G_S values (the E_{tot} + G_S and E_{melt} + G_S rows in Table C.1), their biases fall from 11.98 to

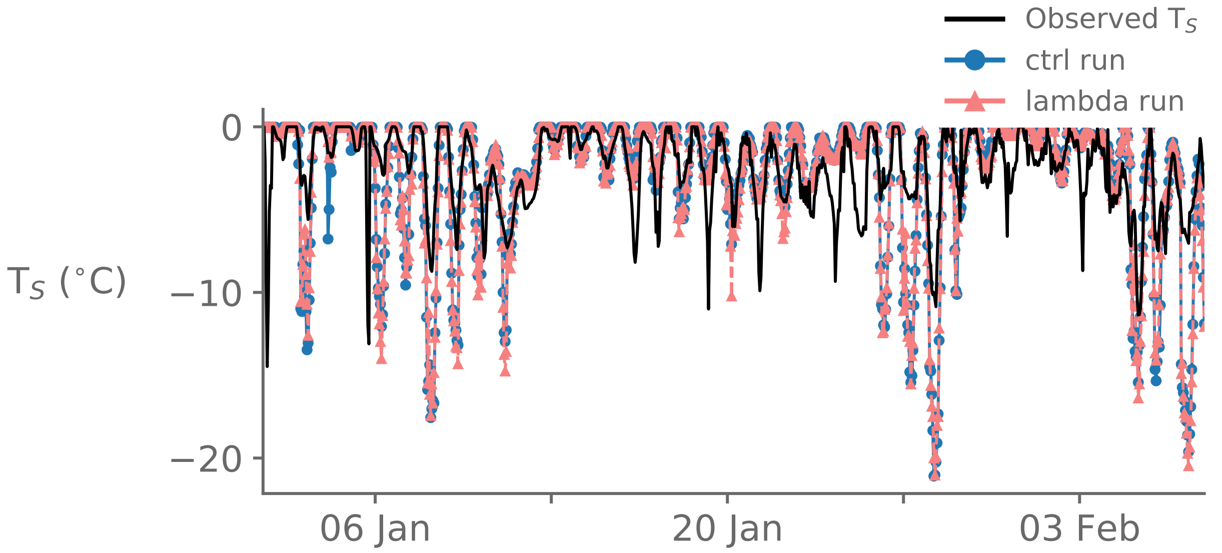

Figure C.1.: Mean surface temperature, T_S, as in Figure 5.8, during the OFCAP period in observations (black) and as modelled by the control RA1M_mod (blue, with circle markers) and lambda (pink, dashed, with triangle markers) simulations.

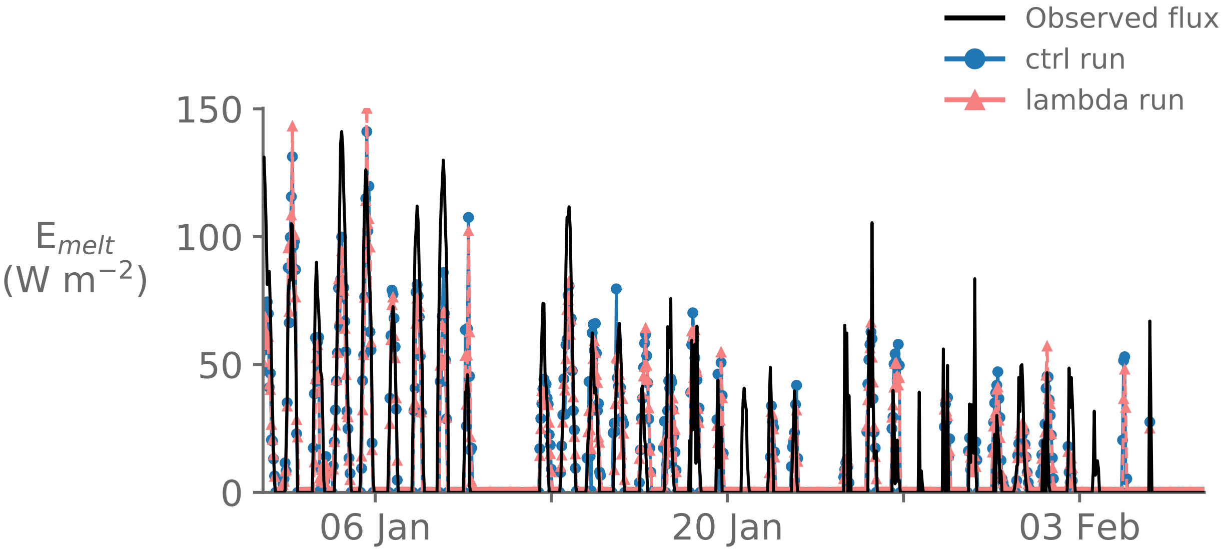

Figure C.2.: As in Figure C.1, but for melt energy, E_{melt}.

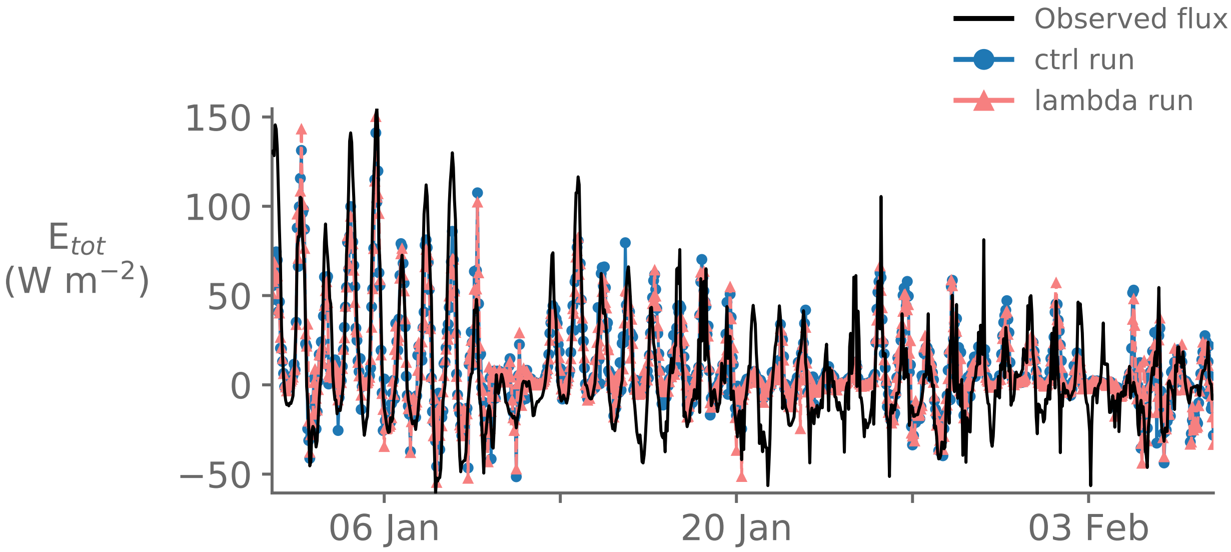

Figure C.3.: As in Figure C.1, but for E_{tot}.

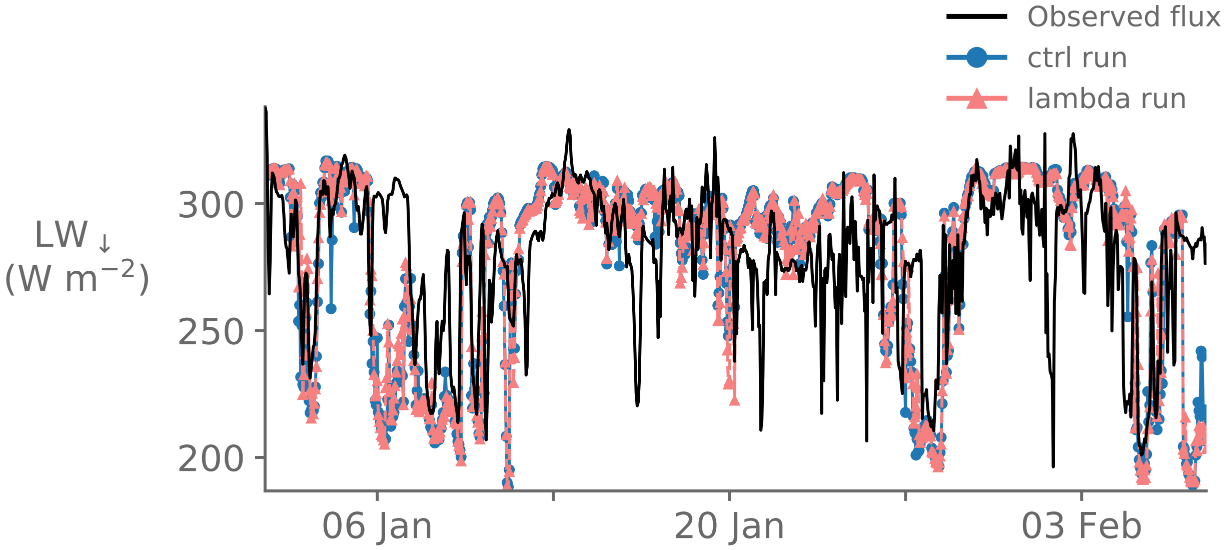

Figure C.4.: As in Figure C.1, but for $LW_{\downarrow}$.

Table C.1.: Mean observed surface energy fluxes at AWS 14 and mean model biases of the RA1M_mod control and "lambda" experiments during the OFCAP period, as in Table 5.3. Validation statistics for near-surface meteorological parameters (1.5 m air temperature, T_{air}, surface temperature, T_S, relative humidity, RH, and 10 m wind speed, FF) are also given in addition to the SEB terms shown in Table 5.3. Mean biases, RMSEs and Pearson correlation coefficients (r) in the RA1M_mod and lambda OFCAP simulations are given in columns three to five and six to eight, respectively. E_{tot} and E_{melt} fluxes, both with and without observed G_S prescribed ($+G_S$), are shown in the bottom four rows for each. As in Table 5.3, the smallest biases are highlighted in bold, and fluxes and biases are positive when directed towards the surface. Values for temperatures are given in °C, RH is given in %, FF is given in m s^{-1} and all fluxes are given in W m^{-2}.

		RA1M_mod ('ctrl')			**'lambda'**		
Flux	AWS 14 (observed)	Mean bias	RMSE	Correlation coefficient	Mean bias	RMSE	Correlation coefficient
T_{air}	-2.61	-0.27	3.29	0.63	-0.31	3.27	0.63
T_S	-2.72	0.45	2.27	0.62	0.20	2.47	0.61
RH	2.79	0.24	0.54	0.64	0.23	0.55	0.63
FF	3.77	-0.32	1.97	0.69	-0.32	2.04	0.67
$SW_{\downarrow}$	277.86	-20.95	105.03	0.91	-22.90	106.24	0.91
$SW_{\uparrow}$	232.69	-12.78	87.78	0.91	-14.06	88.17	0.91
SW_{net}	280.10	-0.33	33.01	0.49	0.46	32.82	0.49
$LW_{\downarrow}$	303.88	-1.17	14.12	0.63	-1.35	14.09	0.63
$LW_{\uparrow}$	45.17	-8.16	24.88	0.85	-8.84	25.52	0.85
LW_{net}	-23.79	0.84	25.70	0.47	1.81	25.61	0.47
H_L	-5.11	6.35	11.46	0.48	5.43	10.41	0.51
H_S	-9.34	4.59	8.70	0.71	4.77	8.62	0.72
E_{tot}	-1.43	11.98	31.71	0.78	11.54	32.08	0.77
$E_{tot} + G_S$	-1.43	3.61	21.08	0.90	3.17	21.57	0.89
E_{melt}	13.53	-1.72	16.27	0.82	-2.23	16.34	0.82
$E_{melt} + G_S$	13.53	-2.25	16.48	0.81	-2.74	16.52	0.81

3.61 and from 11.54 to 3.17 W m^{-2}, for the control and lambda runs, respectively. RMSE values improve from 31.71 to 21.08 and from 32.08 to 21.57 W m^{-2}, respectively. Meanwhile, modelled E_{melt} bias increases from -1.72 to -2.25 W m^{-2} and from -2.23 to -2.74 W m^{-2}, respectively. This demonstrates the importance of the ground heat flux during night time, which is not well simulated by the single-layer snow model used in this version of the MetUM (MOSES II: Essery et al., 2001).

C.2 Summary of sensitivity tests

Although limited improvements are shown by the lambda run relative to RA1M_mod during the OFCAP period, amendments to the λ are expected to have a more important effect during winter, when the boundary layer is extremely stable. The demonstrated minor improvements to T_S offer promise, and for these reasons, the lambda set-up is used in Chapter 6 to simulate conditions on Larsen C over 20 years. Moreover, Table C.1 shows that accurately representing G_S has a more notable effect on E_{tot} and to an extent, E_{melt}, than amending λ, but it is beyond the scope of this thesis to examine this further. This would be a promising area to direct future research efforts and to improve the representation of the polar regions in the MetUM.

Appendix: Detailed hindcast validation

D

This appendix includes detailed model validation of the MetUM model hindcast.

Figures D.1 and D.2 show time series of monthly mean surface meteorological variables at inlet and ice shelf stations respectively. Solid lines indicate monthly means, where darker colours show observed values, lighter colours indicate modelled values, and the shaded region shows the complete range of values modelled over the entire time period.

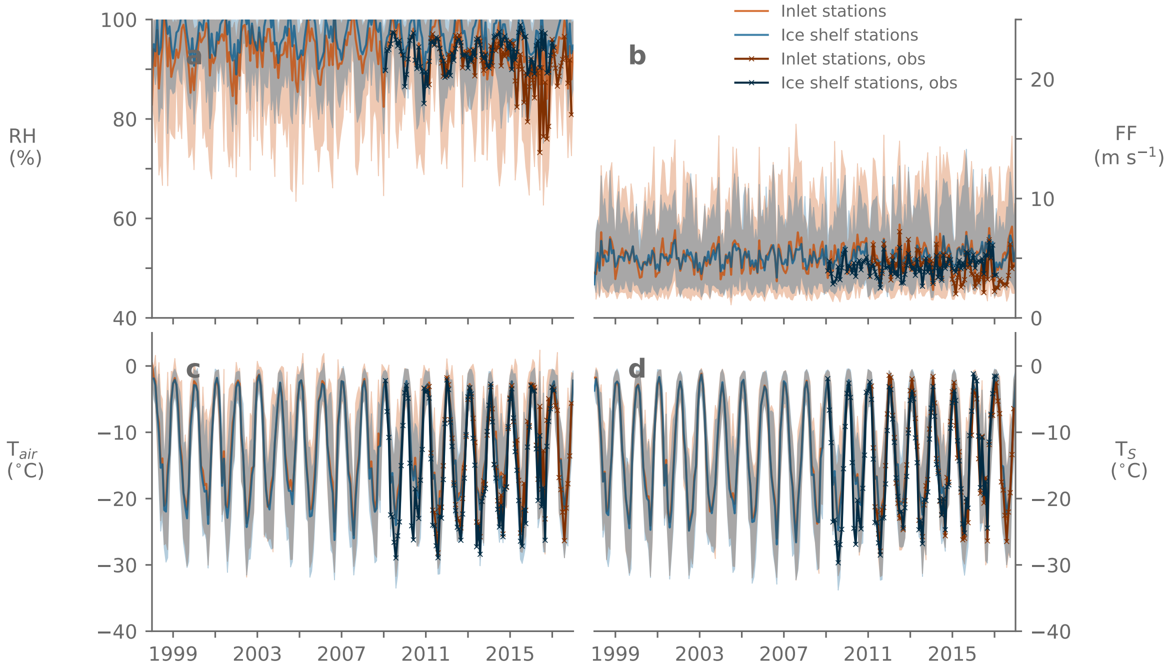

Figure D.1.: Monthly mean MetUM modelled and observed surface meteorological variables (relative humidity, RH, wind speed, FF, 1.5 m air temperature, T_{air}, and surface temperature, T_S) during the hindcast period 1998-2017 at inlet and ice shelf stations. Modelled time series are shown with lighter hues, while observed time series are indicated with darker hues and crosses, and the modelled monthly minima and maxima are shown with the shaded region.

As also shown in Chapter 6, Figure D.1 shows that inlet stations are on average warmer, windier and drier than ice shelf stations in both observations and model output. Table D.1 shows that modelled T_S and T_{air} are both positively biased compared to observations at all stations, in all seasons. Observed and modelled monthly mean relative humidity is above 90% at all stations, but as shown in Figure D.1, the hindcast does not capture the decline in monthly mean relative humidity at inlet stations observed after ~2015. This period is explored in section 6.6.3, Chapter 6. Consistent with Kuipers Munneke et al. (2012), observed mean wind speeds at all stations are typically ~4 m s^{-1} and vary between 5 – 8 m s^{-1}, while modelled wind speeds are ~5 m s^{-1} (Table 6.1, Figure D.1).

Wind roses of modelled wind speed and direction for all stations and all seasons during 1998-2017 (Figure D.3) reveal that strong southerly and southwesterly winds dominate at ice shelf stations, associated with the barrier jet that forms as cold air flows down off the higher-elevation Antarctic plateau. By contrast, winds at inlet stations are more localised, and strongly influenced by surrounding topography. At AWS 18 westerly and north-westerly winds dominate, characteristic of cross-peninsula flow and foehn events, although southerly winds are also common. At AWS 17 winds blow almost exclusively from the south or southwest (south, southwesterly or south-southwesterly winds occur approximately 55% of the time), which is due to airflow being channelled by local orography. Modelled wind speed variability is higher in inlets (Figure D.1), which reflects the more transient forcing of winds and the localised orographic features that produce them. This also leads to a relatively high RMSE and low correlation between observed and modelled winds (Table D.1, Figure 6.1) and higher variability in turbulent fluxes compared to radiative fluxes (Table 6.1, Figure D.2).

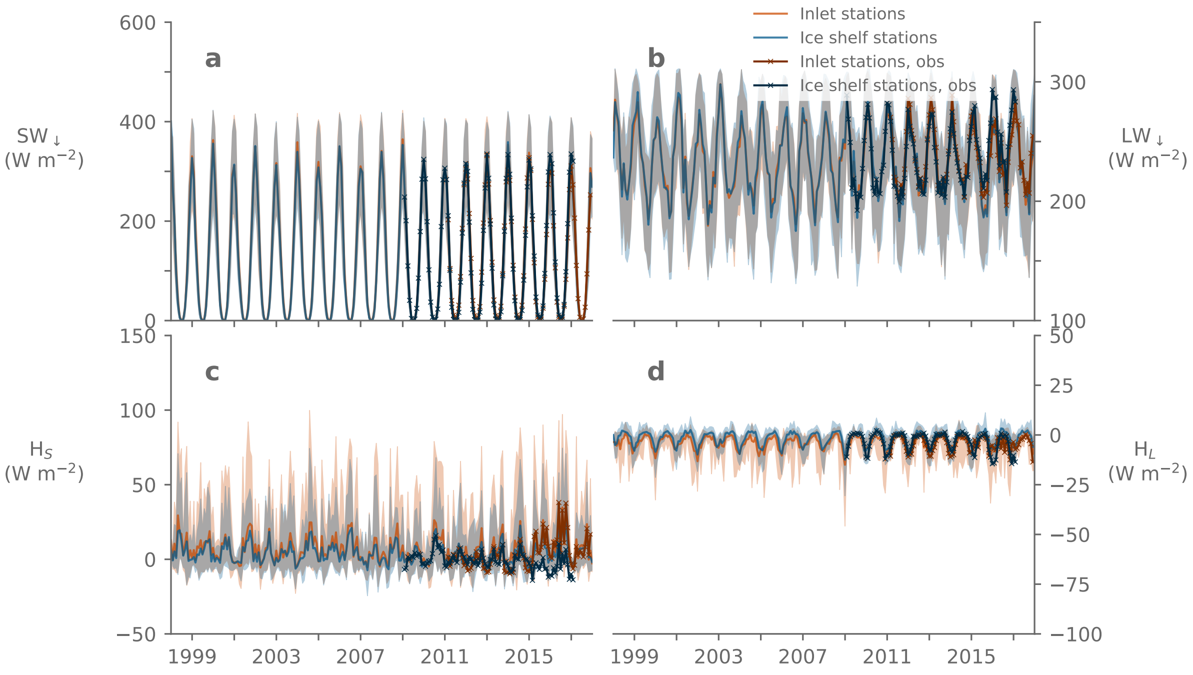

Figure D.2.: As in Figure D.1, but for monthly mean surface energy fluxes (downwelling shortwave, $SW_{\downarrow}$, downwelling longwave, $LW_{\downarrow}$, sensible heat, H_S, and latent heat, H_L) during the MetUM hindcast period.

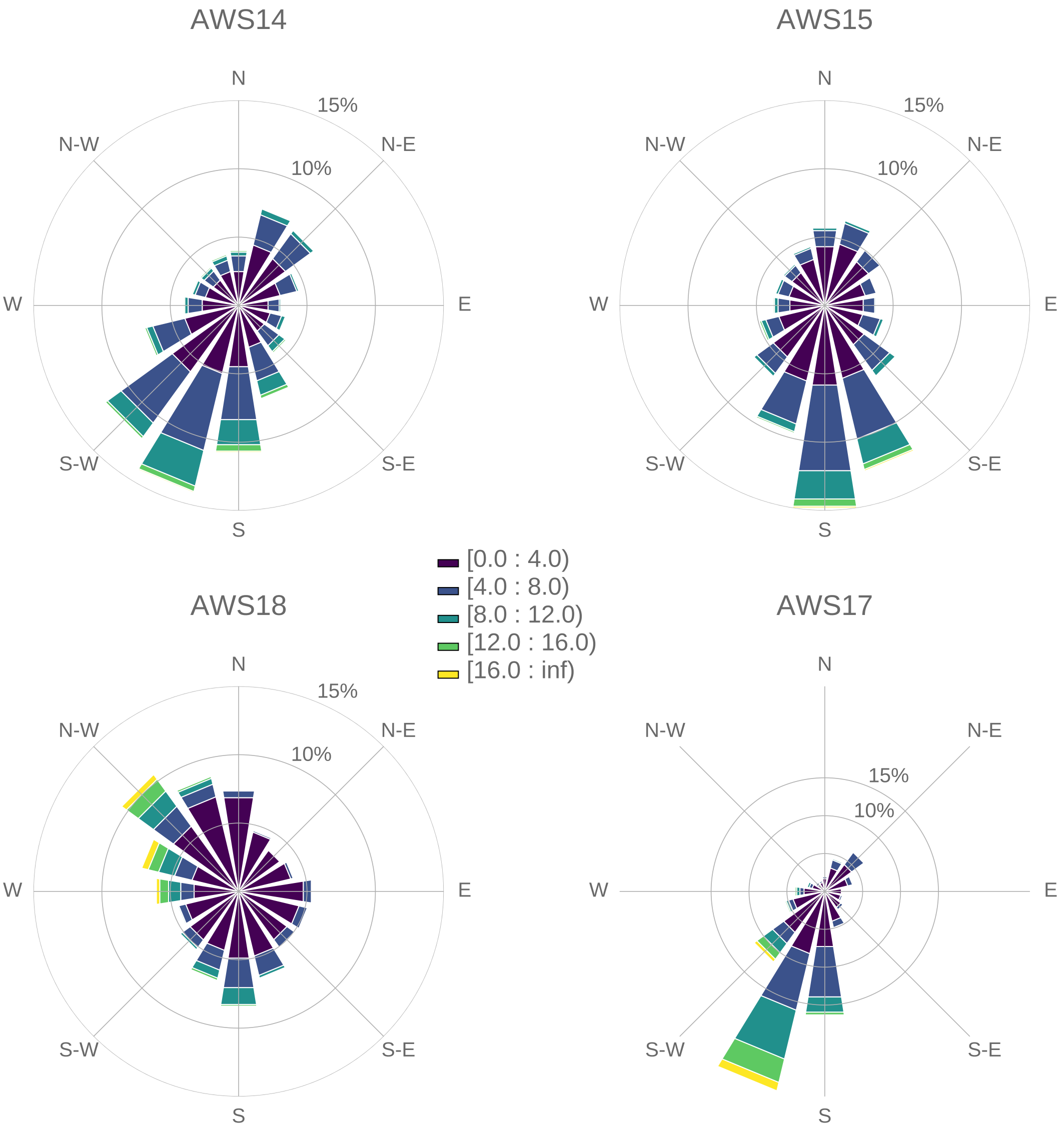

Figure D.3.: Wind roses of MetUM modelled wind speed and direction at each of the four AWSs shown in Figure 3.1 during the hindcast period, 1998-2017.

Figure D.2 shows time series of observed and modelled monthly mean SEB components during the hindcast period. At all stations, modelled monthly mean radiative fluxes are typically hundreds of W m^{-2} in magnitude, whereas H_S and H_L are usually smaller, in the tens of W m^{-2}. Mean SW_{net} and H_S are positive, while mean LW_{net} and H_L are negative. Modelled monthly mean $SW_{\downarrow}$ and $LW_{\downarrow}$ vary little across the relatively small area of Larsen C but monthly mean H_S and H_L are more positive and negative, respectively, at inlet stations compared to ice shelf stations (Figure D.2). Variations are caused by the differences in wind speed, temperature and humidity at inlet vs. ice shelf stations discussed above and in Chapter 6.

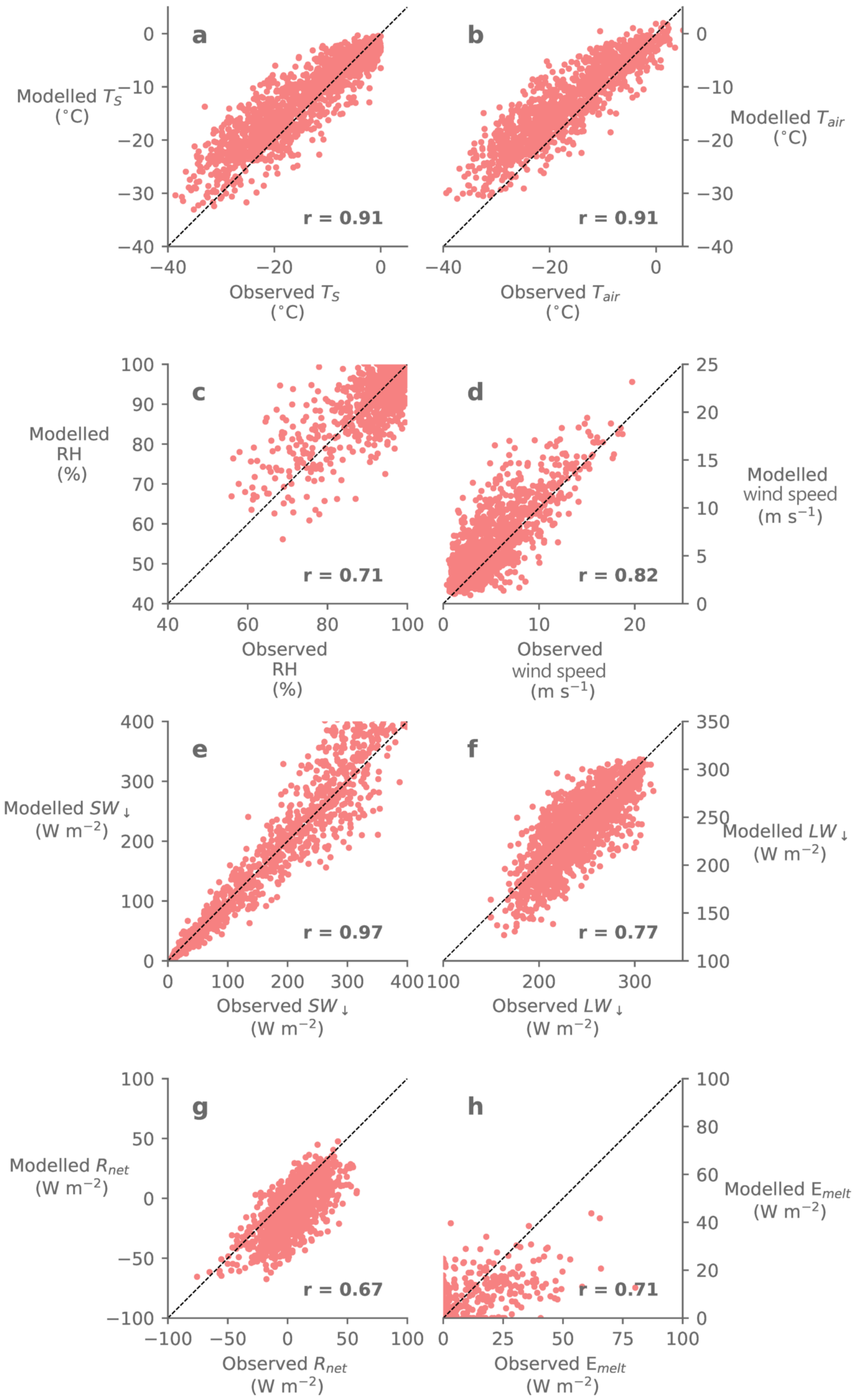

Figure D.4.: Scatterplots of observed vs. modelled surface variables at AWS 17. Correlation coefficients (r values) are given in the bottom right hand corner of each panel: all are statistically significant at the 99% level. The dashed line in each plot indicates perfect agreement between model and observations. Panels a - d show surface meteorological variables: surface temperature, T_S; near-surface air temperature, T_{air}; relative humidity; and wind speed; and panels e - h show surface energy budget terms: downwelling longwave, $LW_\downarrow$; downwelling shortwave, $SW_\downarrow$; net radiative, R_{net} and melt, E_{melt}, fluxes.

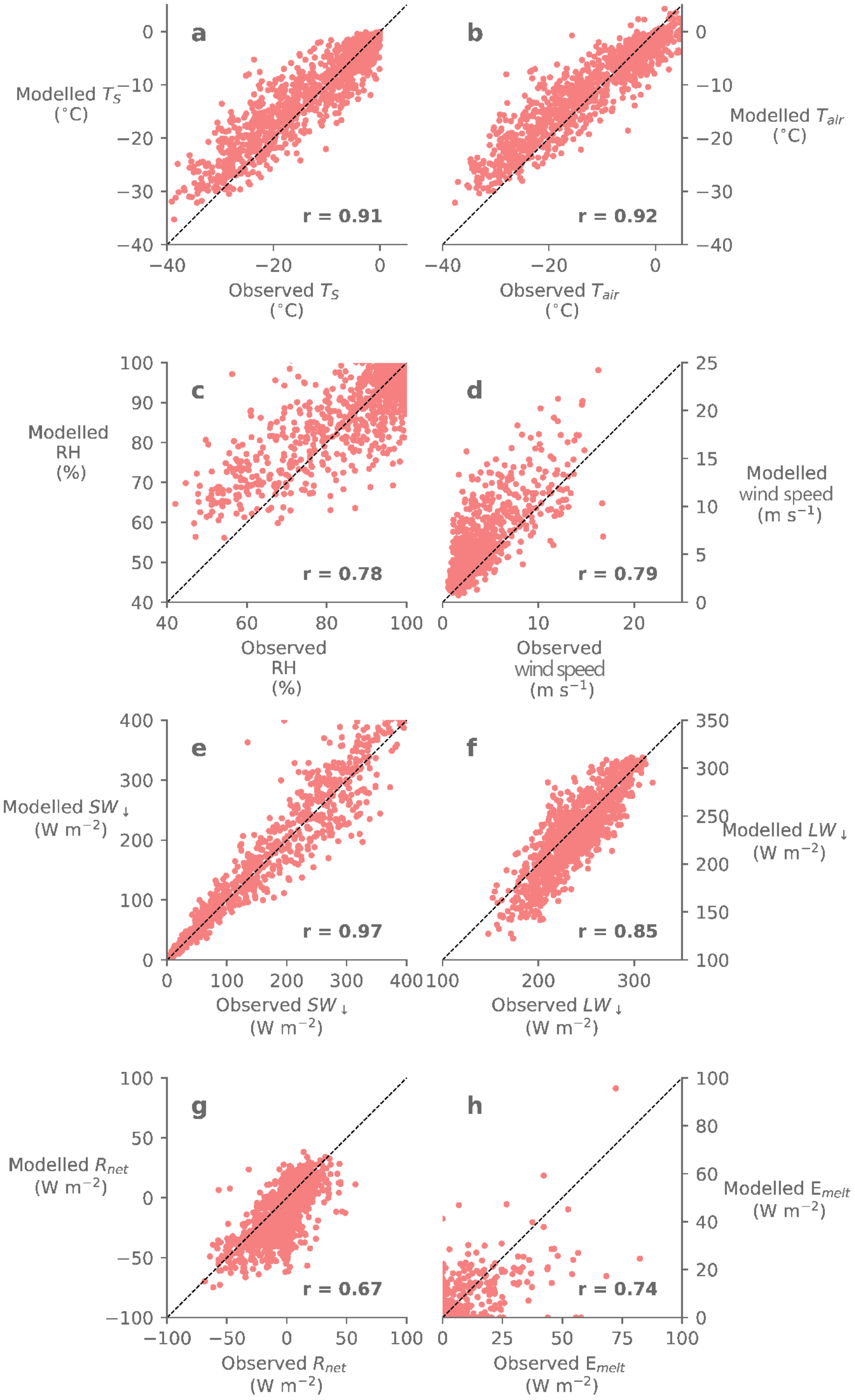

Figure D.5.: As in D.4, but showing observed vs. modelled correlations at AWS 18.

Table D.1 contains mean validation statistics in JJA and DJF for each AWS, while Figures D.4 and D.5 show scatterplots of observed vs. modelled surface variables at AWS 17 and 18, as in Figure 6.1, Chapter 6. As seen in these figures and Table D.1, modelled temperatures are over-estimated at all stations, and this is especially evident in JJA. This is likely due to the combined effect of forcing the global model with ERA-Interim, and of model biases. ERA-Interim has a known surface warm bias in Antarctica, particularly in winter (Fréville et al., 2014; Dutra et al., 2015). The warm bias is especially pronounced during stable conditions, when the turbulent fluxes are over-estimated because surface roughness lengths are too large and surface exchange coefficients used in mixing parameterisations are poorly constrained (Fréville et al., 2014; Dutra et al., 2015). This is a common model problem, and the MetUM also struggles to represent strongly stratified stable boundary layers, as discussed in Chapter 5. This hypothesis is consistent with greater biases at ice shelf stations, where radiative cooling of the surface can produce an extremely stable boundary layer, in contrast to inlet stations, where topographic effects have a greater influence on temperatures.

Wind speeds and the lowest values of relative humidity, which are usually associated with foehn events, are also over-estimated by the model, consistent with the findings of Chapter 4. The over-estimation of wind speeds and low relative humidities in the model hindcast is more pronounced at AWS 17 and 18 (Figures D.4 and D.5). $SW_{\downarrow}$ is well-represented, especially in JJA ($r > 0.92$) because there is very little daylight and the model is able to reproduce the diurnal and seasonal cycle. $SW_{\uparrow}$ is also simulated well, suggesting that the model albedo is accurately captured. Conversely, $LW_{\downarrow}$ is under-estimated throughout the year: annual mean modelled $LW_{\downarrow}$ is 191 and 188 W m s^{-1} at inlet and ice shelf stations, respectively, whereas observed values are 238 and 239 W m s^{-1} (Table 6.1). However, this masks seasonal variations, because as shown in Table D.1, $LW_{\downarrow}$ is over-estimated by 2.6 W m^{-2} in JJA but under-estimated by -0.2 W m^{-2} in DJF.

R_{net} is under-estimated throughout the observational period at all stations because LW_{net} is consistently too small, especially in JJA (Table D.1), and the slight positive SW_{net} bias is not large enough to offset this. This is due to the warm surface temperature bias shown in Table D.1 and Figures 6.1, D.4 and D.5, which causes the surface to radiate too strongly, and $LW_{\uparrow}$ to be over-estimated by 2.9%, producing an energy deficit at the surface that is especially pronounced over the ice shelf during JJA. LW_{net} is under-estimated by around the same amount at all stations (between -13 to -18 W m^{-2} in JJA, and -7 to -10 W m^{-2} in DJF), although $LW_{\downarrow}$ biases account for most of the LW_{net} bias at inlet stations, while on the ice shelf, $LW_{\uparrow}$ errors contribute more. In contrast to the radiative fluxes, turbulent fluxes are simulated more closely during JJA than DJF. Modelled H_L and H_S are both more highly correlated with observations in inlets (Table D.1, Figures D.4 and D.5), particularly at AWS 18, which suggests that the model is able to correctly capture dynamical features related to topography, such as foehn events, which can alter turbulent fluxes considerably.

E_{tot} is simulated relatively poorly at all stations, with low correlation coefficients (0.50-0.51 during JJA and 0.24-0.53 in DJF, Table D.1) and high RMSE (11.94-16.43 during DJF and 19.07-22.24 W m^{-2} in JJA). E_{tot} is simulated worst at AWS 14, and is positively biased at all stations in DJF, (by 1.05 to 9.43 W m^{-2}), but is negatively biased in JJA, (by -7.81 to -10.87 W m^{-2}). The more negative JJA E_{tot} bias is mostly related to the negative LW_{net} bias discussed above. Despite this positive E_{tot} bias, summertime E_{melt} is under-estimated at inlet stations, most considerably at AWS 17 (Table D.1 and Figures D.4 and D.5), a result also found in Chapter 5 during OFCAP.

As noted in Chapter 6, the hindcast under-estimates E_{melt} at AWS 14 through most of the period, but the monthly mean bias shown in Table D.1 is positive (0.30 W m^{-2}). However, the correlation coefficient at AWS 14 is lower (r = 0.61) and standard error is larger (0.1 W m^{-2}) than at inlet stations. The hindcast particularly under-estimates E_{melt} at AWS 14 from 2015 onwards, when observed E_{melt} more than doubled. This increase in observed melting towards the end of the hindcast period is evident in time series of observed and modelled daily mean E_{melt} at all available AWSs (Figures D.6 to D.8). During this period, modelled E_{melt} did not increase, resulting in a negative bias in these years. Because the monthly mean presented in Table D.1 is calculated over nine separate melt seasons, the mean bias is positive, but this does not reflect the relatively large negative bias since 2015. The under-estimate at AWS 14 since 2015 and at inlet stations is consistent with the model under-predicting foehn-driven melting, also suggested by the positive RH bias in Figure D.1. Similarly, Chapter 4 showed a positive and negative bias in E_{melt} during the first and second case studies, respectively, but an overall under-estimate in the amount of meltwater produced, and during the OFCAP period evaluated in Chapter 5, E_{melt} and meltwater production were both under-estimated.

Throughout the time series shown in Figures D.6 - D.8, observed and modelled daily mean E_{melt} is generally lower at AWS 14 than at the two inlet stations, and the largest E_{melt} fluxes are seen at AWS 18. Modelled daily mean E_{melt} is mostly lower than observed, particularly at AWS 14, as also shown in Table D.1. Throughout most of the series shown in Figures D.6 - D.8, E_{melt} typically ranges between 0 and 50 W m^{-2} at AWS 14, 0 and 75 W m^{-2} at AWS 17 and between 0 and 100 W m^{-2} at AWS 18. However, during 2015 and 2016, peak melt fluxes at AWS 14 are almost twice as high (Figure D.6) and large melt fluxes are observed

Table D.1.: Daily mean model validation statistics (bias, correlation coefficient, standard error and root mean square error) for the period 1998-2017 at all stations during summer (DJF) and winter (JJA). Correlation coefficients between observed and modelled time series are emboldened when significant at the 99% level, and given in italics when significant at the 95% level. Insignificant correlations are given in plain text..

DJF	AWS 14				AWS 15				AWS 17				AWS 18			
	bias	r	sterr	RMSE	bias	r	sterr	RMSE	bias	r	sterr	RMSE	bias	r	sterr	RMSE
T_S	1.83	0.63	0.05	3.36	-	-	-	-	1.13	0.80	0.04	4.27	0.28	0.86	0.05	2.65
T_{air}	1.91	0.65	0.05	3.36	1.31	0.71	0.05	2.87	2.16	0.83	0.04	4.51	0.03	0.86	0.05	2.75
$T_{air,min}$	-0.95	0.52	0.06	3.20	-1.49	0.61	0.05	3.23	-0.52	0.85	0.03	3.86	-4.01	0.38	0.10	6.83
$T_{air,max}$	3.50	0.48	0.03	4.74	3.12	0.56	0.03	4.38	4.86	0.83	0.03	6.45	4.35	0.61	0.05	6.08
RH	2.79	0.41	0.08	7.64	5.11	0.67	0.10	6.52	0.48	0.76	0.09	4.71	-0.90	0.81	0.05	8.99
FF	-0.04	0.61	0.10	1.51	0.10	0.70	0.08	1.36	0.63	0.89	0.06	1.92	1.21	0.89	0.07	2.00
P	-0.77	0.99	0.02	1.25	-1.16	0.99	0.02	1.47	-1.95	0.99	0.02	2.78	0.04	0.99	0.01	0.89
u	-1.71	-0.08	0.49	3.23	-1.93	-0.02	0.41	3.02	0.96	0.23	0.42	3.25	0.78	0.15	0.41	3.01
v	0.46	0.14	0.46	3.03	0.54	0.00	0.42	3.01	1.95	-0.19	0.64	5.22	0.04	0.22	0.75	3.76
$SW_{\downarrow}$	-2.12	0.83	0.08	44.93	-4.78	0.85	0.07	43.34	11.10	0.92	0.06	47.51	-5.21	0.92	0.05	38.17
$SW_{\uparrow}$	6.94	0.84	0.07	34.51	15.58	0.86	0.07	36.02	-11.27	0.93	0.06	38.19	8.31	0.92	0.05	31.08
SW_{net}	4.83	0.72	0.10	14.71	11.05	0.77	0.10	16.81	-0.18	0.85	0.06	13.03	3.10	0.88	0.05	11.53
$LW_{\downarrow}$	-0.24	0.61	0.12	22.69	0.60	0.67	0.12	21.71	-5.48	0.18	0.12	30.59	-6.38	0.86	0.09	18.70
$LW_{\uparrow}$	-7.63	0.63	0.05	14.21	-7.89	0.71	0.05	13.55	-4.03	0.80	0.04	17.33	-0.91	0.86	0.06	10.90
LW_{net}	-7.88	0.69	0.14	17.38	-7.30	0.65	0.13	18.14	-9.51	0.67	0.13	19.75	-7.29	0.80	0.09	16.27
H_S	3.72	0.35	0.10	7.11	-	-	-	-	5.17	0.69	0.12	9.47	3.36	0.94	0.04	9.81
H_L	3.17	0.27	0.12	6.65	-	-	-	-	2.14	0.47	0.10	5.61	-1.19	0.81	0.08	6.43
E_{tot}	9.43	0.24	0.13	16.43	-	-	-	-	5.56	0.35	0.09	15.01	1.05	0.53	0.10	11.94
E_{melt}	0.30	0.61	0.10	7.32	-	-	-	-	-4.29	0.78	0.04	9.62	-0.28	0.77	0.06	5.56

JJA	AWS 14				AWS 15				AWS 17				AWS 18			
	bias	r	sterr	RMSE	bias	r	sterr	RMSE	bias	r	sterr	RMSE	bias	r	sterr	RMSE
T_S	6.05	0.83	0.04	8.04	-	-	-	-	1.67	0.86	0.04	4.13	2.43	0.85	0.04	5.08
T_{air}	6.01	0.85	0.04	7.83	5.03	0.87	0.04	7.15	2.79	0.91	0.03	4.52	2.31	0.87	0.04	5.23
$T_{air,min}$	0.61	0.72	0.04	6.67	-0.17	0.74	0.04	6.77	-1.78	0.40	0.05	7.51	-2.84	0.65	0.04	7.72
$T_{air,max}$	11.55	0.78	0.05	12.92	10.38	0.77	0.05	12.05	8.95	0.63	0.06	10.93	9.61	0.67	0.07	12.00
RH	1.45	0.56	0.17	6.34	6.50	0.54	0.15	8.95	4.51	0.72	0.10	8.40	4.43	0.82	0.05	8.90
FF	1.26	0.87	0.04	2.05	1.33	0.82	0.05	2.21	1.12	0.85	0.06	2.33	2.09	0.71	0.10	3.20
P	-1.60	0.99	0.02	2.39	-1.58	0.99	0.01	2.23	-1.17	0.99	0.01	1.93	-0.58	0.99	0.02	1.59
u	0.87	0.03	0.40	3.14	0.21	0.09	0.53	2.47	1.44	0.01	0.36	2.92	1.52	-0.07	0.38	2.97
v	1.31	0.18	0.52	4.25	1.66	-0.15	0.48	4.25	2.78	-0.18	0.55	5.63	1.12	0.07	0.85	4.58
$SW_{\downarrow}$	-1.40	0.95	0.03	4.34	-0.43	0.92	0.04	4.79	-2.54	0.97	0.03	10.32	0.40	0.96	0.03	6.08
$SW_{\uparrow}$	1.72	0.96	0.02	3.94	1.83	0.93	0.03	5.18	3.33	0.97	0.03	8.77	0.10	0.96	0.03	4.84
SW_{net}	0.32	0.75	0.08	1.28	1.40	-0.07	0.09	3.07	0.79	0.91	0.04	3.29	0.50	0.84	0.06	1.86
$LW_{\downarrow}$	2.60	0.74	0.11	27.69	2.60	0.78	0.09	25.07	-7.64	0.76	0.10	23.06	-8.47	0.78	0.09	23.04
$LW_{\uparrow}$	-19.87	0.82	0.05	26.63	-18.20	0.82	0.04	25.62	-5.19	0.87	0.04	14.35	-8.31	0.85	0.05	18.69
LW_{net}	-17.27	0.22	0.19	27.84	-15.66	0.33	0.17	25.71	-12.84	0.54	0.12	21.09	-16.77	0.50	0.10	23.89
H_S	4.25	0.82	0.08	9.74	-	-	-	-	1.01	0.82	0.08	9.14	4.34	0.72	0.09	17.98
H_L	0.29	0.29	0.11	2.32	-	-	-	-	-0.12	0.37	0.35	4.31	-0.65	0.63	0.12	7.52
E_{tot}	-10.87	0.51	0.10	22.24	-	-	-	-	-10.68	0.50	0.10	19.07	-7.81	0.50	0.09	19.80
E_{melt}	0	0	0	0	-	-	-	-	0	0	0	0	-0.48	0.77	0.05	3.69

outside DJF. This is also seen at AWS 18 (Figure D.8), especially in April/May 2015 and April/May 2016. However, these short-term excursions are not enough to impact the seasonal mean, and wintertime melt is only consistently simulated at AWS 18, although as in Chapter 4, wintertime melt at AWS 18 is negatively biased by -0.48 W m^{-2} (Table D.1).

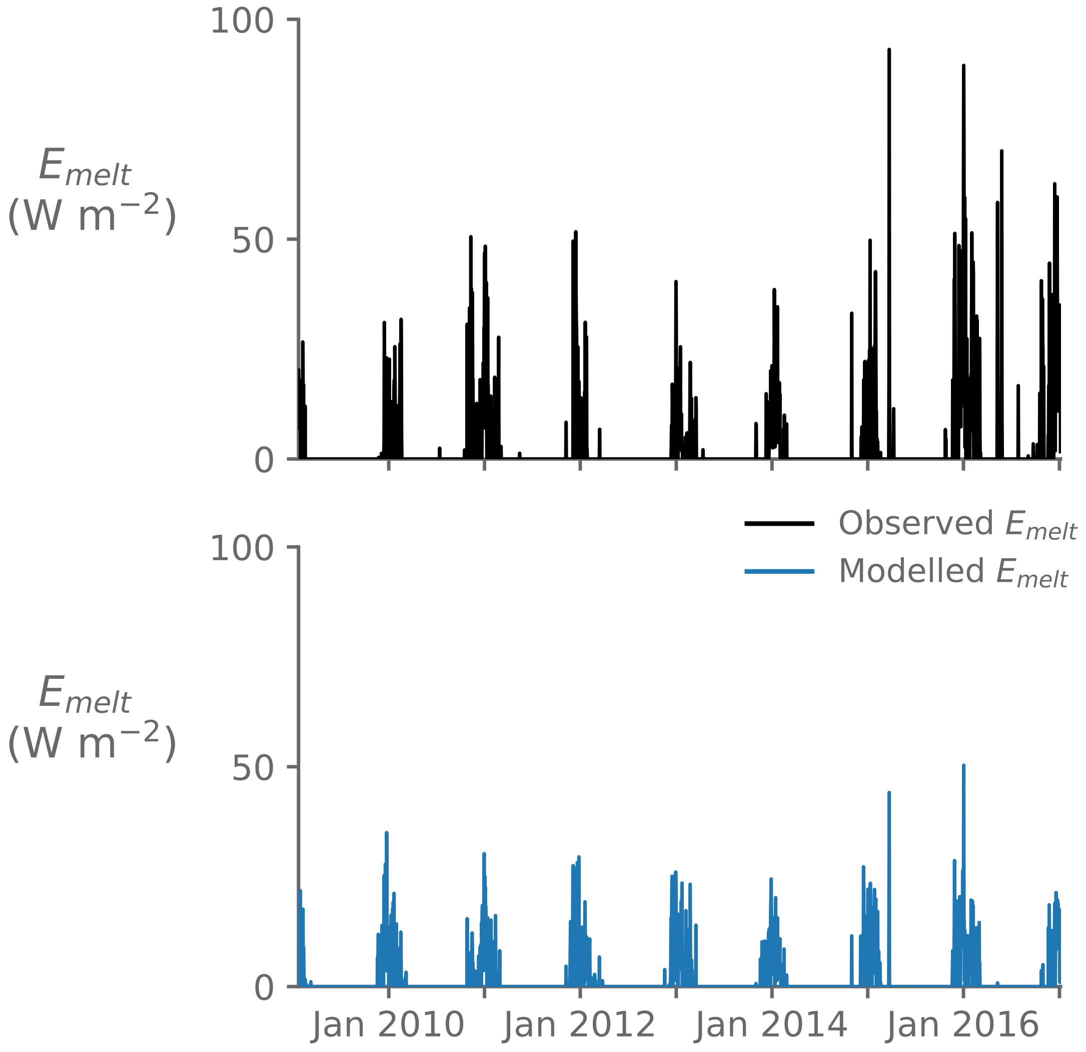

Figure D.6.: Daily mean melt flux, E_{melt}, at AWS 14 for all times where observations are available. Observed fluxes are shown in black, while modelled values at the corresponding location are shown in blue.

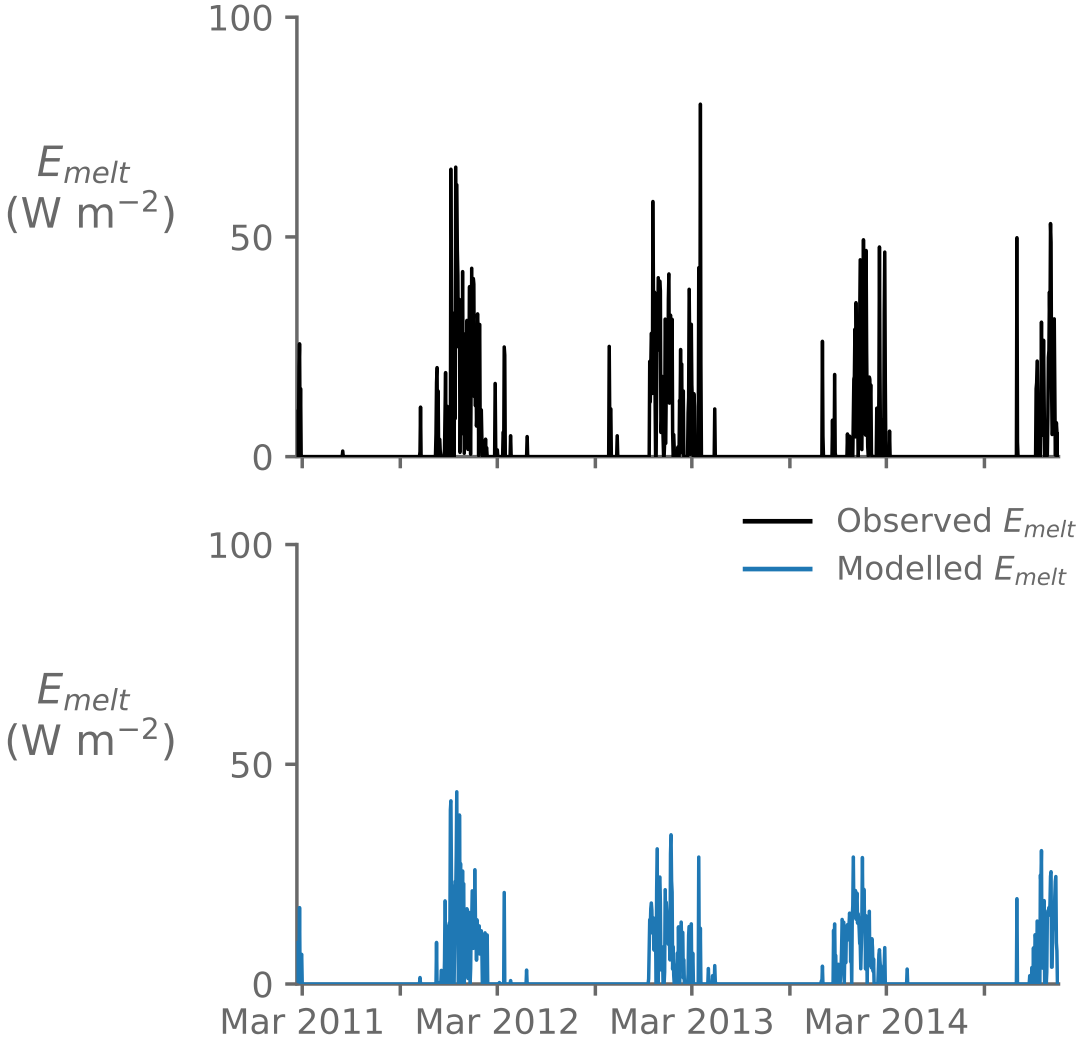

Figure D.7.: As in Figure D.6, but at AWS 17.

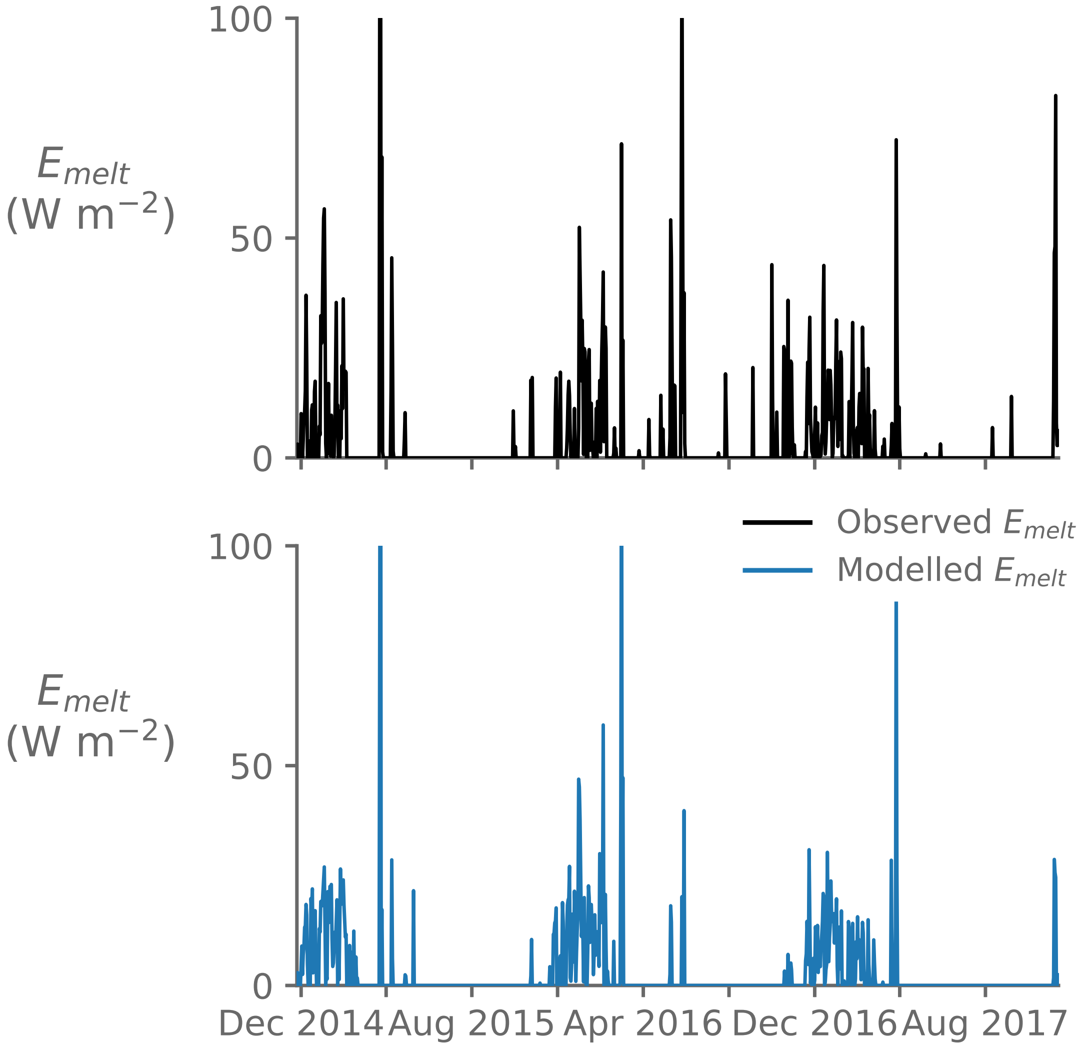

Figure D.8.: As in Figure D.6, but at AWS 18.

.

E

Appendix: Diagnosing foehn events from hindcast model output, data processing and sensitivity testing

E.1 Methods for detecting foehn in model output and observations

To make reliable estimates of the role of foehn on Larsen C, they must first be detected. Foehn must be detected in surface observations using a threshold approach, though they can be diagnosed from model output in several ways, which may affect the way foehn events are counted. These can be summarised as: the 1) surface, 2) Froude number and 3) isentrope methods. Bannister (2015) comprehensively evaluated these three key methods to detect foehn on South Georgia from WRF model output, as well as several variants of each. He concluded that method 3) was capable of capturing the occurrence of foehn most reliably.

Method 1) is most commonly used because it can be applied to surface observations, for example from AWSs. The algorithm is typically as follows:

If over a six-hour period, the following conditions are met, a foehn wind is detected:

- Wind direction (WD) is cross-barrier
- Wind speeds (ws) increase by a threshold amount, typically 3.5 m s^{-1}
- Relative humidity (RH) decreases by a threshold amount, typically 5%
- Temperature (T) increases by a threshold amount, typically 1°C

However, the thresholds used are often adapted to the location of interest, for example Wiesenekker et al. (2018) use only wind direction and wind speed criteria (ws $>$ 4 m s^{-1} and WD 225-0°) to assess foehn at AWS 18, while Turton et al. (2018) use RH-based criteria (RH $<$ 10^{th} percentile OR a decrease by a location-specific amount OR RH $<$ 15^{th} percentile plus T increase $>$ 3 K) all over 12 hours. Datta et al. (2019) use WD, ws, temperature and RH criteria, specifying that WD must be westerly, there must be an increase in ws of 3.5 m s^{-1}, T increase $>$ 1 K and a decline in RH $>$ 5%, and Cape et al. (2015) use (almost) the same criteria, except their ws threshold is 5 m s^{-1}.

Method 2) uses a Froude number approach to diagnose flow-over conditions and thus foehn, as follows:

- Determine the westerly component of the wind, u_{Z1}, at an upstream location (Z_1) at least one Rossby radius of deformation away from the barrier and above the peak height of orography such that the wind is unaffected by the mountains. In this thesis, u_{Z1} was calculated as the mean u wind at 2500 m altitude in the region marked "X" in Figure H.1.
- The upstream Froude number is calculated at location Z_1
- If the Froude number exceeds a critical value, for instance 0.9 in Bannister (2015), then foehn conditions are detected.

Method 3) is shown by Bannister (2015) to most closely simulate foehn occurrence on South Georgia, and is applied by King et al. (2017) to Larsen C. Their algorithm is as follows:

- Determine the westerly component of the wind at an upstream location at the height of the mountain barrier, u_{Z1}, as in method 2). If this westerly component, u_{Z1}, exceeds 2 m s^{-1} (and there is therefore a clear cross-barrier flow):
  - Determine the minimum elevation, Z_2, of the isentrope θ_{Z1} (i.e. the potential temperature at the location of u_{Z1}) on the lee side of the mountains upwind of Larsen C.
  - Determine the maximum change in height of the isentrope θ_{Z1} upwind and downwind of the barrier, i.e. $Z_3 = Z_1 - Z_2$. If $Z_3 > 500$ m over 6 hours, foehn conditions are detected.

The method is summarised in Figure E.1. Bannister (2015) comprehensively evaluated these three methods to detect foehn on South Georgia from WRF model output, as well as several variants of each. He concluded that method (3) was capable of capturing the occurrence of foehn most reliably, capturing 75% of the events observed. King et al. (2017) also use method (3) to diagnose foehn over Larsen C. Work by Bannister (2015) and King et al. (2017) suggests that an isentrope-based approach (method 3) is best for diagnosing foehn in the Antarctic, and should be used if possible (i.e. when four-dimensional information is available). These methods are commonly used to determine foehn frequency in the literature, as shown in Table 6.3, Chapter 6.

E.1.1 Optimum thresholds for foehn detection on Larsen C using the surface method for observations

Without upper air information, foehn frequency must necessarily be diagnosed from observations using method (1). The thresholds are often adapted to the location under consideration, and some can be omitted completely. For instance, the inclusion of a wind speed threshold of 3.5 m s^{-1}, approximately the mean annual 10 m wind speed on Larsen

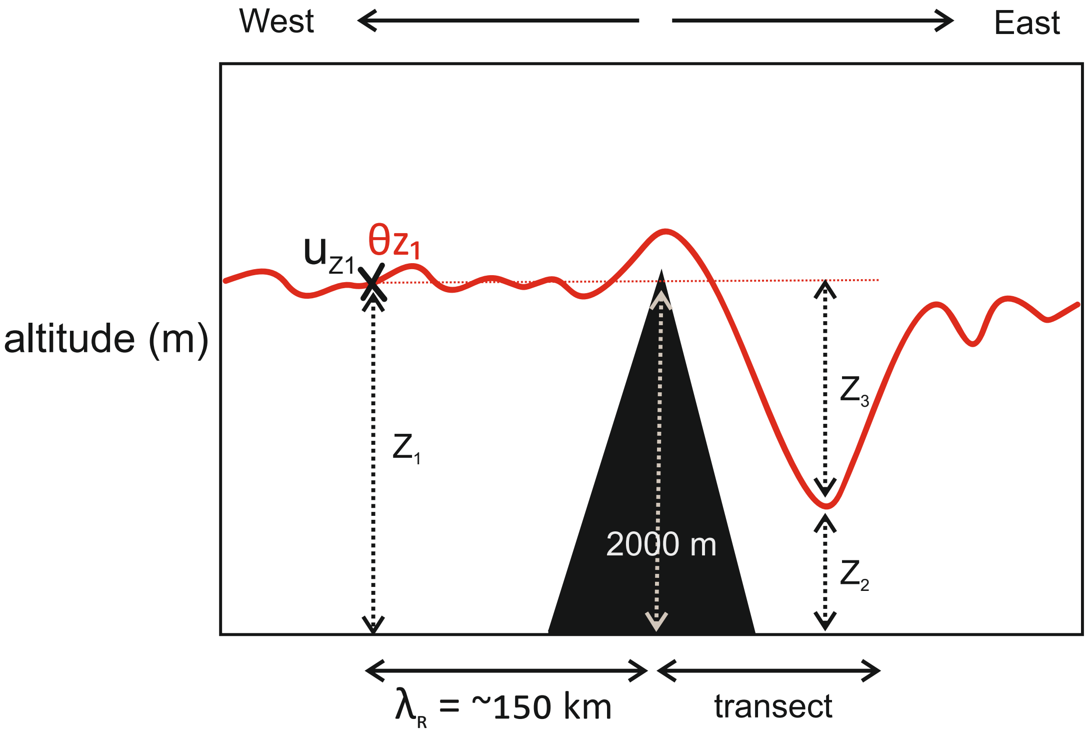

Figure E.1.: Schematic diagram of the isentrope-based method of foehn detection (method 3), after Bannister (2015). u_{Z1} refers to the mean zonal wind at height Z_1, the peak height of orography, at an upstream location one Rossby radius of deformation from the peak of the mountains (λ_R). The isentrope θ_{Z1} is calculated at this point and its minimum height (Z_2) on the lee side over a given transect distance is calculated. If the change in height of the isentrope, i.e. $Z_3 = Z_1 - Z_2$ is $>$ 500 m over 6 hours, foehn is detected.

C, may negatively bias the results to exclude less intense foehn events. Additional sensitivity testing to identify appropriate thresholds for diagnosing foehn winds on Larsen C from observations and model output is summarised below.

Table E.1 shows a comparison between the thresholds of Wiesenekker et al. (2018), Turton et al. (2018) and Datta et al. (2019) applied to observations at AWS 14, which has the longest record. After testing it was determined that the thresholds of Turton et al. were best suited because the thresholds of Wiesenekker et al. are tuned to AWS 18 specifically and yield questionable results elsewhere, and because the thresholds of Datta et al. (2019) produced extremely low estimates. The number of foehn diagnosed with the thresholds of Turton et al. was much more comparable to values reported in the literature.

Method (2) calculates the upstream Froude number at a location at least one Rossby radius of deformation away from the barrier such that the wind is unaffected by the mountains. If

Table E.1.: Percentage of time foehn were diagnosed from observations at AWS 14 using the surface method and thresholds specified in Turton et al. (2018), Wiesenekker et al. (2018) and Datta et al. (2019).

	2009	2010	2011	2012	2013	2014	2015	2016
Turton et al. (2018)	22.2 %	25.2 %	21.7 %	22.2 %	22.3 %	21.2 %	24.0 %	22.8 %
Wiesenekker et al. (2018)	35.2 %	45.7 %	25.3 %	23.3 %	26.6 %	19.0 %	35.9 %	55.0 %
Datta et al. (2019)	0.7 %	1.3 %	0.7 %	0.4 %	1.4 %	0.8 %	0.9 %	2.5 %

the Froude number exceeds a threshold value, e.g. 0.9 (Bannister, 2015) for 6 continuous hours, then foehn is detected.

Method (3) measures the change in height of an upstream isentrope on the lee side of the mountain barrier. A schematic of the method is given in Chapter 2 (Figure 2). A typical algorithm from King et al. (2017) is as follows:

- Determine the westerly component of the wind at an upstream location at the height of the mountain barrier, Z_1, as in method (2). If this westerly component, uZ_1, exceeds 2 m s^{-1} (and there is therefore a clear cross-barrier flow):
  - Find the potential temperature at Z_1, θZ_1, and trace this isentrope across the mountain barrier
  - Determine the minimum elevation, Z_2, of θZ_1 on the lee side of the mountains over Larsen C
  - Determine the maximum change in height of the isentrope θZ_1 upwind and downwind of the barrier, i.e. $Z_3 = Z_1 - Z_2$. If $Z_3 > 500$ m over 6 hours, foehn conditions are detected.

The results of the four foehn diagnosis methods for the period 1998-2017 are summarised in Table E.2. When applied to observations, the surface method diagnoses a similar number of foehn events at ice shelf stations and in inlets, in contrast to theoretical expectation, which suggests that the number of foehn events decreases with distance from the mountains. However, the statistics for inlet stations are biased by lower foehn frequencies at AWS 17 (6.8% of the year), where foehn is recorded half as much of the time as at AWS 18 (14.2% of the year). The surface method may be less well-suited to AWS 17 because it is further north where temperatures are warmer and the conditions stipulated in the foehn diagnosis algorithm are reached more readily during non-foehn conditions. Foehn occurs at both AWS 14 and 15 during 7.6% of the year, approximately half the frequency observed at AWS 18. Considering only results from AWS 14, 15 and 18, the expected spatial gradient is observed. However, it is difficult to draw robust conclusions from these results because there are very few

Table E.2.: Summary statistics for the foehn diagnosis methods tested, at inlet (AWS 17 and 18) and ice shelf (AWS 14 and 15) stations. Means, medians and standard deviations ("SD") are presented as percentages of time that foehn conditions are diagnosed per year. The results of a dependent variable student's t-test to test the difference between inlet and ice shelf stations using each method are shown in the final column ("Sig dif?").

	Inlet stations			Ice shelf stations			Sig dif?
Method	Mean	Median	SD	Mean	Median	SD	
Observed	4.8 %	3.5 %	1.8 %	6.1 %	7.3 %	1.8 %	x
Surface	5.8 %	5.7 %	0.6 %	5.9 %	5.8 %	0.7 %	x
Froude	6.3 %	6.0 %	1.6 %	6.8 %	6.7 %	1.7 %	99 %
Isentrope	46.3 %	45.9 %	5.3 %	35.5 %	35.7 %	4.7 %	99 %
Goldilocks	16.1 %	16.1 %	1.7 %	12.7 %	12.6 %	1.6 %	99 %

years of observational data available, particularly at AWS 17 and 18, and there is considerable variability, as indicated by the relatively high standard deviations (1.8%).

Applying the surface method to model output produces foehn frequencies that are very similar, although the standard deviations are lower (0.6% and 0.7% at inlet and ice shelf stations, respectively). However, there is no statistically significant difference between inlet and ice shelf stations using the surface method on model output. This may indicate that other meteorological factors are being counted as foehn, such as temperature advection events, and that the surface method is not the best way of diagnosing foehn events on Larsen C.

Conversely, applying the Froude, isentrope and Goldilocks methods to model output, the difference between inlet and ice shelf stations is significant at the 99% level. The Froude number method diagnoses a similar number of foehn as the surface method during the simulation, which is around half the number expected from the literature. This may indicate that the threshold chosen (0.9) was not suitable to capture the full range of foehn dynamics in the study region or that the algorithm is too simplistic. The isentrope method diagnoses too many foehn events, but does produce the expected difference between inlet and ice shelf stations. However, high standard deviations are recorded because diagnosed foehn frequencies vary considerably year-to-year. The Goldilocks method is demonstrably best: it produces results that are comparable to the literature; a clear, statistically significant difference between inlet and ice shelf stations; relatively low standard deviation; and makes use of four-dimensional variables to incorporate foehn dynamics into the diagnosis algorithm. This supports the conclusions of Bannister (2015) and King et al. (2017) that isentrope-based approaches are most rigorous.

F

Appendix: Modelled seasonal mean foehn occurrence during the hindcast period

This appendix shows the seasonal frequency of foehn events identified from the model hindcast presented in Chapter 6. Table F.1 shows mean foehn frequencies in each season of every year included in the hindcast for all four AWSs used. It also shows the seasonal mean, median and standard deviation of foehn frequency for the entire period.

Table F.1.: Percentage of time foehn conditions are diagnosed from model output at each AWS during each season and each year using the combined method detailed in Chapter 6. Foehn conditions are given as percentages of time. The mean, median and standard deviation of each time series is also given (also in percent) at far right.

	1998	1999	2000	2001	2002	2003	2004	2005	2006	2007	2008	2009	2010	2011	2012	2013	2014	2015	2016	2017	Mean	Median	SD
										AWS 14													
DJF	13.8	14.6	15.8	8.9	13.3	6.0	14.7	14.3	12.2	17.2	18.8	11.0	7.9	13.3	15.7	14.6	14.6	17.1	11.7	7.8	13.2	14.0	3.3
MAM	21.8	16.3	13.2	10.6	13.2	15.7	13.6	11.3	15.1	10.4	11.7	11.3	11.1	8.2	12.1	13.2	11.4	17.8	22.8	18.1	13.9	13.2	3.7
JJA	10.7	16.4	14.9	18.9	18.6	11.3	17.4	18.1	16.4	11.7	18.6	12.6	17.5	14.7	9.6	12.1	13.6	16.3	20.4	12.9	15.1	15.6	3.1
SON	15.4	23.2	16.9	17.6	13.8	17.4	16.7	17.9	16.8	14.3	15.4	13.5	15.4	14.7	13.8	18.1	11.0	20.0	17.5	17.2	16.3	16.7	2.6
ANN	15.5	16.4	14.9	13.6	14.3	12.3	15.5	15.3	15.2	13.3	15.7	12.0	12.6	11.7	12.2	14.7	13.3	17.7	17.7	14.0	14.4	14.5	1.7
										AWS 15													
DJF	11.0	10.3	12.2	7.8	10.3	5.1	8.2	10.4	10.1	11.0	16.3	7.5	3.5	8.1	10.8	11.3	10.8	10.7	6.7	4.0	9.3	10.3	2.9
MAM	17.8	12.2	8.9	9.9	7.8	12.1	9.4	9.3	9.3	6.5	8.1	8.5	7.4	5.7	10.4	9.4	9.0	13.1	18.3	12.6	10.3	9.4	3.2
JJA	7.9	11.9	12.2	13.8	15.3	9.3	14.4	12.5	13.5	7.6	13.1	7.6	15.1	11.0	8.2	10.6	13.2	11.8	14.9	10.3	11.7	12.1	2.5
SON	12.4	18.8	12.9	13.1	10.7	12.2	12.5	14.6	13.6	12.1	12.4	8.9	16.7	10.7	11.0	11.8	7.9	15.1	14.4	13.1	12.7	12.4	2.4
ANN	12.5	13.5	11.9	11.0	10.6	9.3	10.8	12.4	11.1	9.2	13.0	8.2	11.0	8.1	9.9	10.9	10.5	13.0	13.4	10.1	11.0	11.0	1.6
										AWS 17													
DJF	18.8	20.3	17.4	10.3	17.8	9.6	18.6	19.6	16.1	20.0	22.9	15.1	8.8	15.7	19.2	18.1	17.2	20.3	16.3	9.2	16.5	17.6	4.0
MAM	20.7	22.6	18.8	13.6	12.4	16.7	15.8	10.0	16.0	10.1	16.0	13.2	13.3	11.0	14.0	16.8	13.8	18.3	21.5	20.1	15.7	15.9	3.6
JJA	12.1	18.2	16.5	18.8	17.5	14.0	15.8	17.1	16.4	10.4	18.2	11.7	19.7	14.6	12.4	14.6	15.8	18.6	20.7	12.4	15.8	16.1	2.8
SON	18.6	24.9	17.4	23.5	15.6	21.5	21.8	19.7	21.8	17.9	19.4	15.3	20.0	16.5	17.8	22.1	15.8	20.6	21.3	19.0	19.5	19.6	2.6
ANN	17.2	20.3	17.2	16.4	15.8	15.2	18.3	17.0	17.0	14.4	18.8	13.8	15.2	13.8	14.3	16.9	16.0	18.3	19.3	16.1	16.6	16.6	1.8
										AWS 18													
DJF	15.4	15.1	16.0	11.0	14.9	7.1	15.1	15.8	14.7	17.5	19.2	10.0	7.8	15.0	15.1	17.6	15.0	19.7	14.4	7.4	14.2	15.1	3.6
MAM	23.8	17.6	15.6	13.1	13.9	16.5	15.1	11.5	14.7	11.1	12.5	12.9	13.8	10.8	11.8	15.6	10.8	18.3	24.2	18.3	15.1	14.3	3.8
JJA	12.4	17.6	16.4	20.3	19.9	14.9	19.4	18.9	17.5	13.1	20.1	12.5	18.2	17.4	10.3	12.8	18.1	17.9	19.3	12.6	16.5	17.6	3.1
SON	18.3	23.1	17.2	19.2	15.0	16.1	18.6	19.7	18.8	14.7	19.7	13.8	16.4	15.7	17.2	17.6	13.6	17.9	20.0	16.8	17.5	17.4	2.3
ANN	17.6	17.8	15.5	15.2	15.0	14.0	16.4	16.6	16.0	14.1	17.1	12.1	14.3	14.7	13.5	15.7	14.6	18.5	19.4	13.6	15.6	15.4	1.8

G

Appendix: Seasonal mean derived "foehn index" during the hindcast period

Figure G.1 shows the annual and seasonal mean derived foehn index, FI (calculated as in 6.1 - see main text of Chapter 6 for details), during the hindcast period 1998-2017 (Figure G.1). FI is calculated when there is a dominant westerly wind component, i.e. $\mathrm{u}_{Z1} \geq 2.0$ m s^{-1}. Blue colours in Figure G.1 indicate regions where temperature and relative humidity are falling and rising, respectively, during such conditions, while red colours indicate warming and drying, i.e. foehn conditions.

Figure G.1 shows that foehn conditions are strongest and most prevalent in the immediate lee of steep topography, in all seasons. FI is larger in the northwestern inlets than the southern inlets because temperatures are more frequently able to reach melting point in the north of the ice shelf. The largest values of FI are visible in DJF, but these are mostly confined to inlets, suggesting that summertime foehn may be more intense and confined than in other seasons. By contrast, Figure G.1d indicates that foehn events are most extensive during SON, with higher values of FI across the ice shelf, and a less stark contrast between inlet and ice shelf locations.

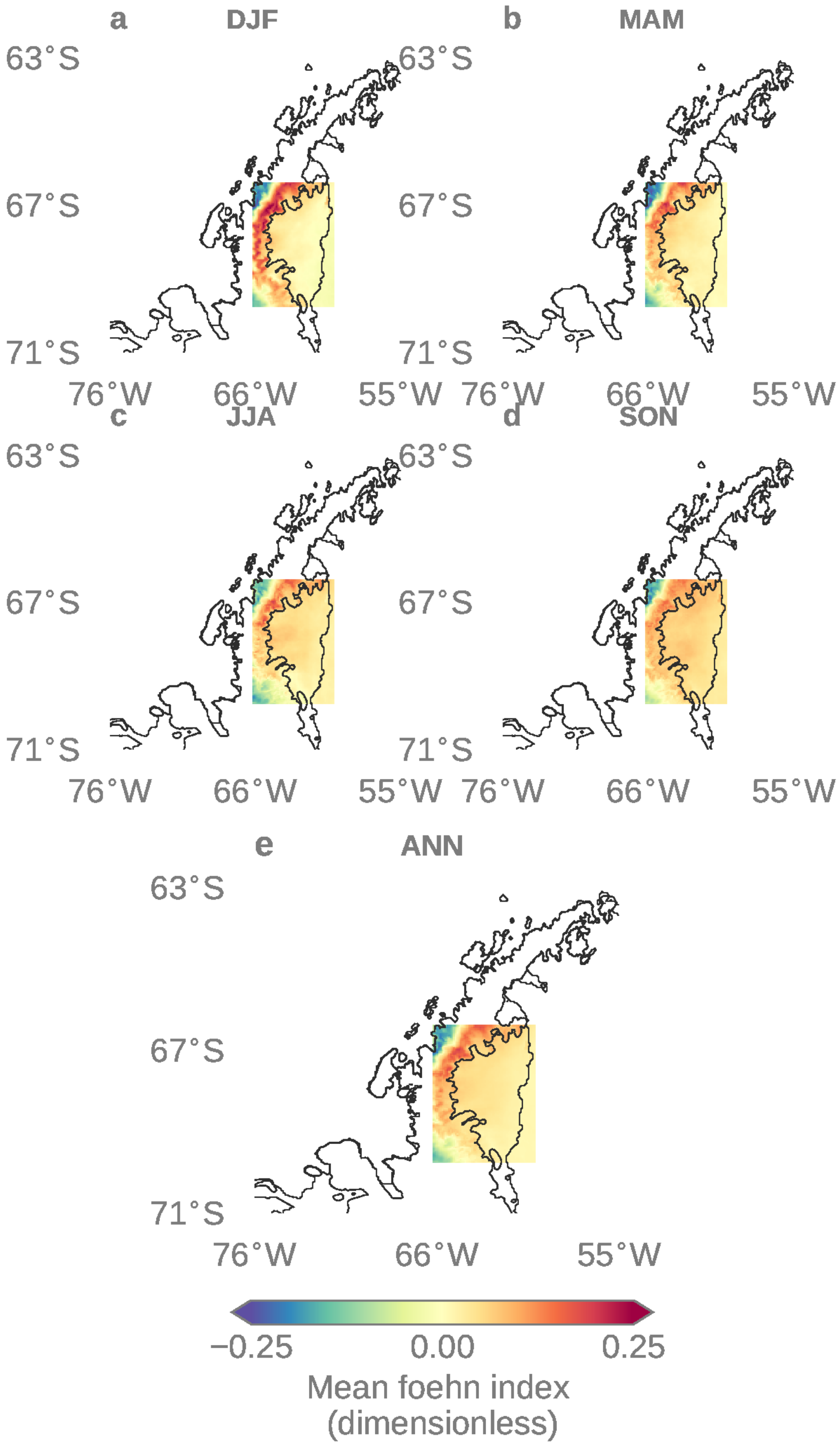
a
DJF
b
MAM
c
JJA
d
SON
e
ANN
63°S
67°S
71°S
76°W
66°W
55°W
−0.25
0.00
0.25
Mean foehn index
(dimensionless)

Figure G.1.: Mean modelled foehn index during 1998-2017 for each season: a) DJF, b) MAM, c) JJA, d) SON and e) annually (ANN).

Appendix: Hindcast regime criteria and regions used for compositing

H

This appendix summarises the methods used to identify the various regimes discussed in Chapter 6 from hindcast data.

To determine regimes used for composites in Chapter 6, various indicator variables, thresholds and regions are established. These are summarised in Table H.1. The regions used for averaging are shown in Figure H.1. Data sources and treatments are described below. For example, the barrier wind regime is diagnosed when meridional wind speeds in the box given in Table H.1 and Figure H.1 exceed 5.0 m s^{-1}.

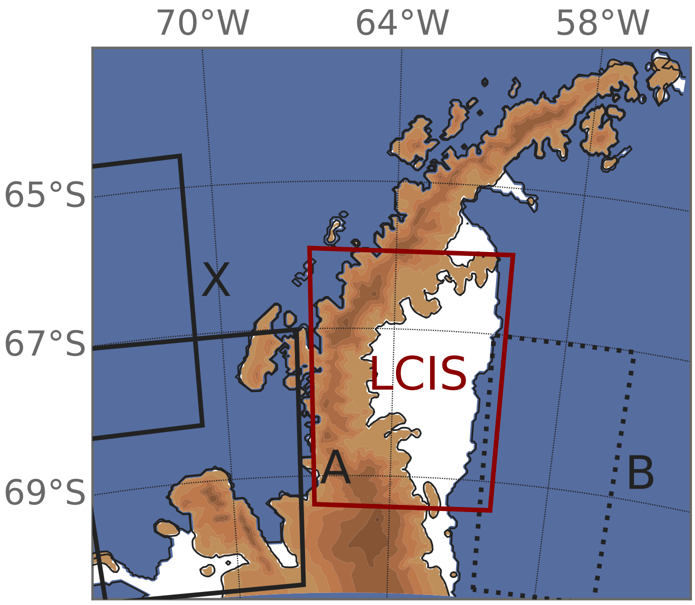

Figure H.1.: Map showing the four regions used in the diagnosis of large-scale regimes. Abbreviations used in the plot are as follows. "X": location at which u_{Z1} is calculated, used in "blocked" and "flow-over" regimes, as well as for foehn diagnosis, "A": Deep Amundsen Sea Low regime, "B": barrier wind regime, "LCIS": Larsen C box used to calculate means for "melt25", "melt75", "cloudy", "clear", "LWP25" and "LWP75" regimes (high/low).

H.1 Data sources and treatment

The daily mean SAM index is that of NOAA's NWS Climate Prediction Centre, and is calculated from NCEP/NCAR reanalysis at 2.5°× 2.5° resolution. The SAM is diagnosed as the leading EOF of geopotential height at 700 hPa, and the daily time series is obtained by projecting daily anomalies onto this leading EOF (Center, 2005). The Nino3.4 dataset (Reynolds et al., 2007), which is used by the World Meteorological Organisation (WMO) and NOAA to diagnose El Niño and La Niña events, is used to diagnose the phase of ENSO at daily frequency. This index uses SSTs from the OI.v2 SST dataset (which incorporates AVHRR, NOAA and US Navy satellite data and NCEP sea ice data) within the region 5°S - 5°N and 170-120°W. Warmer-than-average Pacific SSTs are associated with El Niño conditions (the negative phase of the southern oscillation index, SOI, another measure of ENSO conditions) while cooler-than-average SSTs are associated with La Niñas (positive SOI). El Niño and La Niña periods are therefore abbreviated to "ENSO-" and "ENSO+", respectively.

The effect of positive and negative phases of these circulation modes is assessed by compositing maps of the variables of interest during periods where certain criteria are met. For the SAM, the threshold for positive and negative periods, respectively, is taken to be plus/minus one standard deviation of the time series 1998-2017. The phase of ENSO is defined according to the WMO by taking the three-month running mean of SST anomalies in the Nino3.4 region. Positive (negative) ENSO periods are diagnosed when three-month running mean anomalies exceed (fall below) +0.5°C (-0.5°C).

The influence of the Amundsen Sea Low (ASL) is examined by taking the mean of MSLP in a region in the southwest of the model domain (shown in Figure H.1) and diagnosing periods when the ASL is especially influential on the Antarctic Peninsula when MSLP anomalies in this box are -5 hPa or lower. This technique is used instead of observed indices because pressure anomalies within the model domain are more influential than the depth and longitude of the ASL in governing the ASL's influence on the climate of the peninsula. Two Froude-number based regimes are also examined: "blocked" and "flow-over" regimes, diagnosed using the threshold of $Fr = 0.5$ given in Orr et al. (2008) and van Lipzig et al. (2008) when upstream flow has a significant westerly component: $u_{Z1} > 2.0$ m s^{-1} as in King et al. (2017).

Table H.1.: Indicator variables, thresholds and regions used in diagnosing each of the regimes used for compositing in Chapter 6. Regimes are defined as in Chapter 6, where the acronyms "SAM", "ENSO", "ASL" and "LWP" refer to the Southern Annular Mode, El Niño Southern Oscillation, Amundsen Sea Low and liquid water path, respectively. The regions used are indicated in Figure H.1.

Regime	Indicator variable	Threshold	Region
Melt25 (low melt)	meltwater production amount	$< 25^{th}$ percentile	69.38°S to 65.91°S, 60.12°W to 66.89°W, Region "LCIS"
Melt75 (high melt)	meltwater production amount	$> 75^{th}$ percentile	69.38°S to 65.91°S, 60.12°W to 66.89°W, Region "LCIS"
Cloudy	Cloud fraction	> 0.75	69.38°S to 65.91°S, 60.12°W to 66.89°W, Region "LCIS"
Clear	Cloud fraction	< 0.31	69.38°S to 65.91°S, 60.12°W to 66.89°W, Region "LCIS"
LWP25 (low LWP)	LWP	$< 25^{th}$ percentile	69.38°S to 65.91°S, 60.12°W to 66.89°W, Region "LCIS"
LWP75 (high LWP)	LWP	$> 75^{th}$ percentile	69.38°S to 65.91°S, 60.12°W to 66.89°W, Region "LCIS"
Barrier wind regime	10 m V wind	5.0 m s^{-1}	70.47°S to 67.01°S, 60.52°W to 55.61°W, Region "B"
Blocked regime	mean U wind between 100-2000 m, Fr	$u_{Z1} \geq 2.0$ m s^{-1} and Fr < 0.5	68.24°S to 64.57°S, 75.46°W to 70.94°W, Region "X"
Flow-over regime	mean U wind between 100-2000 m, Fr	$u_{Z1} \geq 2.0$ m s^{-1} and Fr > 0.5	68.24°S to 64.57°S, 75.46°W to 70.94°W, Region "X"
Deep ASL	MSLP anomaly	-5.0 hPa	70.47°S to 67.01°S 75.46°W to 67.40°W, Region "A"
SAM+	SAM index	+1 σ (1.36)	-
SAM-	SAM index	-1 σ (-1.36)	-
ENSO+ (La Niña conditions)	Nino3.4 index	+0.5°C	-
ENSO- (El Niño conditions)	Nino3.4 index	-0.5°C	-

Bibliography

Abdul-Razzak, H. and S. J. Ghan (2000). “A parameterization of aerosol activation: 2. Multiple aerosol types”. In: *Journal of Geophysical Research* 105.D5, pages 6837–6844.

Abel, S. J. and I. A. Boutle (2012). “An improved representation of the raindrop size distribution for single-moment microphysics schemes”. In: *Quarterly Journal of the Royal Meteorological Society* 138.669, pages 2151–2162.

Abel, S. J., I. A. Boutle, K. Waite, S. Fox, P. R. A. Brown, R. Cotton, G. Lloyd, T. W. Choularton, and K. N. Bower (2017). “The Role of Precipitation in Controlling the Transition from Stratocumulus to Cumulus Clouds in a Northern Hemisphere Cold-Air Outbreak”. In: *Journal of the Atmospheric Sciences* 74.7, pages 2293–2314.

Abel, S. J. and B. J. Shipway (2007). “A comparison of cloud-resolving model simulations of trade wind cumulus with aircraft observations taken during RICO”. In: *Quarterly Journal of the Royal Meteorological Society* 133.55, pages 781–794.

Adusumilli, S., H. A. Fricker, M. R. Siegfried, L. Padman, F. S. Paolo, and S. R.M. Ligtenberg (2018). “Variable Basal Melt Rates of Antarctic Peninsula Ice Shelves, 1994–2016”. In: *Geophysical Research Letters* 45.9, pages 4086–4095.

Agosta, C., C. Amory, C. Kittel, A. Orsi, V. Favier, H. Gallée, M. R. van den Broeke, J. T. M. Lenaerts, J. M. van Wessem, and X. Fettweis (2018). “Estimation of the Antarctic surface mass balance using MAR (1979-2015) and identification of dominant processes”. In: *The Cryosphere Discussions* D, pages 1–22.

Andreas, E. L. (1987). “A theory for the scalar roughness and the scalar transfer coefficients over snow and sea ice”. In: *Boundary Layer Meteorology* 38, pages 159–184.

Ashmore, D. W, B. Hubbard, A. Luckman, B. Kulessa, H. Sevestre, and P. R. Holland (2017). “Ice and firn heterogeneity within Larsen C ice shelf from borehole optical viewing”. In: *Journal of Geophysical Research: Earth Surface* 122, pages 1139–1153.

Bannister, D. (2015). “Föhn winds on South Georgia and their impact on regional climate”. PhD thesis. University of East Anglia, page 365.

Baran, A. J., P. Hill, K. Furtado, P. Field, and J. Manners (2014). “A Coupled Cloud Physics – Radiation Parameterization of the Bulk Optical Properties of Cirrus and Its Impact on the Met Office Unified Model Global”. In: *Journal of Climate* 27.20, pages 7725–7752.

Barrand, N. E., D. G. Vaughan, N. Steiner, M. Tedesco, P. Kuipers Munneke, M. R. Van Den Broeke, and J. S. Hosking (2013). “Trends in Antarctic Peninsula surface melting conditions from observations and regional climate modeling”. In: *Journal of Geophysical Research: Earth Surface* 118.1, pages 315–330.

Barrett, A. I., R. J. Hogan, and R. M. Forbes (2017a). “Why are mixed-phase altocumulus clouds poorly predicted by large-scale models? Part 1. Physical processes”. In: *Journal of Geophysical Research: Atmospheres* 122.18, pages 9903–9926.

Barrett, A. I., R. J. Hogan, and R. M. Forbes (2017b). “Why are mixed-phase altocumulus clouds poorly predicted by large-scale models? Part 2: Vertical resolution sensitivity and parameterization”. In: *Journal of Geophysical Research: Atmospheres* 122.18, pages 9903–9926.

Bastola, S. and V. Misra (2014). “Evaluation of dynamically downscaled reanalysis precipitation data for hydrological application”. In: *Hydrological Processes* 28.4, pages 1989–2002.

Baumgardner, D., H. Jonsson, W. Dawson, D. O’Connor, and R. Newton (2001). “The cloud, aerosol and precipitation spectrometer: A new instrument for cloud investigations”. In: *Atmospheric Research* 59-60, pages 251–264.

Beljaars, A., A. Betts, E. Dutra, A. Ghelli, M. Köhler, I. Sandu, S. Serrar, P. Viterbo, and S. Park (2011). “The stable boundary layer in the ECMWF model”. In: *Europe* January, pages 7–10.

Bell, R. E, A. F Banwell, L. D Trusel, and J. Kingslake (2018). “Antarctic surface hydrology and impacts on ice-sheet mass balance”. In: *Nature Climate Change* 8.December, pages 1044–1052.

Bennartz, R., M. D. Shupe, D. D. Turner, V. P. Walden, K. Steffen, C. J. Cox, M. S. Kulie, N. B. Miller, and C. Pettersen (2013). “July 2012 Greenland melt extent enhanced by low-level liquid clouds”. In: *Nature* 496.7443, pages 83–86.

Best, M. J., M. Pryor, D. B. Clark, G. G. Rooney, and R. L. H. Essery (2011). “The Joint UK Land Environment Simulator (JULES), model description – Part 1 : Energy and water fluxes”. In: *Geoscientific Model Development* 4, pages 677–699.

Bevan, S., A. Luckman, B. Hubbard, B. Kulessa, D. Ashmore, P. Kuipers Munneke, M. O&apos;Leary, A. Booth, H. Sevestre, and D. McGrath (2017). “Centuries of intense surface melt on Larsen C Ice Shelf”. In: *The Cryosphere Discussions*, pages 1–21.

Bevan, S. L., A. J. Luckman, P. Kuipers Munneke, B. Hubbard, B. Kulessa, and D.W. Ashmore (2018). “Decline in Surface Melt Duration on Larsen C Ice Shelf Revealed by The Advanced Scatterometer (ASCAT)”. In: *Earth and Space Science* 5.10, pages 578–591.

Bodas-Salcedo, A., P. G. Hill, K. Furtado, K. D. Williams, P. R. Field, J. C. Manners, P. Hyder, and S. Kato (2016). “Large contribution of supercooled liquid clouds to the solar radiation budget of the Southern Ocean”. In: *Journal of Climate* 29.11, pages 4213–4228.

Bodas-Salcedo, A., K. D. Williams, P. R. Field, and A. P. Lock (2012). “The surface downwelling solar radiation surplus over the southern ocean in the met office model: The role of midlatitude cyclone clouds”. In: *Journal of Climate* 25.21, pages 7467–7486.

Borstad, C. P., D. Mcgrath, and A. Pope (2017). “Fracture propagation and stability of ice shelves governed by ice shelf heterogeneity”. In: *Geophysical Research Letters* 44, pages 4186–4194.

Borstad, C. P., E. Rignot, J. Mouginot, and M. P. Schodlok (2013). “Creep deformation and buttressing capacity of damaged ice shelves: Theory and application to Larsen C ice shelf”. In: *Cryosphere* 7.6, pages 1931–1947.

Bracegirdle, T. J. and G. J. Marshall (2012). “The reliability of antarctic tropospheric pressure and temperature in the latest global reanalyses”. In: *Journal of Climate* 25.20, pages 7138–7146.

Bromwich, D. H., J. P. Nicolas, K. M. Hines, J. E. Kay, E. L. Key, M. A. Lazzara, D. Lubin, G. M. McFarquhar, I. V. Gorodetskaya, D. P. Grosvenor, T. Lachlan-Cope, and N. P. M. van Lipzig (2012). “Tropospheric clouds in Antarctica”. In: *Reviews of Geophysics* 50.1, pages 1–40.

Bromwich, D. H., F. O. Otieno, K. M. Hines, K. W. Manning, and E. Shilo (2013). “Comprehensive evaluation of polar weather research and forecasting model performance in the antarctic”. In: *Journal of Geophysical Research Atmospheres* 118.2, pages 274–292.

Brown, A. R., R. J. Beare, J. M. Edwards, A. P. Lock, S. J. Keogh, S. F. Milton, and D. N. Walters (2008). “Upgrades to the boundary-layer scheme in the met office numerical weather prediction model”. In: *Boundary-Layer Meteorology* 128.1, pages 117–132.

Brown, P. R. A. and P. N. Francis (1995). “Improved measurements of the ice water content in cirrus using a total-water probe”. In: *Journal of Atmospheric and Oceanic Technology* 12.4, pages 410–414.

Bush, M., T. Allen, C. Bain, I. Boutle, J. Edwards, A. Finnenkoetter, C. Franklin, K. Hanley, H. Lean, A. Lock, J. Manners, M. Mittermaier, C. Morcrette, R. North, J. Petch, C. Short, S. Vosper, D. Walters, S. Webster, M. Weeks, J. Wilkinson, and N. Wood (2019). “The first Met Office Unified Model / JULES Regional Atmosphere and Land configurations, RAL1”. In: *Geoscientific Model Development Discussions* in review.June, pages 1–48.

Cape, M. R., M. Vernet, P. Skvarca, S. Marinsek, T. Scambos, and E. Domack (2015). “Foehn winds link climate-driven warming to ice shelf evolution in Antarctica”. In: *Journal of Geophysical Research: Atmospheres* 120.21, pages 11037–11057.

Castro, C. L., H. I. Chang, F. Dominguez, C. Carrillo, J. K. Schemm, and H. M. H. Juang (2012). “Can a regional climate model improve the ability to forecast the North American monsoon?” In: *Journal of Climate* 25.23, pages 8212–8237.

Ceccaldi, M., J. Delanoë, R. J. Hogan, N. L. Pounder, A. Protat, and J. Pelon (2013). “From CloudSat-CALIPSO to EarthCare: Evolution of the DARDAR cloud classification and its comparison to airborne radar-lidar observations”. In: *Journal of Geophysical Research Atmospheres* 118.14, pages 7962–7981.

Center, Climate Prediction (2005). *Teleconnection pattern calculation procedures*.

Chen, J., C. Ke, X. Zhou, Z. Shao, and L. Li (2016). “Surface velocity estimations of ice shelves in the northern Antarctic Peninsula derived from MODIS data”. In: *Journal of Geographical Sciences* 26.2, pages 243–256.

Chuter, S. J. and J. L. Bamber (2015). “Antarctic ice shelf thickness from CryoSat-2 radar altimetry”. In: *Geophysical Research Letters* 42.24, pages 10721–10729.

Clem, K. R. and R. L. Fogt (2013). “Varying roles of ENSO and SAM on the Antarctic Peninsula climate in austral spring”. In: *Journal of Geophysical Research Atmospheres* 118.20, pages 11481–11492.

Clem, K. R., J. A. Renwick, J. McGregor, and R. L. Fogt (2016). “The relative influence of ENSO and SAM on Antarctic Peninsula climate”. In: *Journal of Geophysical Research : Atmospheres* 121, pages 11038–11054.

Cook, A. J. and D. G. Vaughan (2010). “Overview of areal changes of the ice shelves on the Antarctic Peninsula over the past 50 years”. In: *The Cryosphere Discussions* 3.2, pages 579–630.

Cooper, W. A. (1986). “Ice Initiation in Natural Clouds”. In: *Precipitation Enhancement - A Scientific Challenge*. Boston, MA: Meteorological Monographs. American Meteorological Society. Chapter Ice Initia, pages 29–32.

Cotton, W. R., G. Bryan, and S. C. van den Heever (2011). “The Mesoscale Structure of Extratropical Cyclones and Middle and High Clouds”. In: *Storm and Cloud Dynamics*. Edited by W. R. Cotton, G. Bryan, and S. C. van den Heever. Academic Press. Chapter 10, pages 527–672.

Cox, P. M., R. A. Betts, C. B. Bunton, R. L.H. Essery, P. R. Rowntree, and J. Smith (1999). “The impact of new land surface physics on the GCM simulation of climate and climate sensitivity”. In: *Climate Dynamics* 15.3, pages 183–203.

Crosier, J., K. N. Bower, T. W. Choularton, C. D. Westbrook, P. J. Connolly, Z. Q. Cui, I. P. Crawford, G. L. Capes, H. Coe, J. R. Dorsey, P. I. Williams, A. J. Illingworth, M. W. Gallagher, and A. M. Blyth (2011). “Observations of ice multiplication in a weakly convective cell embedded in supercooled mid-level stratus”. In: *Atmospheric Chemistry and Physics* 11.1, pages 257–273.

Datta, R. T., M. Tedesco, X. Fettweis, C. Agosta, S. Lhermitte, J. T. M. Lenaerts, and N. Wever (2019). “The Effect of Foehn-Induced Surface Melt on Firn Evolution Over the Northeast Antarctic Peninsula”. In: *Geophysical Research Letters* 46, pages 3822–3831.

Datta, Rajashree Tri, Marco Tedesco, Cecile Agosta, Xavier Fettweis, Peter Kuipers Munneke, and Michiel R. Van Den Broeke (2018). “Melting over the northeast antarctic peninsula (1999-2009): Evaluation of a high-resolution regional climate model”. In: *Cryosphere* 12.9, pages 2901–2922.

Dätwyler, C., M. Grosjean, N. J. Steiger, and R. Neukom (2019). “Teleconnections and relationship between ENSO and SAM in reconstructions and models over the past millennium”. In: *Climate of the Past Discussions* September, pages 1–20.

De Rydt, J., G. H. Gudmundsson, H. Rott, and J. L. Bamber (2015). “Modeling the instantaneous response of glaciers after the collapse of the Larsen B Ice Shelf”. In: *Geophysical Research Letters* 42.12, pages 5355–5363.

Deb, P., A. Orr, D. H. Bromwich, J. P. Nicolas, J. Turner, and J. S. Hosking (2018). “Summer Drivers of Atmospheric Variability Affecting Ice Shelf Thinning in the Amundsen Sea Embayment, West Antarctica”. In: *Geophysical Research Letters* 45.9, pages 4124–4133.

Deb, P., A. Orr, J. S. Hosking, T. Phillips, J. Turner, D. Bannister, J. Pope, and S. Colwell (2016). “An assessment of the Polar Weather Research and Forecasting (WRF) model representation of near-surface meteorological variables over West Antarctica.” In: *Journal of Geophysical Research: Atmospheres* 121.4, pages 1532–1548.

Delanoë, J. and R. J. Hogan (2010). “Combined CloudSat-CALIPSO-MODIS retrievals of the properties of ice clouds”. In: *Journal of Geophysical Research Atmospheres* 115.4, pages 1–17.

DeMott, P. J., A. J. Prenni, G. R. McMeeking, R. C. Sullivan, M. D. Petters, Y. Tobo, M. Niemand, O. Möhler, J. R. Snider, Z. Wang, and S. M. Kreidenweis (2015). “Integrating laboratory and field data to quantify the immersion freezing ice nucleation activity of mineral dust particles”. In: *Atmospheric Chemistry and Physics* 15.1, pages 393–409.

DeMott, P. J., A.J. Prenni, X. Liu, S. M. Kreidenweis, M. D. Petters, C. H. Twohy, M .S. Richardson, T. Eidhammer, and D. C. Rogers (2010). “Predicting global atmospheric ice nuclei distributions and their impacts on climate.” In: *Proceedings of the National Academy of Sciences of the United States of America* 107.25, pages 11217–22.

Ding, Q., E. J. Steig, D. S. Battisti, and M. Küttel (2011). “Winter warming in West Antarctica caused by central tropical Pacific warming”. In: *Nature Geoscience* 4.6, pages 398–403.

Donahue, A. S. and P. M. Caldwell (2018). “Impact of Physics Parameterization Ordering in a Global Atmosphere Model”. In: *Journal of Advances in Modeling Earth Systems* 10.2, pages 481–499.

Dutra, E., I. Sandu, G. Balsamo, A. Beljaars, H. Freville, E. Vignon, and E. Brun (2015). *Understanding the ECMWF winter surface temperature biases over Antarctica*. Technical report January 2016.

Edwards, J. M., S. Havemann, J. Thelen, and A. J. Baran (2007). “A new parametrization for the radiative properties of ice crystals : Comparison with existing schemes and impact in a GCM”. In: *Atmospheric Research* 83, pages 19–35.

Edwards, J. M. and A. Slingo (1996). “Studies with a flexible new radiation code. I: Choosing a configuration for a large-scale model”. In: *Quarterly Journal of the Royal Meteorological Society* 122, pages 689–719.

Ekström, M., M. R. Grose, and P. H. Whetton (2015). “An appraisal of downscaling methods used in climate change research”. In: *Wiley Interdisciplinary Reviews: Climate Change* 6.3, pages 301–319.

Elvidge, A. D. (2013). “Polar föhn winds and warming over the Larsen C Ice Shelf, Antarctica”. PhD thesis. University of East Anglia.

Elvidge, A. D., P. Kuipers Munneke, J. C. King, I. A. Renfrew, and E. Gilbert (2020). “Atmospheric drivers of melt on Larsen C Ice Shelf: surface energy budget regimes and the impact of foehn”. In: *Journal of Geophysical Research: Atmospheres* submitted.

Elvidge, A. D. and I. A. Renfrew (2016). “The causes of foehn warming in the lee of mountains”. In: *Bulletin of the American Meteorological Society* 97.3, pages 455–466.

Elvidge, A. D., I. A. Renfrew, J. C. King, A. Orr, T. A. Lachlan-Cope, M. Weeks, and S.L. Gray (2015). “Foehn jets over the Larsen C Ice Shelf, Antarctica”. In: *Quarterly Journal of the Royal Meteorological Society* 141.688, pages 698–713.

Elvidge, A. D., Ian A. Renfrew, John C. King, Andrew Orr, and Tom A. Lachlan-Cope (2016). “Foehn warming distributions in nonlinear and linear flow regimes: A focus on the Antarctic Peninsula”. In: *Quarterly Journal of the Royal Meteorological Society* 142.695, pages 618–631.

Essery, R. L. H., M. J. Best, R. A. Betts, P. M. Cox, and C. M. Taylor (2003). “Explicit representation of subgrid heterogeneity in a GCM land surface scheme”. In: *Journal of Hydrometeorology* 4.3, pages 530–543.

Essery, R. L. H., M.J. Best, and P.M. Cox (2001). “MOSES 2.2 technical documentation. Hadley Centre Technical Note 30”. In:

Fahnestock, M. A., W. Abdalati, and C. A. Shuman (2002). “Long melt seasons on ice shelves of the Antarctic Peninsula: An analysis using satellite-based microwave emission measurements”. In: *Annals of Glaciology* 34, pages 127–133.

Favier, V., G. Krinner, C. Amory, H. Gallée, J. Beaumet, and C. Agosta (2017). “Antarctica-Regional Climate and Surface Mass Budget”. In: *Current Climate Change Reports* 3.4, pages 303–315.

Field, P. R., R. J. Cotton, K. Mcbeath, A. P. Lock, S. Webster, and R. P. Allan (2014). “Improving a convection-permitting model simulation of a cold air outbreak”. In: *Quarterly Journal of the Royal Meteorological Society* 140, pages 124–138.

Field, P. R., R. J. Hogan, P. R. A. Brown, A. J. Illingworth, T. W. Choularton, and R. J. Cotton (2005). “Parametrization of ice-particle size distributions for mid-latitude stratiform cloud”. In: *Quarterly Journal of the Royal Meteorological Society* 131.609, pages 1997–2017.

Fréville, H., E. Brun, G. Picard, N. Tatarinova, L. Arnaud, C. Lanconelli, C. Reijmer, and M. Van Den Broeke (2014). “Using MODIS land surface temperatures and the Crocus snow model to understand the warm bias of ERA-Interim reanalyses at the surface in Antarctica”. In: *Cryosphere* 8.4, pages 1361–1373.

Fürst, J. J., G. Durand, F. Gillet-chaulet, L. Tavard, M. Rankl, M. Braun, and O. Gagliardini (2016). “The safety band of Antarctic ice shelves”. In: *Nature Climate Change* 6.February, pages 2014–2017.

Furtado, K. and P. R. Field (2017). “The Role of Ice Microphysics Parametrizations in Determining the Prevalence of Supercooled Liquid Water in High-Resolution Simulations of a Southern Ocean Midlatitude Cyclone”. In: *Journal of the Atmospheric Sciences*. Volume 74. 6, pages 2001–2021.

Furtado, K., P. R. Field, I. A. Boutle, C. J. Morcrette, and J. M. Wilkinson (2016). “A Physically Based Subgrid Parameterization for the Production and Maintenance of Mixed-Phase Clouds in a General Circulation Model”. In: *Journal of the Atmospheric Sciences* 73.1, pages 279–291.

Gettelman, A., X. Liu, S. J. Ghan, H. Morrison, S. Park, A. J. Conley, S. A. Klein, J. Boyle, D. L. Mitchell, and J. L.F. Li (2010). “Global simulations of ice nucleation and ice supersaturation with an improved cloud scheme in the Community Atmosphere Model”. In: *Journal of Geophysical Research Atmospheres* 115.18, pages 1–19.

Gilbert, E., A. Orr, J. C. King, I. A. Renfrew, T. Lachlan-Cope, P. F. Field, and I. A Boutle (2020). “Summertime cloud phase strongly influences surface melting on the Larsen C ice shelf, Antarctica”. In: *Quarterly Journal of the Royal Meteorological Society*, pages 1–16.

Gillett, N. P., T. D. Kell, and P. D. Jones (2006). “Regional climate impacts of the Southern Annular Mode”. In: *Geophysical Research Letters* 33.23, pages 1–4.

Gorodetskaya, I. V., S. Kneifel, M. Maahn, W. Thiery, J. H. Schween, A. Mangold, S. Crewell, and N. P.M. Van Lipzig (2015). “Cloud and precipitation properties from ground-based remote-sensing instruments in East Antarctica”. In: *Cryosphere* 9.1, pages 285–304.

Gossart, A., S. Helsen, J. T. M. Lenaerts, S. van den Broucke, N. P. M. van Lipzig, and N. Souverijns (2019). “An evaluation of surface climatology in state-of-the-art reanalyses over the Antarctic Ice Sheet”. In: *Journal of Climate* 32.20, pages 6899–6915.

Griggs, J. A. and J. L. Bamber (2009). “Ice shelf thickness over Larsen C, Antarctica, derived from satellite altimetry”. In: *Geophysical Research Letters* 36.19, pages 1–5.

Grosvenor, D. P., T. W. Choularton, T. Lachlan-Cope, M. W. Gallagher, J. Crosier, K. N. Bower, R. S. Ladkin, and J. R. Dorsey (2012). “In-situ aircraft observations of ice concentrations within clouds over the Antarctic Peninsula and Larsen Ice Shelf”. In: *Atmospheric Chemistry and Physics* 12.23, pages 11275–11294.

Grosvenor, D. P., P.R. Field, A. A. Hill, and B. J. Shipway (2017). “The relative importance of macrophysical and cloud albedo changes for aerosol-induced radiative effects in closed-cell stratocumulus: Insight from the modelling of a case study”. In: *Atmospheric Chemistry and Physics* 17.8, pages 5155–5183.

Grosvenor, D. P., J. C. King, T. W. Choularton, and T. Lachlan-Cope (2014). “Downslope foehn winds over the antarctic peninsula and their effect on the larsen ice shelves”. In: *Atmospheric Chemistry and Physics* 14.18, pages 9481–9509.

Haensler, A., S. Hagemann, and D. Jacob (2011). “Dynamical downscaling of ERA40 reanalysis data over southern Africa: Added value in the simulation of the seasonal rainfall characteristics”. In: *International Journal of Climatology* 31.15, pages 2338–2349.

Hastings, D. and P. K. Dunbar (1999). *Global Land One-kilometer Base Elevation (GLOBE) v.1*.

Hill, A. A., B. J. Shipway, and I. A. Boutle (2015). “How sensitive are aerosol-precipitation interactions to the warm rain representation?” In: *Journal of Advances in Modeling Earth Systems* 7, pages 987–1004.

Hines, K. M., D. H. Bromwich, S. H. Wang, I. Silber, J. Verlinde, and D. Lubin (2019). “Microphysics of summer clouds in central West Antarctica simulated by the Polar Weather Research and Forecasting Model (WRF) and the Antarctic Mesoscale Prediction System (AMPS)”. In: *Atmospheric Chemistry and Physics* 19.19, pages 12431–12454.

Hoinka, K. P. (1985). “What is a Foehn Clearance?” In: *Bulletin of the American Meteorological Society* 66.9, pages 1123–1132.

Holland, P. R., A. Brisbourne, H. F J Corr, D. McGrath, K. Purdon, J. Paden, H. A. Fricker, F. S. Paolo, and A. H. Fleming (2015). “Oceanic and atmospheric forcing of Larsen C Ice-Shelf thinning”. In: *Cryosphere* 9.3, pages 1005–1024.

Holland, P. R., H. F. J. Corr, H. D. Pritchard, D.G. Vaughan, R. J. Arthern, A. Jenkins, and M. Tedesco (2011). “The air content of Larsen Ice Shelf”. In: *Geophysical Research Letters* 38.10, pages 1–6.

Hong, S. Y. and J. Dudhia (2012). “Next-Generation Numerical Weather Prediction: Bridging Parameterization, Explicit Clouds, and Large Eddies”. In: *Bulletin of the American Meteorological Society* 93.1, ES6–ES9.

Hong, S. Y. and M. Kanamitsu (2014). “Dynamical downscaling: Fundamental issues from an NWP point of view and recommendations”. In: *Asia-Pacific Journal of Atmospheric Sciences* 50.1, pages 83–104.

Hubbard, B., A. Luckman, D. W. Ashmore, S. Bevan, B. Kulessa, P. Kuipers Munneke, M. Philippe, D. Jansen, A. Booth, H. Sevestre, J.-L. Tison, M. O’Leary, and I. Rutt (2016). “Massive subsurface ice formed by refreezing of ice-shelf melt ponds.” In: *Nature communications* 7.May, page 11897.

Hyder, P., J. M. Edwards, R. P. Allan, H. T. Hewitt, T. J. Bracegirdle, J. M. Gregory, R. A. Wood, A. J. S. Meijers, J. Mulcahy, P. R. Field, K. Furtado, A. Bodas-Salcedo, K. D. Williams, D. Copsey, S. A. Josey, C. Liu, C. D. Roberts, C. Sanchez, J. Ridley, L. Thorpe, S. C. Hardiman, M. Mayer, D. I. Berry, and S. E. Belcher (2018). “Critical Southern Ocean climate model biases traced to atmospheric model cloud errors”. In: *Nature Communications* 9.1, page 3625.

Jonassen, M. O., I. Välisuo, T. Vihma, P. Uotila, A. P. Makshtas, and J. Launiainen (2019). “Assessment of atmospheric reanalyses with independent observations in the Weddell Sea, the Antarctic”. In: *Journal of Geophysical Research: Atmospheres* 124.23, pages 12468–12484.

Jones, R. W., I. A. Renfrew, A. Orr, B. G. M. Webber, D. M. Holland, and M. A. Lazzara (2016). “Evaluation of four global reanalysis products using in situ observations in the Amundsen Sea Embayment, Antarctica”. In: *Journal of Geophysical Research : Atmospheres* 121.11, pages 6240–6257.

Kalesse, H., G. de Boer, A. Solomon, M. Oue, M. Ahlgrimm, D. Zhang, M. D. Shupe, E. Luke, and A. Protat (2016). “Understanding Rapid Changes in Phase Partitioning between Cloud Liquid and Ice in Stratiform Mixed-Phase Clouds: An Arctic Case Study”. In: *Monthly Weather Review* 144.12, pages 4805–4826.

Kay, J. E., T. L’Ecuyer, A. Gettelman, G. Stephens, and C. O’Dell (2008). “The contribution of cloud and radiation anomalies to the 2007 Arctic sea ice extent minimum”. In: *Geophysical Research Letters* 35.8, pages 1–5.

Khazendar, A., E. Rignot, and E. Larour (2011). “Acceleration and spatial rheology of Larsen C Ice Shelf , Antarctic Peninsula”. In: *Geophysical Research Letters* 38.January, pages 1–5.

King, J. C., A. Gadian, A. Kirchgaessner, P. Kuipers Munneke, T. A. Lachlan-Cope, A. Orr, C. Reijmer, M. R. van Den Broeke, J. M. van Wessem, and M. Weeks (2015). “Validation of the summertime surface energy budget of Larsen C Ice Shelf (Antarctica) as represented in three high-resolution atmospheric models”. In: *Journal of Geophysical Research Atmospheres* 120.4, pages 1335–1347.

King, J. C., A. Kirchgaessner, A. Orr, A. Luckman, S. Bevan, A. Elvidge, I. A. Renfrew, and P. Kuipers Munneke (2017). “The impact of foehn winds on surface energy balance and melt over Larsen C Ice Shelf, Antarctica”. In: *Journal of Geophysical Research: Atmospheres* 122.22, pages 12062–12076.

King, J. C., T. A. Lachlan-Cope, R. S. Ladkin, and A. Weiss (2008). “Airborne Measurements in the Stable Boundary Layer over the Larsen Ice Shelf , Antarctica”. In: *Boundary Layer Meteorology* 127.3, pages 413–428.

King, W. D., D. A. Parkin, and R. J. Handsworth (1978). *A Hot-Wire Liquid Water Device Having Fully Calculable Response Characteristics*.

Kirchgaessner, A. (2010). “An analysis of cloud observations from Vernadsky, Antarctica”. In: *International Journal of Climatology* 30.10, pages 1431–1439.

Kirchgaessner, A., J. C. King, and A. Gadian (2019). “The Representation of Föhn Events to the East of the Antarctic Peninsula in Simulations by the Antarctic Mesoscale Prediction System”. In: *Journal of Geophysical Research: Atmospheres*, pages 1–17.

Klein, S. A, R. B Mccoy, H. Morrison, A. S. Ackerman, G. de Boer, M. Chen, J. N. S. Cole, D. D. Genio, M. J. Foster, A. Fridlind, J.-c. Golaz, T. Hashino, Y. Jerry, C. Hoose, M. F. Khairoutdinov, V. E. Larson, X. Liu, G. M. Mcfarquhar, S. Menon, R. A. J. Neggers, S. Park, R. Michael, J. M. Schmidt, I. Sednev, B. J. Shipway, M. D. Shupe, D. A. Spangenberg, Y. C. Sud, D. D. Turner, D. E. Veron, K. Von, G. K. Walker, Z. Wang, A. B. Wolf, and S. Xie (2009). “Intercomparison of model simulations of mixed-phase clouds observed during the ARM Mixed-Phase Arctic Cloud Experiment . I : Single-layer cloud”. In: *Quarterly Journal of the Royal Meteorological Society* 1002.May, pages 979–1002.

Komurcu, M., T. Storelvmo, I. Tan, U. Lohmann, Y. Yuxing, J. E. Penner, Y. Wang, X. Liu, and T. Takemura (2014). “Intercomparison of the cloud water phaseamong global climate models”. In: *Journal of Geophysical Research: Atmospheres* 119.6, pages 3372–3400.

Krapp, M., A. Robinson, and A. Ganopolski (2017). “SEMIC: An efficient surface energy and mass balance model applied to the Greenland ice sheet”. In: *Cryosphere* 11.4, pages 1519–1535.

Kuipers Munneke, P., S. R. M. Ligtenberg, M. R. van den Broeke, and D. G. Vaughan (2014). “Firn air depletion as a precursor of Antarctic ice-shelf collapse”. In: *Journal of Glaciology* 60.220, pages 205–214.

Kuipers Munneke, P., A. J. Luckman, S. L. Bevan, E. Gilbert, C. J. P. P. Smeets, M. R. Van Den Broeke, W. Wang, C. Zender, B. Hubbard, D. Ashmore, A. Orr, and J. C. King (2018). “Intense winter surface melt on an Antarctic ice shelf”. In: *Geophysical Research Letters* 45, pages 7615–7623.

Kuipers Munneke, P., D. McGrath, B. Medley, A. Luckman, S. Bevan, B. Kulessa, D. Jansen, A. Booth, P. Smeets, B. Hubbard, D. Ashmore, M. R. van den Broeke, H. Sevestre, K. Steffen, A. Shepherd, and N. Gourmelen (2017). “Observationally constrained surface mass balance of Larsen C Ice Shelf, Antarctica”. In: *The Cryosphere Discussions* March, pages 1–24.

Kuipers Munneke, P., M. R. van den Broeke, J. C. King, T. Gray, and C. H. Reijmer (2012). “Near-surface climate and surface energy budget of Larsen C ice shelf, Antarctic Peninsula”. In: *Cryosphere* 6.2, pages 353–363.

Kuipers Munneke, P., M. R. van den Broeke, C. H. Reijmer, M. M. Helsen, W. Boot, M. Schneebeli, and K. Steffen (2009). “The role of radiation penetration in the energy budget of the snowpack at Summit, Greenland”. In: *The Cryosphere* 3.1, pages 155–165.

Lachlan-Cope, T. (2010). “Antarctic clouds”. In: *Polar Research* 29.2, pages 150–158.

Lachlan-Cope, T., R. Ladkin, J. Turner, and P. Davison (2001). “Observations of cloud and precipitation particles on the Avery Plateau, Antarctic Peninsula”. In: *Antarctic Science* 13.3, pages 339–348.

Lachlan-Cope, T., C. Listowski, and S. O’Shea (2016). “The microphysics of clouds over the Antarctic Peninsula – Part 1 : Observations”. In: *Atmospheric Chemistry and Physics* 16, pages 15605–15617.

Lawson, R. P. and A. Gettelman (2014). “Impact of Antarctic mixed-phase clouds on climate.” In: *Proceedings of the National Academy of Sciences of the United States of America* 111.51, pages 18156–18161.

Lazzara, M. A., G. A. Weidner, L. M. Keller, J. E. Thom, and J. J. Cassano (2012). “Antarctic automatic weather station program: 30 years of polar observations”. In: *Bulletin of the American Meteorological Society* 93.10, pages 1519–1537.

Lebo, Z. L., B. J. Shipway, J. Fan, I. Geresdi, A. Hill, A. Miltenberger, H. Morrison, P. Rosenberg, A. Varble, and L. Xue (2017). “Challenges for cloud modeling in the context of aerosol-cloud-precipitation interactions”. In: *Bulletin of the American Meteorological Society* under revi.

Lenaerts, J. T. M., S. Lhermitte, R. Drews, S. R. M. Ligtenberg, S. Berger, V. Helm, C. J. P. P. Smeets, M. R. van den Broeke, W. J. van de Berg, E. van Meijgaard, M. Eijkelboom, O. Eisen, and F. Pattyn (2016a). “Meltwater produced by wind–albedo interaction stored in an East Antarctic ice shelf”. In: *Nature Climate Change* 7.1, pages 58–62.

Lenaerts, J. T. M., S. R. M. Ligtenberg, B. Medley, W. J. van de berg, H. Konrad, J. P. Nicholas, J. M. van Wessem, L. D. Trusel, R. Mulvaney, R. J. Tuckwell, A. E. Hogg, and E. R. Thomas (2018). “Climate and surface mass balance of coastal West Antarctica resolved by regional climate modelling”. In: *Annals of Glaciology* 59.76, pt1, pages 29–41.

Lenaerts, J. T. M., M. Vizcaino, J. Fyke, L. van Kampenhout, and M. R. van den Broeke (2016b). “Present-day and future Antarctic ice sheet climate and surface mass balance in the Community Earth System Model”. In: *Climate Dynamics* 47.5-6, pages 1367–1381.

Lenaerts, J. T.M., K. Van Tricht, S. Lhermitte, and T. S. L’Ecuyer (2017). “Polar clouds and radiation in satellite observations, reanalyses, and climate models”. In: *Geophysical Research Letters* 44.7, pages 3355–3364.

Listowski, C., J. Delanoë, A. Kirchgaessner, T. Lachlan-Cope, and J. C. King (2019). “Antarctic clouds, supercooled liquid water and mixed phase, investigated with DARDAR: Geographical and seasonal variations”. In: *Atmospheric Chemistry and Physics* 19.10, pages 6771–6808.

Listowski, C. and T. Lachlan-Cope (2017). “The Microphysics of Clouds over the Antarctic Peninsula – Part 2 : modelling aspects within Polar WRF”. In: *Atmospheric Chemistry and Physics* 17, pages 10195–10221.

Liu, H. (1999). *Development of an Antarctic Digital Elevation model*. Technical report. Byrd Polar Research Center, Ohio State University, page 157.

Liu, H., K. C. Jezek, B. Li, and Z. Zhao (2015). *RadarSat Antarctic Mapping Project Digital Elevation Model, version 2.*

Liu, H., L. Wang, and K. C. Jezek (2006). “Spatiotemporal variations of snowmelt in Antarctica derived from satellite scanning multichannel microwave radiometer and Special Sensor Microwave Imager data (1978-2004)”. In: *Journal of Geophysical Research: Earth Surface* 111.1, pages 1–20.

Lo, J. C. F., Z. L. Yang, and R. A. Pielke (2008). “Assessment of three dynamical climate downscaling methods using the Weather Research and Forecasting (WRF) model”. In: *Journal of Geophysical Research Atmospheres* 113.9.

Lock, A. P. (2001). “The numerical representation of entrainment in parameterizations of boundary layer turbulent mixing”. In: *Monthly Weather Review* 129.5, pages 1148–1163.

– (2011). “Stable boundary layer modelling at the Met Office”. In: *ECMWF GABLS workshop*. November, pages 7–10.

Lock, A. P., A. R. Brown, M. R. Bush, G. M. Martin, and R. N.B. Smith (2000). “A new boundary layer mixing scheme. Part I: Scheme description and single-column model tests”. In: *Monthly Weather Review* 128.9, pages 3187–3199.

Luckman, A., A. Elvidge, D. Jansen, B. Kulessa, P. Kuipers Munneke, J. C. King, and N. E. Barrand (2014). “Surface melt and ponding on Larsen C Ice Shelf and the impact of föhn winds”. In: *Antarctic Science* 26.6, pages 625–635.

Marshall, G. J. (2003). “Trends in the Southern Annular Mode from observations and reanalyses”. In: *Journal of Climate* 16.24, pages 4134–4143.

Marshall, G. J., A. Orr, N. P. M. van Lipzig, and J. C. King (2006). “The impact of a changing Southern Hemisphere Annular Mode on Antarctic Peninsula summer temperatures”. In: *Journal of Climate* 19.20, pages 5388–5404.

McCoy, D. T., I. Tan, D. L. Hartmann, M. D. Zelinka, and T. Storelvmo (2016). “On the relationships among cloud cover, mixed-phase partitioning, and planetary albedo in GCMs”. In: *Journal of Advances in Modeling Earth Systems* 8, pages 650–668.

McGrath, D., K. Steffen, P. R. Holland, T. Scambos, H. Rajaram, W. Abdalati, and E. Rignot (2014). “The structure and effect of suture zones in the Larsen C Ice Shelf, Antarctica”. In: *Journal of Geophysical Research: Earth Surface* 119.3, pages 588–602.

Mechoso, C. R. and A. Arakawa (2015). *Numerical Models: General Circulation Models*. Second Edi. Volume 4. Elsevier, pages 153–160.

Miller, N. B., M.D. Shupe, C. J. Cox, V. P. Walden, D. D. Turner, and K. Steffen (2015). “Cloud radiative forcing at Summit, Greenland”. In: *Journal of Climate* 28.15, pages 6267–6280.

Miltenberger, A. K., P. R. Field, A. A. Hill, P. Rosenberg, B. J. Shipway, M. Wilkinson, R. Scovell, and A. M. Blyth (2018). “Aerosol-cloud interactions in mixed-phase convective clouds . Part 1 : Aerosol perturbations .” In: *Atmospheric Chemistry and Physics* 18, pages 3119–3145.

Morley, B. M., E. E. Uthe, and W. Viezee (1989). “Airborne lidar observations of clouds in the Antarctic troposphere”. In: *Geophysical Research Letters* 16.6, pages 491–494.

Morrison, H., G. De Boer, G. Feingold, J. Harrington, M. D. Shupe, and K. Sulia (2012). “Resilience of persistent Arctic mixed-phase clouds”. In: *Nature Geoscience* 5.1, pages 11–17.

Nicolas, J. P., A. M. Vogelmann, R. C. Scott, A. B. Wilson, M. P. Cadeddu, David H. Bromwich, J. Verlinde, D. Lubin, L. M. Russell, C. Jenkinson, H. H. Powers, M. Ryczek, G. Stone, and J. D. Wille (2017). “January 2016 extensive summer melt in West Antarctica favoured by strong El Niño”. In: *Nature Communications* 8.15799, pages 1–10.

Nott, G.J. and T. J. Duck (2011). “Lidar studies of the polar troposphere”. In: *Meteorological Applications* 18.3, pages 383–405.

Nygard, T., T. Vihma, G. Birnbaum, J. C. King, R. Ladkin, and L. Christof (2016). “Validation of eight atmospheric reanalyses in the Antarctic Peninsula region”. In: *Quarterly Journal of the Royal Meteorological Society* 142.January, pages 684–692.

Orr, A., D. Cresswell, G. J. Marshall, J. C. R. Hunt, J. Sommeria, C. G. Wang, and M. Light (2004). “A ‘low-level’ explanation for the recent large warming trend over the western Antarctic Peninsula involving blocked winds and changes in zonal circulation”. In: *Geophysical Research Letters* 31.6, page L06204.

Orr, A., G.J. Marshall, J.C. R. Hunt, J. Sommeria, C.-G. Wang, N. P. M. van Lipzig, D. Cresswell, and J. C. King (2008). “Characteristics of Summer Airflow over the Antarctic Peninsula in Response to Recent Strengthening of Westerly Circumpolar Winds”. In: *Journal of the Atmospheric Sciences* 65.4, pages 1396–1413.

Orr, A., T. Phillips, S. Webster, A. Elvidge, M. Weeks, S. Hosking, and J. Turner (2014). “Met Office Unified Model high-resolution simulations of a strong wind event in Antarctica”. In: *Quarterly Journal of the Royal Meteorological Society* 140.684, pages 2287–2297.

Oza, Sandip Rashmikant (2015). “Spatial – temporal patterns of surface melting observed over Antarctic ice shelves using scatterometer data”. In: *Antarctic Science* 27.February 2013, pages 403–410.

Parkinson, C. L. (2019). “A 40-y record reveals gradual Antarctic sea ice increases followed by decreases at rates far exceeding the rates seen in the Arctic”. In: *Proceedings of the National Academy of Sciences of the United States of America* 116.29, pages 14414–14423.

Picard, G., M. Fily, and H. Gallee (2007). “Surface melting derived from microwave radiometers: A climatic indicator in Antarctica”. In: *Annals of Glaciology* 46.2002, pages 29–34.

Pielke Sr, R. A. and R. L. Wilby (2012). “Regional Climate Downscaling: What’s the Point?” In: *Eos* 93.5, pages 52–53.

Pruppacher, H. R. and J. D. Klett (1978). *Microphysics of clouds and precipitation*. 1st edition. Boston: D. Riedel.

Pu, Z. and E. Kalnay (2012). “Numerical Weather Prediction Basics: Models, Numerical Methods, and Data Assimilation”. In: *Handbook of Hydrometeorological Ensemble Forecasting*. Edited by Q. Duan, F. Pappenberger, A. Wood, H. L. Cloke, and J. C. Shaake. 1st edition. Berlin: Springer Berlin Heidelberg. Chapter 3, pages 68 –97.

Reynolds, R. W., T. M. Smith, C. Liu, D. B. Chelton, K. S. Casey, and M. G. Schlax (2007). “Daily high-resolution-blended analyses for sea surface temperature”. In: *Journal of Climate* 20.22, pages 5473–5496.

Rignot, E., G. Casassa, P. Gogineni, W. Krabill, A. Rivera, and R. Thomas (2004). “Accelerated ice discharge from the Antarctic Peninsula following the collapse of Larsen B ice shelf”. In: *Geophysical Research Letters* 31.July, pages 2–5.

Rockel, B., C. L. Castro, R. A. Pielke, H. von Storch, and G. Leoncini (2008). “Dynamical downscaling: Assessment of model system dependent retained and added variability for two different regional climate models”. In: *Journal of Geophysical Research Atmospheres* 113.21, pages 1–9.

Rotstayn, L. D., B. F. Ryan, and J. J. Katzfey (2000). “A Scheme for Calculation of the Liquid Fraction in Mixed-Phase Stratiform Clouds in Large-Scale Models”. In: *Monthly Weather Review* 128.4, pages 1070–1088.

Rowe, P. M., C. J. Cox, and P. von Walden (2016). “Toward autonomous surface-based infrared remote sensing of polar clouds: Cloud-height retrievals”. In: *Atmospheric Measurement Techniques* 9.8, pages 3641–3659.

Royston, S. A. M. and G. H. Gudmundsson (2016). “Changes in ice-shelf buttressing following the collapse of Larsen A Ice Shelf , Antarctica , and the resulting impact on tributaries”. In: *Journal of Glaciology* 62.235, pages 905–911.

Sandu, I., A. Beljaars, G. Balsamo, P. Bechtold, and M. Rodwell (2011). “Experience with the representation of stable conditions in the ECMWF model Land-atmosphere coupling”. In: *Weather* November, pages 7–10.

Scambos, T. A., J. A. Bohlander, C. A. Shuman, and P. Skvarca (2004). “Glacier acceleration and thinning after ice shelf collapse in the Larsen B embayment, Antarctica”. In: *Geophysical Research Letters* 31.18, pages 2001–2004.

Scambos, T. A., C. Hulbe, and M. Fahnestock (2003). “Climate-induced ice shelf disintegration in the Antarctic Peninsula”. In: *Antarctic Peninsula Climate Variability: Historical and Paleoenvironmental Perspectives*. Edited by E. Domack, A. Levente, A. Burnet, R. Bindschadler, P. Convey, and M. Kirby. Volume 79. Washington, D.C.: American Geophysical Union. Chapter Climate-in, pages 79–92.

Scambos, T. A., C Hulbe, M.Fahnestock, and J.Bohlander (2000). “The link between climate warming and break-up of ice shelves in the Antarctica Peninsula”. In: *Journal of Glaciology* 46.154, pages 516–530.

Schannwell, C., S. Cornford, D. Pollard, and N. E. Barrand (2018). “Dynamic response of Antarctic Peninsula Ice Sheet to collapse of Larsen C and George VI ice shelves”. In: *The Cryosphere Discussions* i, pages 1–30.

Schlosser, E., F. A. Haumann, and M. N. Raphael (2018). “Atmospheric influences on the anomalous 2016 Antarctic sea ice decay”. In: *The Cryosphere* 12.3, pages 1103–1119.

Schwerdtfeger, W. (1974). “Mountain barrier effect on the flow of stable air north of the Brooks Range”. In: *Proceedings of the 24th Alaskan Science Conference,* Geophysical Institute, University of Alaska, Fairbanks, pages 204–208.

Scott, R. C., D. Lubin, A. M. Vogelmann, and S. Kato (2017). “West Antarctic Ice Sheet Cloud Cover and Surface Radiation Budget from NASA A-Train Satellites”. In: *Journal of Climate* 30.16, pages 6151–6170.

Seinfeld, J. H., C. Bretherton, K. S. Carslaw, H. Coe, P. J. DeMott, E. J. Dunlea, G. Feingold, S. Ghan, A. B. Guenther, R. Kahn, I. Kraucunas, S. M. Kreidenweis, M. J. Molina, A. Nenes, J. E. Penner, K. A. Prather, V. Ramanathan, V. Ramaswamy, P. J. Rasch, A. R. Ravishankara, D. Rosenfeld, G. Stephens, and R. Wood (2016). “Improving our fundamental understanding of the role of aerosolcloud interactions in the climate system”. In: *Proceedings of the National Academy of Sciences* 113.21, pages 5781–5790.

Shepherd, A., D. Wingham, T. Payne, and P. Skvarca (2003). “Progressively Thinned”. In: *Science* 302.5646, pages 856–860.

Shipway, B. J. and A. A. Hill (2012). “Diagnosis of systematic differences between multiple parametrizations of warm rain microphysics using a kinematic framework”. In: *Quarterly Journal of the Royal Meteorological Society* 138.669, pages 2196–2211.

Silber, I., J. Verlinde, E. W. Eloranta, and M. Cadeddu (2018). “Antarctic Cloud Macrophysical, Thermodynamic Phase, and Atmospheric Inversion Coupling Properties at McMurdo Station: I. Principal Data Processing and Climatology”. In: *Journal of Geophysical Research: Atmospheres* 123.11, pages 6099–6121.

Smeets, C. J. P. P. (2006). “Assessing unaspirated temperature measurements using a thermocouple and a physically based model”. In: February, pages 1–116.

Smeets, P. C.J.P., P. Kuipers Munneke, D. van As, M. R. van den Broeke, W. Boot, H. Oerlemans, H. Snellen, C. H. Reijmer, and R. S.W. van de Wal (2018). “The K-transect in west Greenland: Automatic weather station data (1993–2016)”. In: *Arctic, Antarctic, and Alpine Research* 50.1, e1420954.

Smith, R. N. B. (1990a). “A scheme for predicting layer clouds and their water content in a general circulation model”. In: *Quarterly Journal of the Royal Meteorological Society* 116, pages 435–460.

– (1990b). “Why can’t stably stratified air rise over high ground?” In: *Atmospheric processes over complex terrain*.

Soares, P. M.M., R. M. Cardoso, P. M.A. Miranda, J. de Medeiros, M. Belo-Pereira, and F. Espirito-Santo (2012). “WRF high resolution dynamical downscaling of ERA-Interim for Portugal”. In: *Climate Dynamics* 39.9-10, pages 2497–2522.

Souverijns, N., A. Gossart, M. Demuzere, J. T.M. Lenaerts, B. Medley, I. V. Gorodetskaya, S. Vanden Broucke, and N. P.M. van Lipzig (2019). “A New Regional Climate Model for POLAR-CORDEX: Evaluation of a 30-Year Hindcast with COSMO-CLM 2 Over Antarctica”. In: *Journal of Geophysical Research: Atmospheres* 124.3, pages 1405–1427.

Stevens, B. (2017). “Clouds unfazed by haze”. In: *Nature* 546, pages 483–484.

Storch, H. von, F. Feser, B. Geyer, K. Klehmet, D. Li, B. Rockel, M. Schubert-Frisius, N. Tim, and E. Zorita (2017). “Regional reanalysis without local data: Exploiting the downscaling paradigm”. In: *Journal of Geophysical Research: Atmospheres* 122.16, pages 8631–8649.

Swart, N. C., J. C. Fyfe, N. Gillett, and G. J. Marshall (2015). “Comparing trends in the southern annular mode and surface westerly jet”. In: *Journal of Climate* 28.22, pages 8840–8859.

Tan, I. and T. Storelvmo (2016). “Sensitivity Study on the Influence of Cloud Microphysical Parameters on Mixed-Phase Cloud Thermodynamic Phase Partitioning in CAM5”. In: *Journal of the Atmospheric Sciences* 73.2, pages 709–728.

Tedesco, M. (2009). “Assessment and development of snowmelt retrieval algorithms over Antarctica from K-band spaceborne brightness temperature (1979-2008)”. In: *Remote Sensing of Environment* 113.5, pages 979–997.

Thompson, D.W.J. and S. Solomon (2002). “Interpretation of recent Southern Hemisphere climate change”. In: *Science* 296.5569, pages 895–899.

Trusel, L. D., K. E. Frey, S. B. Das, K. B. Karnauskas, P. Kuipers Munneke, E. van Meijgaard, and M. R. van den Broeke (2015). “Divergent trajectories of Antarctic surface melt under two twenty-first-century climate scenarios”. In: *Nature Geoscience* 8.12, pages 927–932.

Trusel, L. D., K. E. Frey, S. B. Das, P. Kuipers Munneke, and M. R. van den Broeke (2013). “Satellite-based estimates of Antarctic surface meltwater fluxes”. In: *Geophysical Research Letters* 40.23, pages 6148–6153.

Turner, J., S. R. Colwell, G. J. Marshall, T. A. Lachlan-Cope, A. M. Carleton, P. D. Jones, V. Lagun, P. A. Reid, and S. Iagovkina (2005). “Antarctic climate change during the last 50 years”. In: *International Journal of Climatology* 25.3, pages 279–294.

Turner, J., H. Lu, I. White, J. C. King, T. Phillips, J. S. Hosking, T. J. Bracegirdle, G. J Marshall, and P. Mulvaney R.and Deb (2016). “Absence of 21st century warming on Antarctic Peninsula consistent with natural variability”. In: *Nature* 535.7612, pages 411–415.

Turner, J., T. Maksym, T. Phillips, G. J. Marshall, and M.P. Meredith (2013). “The impact of changes in sea ice advance on the large winter warming on the western Antarctic Peninsula”. In: *International Journal of Climatology* 33.4, pages 852–861.

Turton, J. V., A. Kirchgaessner, A. N. Ross, and J. C. King (2017). “Does high-resolution modelling improve the spatial analysis of föhn flow over the Larsen C Ice Shelf?” In: *Weather* 72.7, pages 192–196.

– (2018). “The spatial distribution and temporal variability of föhn winds over the Larsen C ice shelf, Antarctica”. In: *Quarterly Journal of the Royal Meteorological Society* 144.713, pages 1169–1178.

van den Broeke, M. R. (2005). “Strong surface melting preceded collapse of Antarctic Peninsula ice shelf”. In: *Geophysical Research Letters* 32, pages 2–5.

van den Broeke, M. R., C. Tijm-Reijmer, and W. Boot (2013). “A new approach to climate observations in the polar regions”. In: *Advances on Ice*, pages 45–47.

van Lipzig, N. P. M., G. J. Marshall, A. Orr, and J. C. King (2008). “The relationship between the Southern Hemisphere annular mode and antarctic Peninsula summer temperatures: Analysis of a high-resolution model climatology”. In: *Journal of Climate* 21.8, pages 1649–1668.

van Oldenborgh, G.J., M. Collins, J. Arblaster, J.H. Christensen, J. Marotzke, S.B. Power, M. Rummukainen, and T. (Eds.) Zhou (2013). “Atlas of Global and Regional Climate Projections.” In: *Climate Change 2013: The Physical Science Basis. Contribution of Working Group I to the Fifth Assessment Report of the Intergovernmental Panel on Climate Change.* Edited by T.F. Stocker, D. Qin, G.-K. Plattner, M. Tignor, S.K. Allen, J. Boschung, A. Nauels, Y. Xia, V. Bex, and P.M. Midgley. Cambridge, UK: Cambridge University Press. Chapter Annex I.

van Tricht, K., S. Lhermitte, J. T.M. Lenaerts, I. V. Gorodetskaya, T. S. L’Ecuyer, B. Noël, M. R. van den Broeke, D. D. Turner, and N. P.M. van Lipzig (2016). “Clouds enhance Greenland ice sheet meltwater runoff”. In: *Nature Communications* 7.May 2015.

van Wessem, J. M., S. R. M. Ligtenberg, C. H. Reijmer, W. J. van de Berg, M. R. van den Broeke, N. E. Barrand, E. R. Thomas, J. Turner, J. Wuite, T. A. Scambos, and E. van Meijgaard (2016). “The modelled surface mass balance of the Antarctic Peninsula at 5.5 km horizontal resolution”. In: *Cryosphere* 10.1, pages 271–285.

van Wessem, J. M., C. H. Reijmer, J. T M Lenaerts, W. J. van De Berg, M. R. van den Broeke, and E. Van Meijgaard (2014). “Updated cloud physics in a regional atmospheric climate model improves the modelled surface energy balance of Antarctica”. In: *Cryosphere* 8.1, pages 125–135.

van Wessem, J. M., C. H. Reijmer, W. J. van de Berg, M. R. van den Broeke, A. J. Cook, L. H. van Ulft, and E. van Meijgaard (2015). “Temperature and wind climate of the Antarctic Peninsula as simulated by a high-resolution Regional Atmospheric Climate Model”. In: *Journal of Climate* 28.18, pages 7306–7326.

van Wessem, J. M., W. J. van de Berg, B. P. Y. Noël, E. van Meijgaard, G. Birnbaum, C. L. Jakobs, K. Krüger, J. T. M. Lenaerts, S. Lhermitte, S. R. M. Ligtenberg, B. Medley, C. H. Reijmer, K. van Tricht, L. D. Trusel, L. H. van Ulft, B. Wouters, J. Wuite, and M. R. van den Broeke (2018). “Modelling the climate and surface mass balance of polar ice sheets using RACMO2, part 2: Antarctica (1979-2016)”. In: *The Cryosphere* 12, pages 1479–1498.

Vergara-Temprado, J., A. K. Miltenberger, K. Furtado, D.P. Grosvenor, B.J. Shipway, Adrian A. Hill, J.M. Wilkinson, P. R. Field, B. J. Murray, and K. S. Carslaw (2018). “Strong control of Southern Ocean cloud reflectivity by ice-nucleating particles”. In: *Proceedings of the National Academy of Sciences* 115.11, pages 2687–2692.

Wallace, J. M. and P. V. Hobbs (2006). *Atmospheric Science: an introductory survey*. 2nd ed. Academic Press, page 483.

Walters, D., I. Boutle, M. Brooks, T. Melvin, R. Stratton, S. Vosper, H. Wells, K. Williams, N. Wood, T. Allen, A. Bushell, D. Copsey, P. Earnshaw, J. Edwards, M. Gross, S. Hardiman, C. Harris, J. Heming, N. Klingaman, R. Levine, J. Manners, G. Martin, S. Milton, M. Mittermaier, C. Morcrette, T. Riddick, M. Roberts, C. Sanchez, P. Selwood, A. Stirling, C. Smith, D. Suri, W. Tennant, P. Luigi Vidale, J. Wilkinson, M. Willett, S. Woolnough, and P. Xavier (2017). “The Met Office Unified Model Global Atmosphere 6.0/6.1 and JULES Global Land 6.0/6.1 configurations”. In: *Geoscientific Model Development* 10.4, pages 1487–1520.

Walther, C. (2016). “Atmospheric Circulation in Antarctica: Analysis of Synoptic Structures via Measurement and Regional Climate Model ,” PhD thesis. Alfred Wegener Institut.

Wang, G., H. H. Hendon, J.M. Arblaster, E. P. Lim, S. Abhik, and P. van Rensch (2019). “Compounding tropical and stratospheric forcing of the record low Antarctic sea-ice in 2016”. In: *Nature Communications* 10.1, pages 1–9.

Wang, W., C. S. Zender, D. Van As, P.C.J.P. Smeets, and M. R. Van Den Broeke (2016). “A Retrospective, Iterative, Geometry-Based (RIGB) tilt-correction method for radiation observed by automatic weather stations on snow-covered surfaces: Application to Greenland”. In: *Cryosphere* 10.2, pages 727–741.

Wendisch, M., P. Pilewskie, J. Pommier, S. Howard, P. Yang, A.J. Heymsfield, C. G. Schmitt, D. Baumgardner, and B. Mayer (2005). “Impact of cirrus crystal shape on solar spectral irradiance: A case study for subtropical cirrus”. In: *Journal of Geophysical Research: Atmospheres* 110.3, pages 1–17.

Wiesenekker, J. M., P. Kuipers Munneke, M. R. van den Broeke, and C. J. P. Smeets (2018). “A multidecadal analysis of Föhn winds over Larsen C ice shelf from a combination of observations and modeling”. In: *Atmosphere* 9.5.

Wilson, D. R. and S. P. Ballard (1999). “A microphysically based precipitation scheme for the UK Meteorological Office Unified Model”. In: *Quarterly Journal of the Royal Meteorological Society* 125.557, pages 1607–1636.

Wilson, D. R., A. C. Bushell, A. M. Kerr-Munslow, J. D. Price, and C. J. Morcrette (2008). “PC2: A prognostic cloud fraction and condensation scheme. I: Scheme description”. In: *Quarterly Journal of the Royal ...* 134.October, pages 2093–2107. arXiv: `arXiv:0801.1618v2`.

Wiscombe, W.J. and S.G. Warren (1980). “A Model for Spectral Albedo I: Pure Snow”. In: *Journal of the Atmospheric Sciences* 37, pages 2712–2733.

Yoshimura, K. and M. Kanamitsu (2008). “Dynamical global downscaling of global reanalysis”. In: *Monthly Weather Review* 136.8, pages 2983–2998.

Yu, L., Z. Zhang, M. Zhou, S. Zhong, D. Lenschow, H. Hsu, H. Wu, and B. Sun (2010). “Validation of ECMWF and NCEP-NCAR reanalysis data in Antarctica”. In: *Advances in Atmospheric Sciences* 27.5, pages 1151–1168.

Zhang, T., K. Stamnes, and S. A. Bowling (1996). “Impact of Clouds on Surface Radiative Fluxes and Snowmelt in the Arctic and Subarctic”. In: *Journal of Climate* 9.9, pages 2110–2123.

Abbreviations

Abbreviation	Definition
ASL	Amundsen Sea Low
AWS	Automatic weather station
CASIM	Cloud and AeroSol Interacting Microphysics
CCN	Cloud condensation nuclei
ENSO	El Niño Southern Oscillation
INP	Ice nucleating particle
IWP	Ice water path
LW	Longwave radiation
LWP	Liquid water path
MetUM	Met Office Unified Model
MSLP	Mean sea level pressure
RA1M	Regional Atmosphere 1 – mid-latitude configuration
RA1T	Regional Atmosphere 1 – tropical configuration
SAM	Southern Annular Mode
SEB	Surface energy balance
SMB	Surface mass balance
SW	Shortwave radiation